Vortex-induced air entrainment rate at intakes

Versuchsanstalt für Wasserbau
Hydrologie und Glaziologie
der Eidgenössischen
Technischen Hochschule Zürich

Mitteilungen 220

Vortex-Induced Air Entrainment Rate at Intakes

Georg Möller

Zürich, 2013

Herausgeber: Prof. Dr. Robert Boes

Zitiervorschlag für VAW-Mitteilungen:

Möller, G. (2013).
Vortex-Induced Air Entrainment Rate at Intakes.
Mitteilungen 220, Versuchsanstalt für Wasserbau, Hydrologie und Glaziologie (VAW),
R. M. Boes, Hrsg., ETH Zürich.

Im Eigenverlag der
Versuchsanstalt für Wasserbau,
Hydrologie und Glaziologie
ETH Zürich
CH-8092 Zürich

Tel.: +41 - 44 - 632 4091
Fax: +41 - 44 - 632 1192
e-mail: info@vaw.baug.ethz.ch

Zürich, 2013

ISSN 0374-0056

Digital Object Identifier (DOI): 10.3929/ethz-a-009932182

Preface

For a long time, intakes at pressurized conduits were designed according to the zero-air-criterion, i.e. no air at all was allowed to reach the intake section, given the adverse effect of air on conduit flow itself and on the downstream hydraulic machinery. To ensure this criterion, either conservative intake submergence or costly structural measures have to be kept or taken, respectively. An alternative intake design would allow for air to enter the conduit which is then removed by de-aeration devices such as small domes at the tunnel ceiling, where air bubbles accumulate and are then evacuated through a rising drill hole to the atmosphere. These de-aeration devices have been investigated in a former VAW Doctoral Dissertation. Their proper design requires knowledge of the air supply, however, which was not available until now.

In his Doctoral Dissertation, Mr. Möller has closed this gap by analyzing the air entrainment rate at horizontal intakes in terms of typical hydraulic parameters. Most importantly, he presents an exponential relation between the air entrainment rate and the submergence Froude number. For a given intake diameter and submergence, the air discharge may now be quantified, allowing for an adequate design of de-aeration devices in pressurized systems. This so-called air-allowance-criterion may be quite cost-efficient by enabling a better reservoir storage management due to a lower admissible drawdown level. Based on the measured air entrainment, a standard critical submergence for the zero-air-criterion has also been developed, which is more severe than the well-known formula of Knauss. Moreover, Mr. Möller proposes new threshold values for Reynolds and Weber numbers to be applied in Froude scale modeling of intake vortices for negligible scale effects of viscous and surface tension forces. These results are an important step forward in the understanding of the air entrainment processes by intake vortices. They further represent a valuable data source for the calibration and validation of numerical simulation tools.

I wish to express my gratitude to swiss*electric* research and the Swiss Federal Office of Energy, who financially supported Mr. Möller's work. My thanks also go to Pöyry Energy AG for their input and to Prof. Dr. A.J. Schleiss, EPF Lausanne, and Prof. J. Gulliver, University of Minnesota, for taking over co-reviews.

Zurich, July 2013 Prof. Dr. Robert M. Boes

Abstract

This research project deals with the investigation, description, and understanding of air entrainment rates due to intake vortices. Large-scale physical model tests have been conducted at VAW in a 50 m^3 laboratory steel tank. The horizontal velocity field around the vortex is measured by 2D Particle Image Velocimetry system. A de-aeration system enables continuous measurements of air entrainment rates. The transferability from model scale test to prototypes is validated via scale family tests. As a result, limiting values for investigations regarding air entrainment due to vortices are developed. The probability of occurrence of intake vortices, the size of the air core, the velocity field, and the related air entrainment rate are compared and analyzed, resulting in two practical design approaches: These both guidelines, an intrinsic and an extrinsic one, enable for the first time to pre-estimate the amount of air that is entrained into the pressure system of hydropower plants (HPP) by intake-vortices. Moreover, a new approach is developed which enables the determination of the critical submergence. The physical process of air entrainment and, therefore, the flow through the air-core tube is examined and a new hypothesis concerning the driving process of air-core flow is developed. With these findings the efficiency of a HPP can be improved significantly, especially with regard to storage management operation as well as according to the design of de-aeration counter-measures.

Kurzfassung

In dieser Arbeit wird der Lufteintrag durch Einlaufwirbel erstmals systematisch untersucht und beschrieben. Kernstück bildet dabei ein 50 m^3 grosser Stahltank eines grossmassstäblichen, physikalischen Modells. Ein 2D Particle Image Velocimetry System ermöglicht die Messung des horizontalen Geschwindigkeitsfeldes des Wasserkörpers um den Wirbel, und ein komplexes Entlüftungssystem erlaubt eine kontinuierliche Messung der Lufteintragsrate. Die Übertragbarkeit der Modellresultate auf Prototypmassstäbe wird mittels Modellfamilienuntersuchungen nachgewiesen. Aus dieser Validierung werden Grenzwerte zur Untersuchung von lufteinziehenden Wirbeln im Modell abgeleitet. Hauptresultate wie die Wahrscheinlichkeit des Auftretens von Einlaufwirbeln, die Grösse des Luftschlauchs, das Geschwindigkeitsfeld um den Wirbel und vor allem die Lufteintragsrate sind die Basis zur Ableitung zweier Bemessungsansätze für die Praxis: Mit Hilfe je eines intrinsischen und eines extrinsischen Berechnungsansatzes ist es nunmehr zum ersten Mal möglich, die Lufteintragsrate von Einlaufwirbeln in Drucksysteme von Wasserkraftanlagen (WKA) zu bestimmen. Darüber hinaus wird ein neuer Ansatz zur Berechnung der kritischen Überdeckungshöhe von Einläufen basierend auf den analysierten Lufteinträgen entwickelt. Der physikalische Prozess des Lufteintrags und damit auch der der Strömung durch den Luftschlauch wird hinsichtlich des antreibenden Prozesses analysiert. Durch die erzielten Erkenntnisse kann der Wirkungsgrad von Wasserkraftwerken nun deutlich verbessert werden. Dies gilt insbesondere im Hinblick auf die Bewirtschaftung von Speichern und für die Gestaltung von Entlüftungseinrichtungen sowie den Umgang mit Luft in Drucksystemen von Wasserkraftanlagen.

Contents

Notation

notation	description	unit	equation
Latin symbols			
A	area	m^2	
a	head wall distance	m	
b	bottom clearance	m	
C	correlation strength	-	
C_a	air concentration	-	
C_Q	discharge coefficient	-	$C_Q = v/\sqrt{2gh}$
c	speed of sound	m/s	
D	intake diameter	m	
DN	nominal diameter	mm	
d_ac	air-core diameter	m	
$d_{\mathrm{ac,\,s}}$	air-core shadow diameter	m	
d_e	diffracted particle diameter on image	m	
d_p	mean particle diameter	px	
d_px	particle diameter recorded on image	px	
d_r	pixel pitch	m	
d_s	diffraction-limited minimum image diameter	m	
d_τ	recorded mean particle diameter on image (image plane)	m	
F_co	combined Froude number	-	$\mathsf{F}_\mathrm{co} = v_D/\sqrt{\mathrm{g}h}$
F_D	intake Froude number	-	$\mathsf{F}_D = v_D/\sqrt{\mathrm{g}D}$
F_h	submergence Froude number	-	$\mathsf{F}_h = v_h/\sqrt{\mathrm{g}h}$
f	focal length	mm	
$f_\#$	f-number	-	
g	gravitational acceleration	$\mathrm{m/s}^2$	
H	intake section height	m	
h	intake submergence (w.r.t. axis)	m	
h/D	relative intake submergence	-	
h_w	de-aeration height	m	

(to be continued)

notation	description	unit	equation
IQR	interquartile range		
K	Kolf number	-	$\mathsf{K}= \Gamma/(v_D D)$
k	turbulent kinetic energy		
l_{ac}	air-core length	m	
$\mathbf{L}$	angular momentum	m^2/s	
L	length	m	
M	Mach number	-	$\mathsf{M} = v/c$
M	magnification	-	
N_Γ	circulation number	-	$N_\Gamma = \Gamma D/Q_{\mathrm{w}}$
n	number	-	
o	dummy variable used for mathematic notations	-	
I	image intensity		
P	wetted perimeter of the cross-section	m	
Pr	prediction band		
p	pressure	bar	
Q	discharge	m^3/s	
Rf	reduction factor	-	
R_D	intake Reynolds number	-	$\mathsf{R}_D = v_D D/\nu$
R_{R}	radial Reynolds number	-	$\mathsf{R}_{\mathrm{R}} = Q_{\mathrm{w}}/(\nu h)$
R_{s}	specific gas constant: $\sim$287.058	J/(kg K)	
Ro	Rossby number	-	
r	radius	m	
S_{VT6VT6}	spectra of vortex type 6 duration	s^2/Hz	
s	length a long a circular path		
T	absolute temperature: $273.15 + \vartheta$	K	
t	time	s	
V	volume	m^3	
u, v	velocities	m/s	
v_{ac}	air-core flow velocity	m/s	
v_D	intake velocity	m/s	$v_D = Q_{\mathrm{w}}/(\pi/4D^2)$
W_D	intake Weber number	-	$\mathsf{W}_D = v_D\sqrt{\rho D/\sigma}$
W_h	submergence Weber number	-	$\mathsf{W}_h = v_h\sqrt{\rho h/\sigma}$
x, y, z	coordinates		

Greek symbols

α	angle	$^\circ$	
β	air entrainment rate	-	$\beta = Q_{\mathrm{a}}/Q_{\mathrm{w}}$
Γ	circulation	m^2/s	
γ	skewness	-	

(to be continued)

notation	description	unit	equation
δ	depth of field	m	
ϵ	eddy viscosity	kg/(m s)	
η	dynamic viscosity	kg/(m s)	
ϑ	temperature	°C	
κ	heat capacity ratio	-	
λ	scale	-	
λ_l	wavelength	nm	
ν	kinematic viscosity	m^2/s	
ξ	critical submergence factor	-	
π	mathematical constant: ∼3.14159	-	
ρ	fluid mass density	kg/m^3	
σ	surface tension	N/m	
τ	shear stress	$\mathrm{kg}/(\mathrm{m\ s}^2)$	
Φ	vector map angle	°	
Ω	vorticity	1/s	
ω	angular velocity	1/s	

mathematics

Δ	difference
f	function
∇	nabla symbol
∂	partial operator
$\vec{o}$	vector
$\mathbf{o}$	matrix
$\dot{o}$	measurements reduced to a point in time series
$\bar{o}$	mean value of time series
$\breve{o}$	mean value of vortex phases
$\tilde{o}$	median value of time series
$\hat{o}$	running average

subscripts

a	air
ac	air-core
atm	atmospheric
cr	critical value
co	combined
D	diameter
H	hydraulic

(to be continued)

notation	description	unit	equation
i	time step or state		
j	vortex phases		
ll	lower limit		
m	time steps within a vortex phase		
o	orifice		
R	radial		
ul	upper limit		
w	water		

abbreviations

ADV	acoustic doppler velocimetry
AOI	area-of-interest
ARL	Alden research laboratory
CCD	charge-coupled device
CSSS	critical spherical sink surface
CW	clockwise
CCW	counter-clockwise
DNS	direct numerical simulation
FOV	field-of-view
HPP	hydro power plant
IA	interrogation area
LES	large eddy simulation
MAG	magnitude
MID	magnetic flow meter
PIV	particle image velocimetry
PSHPP	pumped-storage hydro power plant
RANS	Reynolds-averaged Navier Stokes eq.
SST	shear stress transport

basic dimensions

L	length
T	time
M	mass

Chapter 1

Introduction

1.1 Background

Air entraining vortices are a typical phenomenon at intakes of hydroelectric powerplants (HPP). The possibility of their occurrence and the resulting impact on the pressure system have to be considered during the design and the operation of HPPs. Fig. 1.1 gives a schematic illustration of the phenomenon and the governing boundary conditions.

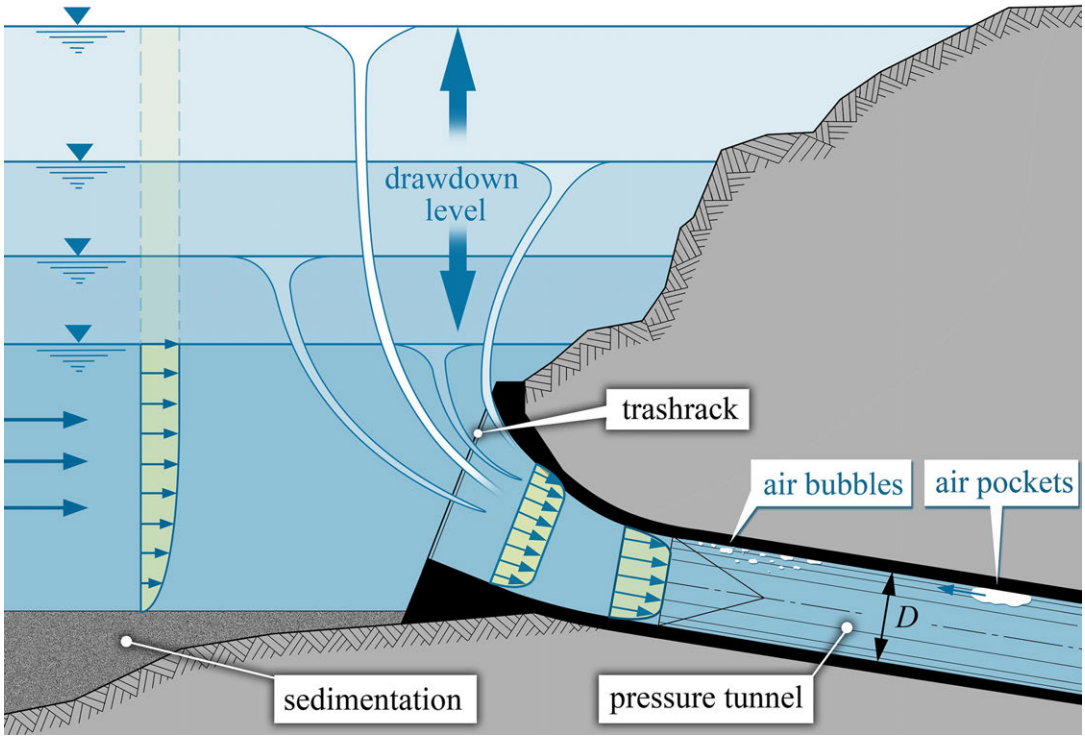

Figure 1.1: Schematic illustration of the phenomenon of air entraining intake vortices with respect to the boundary conditions. The drawdown level is restricted by air entraining vortices and the avoidance of sediment entrainment.

On the one hand the minimal drawdown level is restricted by the occurrence of air-entraining vortices. On the other hand the entry of sediment to the pipe system can be avoided by low reservoir velocities that are, in turn, correlated to high water levels.

In recent years the interest in renewable, flexible, and at any time guaranteed energy supply is growing. Recent market developments in the EU as well as in Switzerland dominate the electric energy sector: Significant changes are caused by the high demand of pump storage capacity and the probable production gap caused by e.g. the nuclear power phase-out. In 2011[1] approximately 54 % of the electric power supply in Switzerland were covered by HPPs. To ensure flexibility and to expand this proportion a large number of the existing HPPs are currently in revision or will be refurbished within the next decades. When a HPP is retrofitted, often a power increase and almost always an increase of flexibility is aimed at. The design of new HPPs has to be adapted to these challenges as well. The intensification of HPP operation has direct consequences on the corresponding hydraulic systems and leads to new demands in their design.

Generally, intakes are one of the main components of every water supply system. HPPs contain a waterway system which provides water to the hydraulic machinery. The water withdrawal is subjected to strict requirements. A basic criterion is the requirement of a single-phase, i.e. pure water flow into the hydraulic system. Due to the overall negative consequences of air in pressure systems a zero-air-criterion has evolved as a classical approach to be on the safe side.

To design an intake, and especially to determine its vertical location, is therefore a task between the conflicting priorities of defining the drawdown level with respect to vortex formation and avoiding sediment entrainment. The latter yields to intakes at higher locations as sufficient reserves, called dead storages, have to be considered to cope with continued sedimentation. Consequently, higher drawdown levels are needed. Particularly, the minimal distance between the drawdown level and the vertical location of the intake to avoid air entraining vortices is based on complex flow structures which depend in turn on different topographies and intake shapes. Intake-vortices, if present, have a considerable potential for air entrainment and are a major source of air entrainment. Significant reserves to avoid their occurrence are required. This is a major problem for the design, the retrofitting and the operation of intakes and leads to a high submergence. Hence, the consequence is a limitation in terms of storage management and a loss of storage volume, respectively. Nevertheless, the entrainment of air cannot be totally prevented, especially at conditions close to operational limits, as even a conservative design constitutes a residual risk.

Air in pressure systems changes the flow properties from a single-phase to a two-

[1] Year 2011: 33'795 GWh of 62'881 GWh, source: Swiss Federal Statistical Office (FSO)

phase flow. This may have strong consequences on the operation, safety, and efficiency of the HPP. These effects can be divided into three main groups: (1) reduction in efficiency of turbines and pumps, (2) unsteady flow behavior, i.e. pulsation and pressure surges in the system with corresponding mechanical loads on the involved components, and (3) stationary effects, e.g. flow reductions from stationary air bubbles and local corrosion damage, respectively.

Two general types of measures are possible: the zero-air-criterion that keeps any air away from the hydraulic system, and the air-allowance-criterion that handles entrained air appropriately. Both criterions are described next. The zero-air-criterion aims to avoid air entrainment by high submergence and low intake velocities, or by anti-vortex devices. Almost one hundred years of research have led to a large number of publications regarding intake vortices and their avoidance. The unique character and the large amount of unsteadiness impede a general solution. In contrast to the zero-air-criterion, the air-allowance-criterion tolerates air entrainment and determines the consequences by using a different design approach. The knowledge of the air entrainment rate β due to intake vortices is a prerequisite to apply an air-allowance-criterion. Once this rate is determined, vortices can be classified as critical ones that must be prevented, or as uncritical ones that may be permitted.

A de-aeration device enables a sustainable intake design by allowing air to enter into the pressure system. Wickenhäuser (2008) gives a design guideline that depends on water discharge, conduit diameter, and the inflowing amount of air, i.e. a proxy of the entrainment rate β. However, knowledge about the quantity of entrained air is required to apply Wickenhäuser's guideline for an appropriate design. Then, the zero-air-criterion could be replaced by a flexible assessment strategy. Knowing the air entrainment rate and quantifying the resulting potential damages finally allows the design of countermeasures such as de-aeration systems. Thereby, the efficiency of a HPP would be improved, especially with regard to storage management. Common measures of zero-air-criterion can be used as well, e.g. the design of an anti-vortex device could retain the efficiency and flexibility. However, this device may need to be of large dimensions and thus it is quite expensive. A de-aeration device is a beneficial alternative and is worth an economical consideration regarding the design of intakes. However, the design of a de-aeration device requires knowledge about air entraining vortices. A forecast tool is needed that is able to adequately estimate the air entrainment rate β.

1.2 Objectives of the Study

This research project focuses on the determination of air entrainment due to intake-vortices. Using a large-scale experimental facility the physical processes of air-entraining vortices are investigated. The phenomenon of air entrainment is highly unstable while having variable boundary conditions. The study aims at two main goals that are described in the following.

First Aim. The first aim of this research project is to determine the air entrainment in terms of the ratio between air discharge Q_{a} and water discharge Q_{w}, i.e. the air entrainment rate β. Sophisticated measurement techniques have to be developed and applied to determine β accurately. The results are to be developed gradually. First results will be assessed to quantify air entrainment. Then a guideline to design and to operate intakes of HPPs with respect to an acceptable, damage-free air entrainment shall be derived, while β can be estimated via classical flow parameters such as intake velocity or submergence. The guideline will categorize three stages of β: First, $\beta = 0$ will be defined as the critical submergence and compared to the common formulas to enhance the design procedure. Then, de-aeratable air entrainment rates are identified. Finally, air entrainment rates that exceed the de-aeration capacity are tagged as well. The latter two-phase flow has to be avoided for safety and economic reasons. The circulation Γ as a parameter describing the rotating flow field is hypothesized to correlate with β. With respect to Γ, a second and more precise guideline shall be established. If present, a correlation would give a linkage between numerical simulations that provide the far-field of the air entraining intake-vortex, characterized by Γ, and the resulting air in the pressure systems, characterized by β.

Second Aim. The second aim of this research project is to significantly improve the understanding of the complex phenomena of the air entrainment process. The velocity field around the vortex shall be tested for its applicability to the solved 2D Navier-Stokes equations of a free vortex. Furthermore, a refinement of the common vortex type classification for air entrainment (Hecker, 1987) shall be verified. In addition, the intensity of the air flow through the air core tube should be analyzed, e.g. with respect to the governing processes.

Once these goals are fulfilled, an enhanced intake design procedure and a significantly improved storage management, respectively, will become feasible.

Chapter 2

Fundamentals

Abstract. *This chapter provides an introduction to the hydraulics of intake-vortices. After a general explanation of vortices the mechanism of intake-vortex formation is discussed. Next, a literature review is given to intake-vortex investigations while focusing on air in pressure systems of hydropower plants (HPP). Practical guidelines are discussed that act as counter measures to avoid air entrainment. Then, a dimensional analysis is conducted for the phenomenon of air entrained by vortices. Finally, concluding remarks are given that summarize the lack of knowledge regarding the phenomenon of air-entraining intake-vortices.*

2.1 Vortices in Fluid Mechanics

Definitions. Levi (1972) defines two basic types of natural vortices. The first type of vortex occurs behind obstacles or close to wall expansions, known as wake eddy or lateral whirl, respectively. The second vortex type develops independently of such obvious asymmetries. In hydraulics this kind of vortex is known as drain or intake-vortex, respectively.
Lugt (1983) states that vortices are present everywhere in nature and in technical applications. He defines two main clauses:

- A vortex is the rotating motion of a multitude of material particles around a common center.
- The angular velocity of matter at a point in continuum space is called vorticity.

The former definition is discussed next, the latter aspect is dealt with in the subsequent section.

Rotating Motion. One way to distinguish between different vortices is a classification based on the path where particles rotate (Fig. 2.1). For a closed path the vortex is called plane. The closed path can be concentric circular (Fig. 2.1a) or asymmetrical (Fig. 2.1b). A special form of plane vortices is the cylindrical vortex, which has closed paths and a spatial expansion. However, in most of the cases vortices do not have a closed path. The path lines are not perpendicular to the axis of rotation and have a spatial structure. The spiral vortex (Fig. 2.1c) is an example of such a kind of vortex with spatial structure. Typically, a spiral vortex occurs at intakes. This kind of vortex can be classified by its diameter or by the ratio of its diameter to its axis length. For a high value of the latter ratio, e.g. the 2D case, the vortex gets a characteristic disk-like shape (Fig. 2.1d). A hurricane with lateral expansions of about 1000 km and confined by the atmosphere to a height of 10 km gives a typical example. If the ratio of diameter to axis-length is small the vortex is denoted to be columnar (Fig. 2.1e). Here, a typical example can be given by dust devils. These local vortices have lateral diameters of up to 10 m and heights of about 1000 m. The ratio of diameter to axis-length is contrary to those of hurricanes.

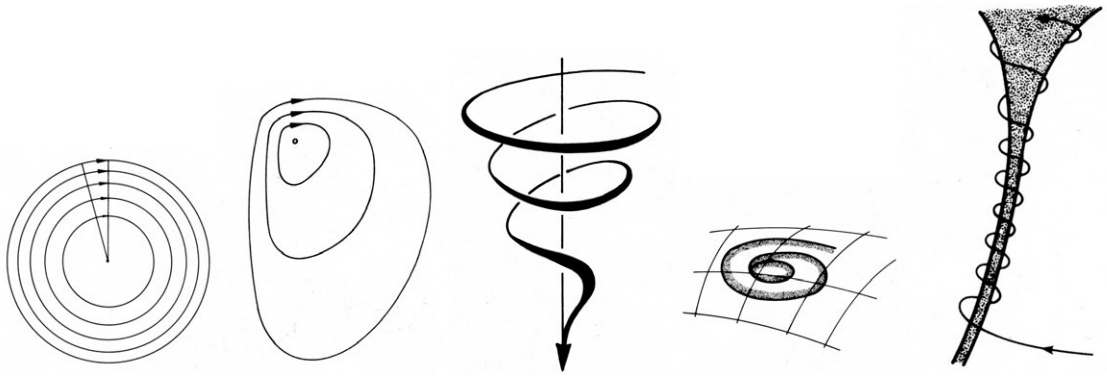

(a) concentric circular (b) asymmetrical (c) spiral (d) disk-like (e) columnar

Figure 2.1: Classification of vortices by regarding particles' pathlines in the fluid motion (Lugt, 1983).

Fig. 2.2 shows the three basic modes of how a particle can move. Vortical or rotational motion is one of the basic kind of motion of each fluid at a point in space. The two other modes are translation and deformation. Every motion can be combined by these three modes.

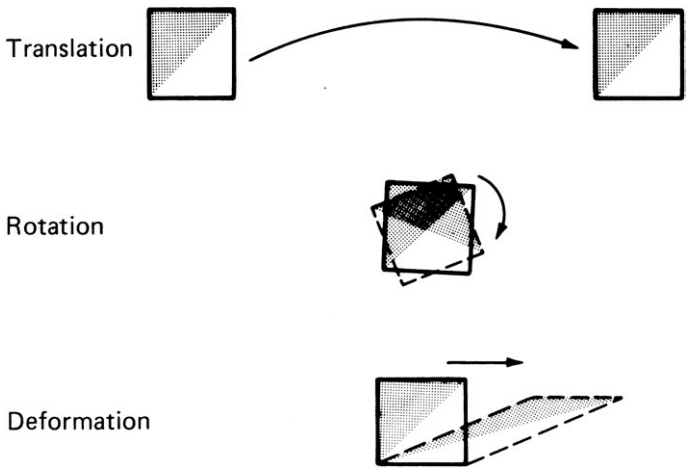

Figure 2.2: Basic modes of motion (Lugt, 1983).

Angular Velocity. The nomination of the angular velocity as vorticity was originally given by Cauchy[1] and Stokes[2]. The meaning is that there is no vortex without vorticity (see chapter 2.2.2). However, the presence of vorticity does not implicitly cause a vortex. Flow without rotation and without vorticity is called potential flow or irrotational flow.

2.2 Mechanism of Intake-Vortex Formation

2.2.1 Surface Vortex vs. Subsurface Vortex

To characterize vortices that occur at intakes a distinction can be made by identifying the location of their generation. A free-surface vortex initiates from the surface of the water, enabling the entrainment of air and angular momentum, called swirl. The origin of a subsurface vortex is situated at a boundary, e.g. the wall or the bottom. Here only swirl, but no air can be entrained. Nevertheless, a vortex core tube can be formed by a large pressure decrease where water vapor is present, known as cavitation. Furthermore, the core can contain dissolved air. They form at high intake velocities and/or low submergence. Particles can be entrained from the bottom into the intake. The formation of surface vortices is independent of subsurface vortices. They could appear either separately or together (Anwar, 1983).

Hereinafter a free surface vortex will be denoted as intake-vortex.

[1]Baron Augustin-Louis Cauchy (⋆21 August 1789 in Paris, †23 May 1857 in Sceaux) was a French mathematician who was an early pioneer of analysis.

[2]Sir George Gabriel Stokes (⋆13 August 1819 in Skreen, †1 February 1903 in Cambridge), was an Irish mathematician, physicist, politician and theologist.

2.2.2 Vorticity

General. Vorticity describes the spin of fluid elements. It is a fundamental concept in fluid mechanics originally from Cauchy and Stokes. Vorticity is defined as a vector quantity at every point within the fluid:

$$\vec{\Omega} = \text{curl } \vec{v} = \nabla \times \vec{v} = \left(\frac{\partial}{\partial x}, \frac{\partial}{\partial y}, \frac{\partial}{\partial z}\right) \times (v_x, v_y, v_z) = \begin{bmatrix} \frac{\partial v_z}{\partial y} & - & \frac{\partial v_y}{\partial z} \\ \frac{\partial v_x}{\partial z} & - & \frac{\partial v_z}{\partial x} \\ \frac{\partial v_y}{\partial x} & - & \frac{\partial v_x}{\partial y} \end{bmatrix}. \quad (2.1)$$

The vorticity vector $\vec{\Omega}$ is defined as the curl of the velocity vector $\vec{v}$. The definition gives a value of the rotation or spin of a fluid element. For simplification, the vorticity vector $\vec{\Omega}$ is often called vorticity.
The physical interpretation of this microscopically-scaled process is non-trivial (Lugt, 1985), especially in case of an intake-vortex that is quite larger than the typical extension of fluid motion described by vorticity. Nonetheless, in physical considerations the term rotation is closely associated with vorticity and thus an intake-vortex depends on vorticity.
To explain vorticity, Tritton (1988) chooses a 2D channel flow, where x and y are the horizontal components and z the vertical one. However, in this case, the z-component of the vorticity is non-zero. The change of the z-component leads to rotation of the fluid particles. The value of the vorticity is large if the change in velocity profile is large as well. The three-dimensional formulation in eq. 2.1 can be simplified to:

$$\Omega_z = \left(\frac{\partial}{\partial x}, \frac{\partial}{\partial y}\right) \times (v_x, v_y) = \frac{\partial v_y}{\partial x} - \frac{\partial v_x}{\partial y}. \quad (2.2)$$

Tritton (1988) gives three examples concerning the physical significance of vorticity in 2D channel flow. They are described below and illustrated in Fig. 2.3.

1. A fluid is rotating as rigid body with angular velocity ω. The vorticity is equal at every point. In cylindrical polar coordinates a description can be given by:

$$v_\mathrm{t} = \omega r,\ v_r = v_z = 0 \quad (2.3a)$$
$$\Omega_z = 2\omega,\ \Omega_r = \Omega_\mathrm{t} = 0\ , \quad (2.3b)$$

   where r denotes the radius from the vortex center, Ω_z the z-component of the vorticity, Ω_r and Ω_t are the radial and tangential vorticity component.

2. A fluid particle is moving on a circular path about the z-axis, but with a different radial distribution of tangential velocity:

$$v_\mathrm{t} = \frac{\text{const.}}{r},\ v_r = v_z = 0. \tag{2.4a}$$

$$\Omega_\mathrm{t} = 0,\ \Omega_r = 0, \tag{2.4b}$$

$$\Omega_z = \frac{1}{r}\frac{\partial}{\partial r}(r v_\mathrm{t}) = 0 \text{ for } r \neq 0\ . \tag{2.4c}$$

The tangential velocity v_t varies inversely with the radius r. According to Stokes's theorem, Ω_z becomes infinite at the center, thus a singularity occurs. Irrotational flow, similar to potential flow, is present except at the center. However, this flow does not occur in practice, as theoretically infinite high vorticity had to be present in an infinitive small region. Furthermore, in the surrounding field the vorticity is equal to zero.

3. Each fluid particle moves on a straight line but it has vorticity, giving the triviality of shear flow. Then, the flow is described by

$$v_x = v_x(y),\ v_y = v_z = 0 \tag{2.5a}$$

$$\Omega_x = \Omega_y = 0,\ \Omega_z = -\frac{\partial v_x}{\partial y}\ . \tag{2.5b}$$

Fig. 2.3a illustrates the concept (1) of an isolated rigid particle moving on a circular path without rotating. Its vorticity corresponds to its changing orientation.

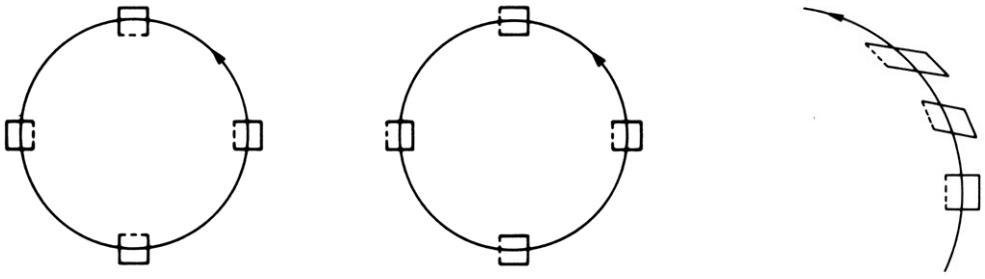

1) Rigid body rotation 2) Circulation without rotation 3) Circulation without vorticity

Figure 2.3: Physical significance of vorticity in 2D after Tritton (1988). One side of each particle is shown dotted to indicate its orientation. (1, 2) Successive positions of solid particles. (3) Positions and shapes of initially squared fluid particles exaggerated relative to the radius of the circle.

As shown in Figs. 2.3b and 2.3c, irrotational flow (2) and simple shear flow (3) are entirely different. Rotation or vorticity changes the orientation of a fluid particle in space. However, their motion stays on a closed path. Particles in irrotational flow move around a circular path and change their orientation in space. However, they

get deformed as well. Their vorticity is zero. Particles in simple shear flow move in a straight line and have vorticity. For small displacements, the particles are not changing their orientation. To give zero vorticity the sides of the particles rotate to be perpendicular to the path.

Shear Flow Vorticity. The shear flow pictured in Fig. 2.4 is rotational flow on straight lines with vorticity. The initially squared fluid particle changes its shape by α to a parallelogram. Similar geometries may be reached by a non-rotational distortion. Considering small displacements, instantaneously two perpendicular sides rotate and two sides do not rotate. Therefore, the average shear is non-zero and vorticity is present.

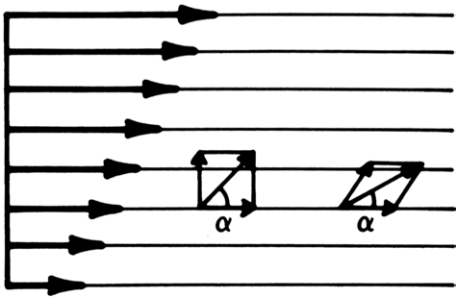

Figure 2.4: Parallel shear flow (Lugt, 1983).

Fig. 2.5 shows two regions which can be distinguished in a flow along a boundary. The velocity profile near the surface is associated with the vorticity distribution. Near the surface, a thin friction layer, known as boundary layer, exists in which vorticity is present. The region outside is essentially frictionless. Far away from the body surface, fluid layers with vorticity can exist as well. This happens when boundary layers detach from the surfaces and move into the fluid. These free boundary layers are known as shear layers or shear flows.

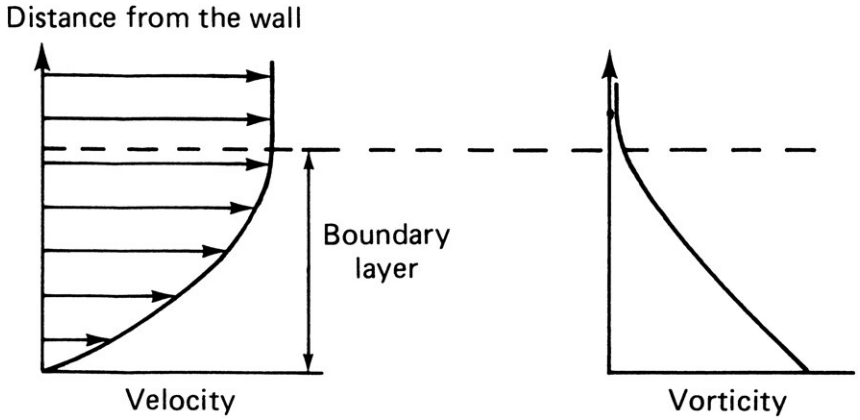

Figure 2.5: Example of vorticity without vortices given by the concept of boundary layer, the distribution of velocity and the vorticity (Lugt, 1996).

Vorticity Tubes. Lugt (1983) gives four prototypes of vorticity tubes as shown in Fig. 2.6. They are described in detail below.

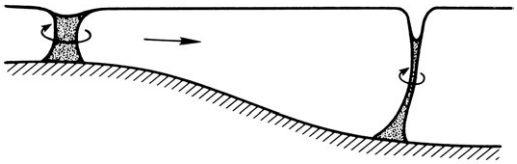

(a) Stretching of a vorticity tube between water surface and river bed due to the increase of the water depth

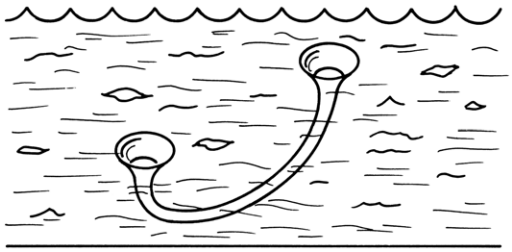

(b) Termination of both ends of a vorticity tube at the surface of the water

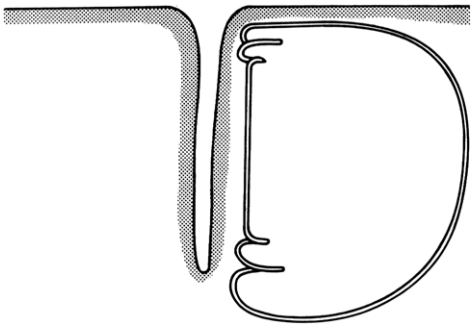

(c) Closed loop of a vorticity tube near a free surface

(d) Corresponding streamline or particle path of vorticity tube with closed loop

Figure 2.6: Samples of vorticity tubes (Lugt, 1983).

Fig. 2.6a shows a perpendicular tube from the water surface of a river to the river bed. Assuming that the decay can be neglected for short distances, the strength of the vorticity is constant. If the tube reaches a region with deeper water, the tangential velocity increases due to the stretching of the tube. The effect is visible by a deeper dimple at the surface. Vortex stretching is a major process in change of vorticity. If the vortex lines are lengthened, the vorticity increases.

The occurrence of such a tube is also possible without being in contact to the river bed. In this case both ends of the tube contact the free surface as shown in Fig. 2.6b. A third form is the appearance of vorticity tubes in a closed loop. Fig. 2.6c shows an example.

The corresponding streamline or particle path is given in Fig. 2.6d. This figure helps to understand the 3D velocity field around an intake-vortex. The generated vorticity increases exponentially on the way from the origin to the intake due to the stretching of vortex lines and tubes, respectively.

Vorticity tubes have to end at a surface or in a closed loop, but not inside the fluid, what is termed as being a solenoidal property. This property is a component of the Kelvin's circulation theorem (Hutter et al., 2011). Space and the corresponding

dominance in the water body is required for the development of such vortex fields. A free-surface vortex often appears if a fluid has to pass through an intake section, independently whether the medium is liquid or gaseous. The origin of vorticity and practical aspects like critical submergences (chapter 2.3.2) of air flow were investigated by De Siervi et al. (1982). They identified two basic mechanisms of intake-vortex generation. The first mechanism is described as follows: The amplification of ambient vorticity leads to a stretching of the vortex lines, which will be drawn into the intake. Fig. 2.7 gives an example. In contrast to the first mechanism, the second one occurs without ambient vorticity. A vortex can arise in an irrotational flow. Along the length of the intake a variation in circulation takes place. Both mechanisms are influenced by the ratio of upstream velocity and intake velocity.

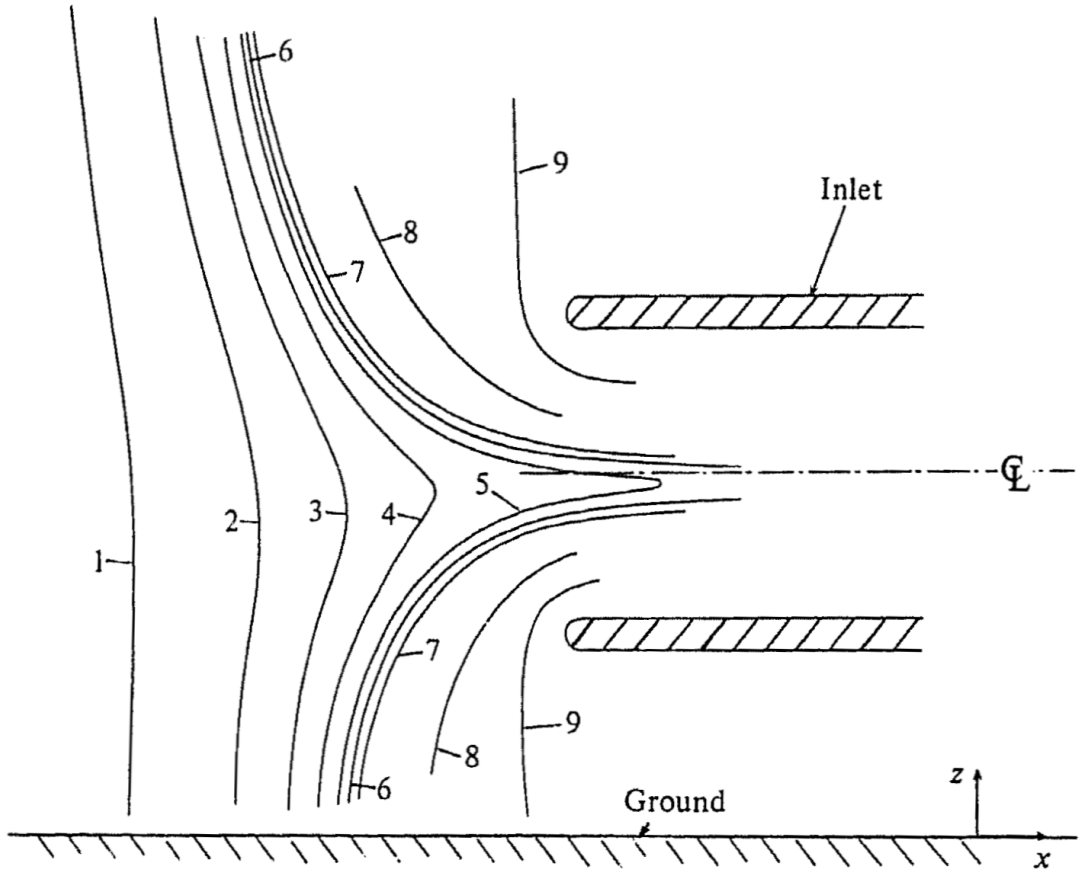

Figure 2.7: Ground vortex investigation of gas-turbines. The termed inlet vortex formates due to vortex line deformation that is initially vertical. This process is also known as vortex line stretching (De Siervi et al., 1982).

The formation of a surface vortex including the onset of a single vortex at an intake was described by Lugt (1983) as follows:

"How do strong vortices like those in pipe intakes form? The explanation is contained in the conservation law of angular momentum. For simplicity, consider a single fluid particle with a tiny angular velocity, located about 30 cm from the outlet. As this

particle is drawn towards the opening, it must increase its azimuthal velocity at a rate inversely proportional to the distance from the opening in order to preserve its angular momentum. At a distance of 0.3 cm from the center of rotation the particle will have increased its velocity 100-fold. Since the angular velocity increases with the square of the distance, the corresponding angular velocity at 0.3 cm distance will have increased 10'000-fold. This may also be expressed in the following way: The number of rotations per second is 10'000 times larger at a distance of 0.3 cm than at 30 cm. This simple although crude calculation shows that a small initial rotation in the fluid is sufficient to create a concentrated vortex."

This can be easily understood by a well-known phenomenon. The example is a rotating ice figure skater with a present angular momentum. Initially, the skater spreads the arms wide out. The angular momentum in this system is constant. To increase the rotation speed, which can be several times per second, the arms have to be pulled. Note, that the angular momentum is still of the same size. Transferred to a reservoir, the whole water body has an angular momentum due to the earth's rotation. Hodkinson (1933) describes how the velocity of a fluid particle increases on the way to the intake assuming that the momentum must be constant. Thus, the pressure in the center of the vortex decreases. This will lead to a pressure drop till the atmospheric pressure is reached and an air core is formed.

Vortices at Hydraulic Structures. Durgin & Hecker (1978) categorize the sources of vorticity at hydraulic structures into three origins, as illustrated in Fig. 2.8. Fig. 2.8a shows the gyration[3] in the approach flow due to the offset. The term gyration is chosen, because it is ambiguous if rotation or circulation exists.

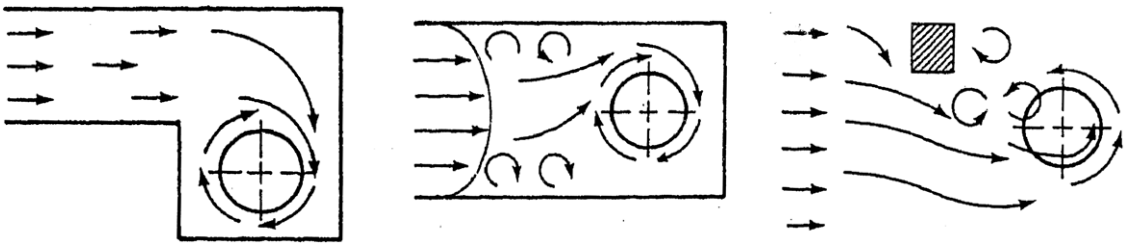

(a) Offset introduction (b) Velocity gradients (c) Obstruction

Figure 2.8: Sources of vorticity at hydraulic structures (Durgin & Hecker, 1978).

The offset introduction is often described as asymmetric approach flow (see Fig. 2.8a). The vorticity flux to the intake is independent of viscosity effects. The velocity profile illustrated in Fig. 2.8b highly depends on the actual viscosity. Due to this, the vorticity develops at the wall itself. The symmetric approach flow in a channel generates vorticity at the boundary layer. The third origin of vorticity that is influenced

[3]Gyration is often used to term a vortex in atmospheric layers.

by viscous effects is pictured in Fig. 2.8c. Behind obstructions or obstacles often a periodically alternating rotation is formed, e.g. Kármán vortex streets. Due to a combination of these three sources of vorticity, a vortex can be initiated near an intake.

Levi (1972) uses friction as criteria to distinguish two different vortex-patterns at hydraulic structures. Vortices of type 1 are induced by shear stress, called friction vortices. Vortices of type 2 are denoted as non-friction vortices. A typical example is an intake-vortex. The mechanism of developing these vortices is attributed to a vorticity distribution in the upstream and near flow field, respectively. Hereby the effect of the stretching process is of major influence.

Fig. 2.9 illustrates the concept of the generation of a non-friction vortex at a horizontal intake, as proposed by Levi (1972). Here, the approach flow is orientated horizontally. Drain and intake-vortices are induced by converging jets. As shown in Fig. 2.9 the jet affects the stagnant region above the intake where the intake vortex is formed.

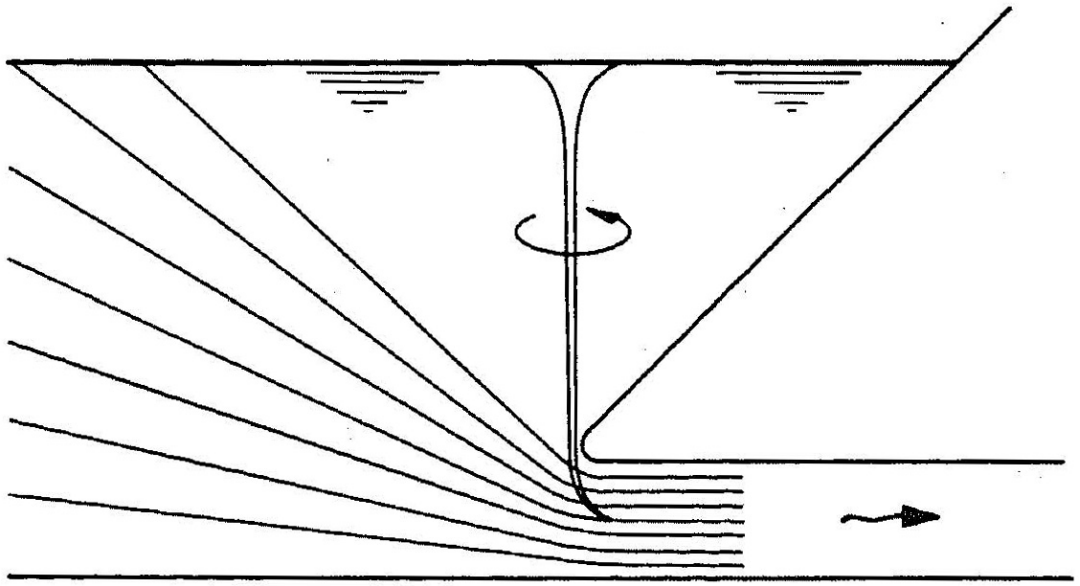

Figure 2.9: Vortex formation due to the flow towards the intake (Levi, 1972). Approach flow is producing the vortex in the stagnant region.

The velocity field around an air-core vortex above a vertical orientated intake, e.g. a hole, is different in comparison to a horizontal orientated intake. A description is given in chapter 2.3.1.

2.2.3 Circulation

In fluid mechanics the circulation Γ is a means to describe the rotation of a flow and is often used as a quantity of the turning of intake-vortices. The circulation *Gamma* is defined as the line integral around a closed curve with the length s of the fluid velocity v. It is described as

$$\Gamma = \oint_L \vec{v} d\vec{s} = \int_A \vec{\Omega} d\vec{A}. \tag{2.6}$$

Eq. 2.6 gives a relation between circulation and vorticity, where A denotes the area within the curve. The curve and the path of integration, respectively, has to be a boundary.

The strength of a vortex is typically characterized by its circulation. Intake-vortices are generated if the strength is high. From the initial vortex formation to a fully developed air-entraining intake vortex some significant phases are passed through. Denny (1956) termed and described the different phases on vortex formation as *"stages in development of air entraining vortex"*. Fig. 2.10 shows a classification of different vortex type stages as given by Alden Research Laboratory (ARL) Holden, USA.

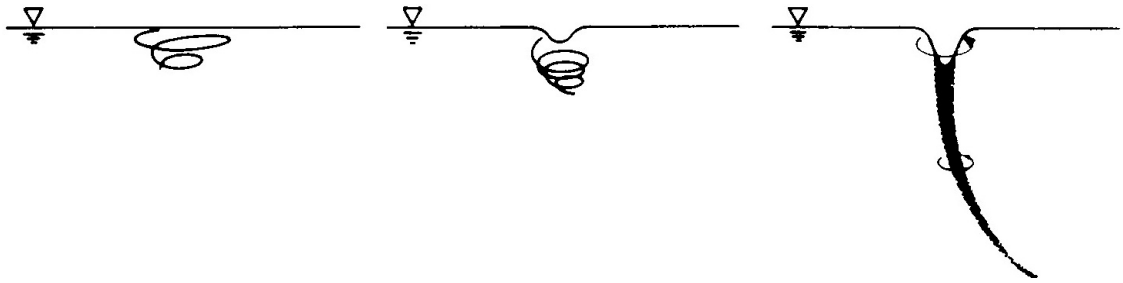

$VT1$: coherent surface swirl

$VT2$: surface dimple; coherent surface swirl

$VT3$: dye core to intake; coherent swirl throughout water column

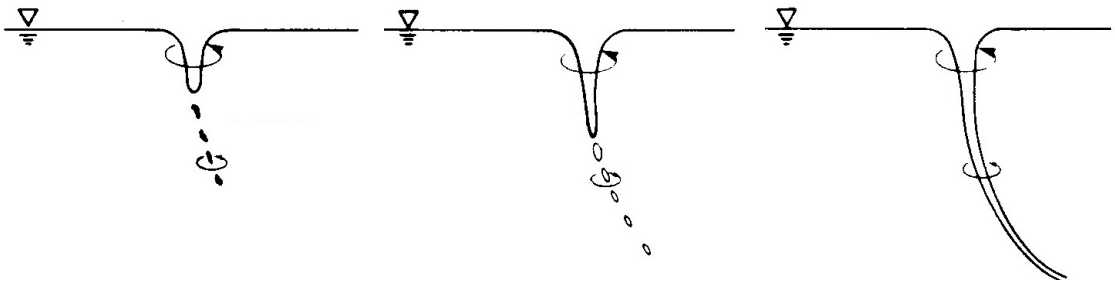

$VT4$: vortex pulling floating trash, but not air

$VT5$: vortex pulling air bubbles to intake

$VT6$: full air core to intake

Figure 2.10: ARL vortex type classification (Hecker, 1987). Recently, this classification has been expanded to vortex type $VT0$ where no activity is present at all.

The stages range from $VT1$, with coherent surface swirl, to $VT6$, a full air core to intake. In recent times, this classification has been expanded to a vortex type $VT0$, i.e. a stage with no activity (Möller et al., 2012).
The vortex types ≤ 5 contain a forced vortex in their cores and a potential vortex in their fields. The vortex type $VT6$ can be assumed entirely as a potential vortex or free vortex. The characteristics of both forced and free vortices are discussed below.
The velocity field around an intake vortex is independent from the diameter of the air core. Tietjens (1960) states that there are two important factors which influence the strength of a vortex: the position in space and the constant $v_i\, r_i$. The strength of a single vortex in which the streamlines are circled around the center can be determined by $v_i\ r_i$. Following eq. 2.6 the circulation of a vortex with a constant velocity v_1 on the circle r_1 reads

$$\Gamma = v_1 \oint ds = 2\pi v_1 r_1 \tag{2.7}$$

Ackeret (1952) quotes Stokes that exact solutions of the hydrodynamic equations exist if the boundary conditions are modified. *"If it can be arranged that the solid boundaries are actually moving with the fluid velocity, then really simple solutions are obtained. Several examples are worked out. As turbulence is unlikely to occur under these conditions the power to move bodies in a viscous fluid at high Reynolds numbers would become extremely low. It seems that even a partial fulfilment of these changed conditions would be of practical interest."* Moreover, Rott (1958) introduces a model which describes a vortex by the Navier-Stokes equation by some simplifications mainly concerning the viscosity. The exact solution of the two-dimensional Navier-Stokes equation for axisymmetrical flow is given by Granger (1966), assuming an incompressible fluid in a steady 3D rotational flow. Thus, $\Gamma/(2\pi)$ is constant.

2.2.4 Combined Vortex

Rankine (1861) was one of the first who conducted intake-vortex investigations. He defined a free spiral vortex, a forced vortex and both together yielding a combined vortex. Due to his pioneering work, until today the combined vortex is also known as a Rankine vortex. The term combination points at the hypothesis of a vortex being a combination of a rotating core and a circulating area. Fig. 2.11 shows a cross-sectional view of a combined vortex above a drain hole. In the upper part the depression or dimple of the water surface is plotted, in the center part the tangential velocity and the vorticity distribution are given.
The outer part is the free vortex, also called vortex field. The inner part is a forced vortex, also called vortex core. The water surface has two inflection points exactly at the border of the two kinds of vortices. The distance from the center of the

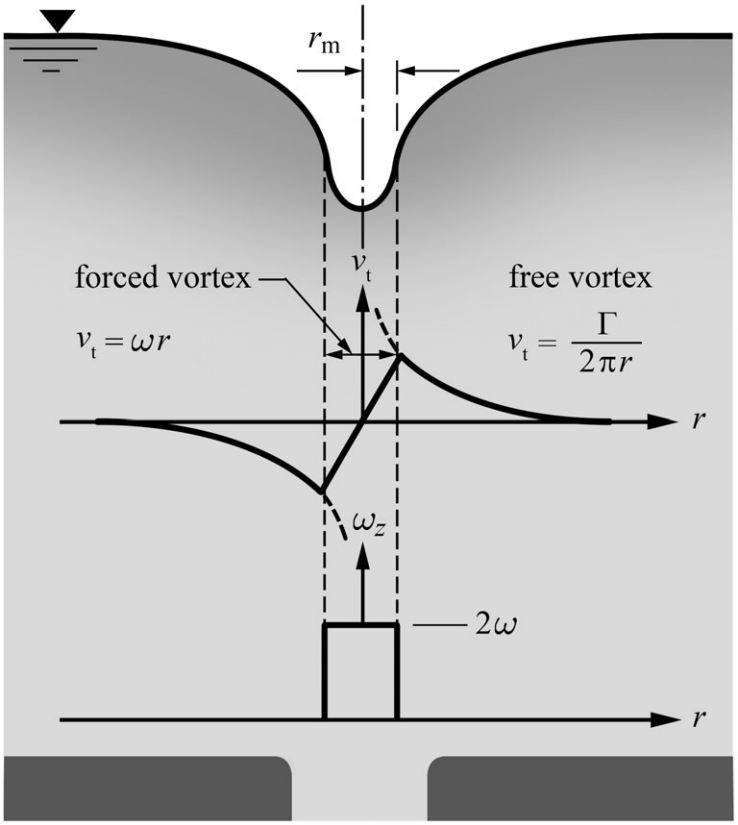

Figure 2.11: Cross-section of an combined vortex above a drain hole. Velocity and vorticity distribution adapted from Hecker (1987).

rotation to an inflection point is defined by the radius of a combined vortex. The tangential velocity v_t increases linearly for increasing distance from the center up to the point of inflection. Outside of the core in the vortex field the tangential velocity decreases exponentially to zero with increasing distance from the center. The idealized tangential velocity profile is shown in Fig. 2.11. The maximum velocity is reached at the inflection points. The vorticity distribution clearly shows the difference between the two vortex regions. The vortex field has no vorticity and the flow is irrotational. The correlation between the tangential velocity v_t and the radius r is described by eqs. 2.8 and 2.9 for both regions. The forced rotational vortex in the inner region can be calculated as

$$v_t = \omega\, r. \tag{2.8}$$

The tangential velocity v_t of the free irrotational vortex in the outer region is

$$v_t = \frac{\Gamma}{2\pi r}. \tag{2.9}$$

Both the free and the forced vortex have their pressure minima at the center were the deepest point of the dimple is located. The pressure minimum at the free vortex

is of one order of magnitude smaller. The rotation of the simplified core as shown in Fig. 2.11 is equal to $2\,\omega$. By visual observation one would get the impression that the free field is driven by the rotating core. However, Tietjens (1960) states that it is rather vice-versa. The field is governing the core. Air entrainment, i.e. the critical design situation, takes place at vortex types $VT5$ and $VT6$ (Fig. 2.10). At this stage the vortex air core is elongated or even reaches the intake cross-section. In this case the vortex core is described as irrotational flow, and the vortex is called a potential and free vortex, respectively. Air entrainment takes place only in connection with this flow phenomenon.

Fig. 2.12 shows the velocity distribution of a combined vortex. Since the core of the vortex is determined by the field of the vortex and not vice-versa, the core is simply a residuum and the velocity distribution is circumstantial (Tietjens, 1960). The diameter of the core is of minor importance and can be neglected. Consequently, a potential vortex has a singularity at $r \to 0$.

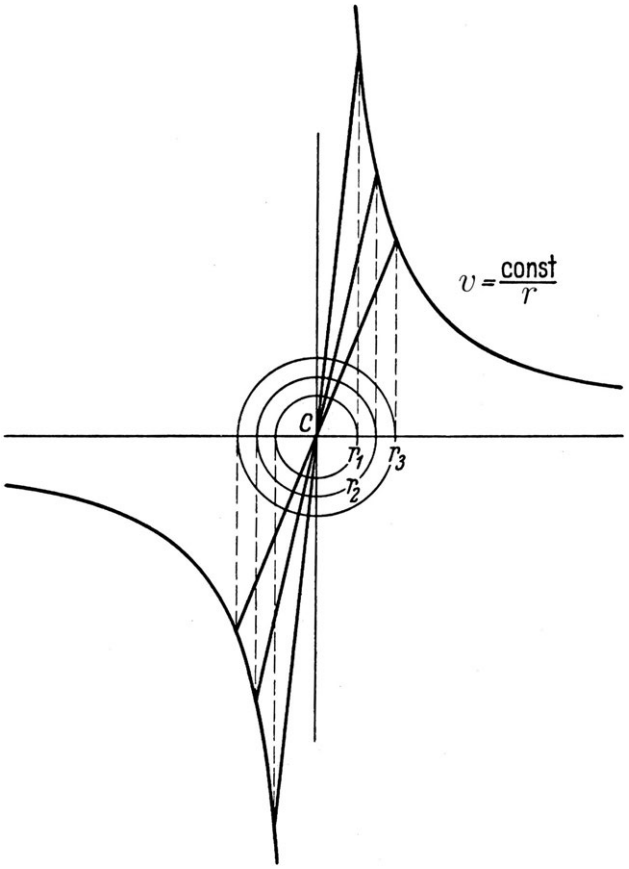

Figure 2.12: Cores of different radii at a given velocity field (Tietjens, 1960).

A Rankine vortex is a combination of a free vortex at the outer region and a forced vortex in the vortex core. A Burgers vortex (Burgers, 1948) is similar to a Rankine vortex, but without discontinuity of the velocity derivatives between the forced and free vortex regions. Therefore, it has a smaller maximum velocity.

Cotel & Breidenthal (1999) investigate the turbulence within a vortex. She analyzed the transition from forced to free vortex in terms of momentum flux inside an isolated, turbulent line vortex of constant density with the help of the effective Richardson number.

2.2.5 Forced Vortex

In the following the generation of a forced vortex is described by the rotation of a water-filled cylindrical vessel. Once this vessel is rotating the near wall water body begins to rotate as well, initiated due to viscosity effects. Fig. 2.13 shows a schematic illustration and Fig. 2.14 gives the related velocity distributions. The water surface profile *I* is formed. Fig. 2.14a gives the corresponding velocity distribution. While continuing the process the entire body is rotated. At final state the water surface profile *III* is reached. The velocity increases linearly by increasing center distance as shown in Fig. 2.14c. The vorticity is non-zero and equal at every point. Water particles at the outside get higher pressure than at the inner side due to the centrifugal force. Water particles at the water surface have a pressure equal to the atmospheric pressure. Therefore, the water level rises from inside to outside. At equilibrium conditions the water behaves like a solid body with the angular velocity ω.

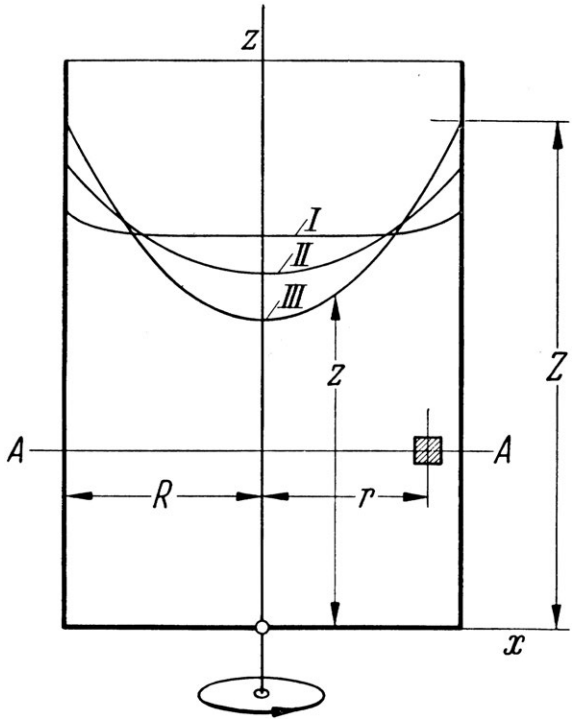

Figure 2.13: Consecutive surface forms of a liquid-filled vessel, which is set in rotation (Tietjens, 1960).

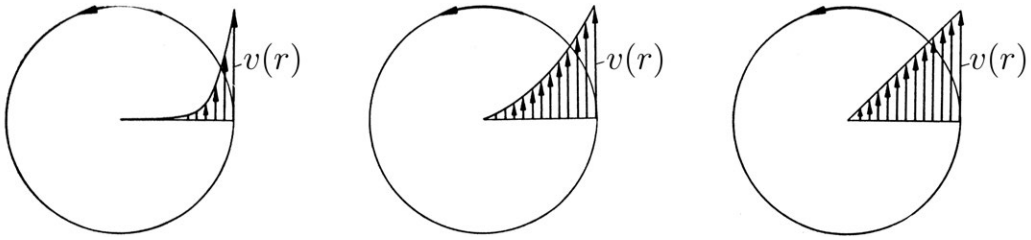

(a) Surface *I* (b) Surface *II* (c) Surface *III*

Figure 2.14: Velocity distribution in cross-section A-A of Fig. 2.13 (Tietjens, 1960).

2.2.6 Free Vortex

A free vortex is a potential vortex which is equal to any other potential flow and can only develop due to pressure differences and forces, respectively. The pressure difference causes the acceleration of water particles.
The moment of momentum or angular momentum in terms of

$$\mathbf{L} = v_{\mathrm{t}}\, r \tag{2.10}$$

is constant for an irrotational vortex in an ideal liquid. Haindl (1959) states that this classical theory is not valid for viscous liquid. The verification was conducted by Einstein & Li (1955) in a theoretical analysis. Lugt (1983) summarizes, that *"in general, there is no potential flow in nature, but many flow regions can be considered irrotational in an approximate way"*.
Shear stress between the layers of the flow can be determined by

$$\tau = \eta\, \frac{\partial v}{\partial r}\ , \tag{2.11}$$

where η = dynamic viscosity[4]. In comparison with the pressure differences the influence of the shear stress due to the low value of the dynamic viscosity η are very small and can be neglected (Tietjens, 1960). This is in contrast to a forced vortex, where the influence of the viscosity plays a decisive role.

[4]The dynamic viscosity mainly depends on the temperature, e.g. for a given $\vartheta = 20\,^{\circ}\mathrm{C} \Rightarrow \eta_{\mathrm{a}} = 1.8 \cdot 10^{-5}$ kg/(m s), $\eta_{\mathrm{w}} = 1.0 \cdot 10^{-4}$ kg/(m s).

Vortex Pairs. At intakes, whether vertical or horizontal, several vortices can form at the same time. A single vortex is an unsteady phenomenon, but if there is more than one vortex the behavior is even more complex. Fig. 2.15a shows the velocity distribution of such a vortex pair. The distribution of one vortex is shown as dashed line. The solid line shows the superimposed distribution of the two vortices. Due to higher velocity between the vortices the pressure is low. The result is a convergence of the two vortices. If the influence in between is sufficiently strong, the vortices will quench. This stage can not be stable. Figs 2.15b and 2.15c illustrate the cases if the direction of rotation and the strength are different.

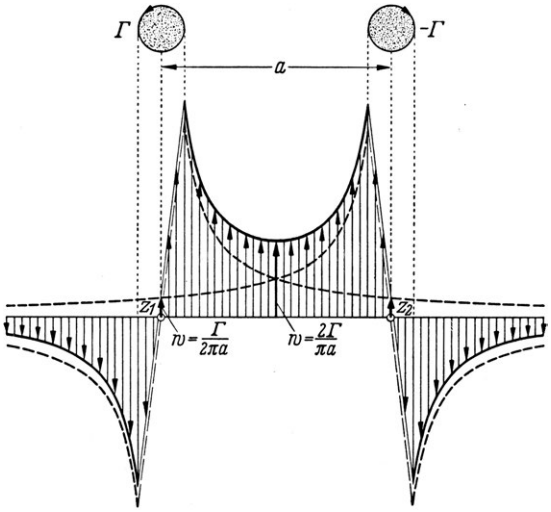

(a) Equal strength but different rotation

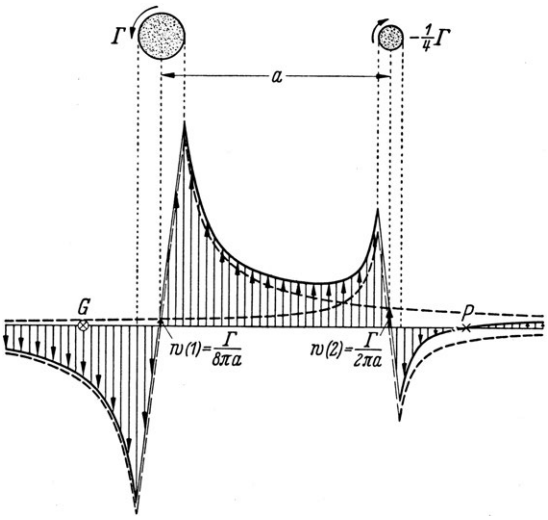

(b) Different strength and different rotation

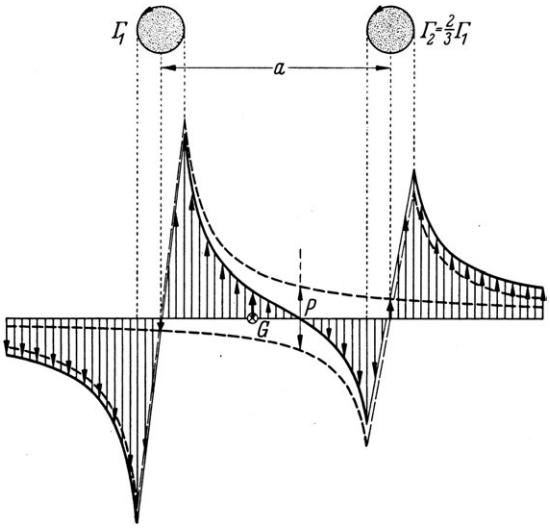

(c) Different strength but equal rotation

Figure 2.15: Three different velocity distributions of two vortices with equal distance but with differences in strength and/or rotation (Tietjens, 1960). The distribution of a single vortex is indicated by a dashed line which gives due to superposition the present velocity distribution indicated by a straight line.

Quenching of a Vortex due to a Wall. The expansion of an idealized field of a single vortex due to the asymptotic trend of the tangential velocity is large. The distance between the streamlines around the center changes close to walls. Fig. 2.16 shows a vortex field at this condition. The streamlines between the center and the wall are tighter than on the opposite side. This means that the velocities are higher and, vice versa due to the Bernoulli effect, the pressure is lower. The result is a movement of the vortex towards the wall. Then, a rotation between the points B and C develops with a direction contrary to the rotation of the main vortex core. Therefore, the vortex quenches very fast, even if strong vortices reach the wall.

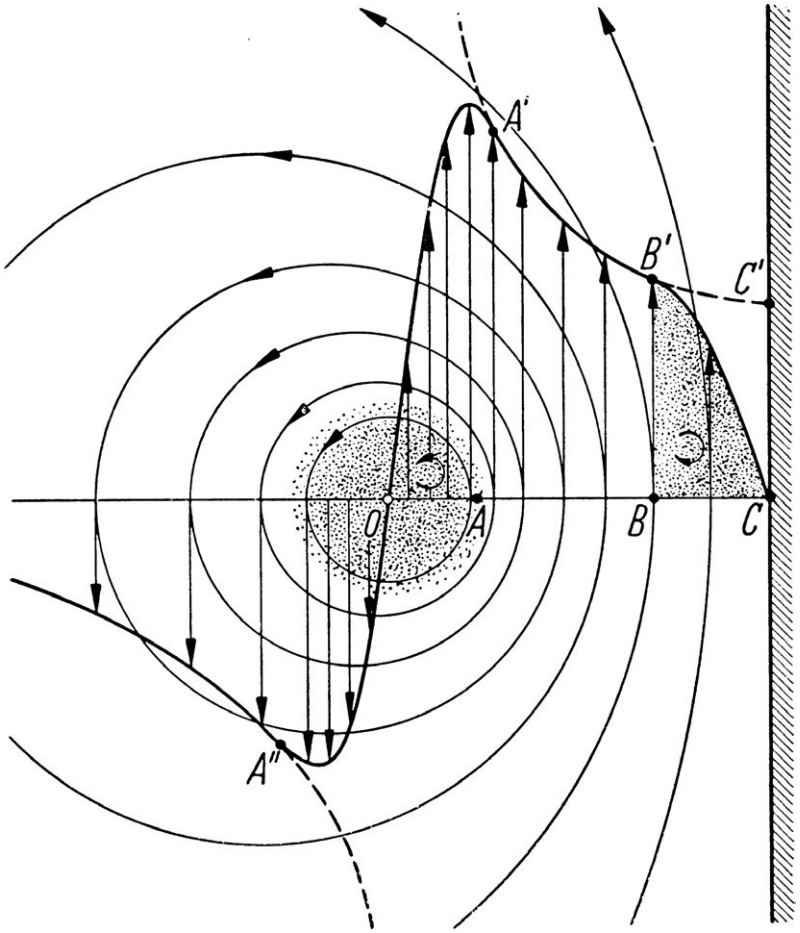

Figure 2.16: Quenching of a vortex due to a wall (Tietjens, 1960).

2.2.7 Coriolis Effect

There is a common story that the sense of rotation of a bath-tub vortex, i.e. a small intake-vortex, is clearly governed by the fact on which hemisphere it is located. This story is not fully true, what is discussed next.
Indeed, the Coriolis effect causes a deflection of moving objects on a rotating reference frame. On the northern hemisphere a free vortex is rotating counter-clockwise (CCW), while it is rotating clockwise (CW) on the southern hemisphere (Fig. 2.17).

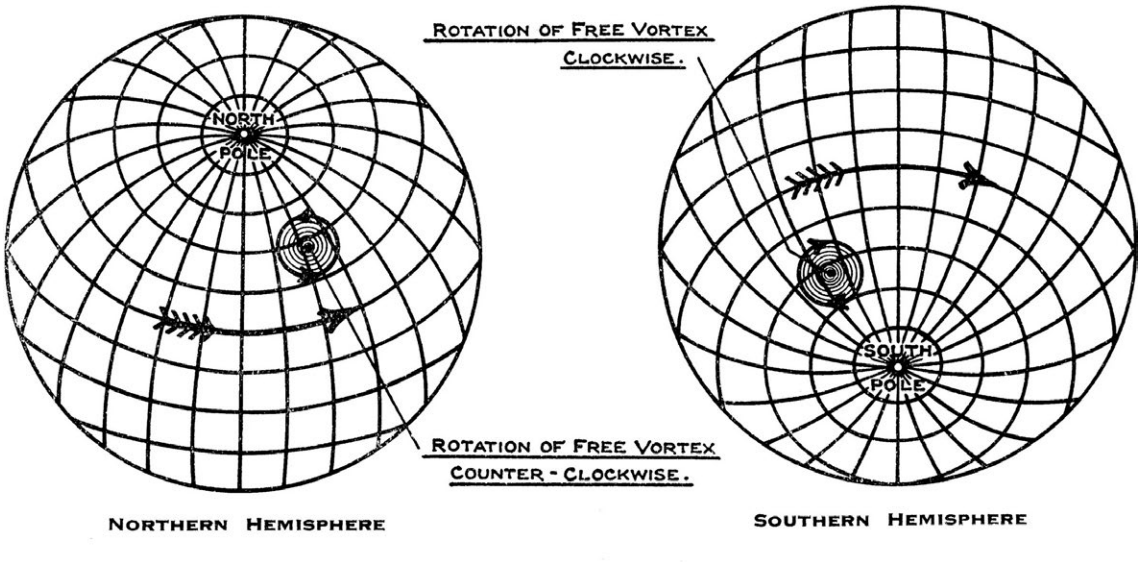

Figure 2.17: Sense of rotation of a vortex according to the hemisphere (Ball, 1933).

Binnie (1964) and Trefethen et al. (1965) have proved the evidence of the Coriolis effect by experiments on the northern and the southern hemisphere, respectively. They showed that the direction of rotation depends mainly on the properties of the approach flow and the viscosity.
However, Fig. 2.18 depicts an intake vortex that turns clockwise, although the photo was taken on the southern hemisphere. Thus, the Coriolis force is not governing the process in the present case (Shapiro, 1962). A closer look to the Rossby number Ro will explain this apparent paradox. The Rossby[5] number Ro is the ratio of inertial forces to Coriolis forces:

$$Ro = \frac{v}{2\omega L} \ , \tag{2.12}$$

where v is the velocity of a fluid element, L the scale of the fluid motion, and

[5]Carl-Gustaf Arvid Rossby (⋆28 December 1898 in Stockholm, †19 August 1957 in Stockholm) was a Swedish-U.S. meteorologist who first explained the large-scale motions of the atmosphere in terms of fluid mechanics.

ω is the earth's rotational velocity = 1 rotation/day. However, the period of one rotation with 86,400 s is not accurate as the sidereal day[6] with 86,164 s has to be used. Basically, for $Ro \gg 1$ the Coriolis force can be neglected. For example, for a weather system $Ro = 0.1$ holds and a hurricane has $Ro = 3$. A typical intake vortex at HPPs has $L = 20$ m and $v = 2$ m/s. Thus, $Ro = 686$. Davis (2012) assumes a limit of Ro, where the Coriolis force is important on fluid motion, which is an order of magnitude smaller than a typical Rossby numbers for intakes of HPPs. Consequently, small rotating fluid systems like intake-vortices are not influenced by the rotation of the earth.

Figure 2.18: Photograph of a clockwise turning intake vortex on the southern hemisphere (Lake Arapuni, NZ). The corresponding diversion tunnel that induces the flow has a diameter of $D = 7.6$ m. The submergence depth at the tunnel intake is about 21 m (Ball, 1933).

[6]A sidereal day is a time scale that is based on the Earth's rotation which especially considers the position relative to the fixed stars.

2.2.8 Influence of the Water Body

While defocussing from the near field of an intake section to the whole water body of a water reservoir or lake different additional influences on the formation of a vortex become prominent. The water body is mainly exposed to three disturbing processes (Fischer, 1979): (1) Meteorological conditions determine the energy transfer across the air-water interface, both the (2) inflow and the (3) outflow are ruling the mass exchange. Fig. 2.19 gives a schematic overview to these processes and the mechanisms, respectively.

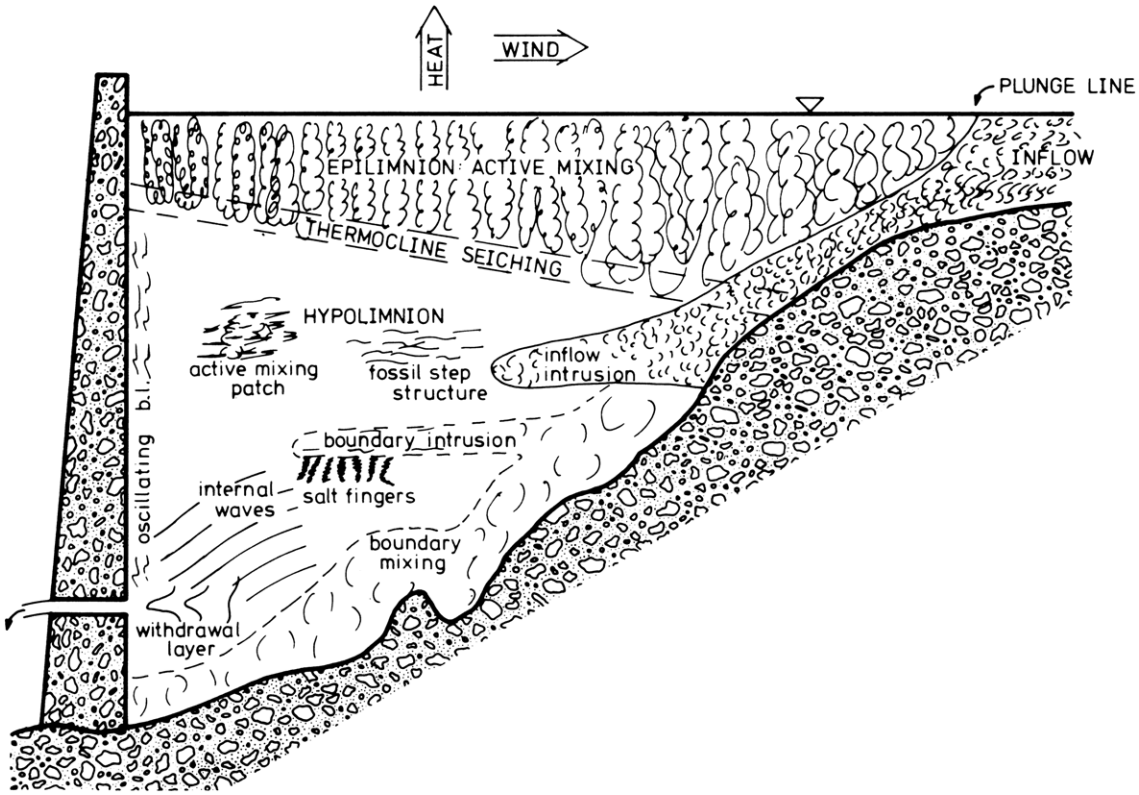

Figure 2.19: Illustration of various possible mixing mechanisms in a lake or reservoir. The intensity of each mechanism is mainly governed by the topography of the lake and meteorological influences (Fischer, 1979).

The inflow can affect the reservoir by the following factors:

- density changes in the water body,
- ice-covered surface or ice floes,
- wind-induced waves at the surface.

As a result, the water body can have several layers or areas of different density and flow. The consequence of a density current due to the inflow or the seiching on the vortex formation is difficult to predict. Both a decreasing and an increasing

influence on the vortex formation are conceivable. However, if a stratification is present in the water body the vortex formation is impeded. Fig. 2.20 illustrates typical flow patterns. Furthermore, it can be assumed that a present stratification remains stable during a reservoir lowering. Depending on the magnitude of the outflow discharge the stratification is provided by different layers of the water body. At higher discharges the impact of the stratification decreases and their influence becomes negligible, similar to a homogeneous water body.

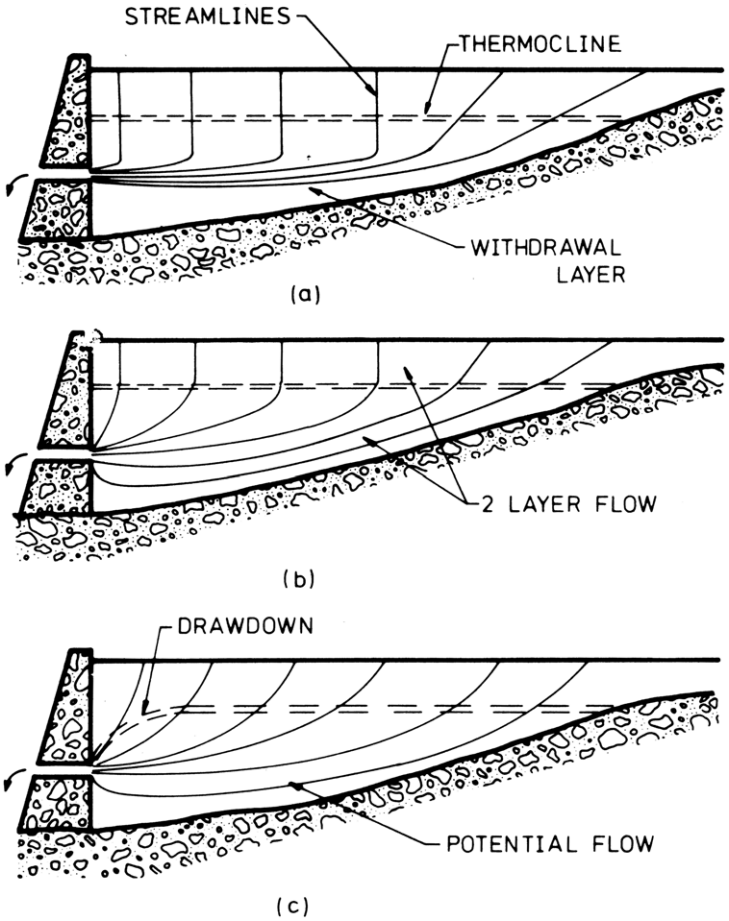

Figure 2.20: Withdrawal flow patterns. (a) Strong stratification in the hypolimnion and small discharges. (b) Weak stratification in the hypolimnion, but strong temperature gradient across the thermocline; medium discharge. (c) Discharge strong enough to overcome buoyancy forces both in the hypolimnion and at the thermocline (Fischer, 1979).

Wind-induced waves are accompanied by an orbital movement that disturbs the formation of secondary flow above the intake. Thus, vortex formation is decreased by waves.

A frozen water surface above the intake behaves like an additional boundary wall and thereby the shear stress reduces secondary flow effects. The impact of ice floes is smaller than a closed ice cover. However, in general ice works in principle like an anti-vortex device.

2.3 Research Works on Intake-Vortices

Since the implementation of the first modern water turbines at the end of the 19th century the problem of vortex formation at the transition from free surface to the pressurized pipe flow and the related air entrainment is present. The number of HPPs is still increasing. However, until the early 1950s, few investigations regarding the vortex phenomenon (see chapter 2.2) and its negative consequences have been conducted. In the following section an overview of intake-vortex investigations is given that have been carried out since then. To get an impression of intake-vortices at prototype HPPs Fig. 2.21 shows four examples.

(a) HPP Laufenburg, River Rhine (CH)

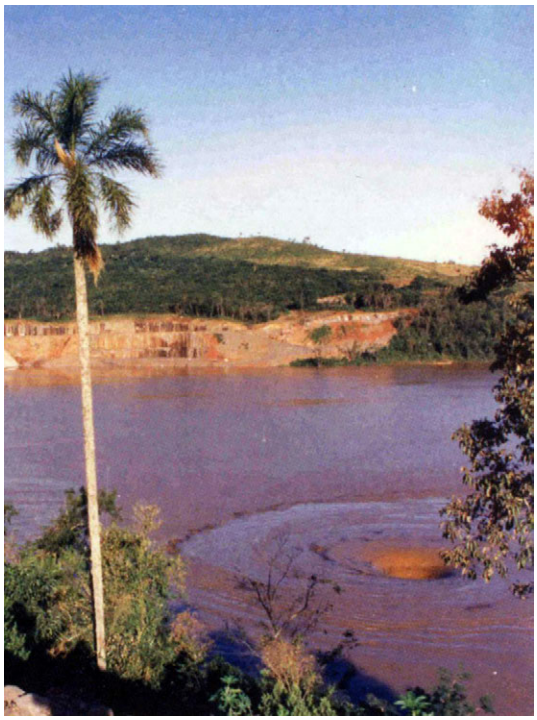

(b) HPP Segredo, River Iguassu (BR), Krüger (2009)

(c) Lake Pukakis (NZ)

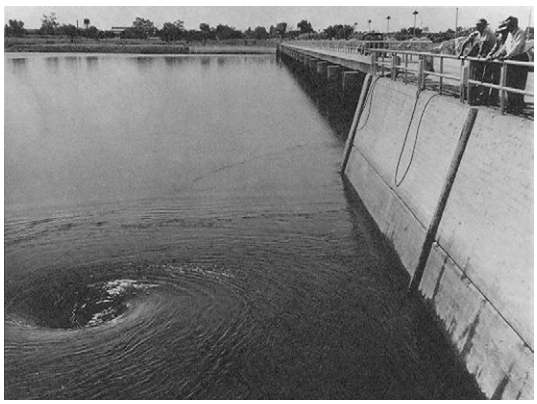

(d) HPP unknown, Uni-KL (2012)

Figure 2.21: Several prototype examples of intake vortices at HPPs.

2.3.1 Basic Cylinder Experiments

General. A distinction can be made between basic cylinder experiments and practical case studies. The former is described next, the latter are described further below.
Cylinder experiments give an elementary access to the vortex phenomenon. Due to the simple symmetric and stable conditions several basic relationships can be found – often supported by additional theoretical considerations.

Experiments by Einstein & Li. A typical cylinder experiment was presented by Einstein & Li (1955). They conducted basic research on intake-vortices in cylinders with a central bottom orifice. The aim of this study was to investigate the behavior of fluid vortices with the presence of friction. Einstein & Li (1955) analyzed the effect of viscosity both theoretically and experimentally. Fig. 2.22 shows the experimental setup. The tank rotates by a known initial moment of the momentum. The assumption that turbulence in the core contributes an additional eddy viscosity to the total effective viscosity leads, in a limited range, to a good agreement between model and theory. A vortex always grows in length until a boundary is reached. Furthermore they found that the momentum at a section can be reduced by obstacles or baffles. The strength of the whole vortex can be reduced by such means.

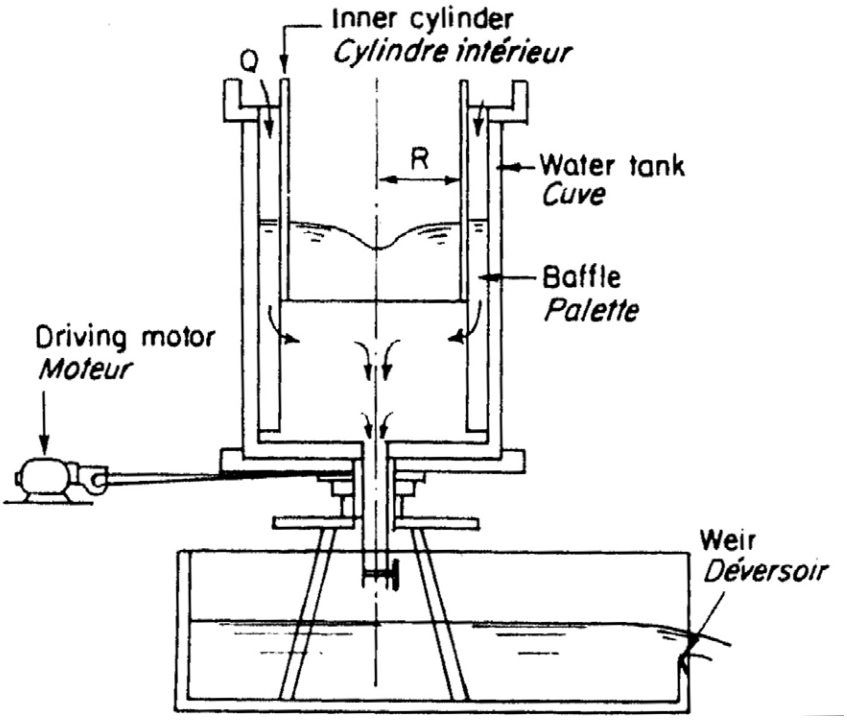

Figure 2.22: Experimental setup to conduct single vortex investigations (Einstein & Li, 1955).

Experiments by Haindl. A similar experimental arrangement was used by Haindl (1959). The experimental procedure provides a forced circulation by rotating the cylinder and a free outflow. Thus, the water level decreases and velocities can be measured. The moment of momentum increases. He identified a dominant role of the circulation for the formation and the strength of the vortex. Due to the outflow a small part of rotation energy is lost and the ratio between energy and water volume in the tank rises. As a result the velocity increases.
Haindl (1959) mentions that the size of the outflow orifice has also a considerable influence on vortex strength. The vortex strength again determines the quantity of air entrainment. Detailed observations were carried out to understand the air-core formation from a dimple to a tip of a tube that reaches the outflow section. Here, the length of the vortex pulsates. Air entrainment starts as the tip passes the point of greatest contraction of the jet in the outflow orifice. The vortex becomes stable and increases its size. Usually, a clearly audible sound described as a loud gurgle accompanies this vortex stadium.
Fig. 2.23 depicts the submergence h at which a fully developed air-entraining vortex is formed for various velocities in the cylinder with $D = 41$ cm (upper axis) and at the outflow orifice with $D = 3.12$ cm (lower axis). Point A gives the largest h for the formation of an air-entraining vortex at a certain velocity v_A. A curve envelops the full formation of an air-entraining vortex. Above this curve a vortex does not form. A rising branch in the transitional region for velocities $< v_A$ was determined. Above several undeveloped vortices are indicated. Velocities $> v_A$ result in a descending branch approaching asymptotically a constant value of h.

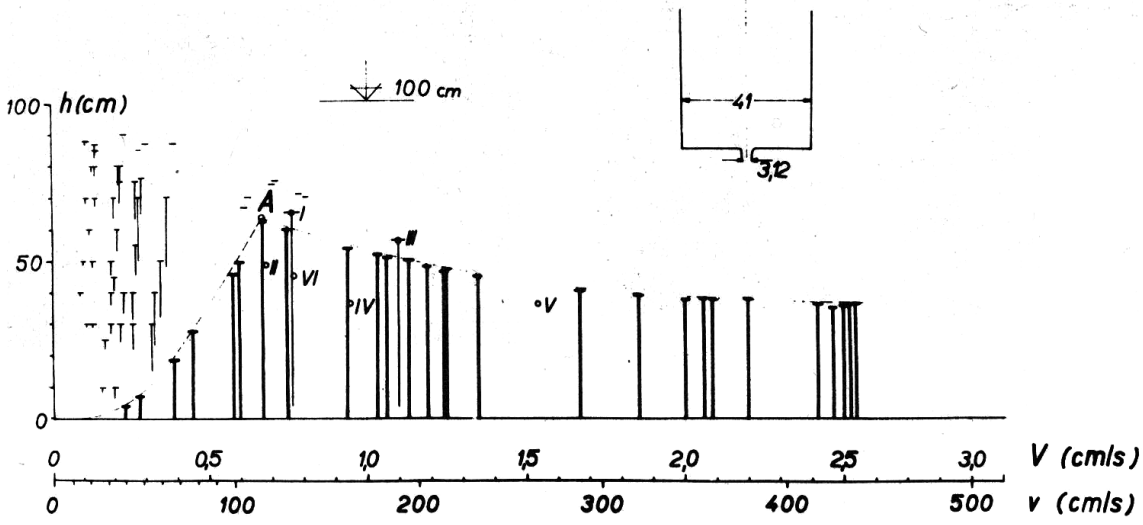

Figure 2.23: The rise of the vortex (Haindl, 1959)

Haindl (1959) suggests several means to prevent vortex formation, e.g. increasing submergence and diameter of the outflow orifice, wings near the walls to prevent rotation, a floating rack on the water surface, equipment to cause losses between water surface, and outflow orifice, respectively.

Experiments by Anwar. Anwar (1965, 1966, 1967, 1968a,b) conducted numerous basic cylinder experiments. The results can be summarized as follows: At small radial and axial velocities, the circulation is constant in the outer region. The circulation influences the discharge coefficient, and, as the axial velocity is almost zero, air bubbles do not move downwards the vortex core tail. Fig. 2.24 depicts the observed occurrence of vortices as a function of the radial Reynolds number:

$$\mathsf{R}_\mathrm{R} = Q_\mathrm{w}/(\nu h) \tag{2.13}$$

and uses the Rossby number in a modified form $Ro = Q/(\Gamma r_0)$. A Reynolds independency for vortices with narrow air cores is given for $\mathsf{R}_\mathrm{R} \geq 10^3$, whereas the formation of a strong vortex with large air-core is mainly ruled by R_R.

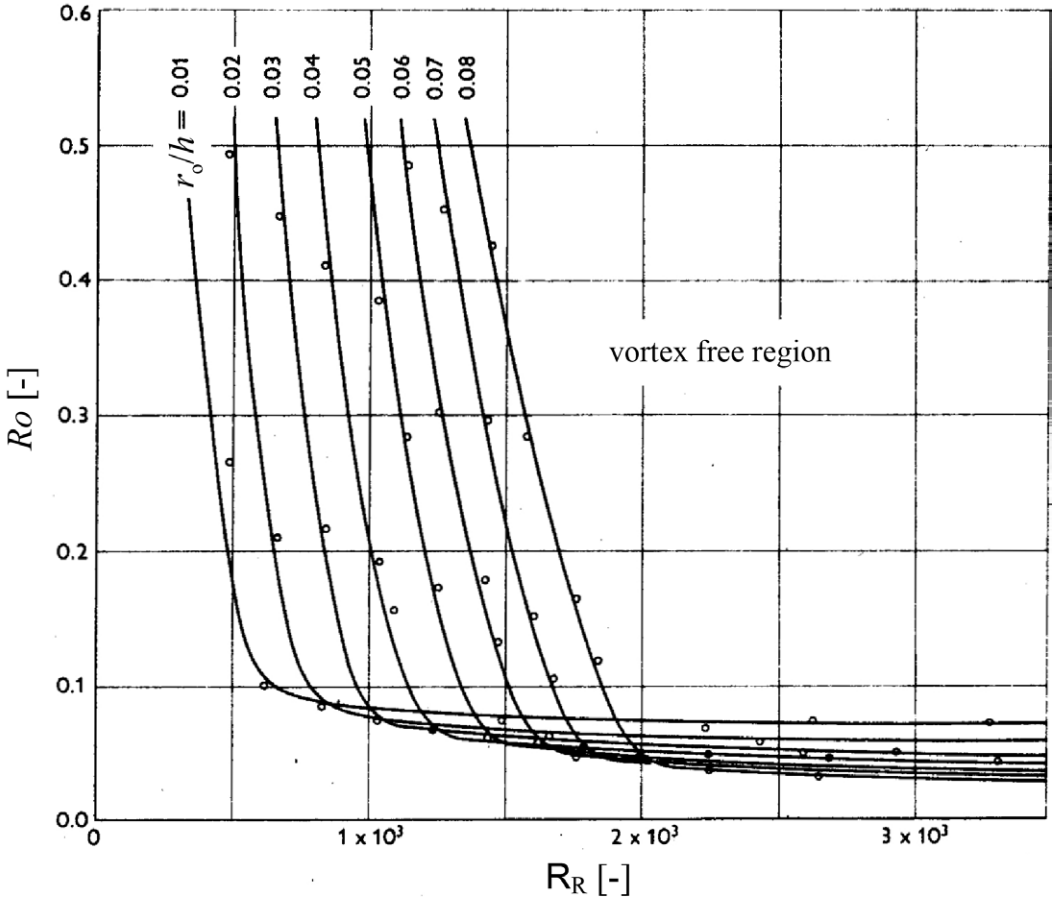

Figure 2.24: Occurrence of intake vortices as a function of $\mathsf{R}_\mathrm{R} = Q_\mathrm{w}/(\nu h)$ and $Ro = Q_\mathrm{w}/(\Gamma r_o)$. Similarity between different dimensions r_o/h, where r_o = orifice radius and h = orifice submergence (Anwar, 1966).

Experiments by Quick. Quick (1962) gave new insights to axial velocities. Fig. 2.25 schematically describes the distribution of the axial velocity. In the main body of liquids the axial velocity reaches maximal values that are up to 10 % of the tangential component. The upwards and downwards flow near the core is originated by the radial flow along the bottom. This flow exceeds the discharge capacity of the orifice and is, in turn, deflected upwards.

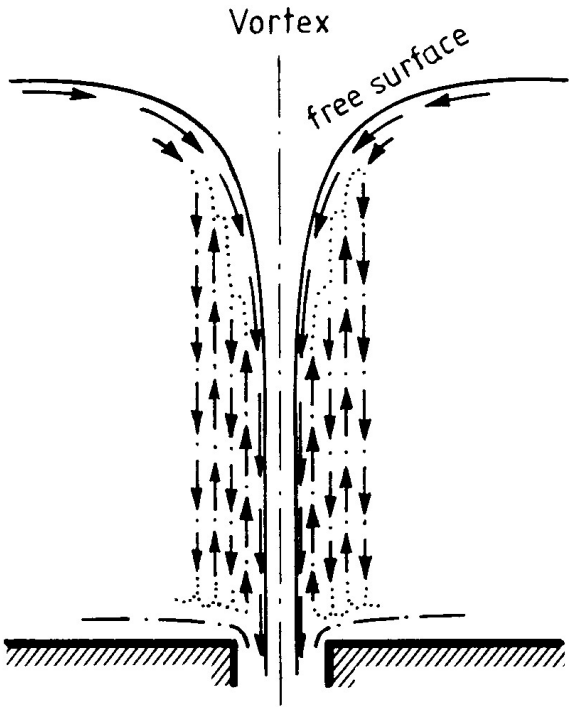

Figure 2.25: Sketch of observed radial and vertical velocity pattern near the core of a vortex (Quick, 1962).

Experiments by Daggett & Keulegan. Daggett & Keulegan (1974) presented considerations about the scale similitude between model and prototype. They conclude that a free-surface vortex flow is affected by viscosity and inertial circulation. The surface tension was of less importance in the range of their investigations (see also chapter 2.3.5). Daggett & Keulegan (1974) measured vertical velocity profiles as shown in Fig. 2.26. A flow meter with a 10 mm propeller was used to measure the velocities in each direction separately. The diameter of the central bottom orifice was $D = 0.1$ m, the discharge $Q_w = 19\,l/s$, and the vanes in the approach flow had an angle of 45°. Particularly striking in Fig. 2.26 is the nearly uniform tangential velocity throughout the whole submergence. Only close to the floor a boundary layer is developed and v_t decreases, confirming the observations of Anwar (1965). Consequently, the tangential velocity is independent of the submergence height h. On the other hand the tangential velocity increases by decreasing radial distance to the orifice, similar to a potential vortex (chapter 2.2.6). However, the measured ra-

dial velocities are not uniform throughout the submergence height and thus strongly differ from theoretical assumptions. The radial velocity increases in the lower half by which the main flow is driven. Anwar (1965) infers that the energy to maintain the open vortex core is provided by the radial flow field. Furthermore, he found that a roughening of the floor prevents an open vortex core.

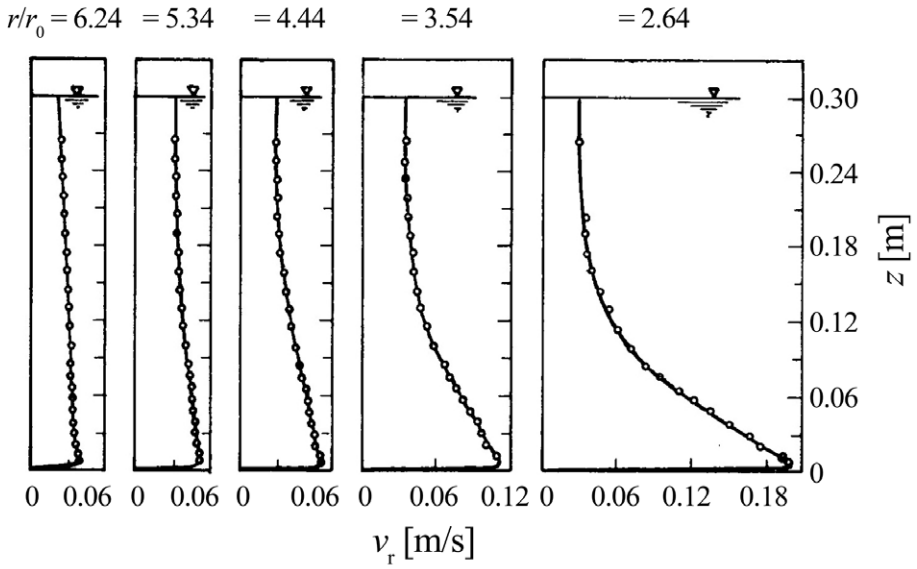

(a) Radial velocities

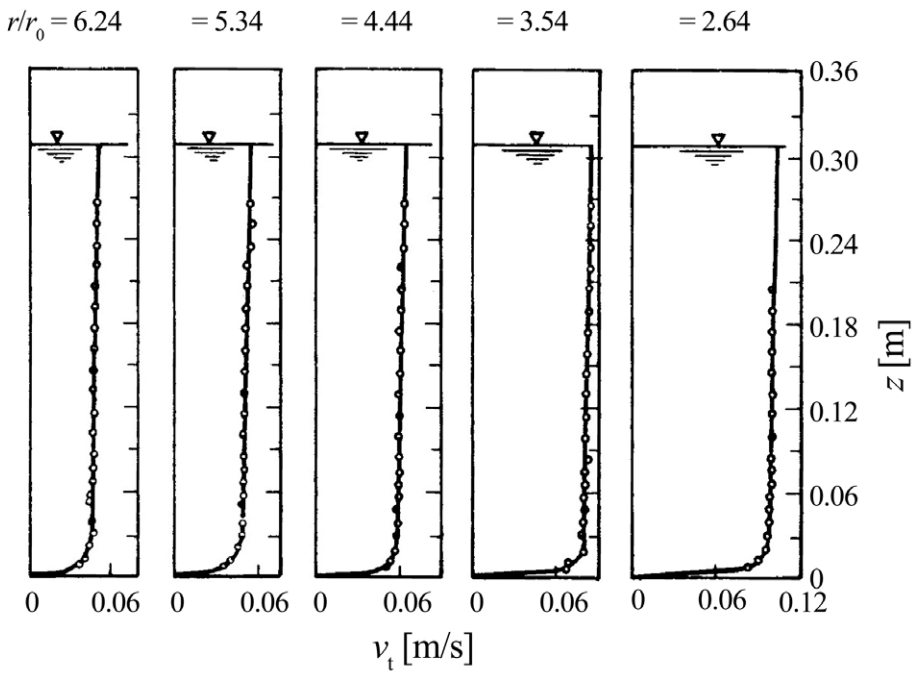

(b) Tangential velocities

Figure 2.26: Vertical velocity profiles measured by a flow meter in a cylindrical tank with a central outlet of $Q_w = 19\,l/s$ (Daggett & Keulegan, 1974).

Experiments by Odgaard. Odgaard (1986) focused on the critical submergence of Rankine vortices. He found that the Froude number and circulation number are decisive non-dimensional parameters and derives critical limits related to surface tension and kinematic viscosity. Note that the use of the Rankine approach (see chapter 2.2.4) entails no singularity in the vortex center and the application of the equations of motion is suitable. For a vortex with laminar core the critical point where the tip of the air-core reaches the intake cross-section leads to the following equation

$$h^2 = -0.9\frac{\sigma}{\rho \mathrm{g}}\sqrt{\frac{vh}{\nu}} + 0.0043\frac{\Gamma^2 v}{\mathrm{g}\nu}, \tag{2.14}$$

where h gives the critical submergence. The surface tension term, i.e. the first term of eq. 2.14 can be neglected, as it only contributes by less than $< 10\,\%$ to h. The critical situation where air reaches the intake section is given by the discharge coefficient

$$C_Q = 12.2\sqrt{\frac{h}{D}}\sqrt{\frac{\nu D}{Q_\mathrm{w}}}\frac{1}{N_\Gamma}, \tag{2.15}$$

where $N_\Gamma = \Gamma D/Q_\mathrm{w}$ is the circulation number. However, the assumption of a laminar core does not hold at an increased imposed circulation. The velocity gradient leads to higher turbulence intensities and shear stresses, and thus, the effective viscosity $\nu+\epsilon$ increases (Einstein & Li, 1955), where ϵ is the eddy viscosity. Odgaard (1986) showed that by replacing ν in eq. 2.15 with $\nu + \epsilon$, the critical submergence can be estimated quite well. The verification with data from Jain et al. (1978) and Gulliver & Rindels (1985) shows good agreement. It has to be noted that in case the orientation of the air tube changes from vertical to horizontal, the imposed circulation changes as well and consequently the approach presented above gives misleading results.

Experiments by Andersen et al. Recently, Andersen et al. (2006) conducted an experimental and theoretical study by using a rotating cylinder. Fig. 2.27 schematically depicts their considerations about the flow field. The depression of the water surface is analyzed via photographs. A bubble separation from the vortex air core tail was photographed and its movement downwards the drain hole was analyzed. For quantitative descriptions the surface tension had be taken into account as well. The boundary layer theory from Ekman[7] and Stewartson[8] was proven experimentally. The central upward flow of the axial flow velocity distribution was visualized

[7]Vagn Walfrid Ekman (⋆3 May 1874; †9 March 1954) was a Swedish oceanographer.
[8]Keith Stewartson (⋆20 September 1925; †7 May 1983) was a British mathematician.

experimentally. Moreover, capillary waves form on the surface of the vortex core, and, based on these waves, the spiral motion was visualized.

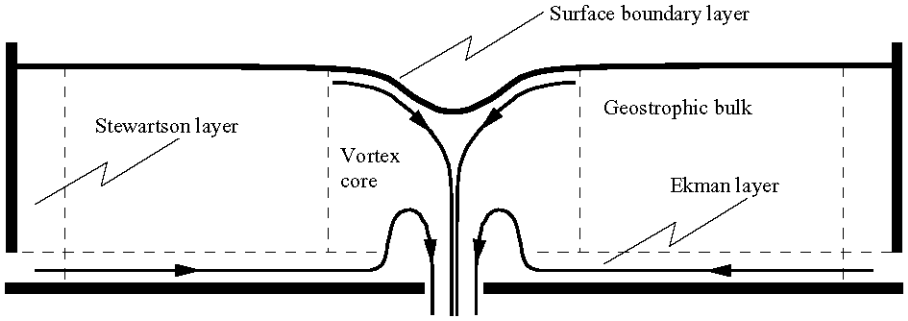

Figure 2.27: Characteristic flow regions of a bathtub-vortex. The main part of the radial in-flow is carried by the Ekman boundary layer, and the upwelling region next to the central region surrounds the drainpipe from the free surface above the drain-hole (Andersen et al., 2006).

Experiments on Pump Sump Intakes. In contrast to intakes at hydraulic structures, a large number of publications regarding pump sump intakes (Fig. 2.28)can be found in literature. They are described hereafter.

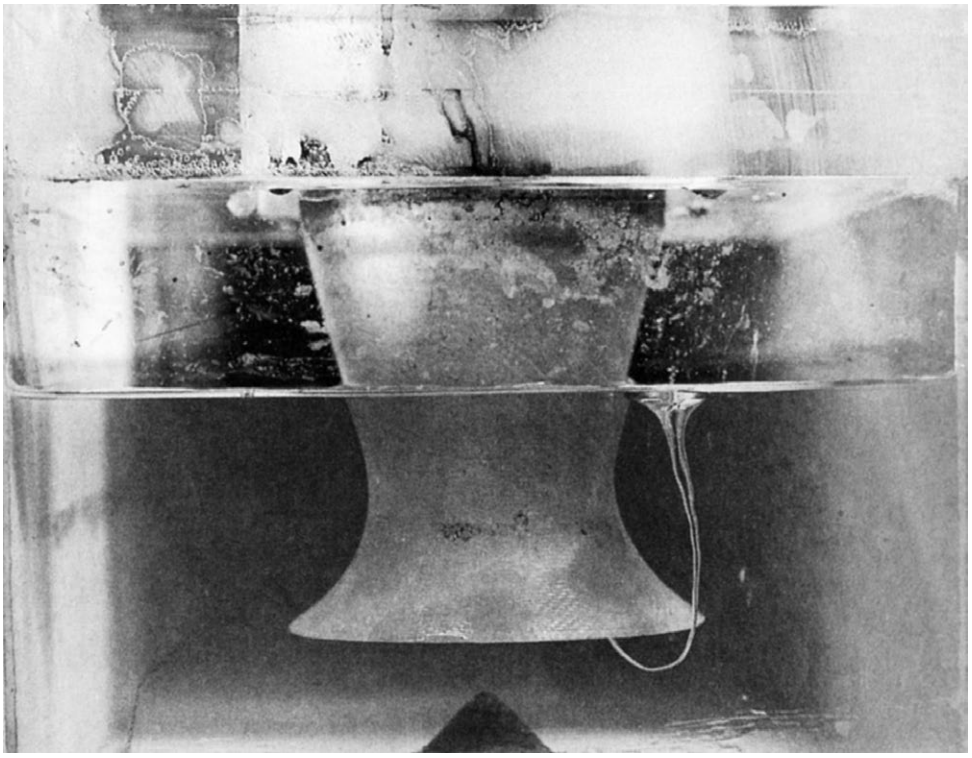

Figure 2.28: Free surface vortex at a pump suction bell entrance. The vortex develops due to a combination of low submergence, high suction velocity, non-uniform approach flow, or other vorticity sources (Karassik et al., 2008).

Earlier works come from Iversen (1953), Denny (1956) and Denny & Young (1957). Iversen (1953) studied the impact of wall and ground distance of the pipe intakes on the critical submergence. The results show that critical wall distances depend on the bell-mouth diameter. Denny (1956) and Denny & Young (1957) investigated the intake velocity, shape, and the strength of the rotational flow.
Berge (1966) describes the inertial formation of a free surface depression and gives F_D an important role. Furthermore, he depicts the dependence of critical submergence, discharge, and circulation for the present installation. Guidelines on the prevention of vortices in the planning of new and existing facilities are developed as well. Hattersley (1965) used a vortometer[9] to measure the swirl of intake vortices in in the pipe. Further studies of intakes in pump sumps originate from Quick (1970), Reddy & Pickford (1972, 1974) and Kohlhase (1973). Prosser (1977), Chang & Prosser (1978) and Prosser et al. (1986) published design and assessment criteria for pump sumps including criteria to prevent air-entraining vortices. Lately Karassik et al. (2008) summarized basic knowledge on pump sumps in a literature review.

[9] A vortometer is a device which is installed at the suction pipe entrance and measure the swirl by recording the revolutions per second of its vanes.

2.3.2 Investigations on Intakes at Hydraulic Structures

Intake structures in hydraulic engineering are different from pump sumps. The majority of intakes at hydraulic structures are part of large plants and their facilities where the topography of reservoir and river, respectively, plays a decisive role. Therefore they are unique in most of the cases. Generally, intakes can be arranged horizontally and vertically. Horizontal intakes are used for river power plants, HPPs/PSHPPs[10], flood protection structures, and intakes of water supply systems. Vertical intakes are most often used at pump sumps, rarely at HPP/PSHPP. Furthermore, a downswing in surge chambers can be considered as well as a vertical intake. Intakes inclined downwards are also common. Fig. 2.29 summarizes these main types of intakes as given by Knauss (1987a).

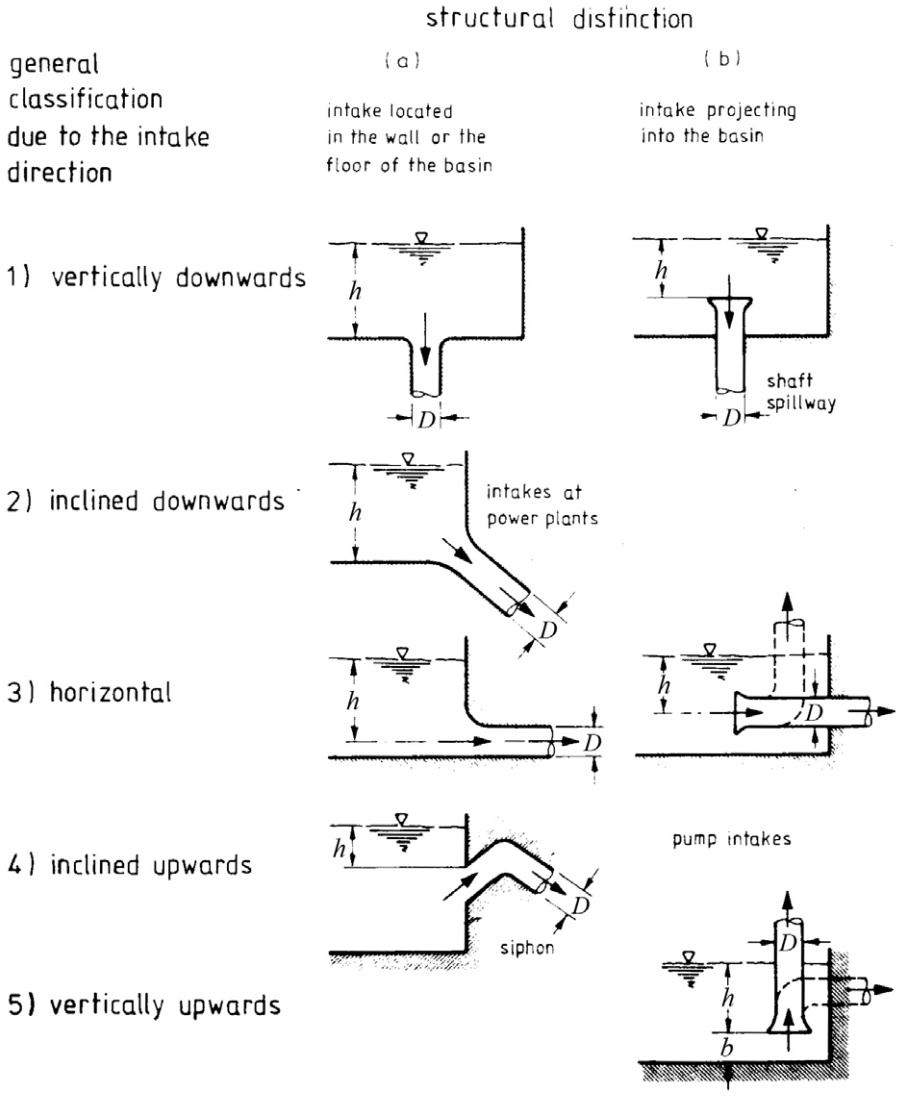

Figure 2.29: Types of intake structures (Knauss, 1987a).

[10]Pumped storage hydro power plant (PSHPP)

2.3.3 Critical Submergence

General. The critical design criterion is typically represented by incipient air entrainment. Some authors define the critical situation as the incident where the vortex core reaches the intake. At this time air bubbles continuously pass the cross-section of an intake (Fig. 2.10, $VT5$). Here, the critical submergence h_{cr} gives the submergence at the critical situation. The definition of the geometrical parameter of the intake submergence varies in different studies. In the current study the definition of Knauss (1987b) is used. Fig. 2.30 gives a definition sketch.

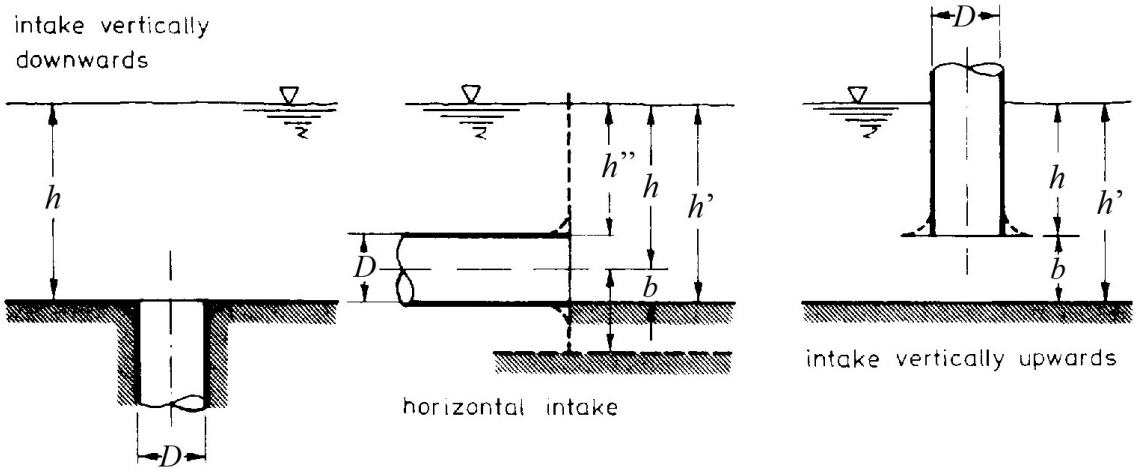

Figure 2.30: Definition of the intake submergence h as given by Knauss (1987b).

Following Denny (1956), Denny & Young (1957), and Anwar & Amphlett (1980) the influence of wall distance and bottom clearance is significant as well. They studied vertical upwards orientated pump intakes and found that if the wall distance increases the critical submergence increases. Generally the submergence becomes independent of the wall distance at $\gtrapprox 8D$. The variation of this value depends on the strength of the swirl. Vice-versa is the dependency on the bottom clearance b. If b increases the critical submergence decreases and becomes almost independent at $h/D < 4$.

Many intake-vortex investigations consider the influence of submergence. Basically, the results of these investigations can be divided into two groups: The results of the first group are based on known parameters, e.g. the intake submergence h and the flow velocity v. The second group deals with parameters describing the rotational flow near the intake. Both groups are dealt with in the following.

Critical Submergence based on Basic Flow Parameters. To estimate the critical relative intake submergence $(h/D)_{\mathrm{cr}}$ the following parameters are used most frequently:

- Intake diameter D
- Velocity head $v^2/(2\mathrm{g})$
- $f(v)$
- Intake Froude number $\mathsf{F}_D = v/\sqrt{\mathrm{g}D}$

Intakes of HPPs including PSHPPs have been examined by Gordon (1970) and Knauss (1972). Gordon (1970) developed an approach to determine the critical submergence at existing plants. Knauss (1972) described the application of existing knowledge and the experience from model investigations regarding the planning of PSHPPs.
For intakes of rectangular pump sumps Prosser (1977) recommends a minimal submergence of $> 2.5D$ and $> v^2/\mathrm{g}$, respectively. Typically, the required submergence is calculated by a function of the intake Froude number F_D and may be expressed by:

$$\left(\frac{h}{D}\right)_{\mathrm{cr}} = \xi\ \mathsf{F}_D + 0.5\ , \tag{2.16}$$

where $\xi = 1.7$ for symmetrical and $\xi = 2.3$ for asymmetrical approach flow, according to Gordon (1970), see also Fig. 2.32. Knauss (1987b) recommends $\xi = 2.0$, but specifies a minimal submergence $\min\,(h/D)_{\mathrm{cr}} = 1$–$1.5$, being independent of the velocity. Fig. 2.31 shows the most valuable approach, which is developed by data from Pennino & Hecker (1979), Hecker (1981) and Knauss (1983). All data originate from prototype experiences, with the critical cross-section marked. The diagram can also be used for intakes orientated in vertical directions (i.e. up- or downwards).
In the field of mechanical engineering several investigations regarding the critical submergence have been carried out, mostly for pump sumps. Due to the complex flow phenomenon and its strongly influencing approach flow, both the vortex formation and the vortex occurrence vary significantly (Fig. 2.32). The wide range of predicted submergence is not useful and shows again the complexity of vortex formation.

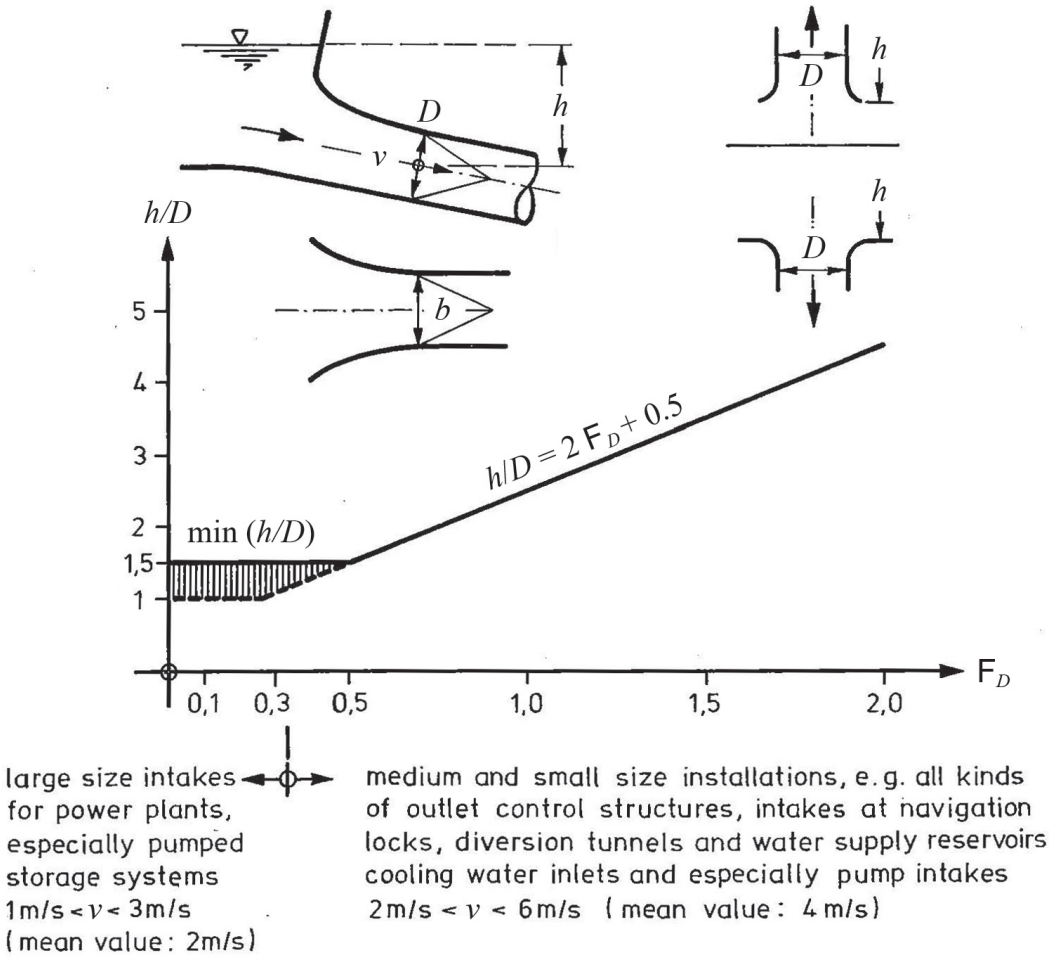

Figure 2.31: Recommended minimum relative intake submergence h/D for intakes with proper approach flow conditions and without use of special devices for vortex suppression (Knauss, 1987b).

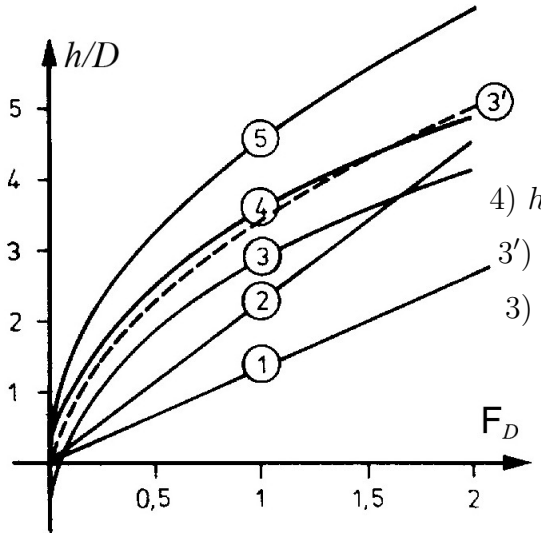

5) $h/D = 4.50\sqrt{F_D}$ (Jain et al., 1978)
4) $h/D + 0.25 = 3.30\sqrt{F_D}$ (Berge, 1966)
3′) $h/D + 0.5 = 3.95\sqrt{F_D}$ (Amphlett, 1976)
3) $h/D + 0.5 = 3.30\sqrt{F_D}$ (Amphlett, 1976)
2) $h/D = 2.30\ F_D$ (Gordon, 1970)
1) $h/D = 1.35\ F_D$ (Chang, 1979)

Figure 2.32: Comparison of approaches that predict the critical submergence due to the intake Froude number (Knauss, 1987b).

Gulliver et al. (1986) handle both prototype and model investigations. Fig. 2.33 shows Gordon's (1970) original plotting of submergence ratio versus Froude number with an indication of vortex formation as updated with additional field data by Gulliver et al. (1986). The additional field data indicate that Gordon's straight line needed to be more of a box with a minimum $h/D = 0.5$ (equal to 1.0 w.r.t intake axis) and a maximum Froude number of 0.5. Referring back to Fig. 2.31 the lower limit of $h/D = 1.0$ is confirmed by these data.

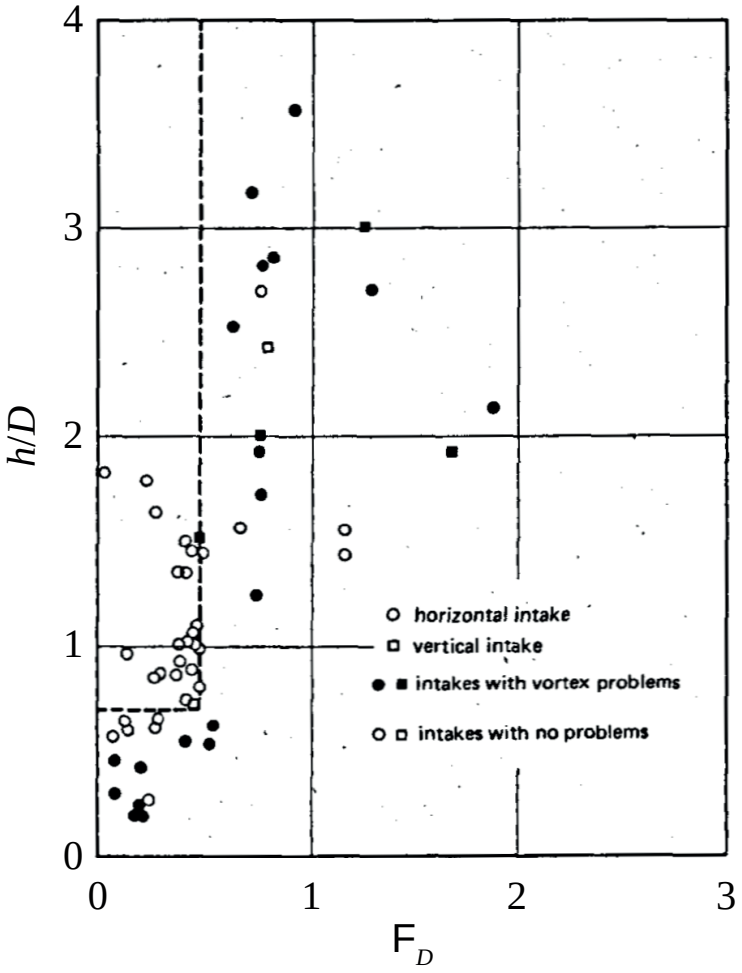

Figure 2.33: Dimensionless plot of data obtained from intakes at existing installations and model studies of proposed installations. Dashed lines represent rule-of-thumb guidelines for horizontal intakes. But caution, $h/D = 0$ refers to the top of horizontal intakes (Gulliver et al., 1986).

Yildirim & Jain (1979) used a separate procedure to predict the critical submergence by simple parameters. The theory of the critical spherical sink surface (CSSS) based on a 3D Rankine ovoid at an intake is shown for some intake directions in Fig. 2.34.

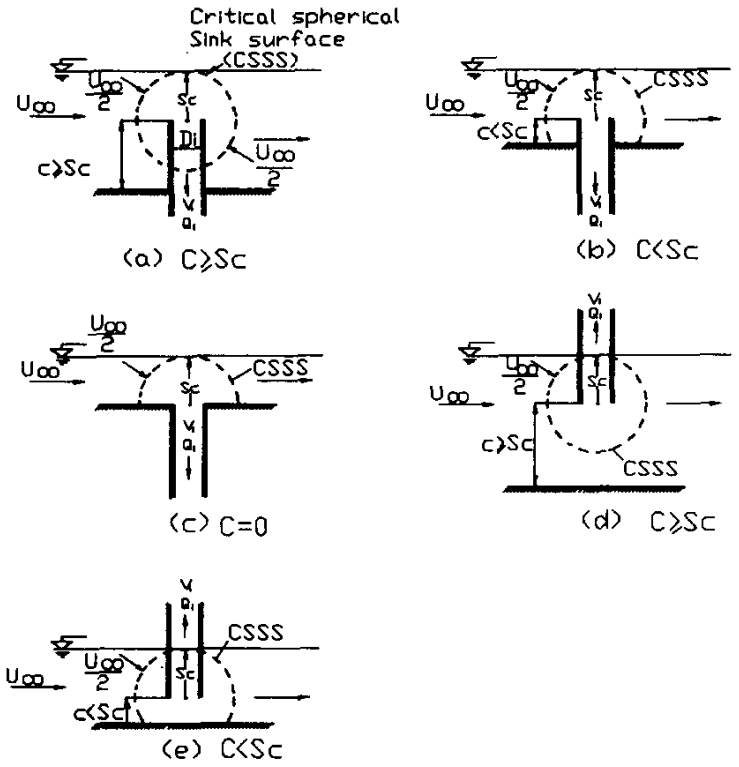

Figure 2.34: Typical critical spherical sink surfaces (CSSS) (Yildirim & Kocabas, 1995). c is referred as b and Sc as h_{cr} in this research project.

In case the CSSS reaches the free surface an air-entraining vortex will occur. The critical value for uniform canal cross flow according to Yildirim & Kocabas (1998), assuming potential flow conditions is

$$\left(\frac{h}{D}\right)_{\mathrm{cr}} = \frac{-b/D + \sqrt{(b/D)^2 + v_D/2v_{\mathrm{cr}}}}{2} \,, \tag{2.17}$$

where b = vertical distance from intake to bottom, v_D = intake velocity, and v_{cr} = critical velocity at CSSS. Note that v_{cr} has to be increased by 10 % to be representative to a real fluid. Yildirim & Kocabas (1998) successfully applied the CSSS procedure to still-water reservoirs. Yildirim et al. (2000) analysed several intake setups. They found that a pipe bell-mouth often used in pump sumps has a negligible effect on critical submergence in the potential solution. In Yildirim (2004), Yildirim et al. (2009), and Yildirim & Tastan (2009) the CSSS approach is extended to rectangular and multiple intakes.

Travis & Mays (2011) implement experimental and prototype data in a stochastic nearest neighbor algorithm. The model is used to calculate the probability of vortex formation given in probability contour plots.

Table 2.1 gives an overview of the most common formulas in practice to estimate the critical submergence h_{cr}.

Table 2.1: Summary of investigations on critical submergence $(h/D)_{cr}$ based on basic flow parameters. Note that h_{cr} refers to the top of the intake cross-section.

authors	h_{cr}	supplements
Rohan (1966)	$= 1.474\, v_D^{0.48}\, D^{0.76}$	
Gordon (1970)	$= \xi\, v_D \sqrt{D} + 0.5D$	$\xi = 0.5434$ for symmetrical approach flow $\xi = 0.7245$ for lateral approach flow
Nagarkar (1986)	$= 4.4(v_D \sqrt{D})^{0.54}$	
Knauss (1987b)	$= (2\frac{v_D}{\sqrt{g\, D}} + 0.5)D$	$\mathsf{F}_D \geq 0.5$

Critical Submergence based on Rotational Parameters. The second group of intake-vortex investigations describes the intake flow by rotational parameters, e.g. the circulation Γ. Test results from Amphlett (1976) indicate a correlation between the coefficient of discharge C_Q and the circulation number $N_\Gamma = \Gamma D/Q_w$ for horizontal pipe intakes. The result is given in Fig. 2.35. If Γ is known, the critical submergence and the critical discharge can be estimated.

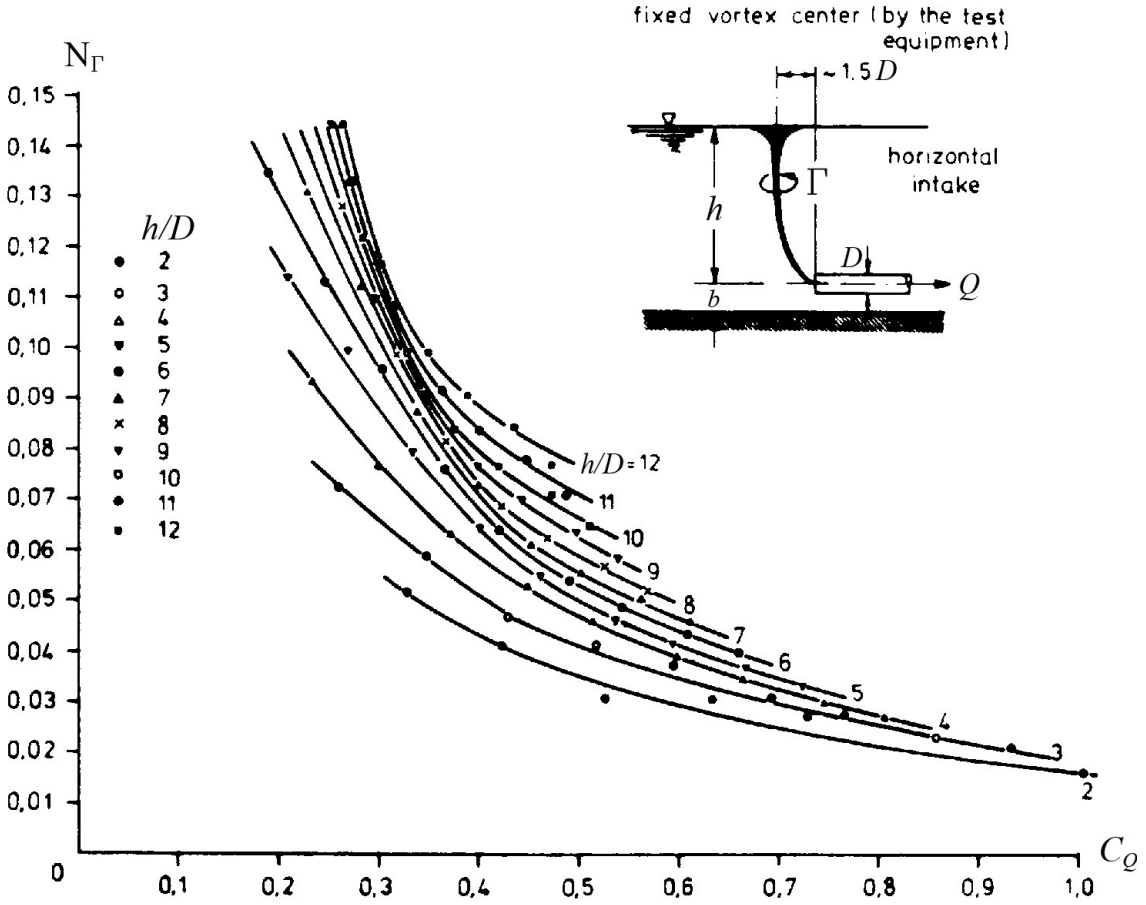

Figure 2.35: Effect of circulation Γ on coefficient of discharge C_Q for the onset of air-entraining vortices (Amphlett, 1976).

Gorbachev et al. (2007) used an integral approach to find the critical submergence at double rectangular prototype intakes. The approach contains a numerical model of the approach flow in the reservoir, a large scale physical model, and an analytical solution. A comparison of the air core lengths determined by the different models shows a factor of 2 between these lengths.

The unique character of intake structures in hydraulic engineering makes a generalized approach challenging. Due to the difficulties explained above, hydraulic model investigations are still a state-of-the-art procedure to find the right critical submergence for a specific intake setup.

2.3.4 Vortex Fluctuations

Vortices are highly unsteady and instationary while the water level and the discharge remain constant. Fig. 2.36 shows the occurrence o of vortex types as a function of time t (Durgin & Hecker, 1978). The diagrams show that almost no air entrainment corresponding to vortex types $VT5$ and $VT6$ was present. Furthermore, fluctuations within almost the full type range with an obvious periodical behavior was obtained, $VT1$ and $VT2$ were present most of the time.

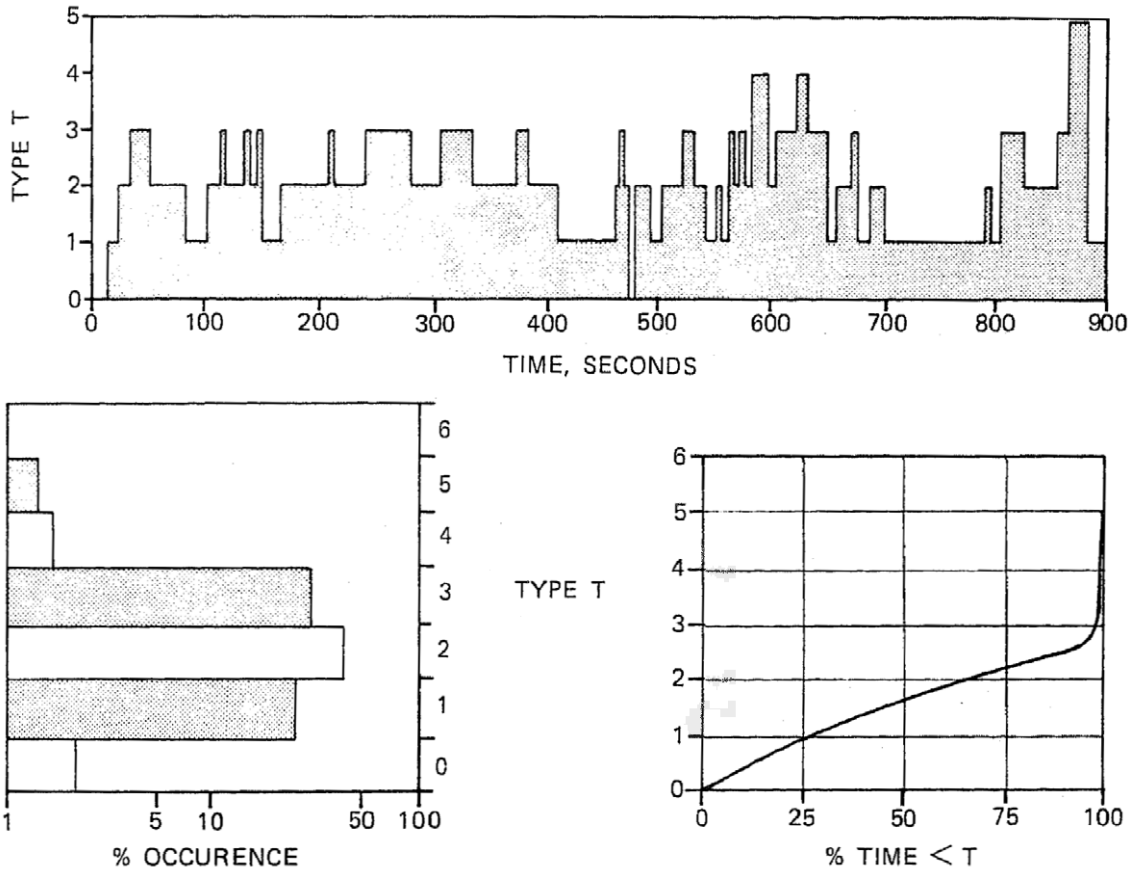

Figure 2.36: Occurrence of the different vortex types (Durgin & Hecker, 1978).

Hecker (1987) describes the time dependency of the vortex strength and gives diagrams of similar appearance as Durgin & Hecker (1978). The reason for the unsteady behavior of the intake-vortex which appears to be varying its strength and position constantly is described by a number of variable flow phenomena. At fixed water level and steady discharge, nevertheless, small changes in approach flow distribution, varying turbulence intensity, flow separation from the boundaries and local variations in energy dissipation interact and cause unsteady vortices. For an assessment of a given intake design Hecker (1987) recommends to record the time dependency of the vortex strength and therefore to avoid arbitrary subjective association of a vortex type.

2.3.5 Modelling of Vortices

General. The investigation of the hydraulic phenomena of intake vortices by physical scale models is based on the principle of a dynamically similar fluid motion. Flow patterns have to be similar in geometrically similar systems. To ensure this, the acting forces on the fluid elements must be convertible between both systems regarding the geometrical scale.
Numerous investigations were carried out to analyze which conditions in a model should be used to get transferable results for prototypes. For the present case of intake vortices the Froude number, circulation number, Reynolds number, and Weber number must be equal in model and prototype to ensure a full similarity. These numbers are used with different length scales.
Haindl (1959) termed this topic as "problem of similarity". His investigation works were carried out in three cylindrical tanks of similar design but different diameters. A main finding is that Froude's law is applicable, whereas for equal Reynolds numbers the results are the same (Reynold's law). However, Raju & Garde (1987) found out that all studies except Haindl (1959) indicated Froude as governing parameter.

Viscosity. The most widely investigated fluid property with respect to vortex formation investigations is viscosity. Daggett & Keulegan (1974) used two cylindrical tanks of similar design with an orifice in the center of the floor. The approach flow enters radially under angles which were set by vanes, so that a pre-circulation can be analyzed. Due to steady flow conditions the surface profile could be measured by a standard point gauge. The influence of viscosity was investigated by using several mixtures of water, glycerin and oil. Daggett & Keulegan (1974) found that the Reynolds number has an effect on the vortex formation even without a present circulation. Furthermore, evidence is given that not only viscosity, but also circulation must affect the vortex properties. Fig. 2.37 shows the relationship between the Reynolds number and the coefficient of discharge.
It becomes obvious that there is only a negligible effect of viscosity for Reynolds numbers $\mathsf{R} = Q/(A\nu) > 5 \cdot 10^4$, representing Reynolds numbers $\mathsf{R}_D = v_D D/\nu > 3.2 \cdot 10^4$ as used in the current study. In Daggett & Keulegan (1974) the circulation is expressed by the Kolf number $\mathsf{K} = \Gamma r/Q$. It is shown that K has a strong influence on the discharge. The higher the circulation, the lower the discharge. However, at low Reynolds numbers the influence of circulation Γ disappears. Thus, viscosity becomes predominant. Zielinski & Villemonte (1968) used different mixtures of fluids as well. They reported similar results, with a predominant role of the circulation at high Reynolds numbers. Incidentally, the direction of rotation has no influence on the discharge coefficient. The formation of an air core and its occurrence at high submergence heights is strongly depending on the viscosity.

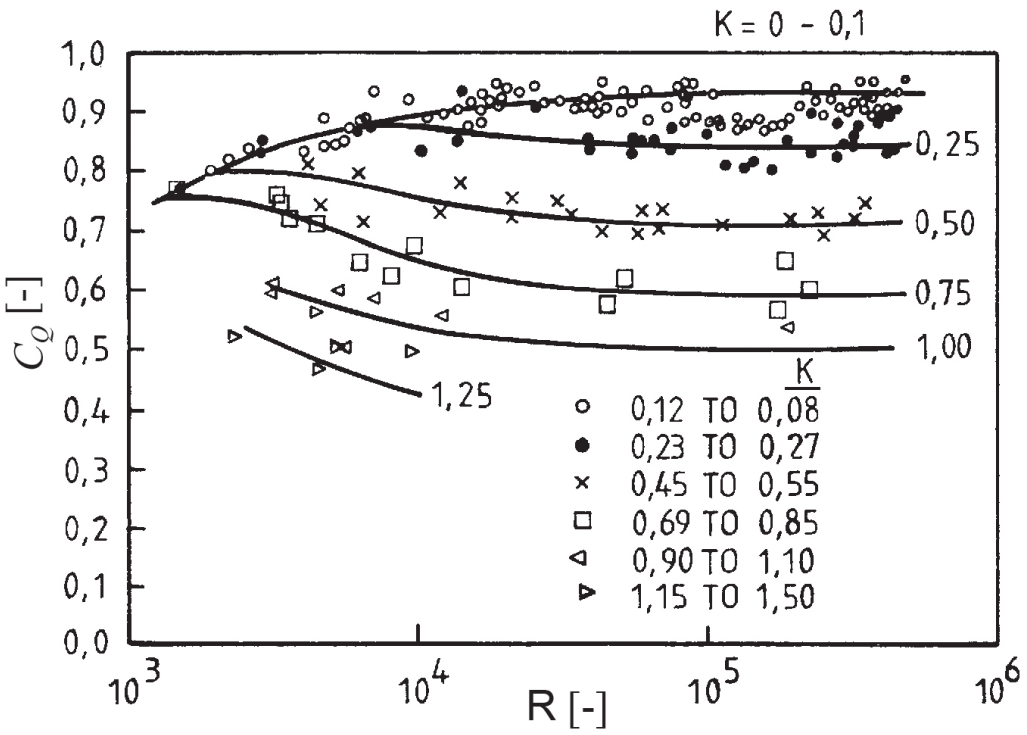

Figure 2.37: Relationship between Reynolds number R and coefficient of discharge C_Q as function of Kolf number $\mathsf{K} = \Gamma r/Q$ (Daggett & Keulegan, 1974).

Anwar et al. (1978) give a limit regarding the viscosity influence of the approach flow, which is described by the radial Reynolds number $\mathsf{R}_R = Q/(\nu h) > 3 \cdot 10^4$.

Surface Tension. The influence of surface tension has been less investigated and is therefore only fairly understood. Daggett & Keulegan (1974) found out that the effect on the discharge coefficient is small. On the one hand the influence of surface tension is not negligible at low circulation. On the other hand the vortex formation is not sufficiently strong enough at this stadium. Anwar et al. (1978) used the approach flow for statements concerning scale similarity. A minimum submergence Weber number $\mathsf{W}_h^2 = \rho h v^2/\sigma = 1000$ should avoid scale effects. Jain et al. (1978) conducted model tests with different liquids at vertical intakes and found that the formation is unaffected for $\mathsf{W} = \rho D v^2/\sigma \geq 120$. In the context of verifications of a theoretical approach, Odgaard (1986) determines the influence of surface tension as less than 10 %. Additionally, it has to be mentioned that under typical model conditions the criterion to neglect surface tension is $\mathsf{W} = \rho D v^2/\sigma > 720$. This value is quite high in comparison to the criterium as defined by Jain et al. (1978).
All presented publications are related to the vortex formation until the vortex core reaches the intake. However, knowledge about the behavior and especially the similarity of air entrainment cases is still missing.

2.3.6 Velocity Measurements Related to Intake-Vortices

Several experimental studies regarding intake vortices with focus on the velocity field were conducted using point measurement systems, e.g. Acoustic Doppler Velocimetry (ADV) and Laser Doppler Anemometry (LDA) (Hite & Mih, 1994). Due to the necessary probe intrusion it is challenging to achieve an almost undisturbed ADV measurement. The free-surface vortex has an unsteady behavior (Hite & Mih, 1994), changing its location by wandering around within certain geometrical limits. For a wandering vortex, an additional measurement method is therefore needed to determine the instantaneous and time-averaged vortex locations or it has to be stabilized to limit the vortex wandering, e.g. by introducing a pier in the tank (Hite & Mih, 1994). Brix (2004) investigated air flow into aircraft engines, comparable to subsurface vortices in water, by hot-wire anemometry. Several probes are rotating around the pipe axis. This enables to track the vortex and its velocity field. No statements about disturbance could be found. A disadvantage of point measurements in general is the lack of spatial resolution. To improve this deficiency other techniques need to be applied, e.g. Particle Tracking Velocimetry (PTV) or Particle Image Velocimetry (PIV). A central advantage of PIV is that turbulence statistics including turbulent kinetic energy (TKE) or Reynolds stresses can be derived from the velocity fields. PTV experiments of an intake vortex at a bottom outlet were conducted by Wang et al. (2011). Li et al. (2008) used 2D PIV to get a horizontal flow field and concluded that the tangential velocity distribution is similar to a Rankine vortex. Surprisingly, the circulation Γ of their air core vortices was not as constant as expected. Time-averaged velocity fields of a vortex at pump-intakes were studied by Rajendran & Patel (2000) and by Okamura et al. (2007) using 2D PIV. Both studies did not consider vortex wandering when calculating the mean velocity and the vorticity fields, respectively. Wang & Gursul (2012) examined ground vortices in air flow. Unsteady characteristics are measured by using a high frame rate 2D PIV system. The vortex meandering was characterized to be quasi periodical.
A study which considers the two-phase flow while resolving the whole velocity field is still missing.

2.3.7 Hydronumeric Approaches

Numerical simulations of highly 3D approach flow to an intake pipe are still sophisticated. A basic question is the choice of the most suitable turbulence model. Direct numerical simulations (DNS) give an exact solution. However, due to their high computation time demand they are difficult to realize. Rajendran et al. (1999) applied Reynolds-averaged Navier-Stokes equations (RANS). The number, location, and the general structure of the central intake vortex was analyzed The computed

vortices were generally larger and weaker than expected. The authors concluded that the differences are due to the unsteadiness of the flow and the inadequacy of the chosen turbulence model. Constantinescu & Patel (2000) analyzed the role of the turbulence model, especially near-wall models. Between the $k-\epsilon$ and the $k-\omega$ model no major difference in the streamline patterns and the vorticity contours were found. The intensity of vortices and secondary motion in the intake pipe are smaller for the $k-\epsilon$ model than in the $k-\omega$ model. Furthermore, an artificial roughness at the pump-bay was used to suppress vortices. Tokyay & Constantinescu (2006) validated a large eddy simulation (LES) model by RANS including a shear stress transport (SST)-module and via PIV measurements. The SST approach yields a good agreement regarding the mean velocity distribution and the mean vortical structures. The LES approach predicts the mean flow and turbulence statistics more accurately. Suerich-Gulick et al. (2008) studied the evolution of vorticity along the length of the vortices both experimentally and numerically at a simplified intake. They applied a simple RANS simulation with a $k-\epsilon$ turbulence model. The leading process of the vortex formation showed to be qualitatively different. Nakayama & Hisasue (2010) used LES and reproduced highly local and unsteady flows. The time development, the merging, and the break-up of vortices are similar to the experimental reference measurements. Large values of the second invariant of the velocity gradient tensor were used to identify the vortex core. Bowden & Hassan (2009) assumed potential flow and computed the dip location and the critical height with an accuracy of 30 % in comparison to experimental reference measurements. Significant discrepancies were found regarding the influence of the present cross flow. Bohling et al. (2010) use direct numerical simulations to study a steady bathtub vortex regarding the influence of the radial Reynolds number in a cylindrical tank with a central drain-hole. Th results are compared and discussed with analytically results of Einstein & Li (1955).

In some cases the one-phase flow can be predicted by proper and therefore comprehensive numerical models. If the free surface is bent at the dimple, the complexity and the velocity gradient in the air core is growing fast. At this stage the actual limit is reached that numerical simulations can provide nowadays. In future times the complex flow structure of an intake-vortex is possibly assessable numerically. It might be possible to compute the complex free surface by two upcoming methods in computational fluid dynamics. The first method is the volume of fluid (VOF) method which is a numerical technique for tracking and locating the free surface. The second promising method is the level set method (LSM), that is a numerical technique for tracking both interfaces and shapes. Both methods are advection schemes which enable to consider of the influence the surface tension. This scheme may work for the air-core itself, but the next step which has to be modeled nu-

merically and which is important for an accurate air entrainment simulation is the bubble separation at the air-core tail. An even more sophisticated step would be an adequate simulation of the air entrainment itself, which is still not possible.

2.3.8 Vortex Prevention

Denny & Young (1957), Bretschneider (1981), Knauss (1983), and Rutschmann et al. (1987) published measures to avoid air entrainment by design recommendations for intake structures. Their approaches to prevent vortex formation follow in principle the following issues:

- sufficient submergence,
- sufficient intake cross-section and discharge reduction, respectively,
- symmetrical approach flow,
- Reduction of circulation region in the close-up range,
- Disturbance of the circulation region,
- Extension of the distance from the free surface to the critical cross-section.

Due to the various approach flow conditions physical scale model tests are often required to find the most successful solution for preventing vortices. Often, the development of anti-vortex devices result in large and cost-intensive constructions. Borghei & Kabiri-Samani (2010) provided some recommendations for vertical orientated intake pipes. Precise design recommendations for engineering purposes regarding horizontal orientated intakes are still missing. Several publications report about special solutions with the help of anti-vortex devices following findings of hydraulic model investigations of intake structures (Rindels & Gulliver, 1983; Rutschmann et al., 1987; Möller et al., 2010).

2.4 Air in Pressure Systems

2.4.1 Negative Effects of Entrained Air

In case air is entrained into the pressure system, the flow properties change from a single phase fluid (pure water) to a two-phase flow (air-water mixture). The consequences on the operation, safety, and efficiency of the whole plant are negative. These effects can be divided into three groups, which are explained in detail below:

1. Reduction in efficiency of turbines and pumps;
2. Unsteady flow behavior, i.e. pulsation and pressure surges in the system with corresponding mechanical loads on the involved components;
3. Stationary effects, e.g. flow reductions from stationary air bubbles, and local corrosion damage.

The first group refers to direct effects of air in hydraulic machineries. Here, minimal air entrainment rates $\beta = Q_a/Q_w$ already causes a reduction in efficiency of around 1 %. An even larger air entrainment rate of $\beta = 1.5\,\%$ leads to an efficiency reduction of up to 16 % (Denny & Young, 1957; Papillon et al., 2000). For air entrainment rates up to $\beta = 4\,\%$ there is a further exponential decrease in efficiency. Depending on the type of pump (axial pumps are more sensitive than centrifugal), at air entrainment rates between $\beta = 7$–$20\,\%$, a sudden drop of efficiency down to a total flow interruption may take place (Chang, 1977; Poullikkas, 2000). Consequently, the efficiency reduction cannot be predicted quantitatively.
According to the second group, the effects due to air bubbles and the resulting compressible air-phase vary in function of bubble size, frequency, absolute pressure, and pressure difference. The pressure peaks can reach extreme values and, due to their periodical return, they generate frequent load alternations. These water hammers are often a source of large pressure heads. Another phenomenon is that air pockets can propagate against the flow direction. Ma et al. (2000) reported about intakes where air spurted out through a manhole in a 10 m high water column and damaged the trash rack at the intake. Extreme pressure changes can cause cavitation as well. The pulsations may cause oscillations in hydraulic machinery, parts of the plant and the whole pressure system, respectively. As a result of discharge fluctuations, the operating characteristics of hydraulic machines are affected, leading to uneconomic handlings and to an increased wearing of machine bearings and runners.
The third group refers to negative stationary effects. An accumulation of air reduces the effective cross-sectional area and consequently, the flow discharge decreases. Furthermore, local corrosion damages of steel linings may occur. These consequences are more static than those of the two former groups.

The effects of the two-phase flow on the hydraulic machinery are complex. Some machinery types can cope with a small amount of air, e.g., in the case of the HPP Veytaux of Alpiq holding AG (CH) a limit of $\beta \leq 2\,‰$ was used (Sulzer, 2012). However, some types have to be operated strictly with no air at all. Nevertheless, the machinery industry typically does not provide sort lists where the main types and their allowable air entrainment limits are described.

2.4.2 De-aeration

Entrained air has to leave the pressure system. The influence on a HPP scheme can reach from uncritical to fatal. In the simplest case the entrained air passes the conduit and de-aerates at the surge chamber. Air bubbles can also concentrate to air pockets and afterwards propagate against the flow direction, where the expansion at atmospheric pressure can cause an explosive incident. The situation where air is transported to the turbines has been described above. In many cases a de-aeration device is a simple but effective solution. Wickenhäuser (2008) showed the de-aeration by structural means. Fig. 2.38 depicts this simple and useful installation schematically.

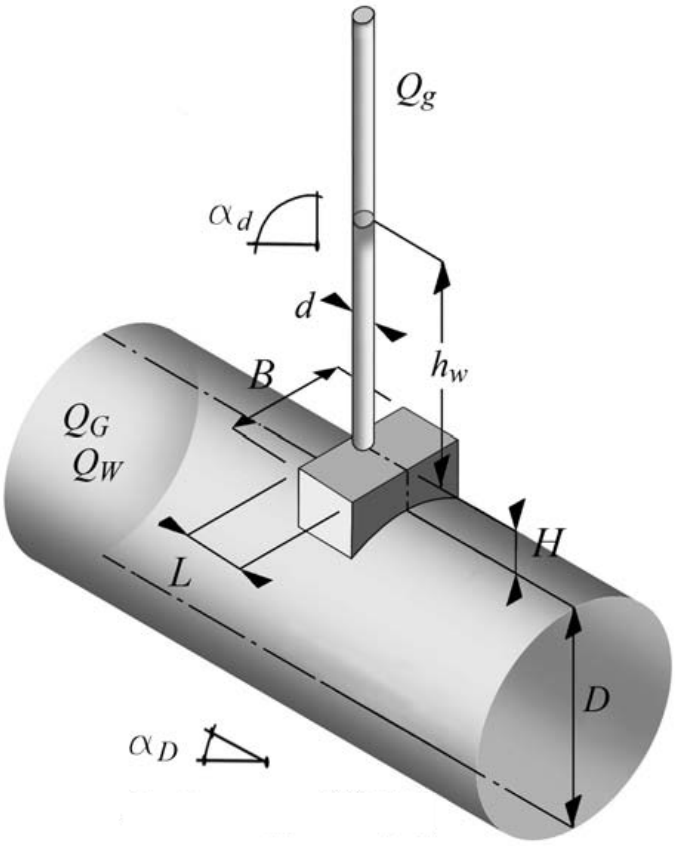

Figure 2.38: Schematic overview of a de-aeration device. On the conduit's roof a chamber with a riser pipe is arranged (Wickenhäuser, 2008).

Wickenhäuser (2008) presents several de-aeration systems by structural means, e.g. a chamber with an attached riser pipe at the top of the conduit to convey the collected air from the tunnel to the atmosphere. The dimensions of the de-aeration device are a function of discharge, conduit diameter, and the inflowing amount of air. Wickenhäuser (2008) provides examples how to de-aerate the full air phase from the pressure tunnel or pipe. However, a more detailed knowledge about the quantity of entrained air is required for an appropriate design.

2.4.3 Air Entrainment Rate due to Vortices

As given above, air in pressure systems of HPP has in general negative consequences such as reductions in efficiency, pulsations, pressure surges and reductions in flow rates. The entrainment of air into pressure systems takes place due to a few processes, for example by intake vortices or hydraulic jumps. The latter was investigated intensively by Dyment (1998) and Ma et al. (2010). Intake vortices are a major source of air entrainment. Their air entrainment rate

$$\beta = \frac{Q_\mathrm{a}}{Q_\mathrm{w}} \tag{2.18}$$

especially any correlation to a flow pattern, is unknown today. The relative air entrainment rate expresses the relationship between the volumetric air discharge Q_a and the volumetric water discharge Q_w. Sometimes the air concentration C_a is used instead of β:

$$C_\mathrm{a} = \frac{Q_\mathrm{a}}{Q_\mathrm{a} + Q_\mathrm{w}} = \frac{\beta}{\beta + 1} \ . \tag{2.19}$$

For small Q_a the values of β and C_a are almost identical. Up to $\beta = C_\mathrm{a}/(1 - C_\mathrm{a}) = 1\,\%$ the difference between β and C_a is less than $1\,\%$.
First approaches to measure the air entrainment rate β at pump sumps have been conducted by Iversen (1953). Fig. 2.39 shows the sump arrangement and the measured air entrainment rate β (here denoted as “Air to water ratio”) as a function of relative intake submergence. The measurement of air entrainment was performed with an air separator, where the pipe is interrupted by a closed cylindrical tank in which the air is separated from the water and accumulates at the crest.

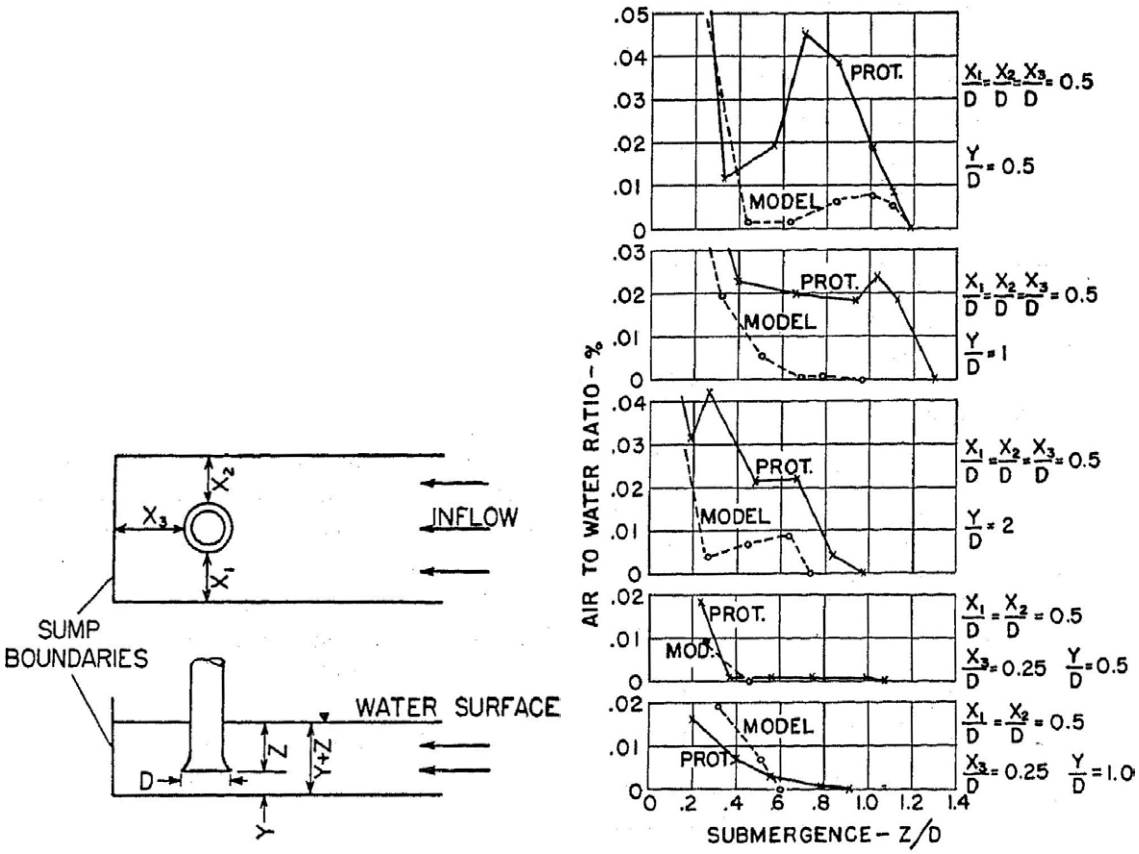

(a) Sump arrangement showing nomenclature (b) Results of β

Figure 2.39: Relative air flow rate β ("Air to water ratio") as a function of the relative intake submergence (Iversen, 1953).

According to Denny & Young (1957) the air entrainment rate at pump sumps is typically $\beta = 5\,\%$ and may reach $\beta = 10\,\%$ in extreme cases. However, investigations of Hattersley (1965) show air entrainment rates between $\beta = 0.06$–$0.73\,\%$, which are one to two magnitudes smaller than the rates reported by Denny & Young (1957). For intakes with horizontal axis Padmanabhan (1984) gives a relation of maximum values of air concentration rates versus a combined Froude number

$$\mathsf{F}_{\mathrm{co}} = \frac{v_D}{\sqrt{\mathrm{g}h}} \,, \tag{2.20}$$

with v_D = intake velocity, h = intake submergence relative to the center of the pipe axis and g = gravitational acceleration. Fig. 2.40 shows the data measured on a physical scale model with two horizontal intake pipes and a basin representing a pump sump. The conducted tests are separated in unperturbed and perturbed flow tests – in relation to a partial blockage of sump screens in the approach flow up to 75 %. A conductivity meter was used, which directly indicated cross-sectional volumetric average void fractions of air. The measurement accuracy of the rotating

electric field was determined to be ±1 % of void fraction. Typically, a test duration of 30 min was chosen. Some tests duration were down to 5 min. It should be noted, that the majority of all data points shown in Fig. 2.40 are below 1 %. With $C_{\mathrm{a,\,max}}$ = 0.15, the maximum relative air entrainment rate reaches β = 18 %. The data scatter is considerably high, hindering a trend analysis. The air entrainment was not correlated with the flow parameters.

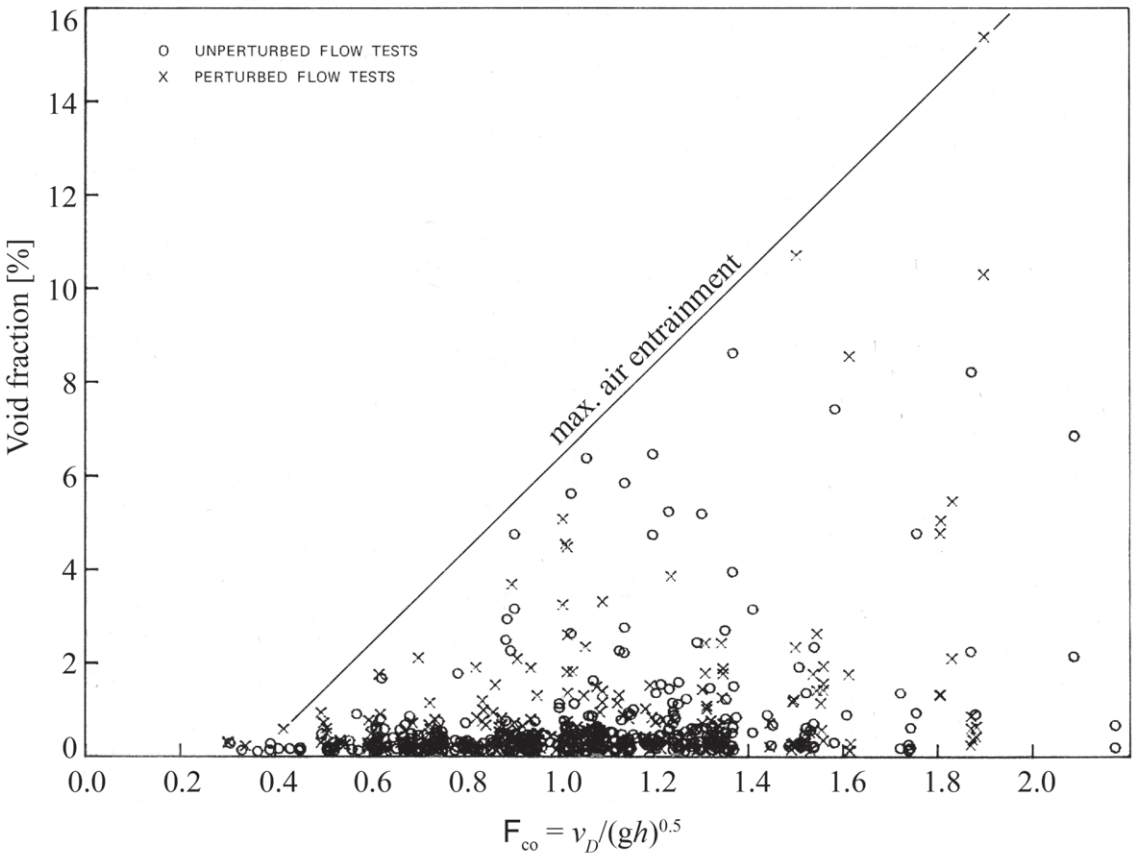

Figure 2.40: Air concentration C_{a} (void fraction) plotted against submergence Froude number F_{co}. The envelope line gives the maximum air entrainment rate as a function of F_{co} after Padmanabhan (1984).

Table 2.2 summarizes relevant publications and their findings regarding the air entrainment rate β. The range is wide and a correlation of the data was not made. Padmanabhan (1984) plotted a large number of data points as can be seen in Fig. 2.40, and accompanied by a plot of an envelope line. A systematic evaluation and continuation of attempts to measure the air entrainment rate was not conducted till today. No other parameters have been correlated. A personal request to Mr. Padmanabhan confirmed that no further research is known on this topic (Padmanabhan, 2008).

Table 2.2: Summary of investigations on air entrainment rate β.

authors	β	$\beta = f(...)$	experimental setup
Iversen (1953)	normal 1–5 %, extreme >10 %	n/a	intake orientated vertically upwards; scale model, prototype
Denny & Young (1957)	normal 1–5 %, extreme >10 %	n/a	intake orientated vertically upwards & horizontal; scale model
Hattersley (1965)	0.06–0.73 %	n/a	intake orientated vertically upwards; prototype
Padmanabhan (1984)	≤18 %	β plotted vs. F_{co}	two intakes orientated horizontal; scale model
	≤23 %	β plotted vs. F_{co}	intake orientated vertically downwards; scale model

2.5 Dimensional Analysis

The scale model design has to be simplified and optimized with the help of a dimensional analysis. A dimensional analysis is a common tool in experimental research of fluid dynamics. It serves primarily to create optimal investigation programs with minimal effort and maximum benefit of information (Kobus, 1974). The description of a physical relationship must be independent of the applied system of measurement. Several dimensional analyses that consider the vortex formation at intakes can be found in literature, e.g. Kolf & Zielinski (1959), Anwar (1968b), Zielinski & Villemonte (1968), Daggett & Keulegan (1974), Anwar et al. (1978), Gulliver & Rindels (1987), and Tastan & Yildirim (2010). The dependent variables are the relative submergence h/D, the discharge coefficient C_Q and the common dimensionless numbers, e.g. F, R, W. In most of the investigations cylindrical tanks and circular orifices in the tank bottom were used. Thus, the bulk flow is along the vertical axis. In opposite to this, Anwar et al. (1978) considered a horizontal pipe intake in a flume. They found six independent non-dimensional parameters:

$$f(\frac{\Gamma D}{Q_{\mathrm{w}}}, \frac{h}{D}, \frac{Q_{\mathrm{w}}}{A\sqrt{2\mathrm{g}h}}, \frac{b}{D}, \frac{Q_{\mathrm{w}}}{\nu h}, \frac{\rho Q_{\mathrm{w}}^2 h}{A^2\sigma}) = 0, \text{ with } A = \frac{\pi}{4}D^2 \ , \tag{2.21}$$

where A is the cross-sectional area. In the following a dimensional analysis with respect to vortex induced air entrainment is conducted. Fig. 2.41 gives a sketch with the parameters assumed to be necessary to define the essential physical processes.

The parameters are listed and described in Table 2.3 in three categories. The basic dimensions are the length L, the time T, and the mass M.

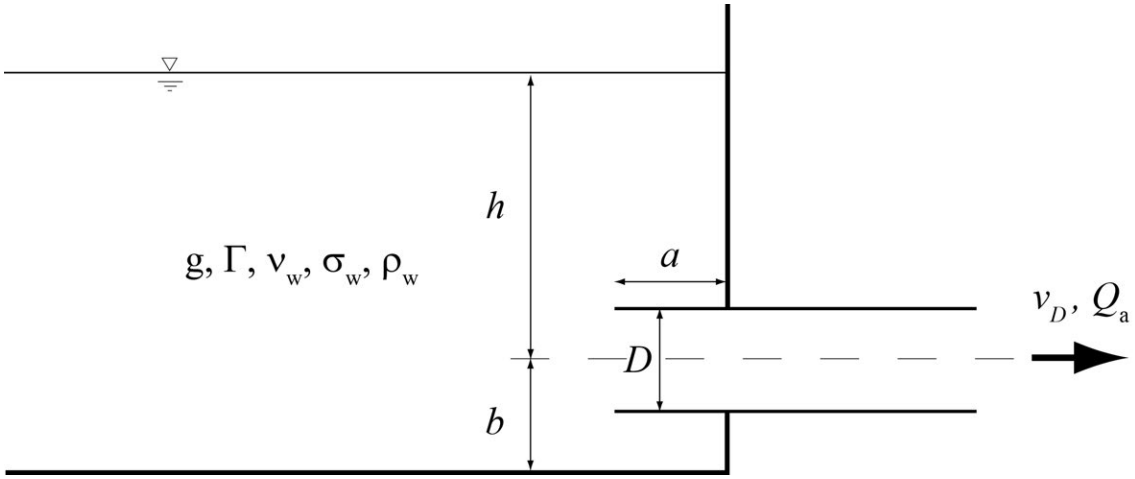

Figure 2.41: Definition sketch including the essential physical parameters.

Table 2.3: Governing dimensional parameters.

category	symbol	unit	basic dimension	description
geometry	D	[m]	L	intake diameter
	h	[m]	L	intake submergence
	a	[m]	L	head wall distance
	b	[m]	L	bottom clearance
external effect	v_D	[m/s]	L/T	intake velocity
	g	[m/s^2]	L/T^2	gravitational acceleration
	Γ	[m^2/s]	L^2/T	circulation
	Q_a	[m^3/s]	L^3/T	air discharge
fluid properties	ν_w	[m^2/s]	L^2/T	kinematic viscosity
	ρ_w	[kg/m^3]	M/L^3	density
	σ_w	[kg/s^2]	M/T^2	surface tension

The idea of a dimensional analysis is to transform the dimensional parameters that govern the process by combining them into dimensionless constants Π. Following the Vaschy-, Π- or Buckingham-theorem (Martin & Pohl, 2009) the function of the parameters can initially be written as:

$$f(D, h, a, b, v_D, Q_\mathrm{a}, \Gamma, \mathrm{g}, \nu_\mathrm{w}, \rho_\mathrm{w}, \sigma_\mathrm{w}) = 0 \tag{2.22}$$

A science-based recommendation for this procedure does not exist. However, with skillful handling hydrodynamic correlations can be detected, investigation programs can be optimized and test results ca be transferred to nature (Martin & Pohl, 2009).

In total Table 2.3 lists eleven parameters and three basic dimensions. Therefore, $11 - 3 = 8$ Π-numbers have to be examined. D, h, a, b can be reordered to:

$$\Pi_1 = h/D \tag{2.23}$$

$$\Pi_2 = a/D \tag{2.24}$$

$$\Pi_3 = b/D \ , \tag{2.25}$$

where Π_1 denotes relative submergence, Π_2 denotes relative head wall distance, and Π_3 denotes the relative bottom clearance. By combining the eleven parameters further non-dimensional Π-numbers can be derived, reading:

$$\Pi_4 = \frac{v_D}{\sqrt{\mathrm{g}D}} = \mathsf{F}_D \tag{2.26}$$

$$\Pi_5 = v_D \sqrt{\frac{\rho_\mathrm{w} D}{\sigma_\mathrm{w}}} = \mathsf{W}_D \tag{2.27}$$

$$\Pi_6 = \frac{v_D D}{\nu_\mathrm{w}} = \mathsf{R}_D \ , \tag{2.28}$$

where Π_4 = intake Froude number, Π_5 = intake Weber number, Π_6 = intake Reynolds number. The parameter D might also be replaced by the intake submergence h, as well as F, W and R according to the submergence. The last two remaining dimensional parameters that have not been listed yet are Γ and Q_w. Both are mainly related to the characteristics of the approach flow, the geometry of the intake and the water discharge Q_a. Consequently, the circulation number N_Γ and the relative air entrainment rate β are introduced as:

$$\Pi_7 = \frac{4\Gamma D}{v_D \pi D^2} = \frac{\Gamma D}{Q_\mathrm{w}} = N_\Gamma \tag{2.29}$$

$$\Pi_8 = \frac{4Q_\mathrm{a}}{v_D \pi D^2} = \frac{Q_\mathrm{a}}{Q_\mathrm{w}} = \beta \ . \tag{2.30}$$

These Π-numbers that have been found are numbers that are well known from literature (Knauss, 1987c). In comparison to Anwar et al. (1978), as mentioned above, five out of his six independent numbers are found here as well.

2.6 Design Practice

Common intake designs are based on assumptions and empirical rules to optimize the minimum tolerable submergence height at the intake versus the storage volume. A rule-of-thumb is to keep the velocity at the trash rack at < 1 m/s. If the intake is situated near the bed the possibility of sediment entrainment increases. According to the drawdown level vortex formation associated with air entrainment has to be considered. Most often a "zero air criteria" is applied to avoid damages at turbines and tunnels. Existing HPPs are designed and operated in such a way that no air enters the pressure system at all. This leads to a high submergence and thus to a limitation in terms of storage management and a loss of storage volume, respectively. Nevertheless, the entrainment of air cannot be prevented at every moment – especially for conditions close to operational limits, as even a conservative design constitutes an element of risk with regard to the aforementioned effects. Hydraulic site-specific scale model investigations are a common way to examine the probability of intake vortices. However, these models do not allow to predict the amount of entrained air. Instead of increasing the efforts to predict the air entrainment rate typically anti-vortex devices are tested and optimized. In most cases these devices are effective to prevent air entrainment, but their construction and maintenance is expensive.

Thus, there is an interest to replace the common design approach of a zero-air-criteria by a flexible assessment strategy. Alternative intake design approaches have been already realized or are currently under construction. For instance, Vorarlberger Illwerke, Austria, have built a PSHPP where water from the Pelton turbines containing air is pumped in a hydraulic circuit. However, as it was not possible to ensure zero-air-criteria conditions, a de-aeration device had to be installed additionally (VAW, 2006). Göckler (2012) reports that the plant is, up to now, entirely well-operating. A further example is given by HPP Handeck 2 of Kraftwerke Oberhasli AG, Switzerland (VAW (2010), Möller et al. (2010)). This plant is currently under construction. Classical hydraulic scale model tests have been conducted to optimize a large anti-vortex device in the planning phase. Alternatively, the feasibility of accepting a slight air entrainment combined with a de-aeration device has been analyzed theoretically. Based on both the design guidelines for de-aeration devices proposed by Wickenhäuser (2008) and on an assumed air entrainment rate β after Padmanabhan (1984), the de-aeration device was pre-designed. However, in favor of the anti-vortex device solution is was discarded afterwards. Furthermore, a similar de-aeration device as predesigned for HPP Handeck 2 is now planned at HPP Veytaux of Alpiq AG, Switzerland (VAW, 2013a).

These modern design approaches stand for a new way in intake design.

2.7 Concluding Remarks

The lack of knowledge concerning the phenomena of air-entraining intake vortices can be summarized as follows:

- The mechanism of the whole phenomenon and the governing processes is still poorly understood.
- No generally accepted criterion exists that defines a critical submergence.
- Hardly any quantitative information could be found concerning the occurrence probability of intake vortices nor the related air entrainment.
- The air core geometry and its inherent 'aero'dynamics is poorly understood.
- Few approaches exist that enable an estimation of the amount of air entrained into pipe systems.
- Systematic investigations with regard to quantitative air entrainment measurements are missing.

To close or at least narrow these in basic knowledge and engineering practice is a challenge to be tackled in this research project.

Chapter 3

Experimental setup

Abstract. *This chapter describes the arrangement and the setup of physical experiments to investigate the air entrainment rate due to intake-vortices. A large scale experimental facility with an overall length of 20 m has been built at the laboratory of VAW at ETH Zurich with respect to the previously derived research strategy. Heart of the setup is a 50 m^3 tank that is subsequently adjoined to a 14 m long pipe system. The scale similarity complies with the common empirical limits for air entraining vortices. A 2D Particle Image Velocimetry system enables to quantify the horizontal flow field around intake-vortices. Furthermore, the present experimental setup allows measurements of air entrainment rates simultaneously to the determination of the circulation of causative vortex systems.*

3.1 Experimental Facilities

The experiments were carried out in an experimental tank-pipe system as depicted in Fig. 3.1. It consists of three main parts: (a) a 50 m^3 experimental steel tank, (b) a 14 m long pressure-pipe system, and (c) a 130 m^3 reservoir. Flow discharge is supplied by two pumps.

Experimental Steel Tank. The experimental steel tank has a length of 6.0 m, a width of 3.2 m, a stilling basin height of 3.4 m, and a main tank height of 2.2 m. The stilling basin is designed to promote a uniform velocity distribution in the main tank. In the stilling basin the end fittings of the feeding pipes are perforated to diffuse the incoming jet homogeneously. The flow is guided through a vertically arranged filter fleece to the main tank. An additional wave absorber raft (not drawn in Fig. 3.1) damps occurring surface waves. In a top view the tank is arranged symmetrically to the main flow direction and contains no other installations. Thus, the unsteady nature of intake vortex generation is judged to be undisturbed by the boundary conditions of the experimental tank. The water flows from the main tank into the pressure pipe system through a horizontal intake pipe. The inflow opening by a

sharp edged circular pipe has an inner diameter $D = 0.389$ m (DN400). Visual access to the tank is given by three glass windows at the bottom wall, the right wall, and the head wall. Planar glass with a thickness of 40 mm is used to avoid distortion.

Pressure Pipe System The pressure-pipe system is made of plexiglass to allow visual observation. The intake pipe[1] extends 0.8 m into the tank and has an outside length of 3.0 m. The intake pipe is installed horizontally and aligned straight to avoid any influences of cross-sectional or slope changes. The measurements are conducted with a pipe diameter D of DN400. Thus the distance to the side walls is $4D$, the bottom clearance is $1D$. The maximum water level in the tank is approx. $4.5D$. Therefore, the critical submergence is seen to be uninfluenced (chapter 2.3.2). The whole horizontal part of the pipe system was optionally replaced by plexiglass pipes of diameters $D = 0.190$ m (DN200), 0.291 m (DN300), and 0.484 m (DN500) for scale family investigations. A subsequent pipe expansion to DN500 combined by a slope change of -5° is used to optimize the de-aeration device. A detailed description is given in chapter 3.5. At the end of the pipe a contraction to DN400, a magnetic flow meter (MID), a 90° bend, and a gate valve are installed.

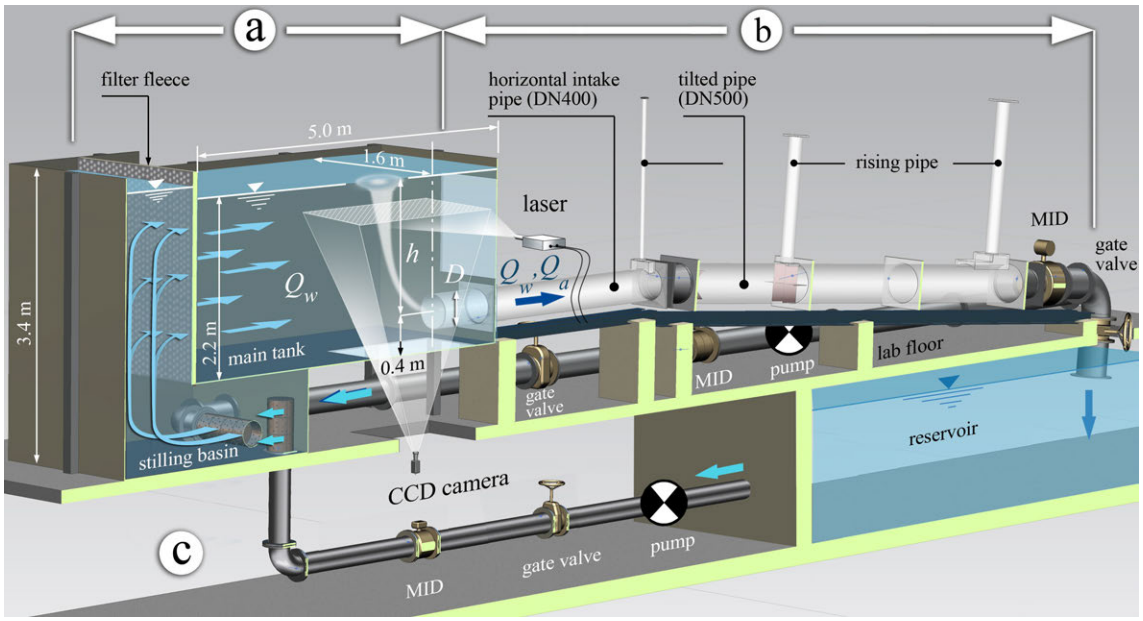

Figure 3.1: Cross sectional view through the experimental facility: (a) experimental tank with stilling basin and filter fleece for flow homogenization, and main tank with intake pipe and 2D Particle Image Velocimetry (PIV), (b) pressure-pipe system with a de-aeration system with three rising pipes, (c) pumps and reservoir.

[1] An extension into the tank is chosen to investigate the physical process of vortex formation at hydraulic structure intakes exempt from external boundary condition effects, e.g. without vortex quenching due to the head wall. The stagnant region above intakes can also be seen in Fig. 2.9 and prototype examples, e.g. chapter 9.

Reservoir & Pumps The reservoir is situated below the lab floor. Two frequency controlled pumps provide a maximum discharge $Q_w = 0.510$ m^3/s. The water level in the tank depends on the in- and outflow discharge. The discharge can be regulated by three gate valves, one in each inflow pipe and one in the pressure-pipe system. The water temperature ϑ_w depends on the surrounding air temperature and the pump operation in terms of duration and power. Typically, the water temperature equals the ambient temperature in a range of ϑ_w = 15–20 °C. However, measurements showed that the pumps heat up the water body up to 0.8 °C/h affecting the fluid properties. For instance, an increase in temperature from 20 to 30 °C during an experiment of 12.5 h leads to changes (air values in parentheses) of (1) density ρ_w = +0.3 (-3.3) %, (2) kinematic viscosity ν_w = -20.8 (+6.2) %, and (3) surface tension between air and water σ_w = -2.1 %. However, due to the high values of Reynolds and Weber numbers these changes are expected to be negligibly small. A detailed analysis of this topic is given in chapter 5.
The experimental facility was designed to cover the full range of hydro power intake conditions in terms of submergence and intake velocity. The intake Froude number $\mathsf{F}_D = v_D/\sqrt{gD}$ (compare: Π_4, chapter 2.5) can be varied from 0 up to 2.2. This range covers the relevant design practice of $0.4 \leq \mathsf{F}_D \leq 2.1$ outlined by Knauss (1987b). The relative submergence h/D (compare: Π_1, chapter 2.5) can be varied from 0.5[2] to 4.5, the critical value at $\mathsf{F}_D = 2.2$ (Knauss, 1987c). Thus, the range of the submergence Froude number $\mathsf{F}_h = v_D/\sqrt{gh}$ is given between 0 and 3.1.

3.2 Scale Similarity

Not all similarities or Π-numbers, respectively, can be reproduced in a hydraulic scale model simultaneously. This means that not all Π-numbers in model and nature have the same size. For the present model a Froude similarity is chosen. To keep the influence of viscosity (eq. 2.28) and surface tension (eq. 2.27) negligible, the experimental conditions must be maintained above corresponding threshold values. Empirical limits can be taken from literature (see chapter 2.3.5). Table 3.1 shows a comparison of empirical limits versus corresponding numbers of the present experimental facility. Model operation is limited to $\mathsf{F}_D = 0.1$–2.2. De facto, experimental runs are conducted within a range of $\mathsf{F}_D = 0.4$–1.4. Furthermore, the full range of $h/D = 0.5$–4.5 is outlined. However, the runs were conducted with $h/D = 1.25$–2.5. Consequently, the conditions provided by the experimental facility are within the limits that have to be adhered while regarding similitude criteria of intake vortex investigations. The relevant model parameters are largely superior to the generally accepted limits regarding similitude criteria of intake vortex investigations, except

[2] $h/D = 0.5$ equals a water level at the upper edge of the pipe, h refering to pipe axis.

Table 3.1: Comparison between model parameters and empirical limits. For R_R and W_h at $h/D = [0.5, 4.5]$ values are given to outline the full range. Bold marked values are below the limit.

F_D [-]	v_D [m/s]	Q_w [m^3/s]	R_D [10^4] $> 3.2^a$	R_R [10^4] $> 3.0^b$		W_D^2 [-] $> 120^c$	W_h [-] $> 31.6^d$	
				$\frac{h}{D}$=0.5	$\frac{h}{D}$=4.5		$\frac{h}{D}$=0.5	$\frac{h}{D}$=4.5
0.1	0.20	0.02	8	12	**1.3**	203	**10**	**30**
0.4	0.78	0.09	30	47	5.3	3248	40	121
1.4	2.73	0.33	105	165	18	39785	141	423
2.2	4.30	0.51	166	260	29	98245	222	665

$^a\mathsf{R}_D$	$= v_D D/\nu_\mathrm{w}$	$> 3.2 \cdot 10^4$	(Daggett & Keulegan, 1974)
$^b\mathsf{R}_\mathrm{R}$	$= Q_\mathrm{w}/(\nu_\mathrm{w} h)$	$> 3.0 \cdot 10^4$	(Anwar et al., 1978)
$^c\mathsf{W}_D^2$	$= \rho_\mathrm{w} v_D^2 D/\sigma_\mathrm{w}$	> 120	(Jain et al., 1978)
$^d\mathsf{W}_h$	$= v\sqrt{\rho_\mathrm{w} h/\sigma_\mathrm{w}}$	> 31.6	(Anwar et al., 1978)

for the radial Reynolds number R_R at $\mathsf{F}_D < 0.23$ ($h/D = 4.5$) and submergence Weber number W_h at $\mathsf{F}_D \leq 0.1$ ($h/D = 4.5$) and $\mathsf{F}_D \leq 0.32$ ($h/D = 0.5$). However, within the range of $\mathsf{F}_D = 0.4$–1.4 as investigated within the present research project no parameter value is below any of the given limiting values (see Table 3.1).

3.3 Instrumentation and Measurement Equipment

Table 3.2 lists the instruments that were used in the experimental investigations. Data acquisition of all measurement subsystems is performed continuously by a frequency of 1 Hz. Measurement data are saved to ASCII-files.

Table 3.2: Instrumentation and measuring equipment of the experimental facility.

instrumentation	quantity	unit	range	accuracy
ADV	v	m/s	± 0.3	$\pm 0.5\,\%$ (measured value)
2 pumps	Q_w	m^3/s	0–0.51	$\pm 2\,\%$
MID	Q_w	m^3/s	$v \leq 0.4$ m/s	± 0.002 m/s
			$v \geq 0.4$ m/s	$\pm 0.5\,\%$ (measured value)
ultra sonic sensors	h	mm	100–1000/400–2500	$\pm 1.5\,\%$ (measured value)
thermometer	ϑ_w	°C	0–40	$\pm 0.2\,\%$
vortex type box	VT	-	0–6	-
conductivity probe	-	-	0, 1	-
pressure sensor rel.	Δp_a	mbar	0–500	$\pm 0.5\,\%$ (measuring range)
pressure sensor abs.	p_atm	mbar	700–1200	$\pm 0.5\,\%$ (measuring range)
PIV	see chapter 3.4 for detailed information			

For preliminary tests, an Acoustic Doppler Velocimetry (ADV) system from *Nortek AS*, Norway was used to measure the flow field within a velocity range of ± 0.3 m/s at a

frequency of 25 Hz at the outset of the main tank in order to evaluate the efficiency of the flow straightener construction. The quality of the ADV measurements is controlled by signal-to-noise ratio (SNR). Due to both a low particle concentration and small velocities the measurement time is set to 60 s at each point. Results are given in chapter 4.1.

Discharge is provided by two pumps that can be steered by their frequency. Both supply pipes with diameters of DN250 and DN300, respectively, are equipped by magnetic flow meters (MID) and each can be regulated manually by a gate valve. At the end of the pressure-pipe system with diameters of DN400 to DN500 to DN400 another pair of gate valves and a magnetic flow meter from *Endress+Hauser Flowtec AG*, Switzerland is installed.

The water level in the main tank is measured by means of an ultra sonic sensor from *Baumer Holding AG*, Switzerland in the center where the surface is independent of the vortex field. The water temperature is continuously recorded by an electric thermometer.

A vortex type box with seven buttons, where only one can be active, in relation to the vortex types $VT = 0$–6 (chapter 2.2.3) enables a continuous and manual documentation of the visually identified vortex types. This box is connected to the measuring computer where the information is recorded.

A conductivity probe is installed in front of each de-aeration device. It consists of two 0.6 mm thin needles with a distance in between of 5 mm which intrudes 6 mm into the pipe. Among these needles the conductivity is measured. A binary signal is recorded by using a threshold value depending on the conductivity difference between air and water. Passing air at the pipe ridge triggers 1, otherwise 0. Depending on the integral time air bubbles can be derived, including their size and frequency. The accuracy of the conductivity probe is unknown.

Each rising pipe of the de-aeration device is equipped with an ultra sonic sensor and a pressure sensor to get information related to the entrained air. Relative pressure sensors are used to determine the difference from the atmospheric or ambient pressure p_{atm} which is measured by an absolute pressure sensor.

3.4 Particle Image Velocimetry

General. Particle Image Velocimetry (PIV) is a state-of-the-art instrumentation in fluid dynamics research. The main benefits are known as whole-flow-field and non-intrusive velocity vector measurement techniques in a flow cross-section. At present, PIV is the most common and best known method for quantitative visualization of flow fields (Zhang & Sarkar, 2012).

Measurement Principle of PIV. Fig. 3.2 shows an overview of the principles of PIV, from laser pulse up to data analysis.

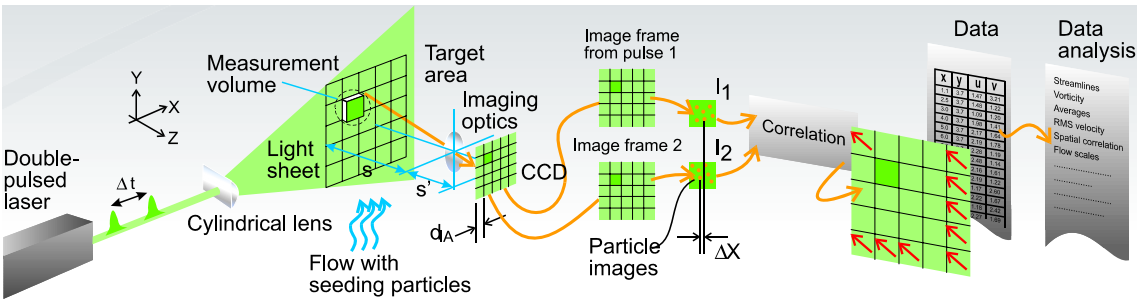

Figure 3.2: Measurement principles of 2D PIV (DantecDynamics, 2012b).

To obtain instantaneous velocity measurements of flow fields, digital image recordings of a 2D plane of the flow have to be taken. The fluid has to be seeded by tracer particles. These particles should be sufficiently small to be able to follow the flow lines. The choice of proper tracer particles is a difficult part of the PIV setup. The tracer particles have to be neutrally buoyant in the fluid. Very small particles are invisible to the camera, or they evoke peak-locking effects, i.e. the vector field contains strong peaks at the position of the integer pixel displacement. Raffel et al. (1998) suggested using particles with a diameter bigger than 1.5 px on the camera chip. If the particles appear smaller, a slight defocussing of the camera optics increases their pixel size in the recordings. If the particles are too large, they do not follow the fluid flow, due to inertial forces. Flow structures can be adequately resolved if their length scale is at least five times bigger than the particle diameter (Raffel et al., 1998). The tracer particles must be able to scatter the light. As the seeding particles are very small, a powerful illumination of the measuring area is needed. Usually, a laser light sheet is used to illuminate a required plane in the flow.

The basic means of obtaining velocity vectors is based on the well-known kinematic equation, i.e. velocity equals distance divided by time. The procedure is as follows: A target area, also known as area-of-interest (AOI), is cut out of the digital image, the field of view (FOV), and divided into small subareas, called interrogation areas

(IA). A local displacement vector is determined for each IA between two sequentially recorded image frames by means of a cross correlation in the following form:

$$C(\Delta x, \Delta y) = \sum_{x=0,\ y=0}^{x<n,\ y<n} I_1(x, y) I_2(x + \Delta x, y + \Delta y) \ . \tag{3.1}$$

Hereby, I_1 and I_2 are the image intensity of the first and second IA. The 2D array C gives the correlation strength for all displacements (Δx, Δy) between the two IA's, while n is the size of the IA (Raffel et al., 1998). The correlation distribution is obtained from eq. 3.2 in which the highest peak represents the most probable displacement. Fig. 3.3 shows an example of cross correlating an IA.

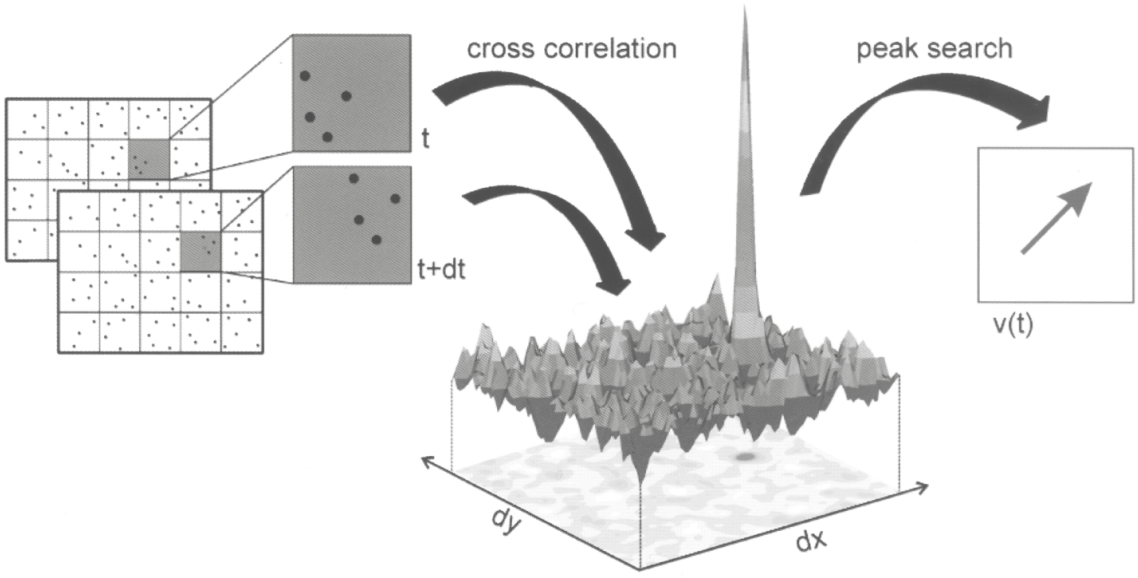

Figure 3.3: Cross correlation of an interrogation area (source: *LaVision GmbH).*

Finally, the velocity vector can be deduced using

$$[u, v] = \frac{[\Delta x, \Delta y](C_{\max})}{\Delta t} \ , \tag{3.2}$$

where $[\Delta x, \Delta y](C_{\max})$ is equal to the most probable displacement and Δt is the time between two image frames. If the velocity vector for each IA is calculated, the result is a time series of vector fields. The temporal and spatial resolution depends on the optical quality of the camera system, the seeding particles, the illumination and the computer power.

PIV-Equipment. The horizontal velocity field around the vortex is measured by means of 2D Particle Image Velocimetry (PIV). Fig. 3.4 shows a schematic sketch of an experimental run, where the FOV surrounding the air core of the intake-vortex is highlighted. The CCD camera with its angle of vision and the stretched laser light sheet is indicated.

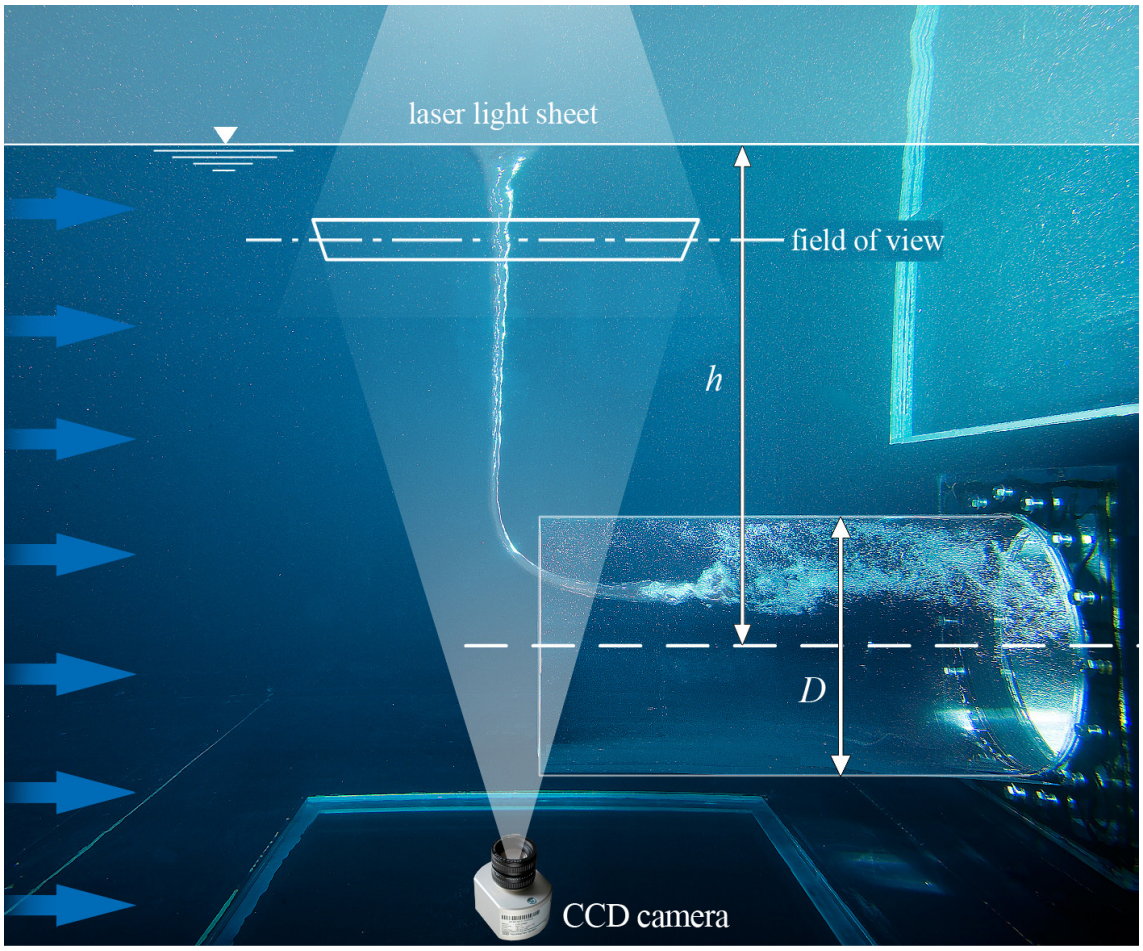

Figure 3.4: Sketch of an experimental run in the main tank. The 2D PIV is used to quantify the horizontal velocity field around the air entraining intake-vortex.

A commercial *Dantec Dynamics* 2D PIV system including DynamicStudio v3.31 software was used. It contains a double-pulsed Nd:YAG laser which typically emits infrared light with a wavelength $\lambda_l = 1064$ nm. For safety reasons the frequency is doubled to generate visible laser light at $\lambda_l = 532$ nm, appearing as green light. The laser *DualPower 200-15* has a maximum pulse energy of 2×200 mJ and a maximum frequency of 15 Hz. Spherical lenses and one single cylindrical lens are mounted in front of the laser. The cylindrical lens expands the laser light beam into a plane, referred to a laser light sheet. Special light sheet optic modules adjusting the thickness and the fan angle are used to compress the plane into a thin sheet at the target area. High pulse energy is chosen to have a sufficient illumination of

the large AOI of approx. 1 m^2 and an additional length through the water from the right wall. Image collection is done by a *HiSense 4M* camera with CCD sensor which has a high spatial resolution and a high sensitivity. The image resolution is 2048 × 2048 px^2 with 12 bits/px. The camera has an anti blooming protection. On the mounted lens *Nikon Nikkor AF* (focal length = 35 mm, maximal aperture F-number = 2.0) a filter suppresses extraneous light.
To get a satisfying spatio-temporal resolution, a double frame mode is used. In this mode two images are captured within a short time. The first image is not read out directly as in a simple single-frame mode, but shifted to the storage position on the camera chip. Then, the second frame is taken. The shortest time allowed between two frames in double frame mode is $\Delta t = 0.1$ ms. For the experiments an interval time of $\Delta t = 6$ ms is used to acquire one double frame of about 16 MB at full resolution. The maximum number of double frames that can be stored successively is 579 which equals about 9 GB. The images have to be transfered from the RAM to the local hard disk drive and later to a NAS[3] system with RAID[4] function, due to the high storage demand and to backup the data. Vectors can only be computed between one image-pair of one double frame, but not between different double frames. The maximum recording frequency of the whole system in double frame mode is 5.6 Hz.

The PIV system is aligned to the large scale hydraulic model investigation of intake-vortices. During the development of an optimal measurement procedure additional adaptations become necessary as described in chapter 4.3.

3.5 De-aeration System

A de-aeration of the two-phase pipe flow is necessary to determine the air entrainment rate β (eq. 2.18). Thus, the volume of air V_a over time t has to be measured.

Fig. 3.5 shows a sketch of the applied de-aeration system. Its design is inspired by Wickenhäuser (2008). A basic de-aeration device consists of a dome (Fig. 3.5 g) on top of the pipe and an adjoining rising pipe (Fig. 3.5 b). The idea is to guide entrained air to the top of the pipe and via a rising pipe up to the free surface. The volume of air can be determined either by pressure or by velocity measurements. The latter quantity is useful at high and constant air discharges Q_a. For the present setup, pressure measurements have proved to be more suitable. They are described in the following.
Air bubbles of different sizes are distributed over the entire cross-section of the pipe.

[3]Network-attached storage (NAS) is file-level computer data storage connected to a computer network providing data access to a heterogeneous group of clients.

[4]Redundant array of independent disks (RAID) is a storage technology that combines multiple disk drive components into a logical unit.

Bubbles have to rise up to the pipe top to be able to de-aerate. At low velocities this can already happen in the horizontal pipe section of DN400 (Fig. 3.5 a). At higher pipe velocities an expansion to a DN500 pipe (Fig. 3.5 c) is necessary to reduce the velocity and the influence of secondary currents so that air bubbles may rise to the pipe top. The water level in the rising pipes (Fig. 3.5 b) equals the piezometric head at atmospheric ambient pressure at the beginning of each measurement. It depends on the water level in the tank and the pipe velocity. Especially at small tank water levels and high pipe velocities the water level in the rising pipes is low. The DN500 pipe is tilted to increase the distance between the ridge of the pipe and the free surface in the rising pipes. The distance is termed as de-aeration height h_w. Therefore, the measurable parameter range is amplified and the measuring time could be extended (compare Fig. 3.5, $h_{w,1}$–$h_{w,3}$). This enhances especially the quality of measurements at high velocities and large air discharges, respectively.

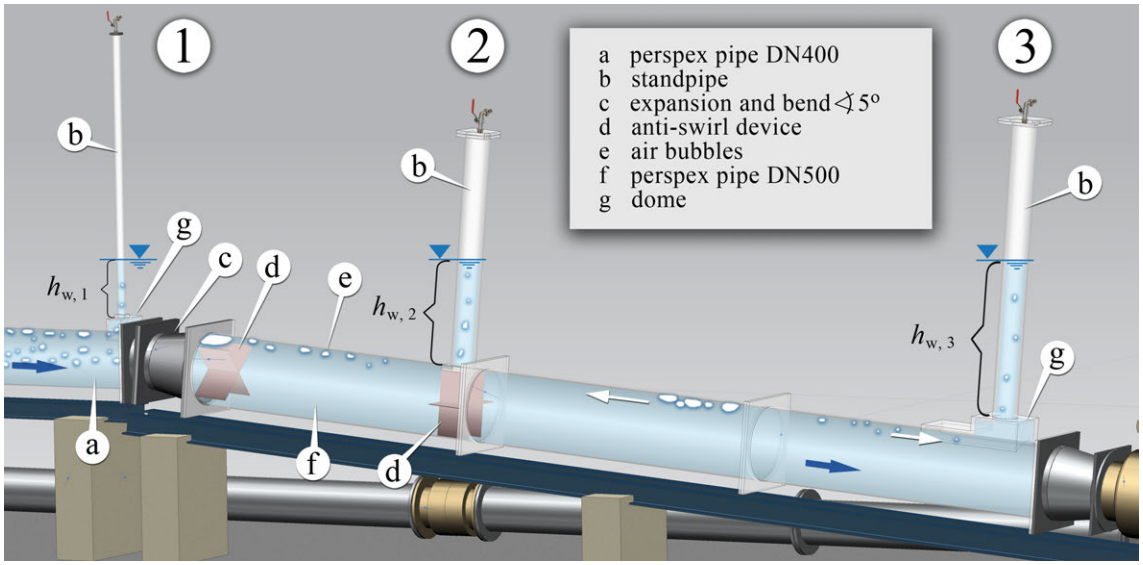

Figure 3.5: Sketch of the de-aeration system using three de-aeration devices.

If the valve on top of a standpipe is closed, the pressure in the pipe increases in relation to the atmospheric pressure with each bubble rising through the pipe. Consequently, the water level is decreasing. Then, V_a within a given measurement time can be calculated by eq. 4.1 (*ideal gas law*). All experiments are conducted with measurements of both the water level and the air pressure.

If a pipe is tilted downwards air bubbles or air pockets can propagate against the flow. Limits can be pre-estimated after Falvey (1980). Given a DN500 pipe with a slope of -5° and an inner diameter of $D = 0.484$ m air bubbles propagate against the flow if $Q_w < 0.16$ m^3/s and air pockets if $0.16 < Q_w < 0.20$ m^3/s. These limits are within the investigated range. Thus, propagation of air bubbles against the flow can be expected. This has to be considered in the forthcoming analysis in chapter 6.1.

The de-aeration system consists of three basic devices (see Fig. 3.5). At small

velocities typically a small air volume is entrained. Then, device #1 is capable of collecting all entrained air. If the velocity is higher and the air entrainment rate remains constant, e.g. due to a higher submergence, a high ratio of air passes device #1. The bubbles reach the tilted pipe and tend to rise up. Two anti-swirl devices are installed to guide the air along the top of the pipe ridge.
Depending on the limits as proposed by Falvey (1980), the bubbles may change their flow direction. Moreover, small bubbles merge to bigger ones and finally air pockets with higher buoyancy forces are present. Often, this takes place between the second and the third de-aeration device. Bigger bubbles propagate against the flow towards device #2 and the remaining bubbles move to device #3. If some bubbles miss device #2 while propagating against the flow they will accumulate downstream of the expansion (Fig. 3.5 c). Over time, additional bubbles that do not reach device #2 further extend this accumulation. In this case the air discharge cannot be measured properly.
De-aeration device #1 or de-aeration devices #2 and #3 can be operated simultaneously. A validation of the complete de-aeration system is given in chapter 4.2.

Chapter 4

Methodology and Procedures

Abstract. *This chapter deals with the methodology and procedures applied to adjust the experimental facility, to perform the experimental campaign, as well as to carry out the forthcoming data analysis. Preliminary tests and scale family investigations have been conducted. Measurement techniques originally developed at VAW in previous two-phase flow investigations have been improved significantly, and special methods of data processing have been evolved and optimized. An air discharge measurement technique has been improved to get continuous long-term recordings. Adaptations of the experimental facility concerning especially the homogenization of the approach flow, the PIV measurements, and their analysis are shown. A new method has been developed to determine the circulation of the horizontal velocity field of the intake vortex based on PIV velocity vector maps. Moreover, shadows of air cores on the PIV images have been analyzed to estimate the air-core diameter by means of object detection techniques and geometric relations. Finally, a description of the procedures applied during the scale family investigation and the experimental program is given.*

4.1 Homogenization of the Approach Flow

To ensure an undisturbed and non-enforced vortex formation at the intake pipe a homogeneous approach flow in the main tank is a prerequisite. Several measures and arrangements in the experimental tank help to ensure a uniform flow distribution in the far field of the intake pipe. They are described in the following.

Fig. 4.1 shows a longitudinal section of the experimental tank and its connections to the water circuit. A stilling basin between the feeding pipes and the main tank tranquilizes and homogenizes the flow. The feeding pipes at the entrance to the stilling basin are equipped with diffusers. Their access position is almost central, so that their orifices promote a homogeneously distributed inflow to the stilling basin. From the stilling basin to the main tank the flow is guided through a filter fleece

with a thickness of 5 cm. It is fixed on a perforated metal plate. The reduced permeability of the filter mat results in a slight head loss in the range of a few centimeters. However, PIV seeding particles with a maximum diameter of 500 μm are able to pass through the filter fleece.

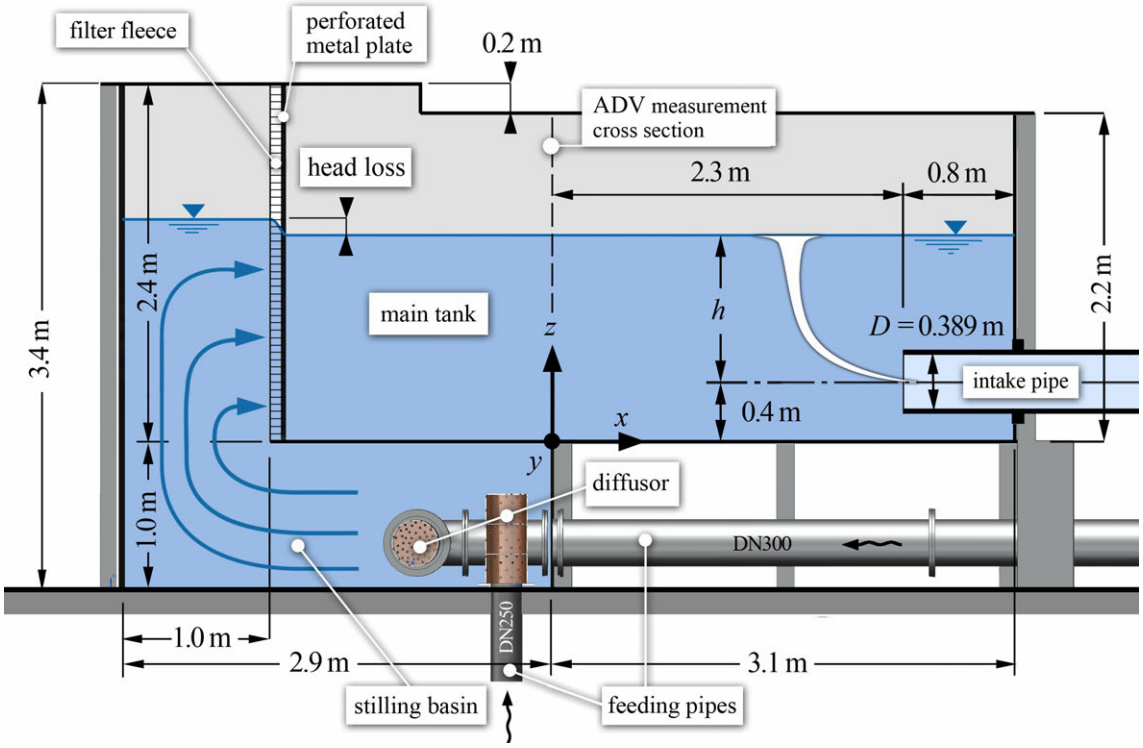

Figure 4.1: Longitudinal section of the experimental tank, with feeding pipes, stilling basin, main tank, and intake pipe. The vertical axis of the ADV measurement cross-section is marked by a dashed line.

To test the performance of the flow homogenization measures, 3D ADV measurements have been conducted in a cross-sectional plane 1.8 m downstream of the filter fleece and 2.3 m in front of the intake pipe (see Fig. 4.1). Fig. 4.2 depicts the flow velocity field measured at $\mathsf{F}_D = 0.8$ and $h/D = 2.5$, representing typical flow conditions of the main measurement campaign.

The contour plot in Fig. 4.2 shows the flow velocity v_x in the main flow direction. The velocity distribution is rather uniform, showing no asymmetry, and no distinguished velocity peaks are present. The median of the measured velocity vectors $\tilde{v}_x = 0.043$ m/s is almost equal to the bulk velocity in the measurement plane, where $Q_\mathrm{w}/A = v_x = 0.045$ m/s. The interquartile range IQR[1] is small with $\mathrm{IQR}(\tilde{v}_x) = 0.015$ m/s. Furthermore, Fig. 4.2 shows velocities v_y and v_z as vectors. Here, $\mathrm{IQR}(\tilde{v}_y) = 0.005$ m/s and $\mathrm{IQR}(\tilde{v}_z) = 0.012$ m/s, respectively.

As neither significant asymmetries, nor strong secondary currents, nor distinct ve-

[1]IQR is a statistical measure for dispersion that gives the range consisting of 50 % of the values around the median.

locity peaks are present, and the IQR is small, the approach flow is judged to be sufficiently homogenized.

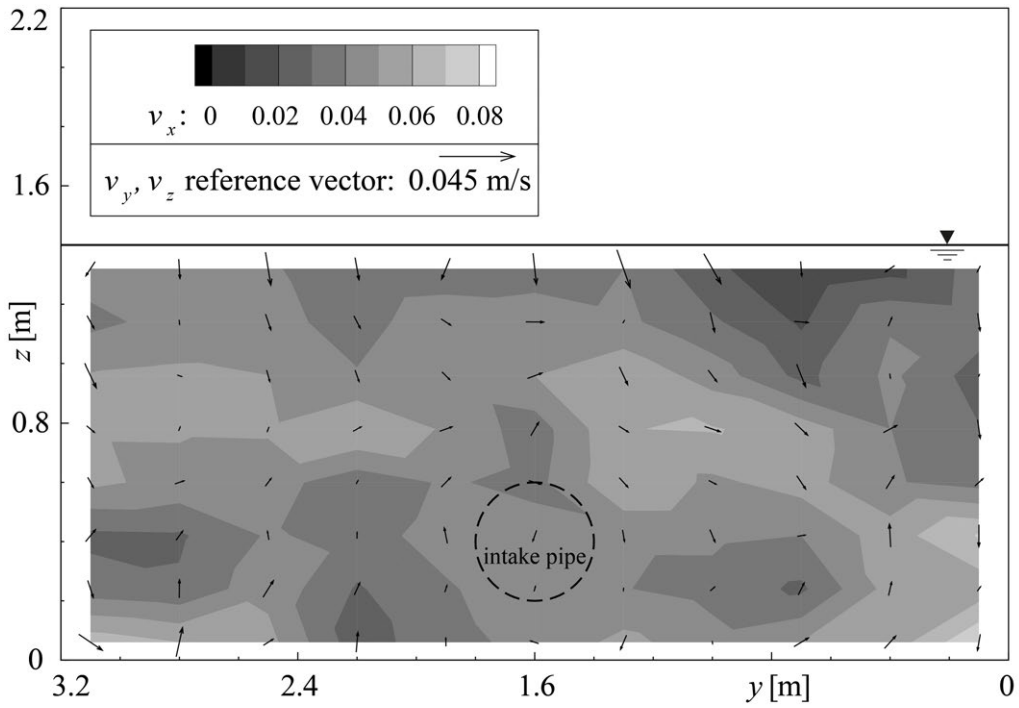

Figure 4.2: 3D velocities in the ADV measurement cross-section (see Fig. 4.1). The measurement duration was 60 s at each point at 25 Hz sample rate.

4.2 Air Discharge

Ideal Gas Law. The ideal gas law is the equation of state of a hypothetical ideal gas. It gives the relationship between pressure, volume, mass, and absolute temperature and can be written as follows:

$$pV = mR_{\mathrm{s}}T \ , \tag{4.1}$$

where p = the pressure, V = volume, m = mass, R_{s} = specific gas constant, and T = absolute temperature.
The following simplifications are necessary to apply the ideal gas law:

- All gas particles are assumed to be mass points and have no expansion.
- The average distances between gas particles are considerably larger than the diameter of the particles.
- All gas particles colliding among themselves or with the walls of the volume only have been perfect elastic collision processes.

In a closed system pressure and volume of an ideal gas of a given mass are inversely proportional if the temperature is unchanged. This relation is known as Boyle-Mariotte's law:

$$pV = k \ , \tag{4.2}$$

with k = constant. The relation between a state 0 and an arbitrary state 1 is given by:

$$p_1 = p_0 + \Delta p \tag{4.3a}$$
$$V_1 = V_0 + \Delta V \tag{4.3b}$$
$$m_1 = m_0 + \Delta m \ . \tag{4.3c}$$

Inserting eqs. 4.3a–c in eq. 4.1 the equations at the two states $i = [0, 1]$ can be written as:

$$p_0 V_0 = m_0 R_\mathrm{s} T \tag{4.4a}$$
$$(p_0 + \Delta p)(V_0 + \Delta V) = (m_0 + \Delta m) R_\mathrm{s} T \ . \tag{4.4b}$$

Eq. 4.4a and 4.4b can be rearranged as:

$$\Delta m = \frac{1}{R_\mathrm{s} T}(p_0 \Delta V + \Delta p V_0 + \Delta p \Delta V) \ . \tag{4.5}$$

Eq. 4.5 allows to determine the differential quantity of air between the two states independent of the present pressure.

Reference Pressure. The choice of the reference pressure p_ref is decisive while determining the air volume V_a passing through a cross-section over a time Δt. The following definitions of reference pressure with respect to the experimental facility (compare Fig. 3.1) should be noted: the pressure at the main pipe axis below the de-aeration device (Wickenhäuser, 2008), the hydrostatic pressure at the intake pipe axis, or the atmospheric pressure p_atm.
Within the current study the determination of air discharge is done with reference to the actual p_atm. Consequently, the results are independent of the considered pressure system. The atmospheric pressure p_atm depends on several parameters, mainly: the elevation above sea level, the ambient temperature, and the geographic latitude. As the experimental tank is located at 490 m a.s.l., the mean atmospheric pressure is 965 mbar. In order to take into account the variability caused by daily or seasonal changes, p_atm has been measured by an absolute pressure sensor (see chapter 3.3).

Determination of Air Discharge. Air has a small density and fulfills the aforementioned simplifications. Hence, it can be assumed to behave like an ideal gas. Regarding Boyle's law (eq. 4.2), $k = m$ is constant and can be used to determine the air discharge Q_a. Air discharge can be determined by using the values at the two states or time steps t_0 and $t_1 = t_0 + \Delta t$.
The entrained air in the pipe system is collected by a de-aeration system (see chapter 3.5). In the following the procedure to determine Q_a is explained. For simplification, only one single de-aeration device is considered (see Fig. 2.38).
Before each measurement is started the valve on top of the rising pipe is closed. The air pressure increases depending on the amount of air rising through the pipe during the measurement combined with a water level decrease. The water level and the pressure Δp are recorded continuously by an ultra sonic sensor and relative pressure sensors, respectively. The initial pressure at state 0, i.e. $p_0 = p_\mathrm{atm}$, is measured by the absolute pressure sensor. V_0 is recalculated via the measured water level in the rising pipe and the geometry of the rising pipe.
ΔV can be recalculated via the measured water levels at stages [0, 1] in the rising pipe and the geometry of the rising pipe, respectively. However, the water levels measured in the rising pipe are affected by a water surface that is disturbed by rising air bubbles or air pockets. Moreover, water drops on the inside walls of the rising pipes lead to measurement errors as well. To avoid misleading interpretation of the measurements ΔV is alternatively determined by:

$$\Delta V = \frac{\Delta p}{\rho_\mathrm{w} g} A \,, \tag{4.6}$$

where $\rho_\mathrm{w} g$ is used to refer the pressure to the length scale equivalent water column and A is the cross-sectional area of the rising pipe. The air discharge Q_a between the two states is determined by using Δm of eq. 4.5, leading to

$$Q_\mathrm{a} = \frac{\Delta m}{\rho_{\mathrm{a},\,0}\, \Delta t} \,, \tag{4.7}$$

where $\rho_{\mathrm{a},\,0} = p_\mathrm{atm} =$ air density at state or time step 0 and Δt gives the time span between two states. Then, the air entrainment rate β follows from

$$\beta = \frac{Q_\mathrm{a}}{Q_\mathrm{w}} \,. \tag{4.8}$$

It has to be noted that the slip phenomenon that considers the different velocities of the air phase and the water phase can be ignored with respect to the required Q_a.
The measurement time Δt has to be adjusted to Q_a and the de-aeration height h_w (see chapter 3.5), where Δt is limited to a range of 5 to 180 s. Based on the measurement time and the data acquisition frequency of 1 Hz, Q_a is calculated by a number of samples from 5 to 180 (see chapter 3.3). Therefore, Q_a represents

the average air discharge for a certain measurement duration. As the air discharge represents a point in a time series it will be denoted as $\dot{Q}_a$. The corresponding air entrainment rate is $\dot{\beta}$. The statistical significance in terms of dispersion and outliers due to this wide range of samples is not comparable. Further developments to maximize the measurement time towards a statistically significant Q_a are described below.
Generally, the methodology described above suits the current circumstances well. It allows a visual control at each measurement and, due to this, systematic errors can be excluded.

Validation of Q_a with Pre-aerated Flow Tests. The de-aeration device (already introduced in chapter 3.5) and the methodology of the air entrainment measurements have to be tested for their accuracy. Therefore, the de-aeration devices are validated by forced aeration tests. Fig. 4.3 shows the related installations at the intake pipe schematically. An anti-vortex device, realized by a horizontal plate, is installed in the main tank between the water level and the pipe intake. The anti-vortex device leads to a complete suppression of air entraining vortices. An air diffuser with a known value of air discharge provided by the forced aeration $Q_{a,f}$ is used.

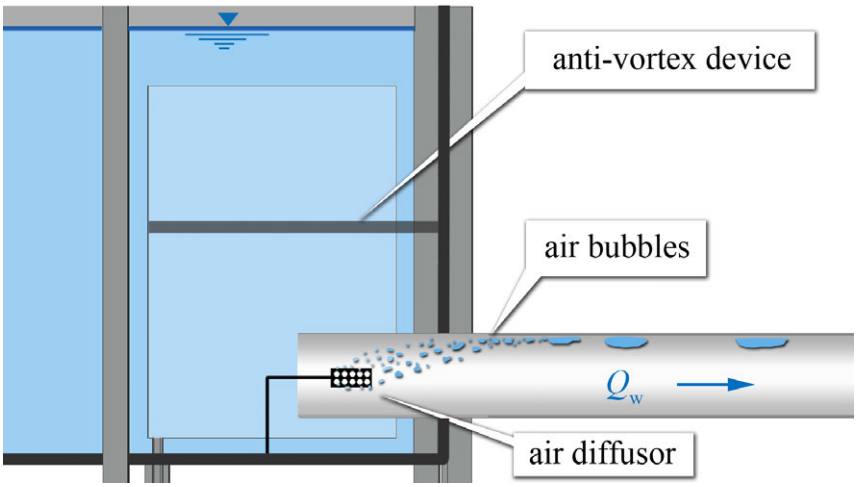

Figure 4.3: Longitudinal section of the experimental setup as used during the forced aeration tests. An anti-vortex device suppresses air-entraining vortices.

The air diffuser provides a similar two-phase flow as generated due to intake-vortices. Here, $Q_{a,f}$ is measured by a calibrated measurement system that consists of a pressure reducing valve, a further valve, a pressure sensor and a float-type flow meter. The pressure is reduced from 8 bar at the supply system to 0.3–1.0 bar. The air discharge at this pressure, i.e. the volumetric flow rate, is measured by a float-type

flow meter. The air discharge $Q_{\mathrm{a,f}}$ has to be recalculated to conditions at p_{atm} by using the eqs. 4.2–4.5 explained above.

Limits of air discharge measurements mainly depend on a combination of F_D and Q_{a}. Tests are performed at flow conditions of $\mathsf{F}_D = 0.2$–1.8 and $Q_{\mathrm{a}} = 1.9 \cdot 10^{-5}$–$3.6 \cdot 10^{-4}$ m^3/s. Each experiment is repeated three times. Fig. 4.4 gives the results of $Q_{\mathrm{a}} = \mathrm{f}(Q_{\mathrm{a,f}})$. A perfect agreement is present if the measured $Q_{\mathrm{a}} \equiv Q_{\mathrm{a,f}}$.

Fig. 4.4a shows the results for a small $\mathsf{F}_D = [0.2,\ 0.4]$ applying device #1. Here, the air bubbles rise up within the horizontal pipe section as displayed in Fig. 4.3. A good agreement between Q_{a} and $Q_{\mathrm{a,f}}$ can be found for small up to medium values of $Q_{\mathrm{a,f}} < 1.5 \cdot 10^{-4}$ m^3/s. Accordingly, device #1 is seen to be validated for small F_D. At larger Q_{a} the statistical dispersion increases. The average of the IQR-median-ratio[2] changes from 3 to 30 %. Due to the small diameter of the rising pipe different air bubble patterns and air pockets cause a high disturbance and fluctuation of the water surface. Their intensity increases with larger $Q_{\mathrm{a,f}}$, thus the dispersion of Q_{a} increases. Furthermore, less air is collected by the dome, thus a part of the air passes the dome and cannot be measured. However, at small F_D the estimated Q_{a} caused by vortices is below $1.5 \cdot 10^{-4}$ m^3/s.

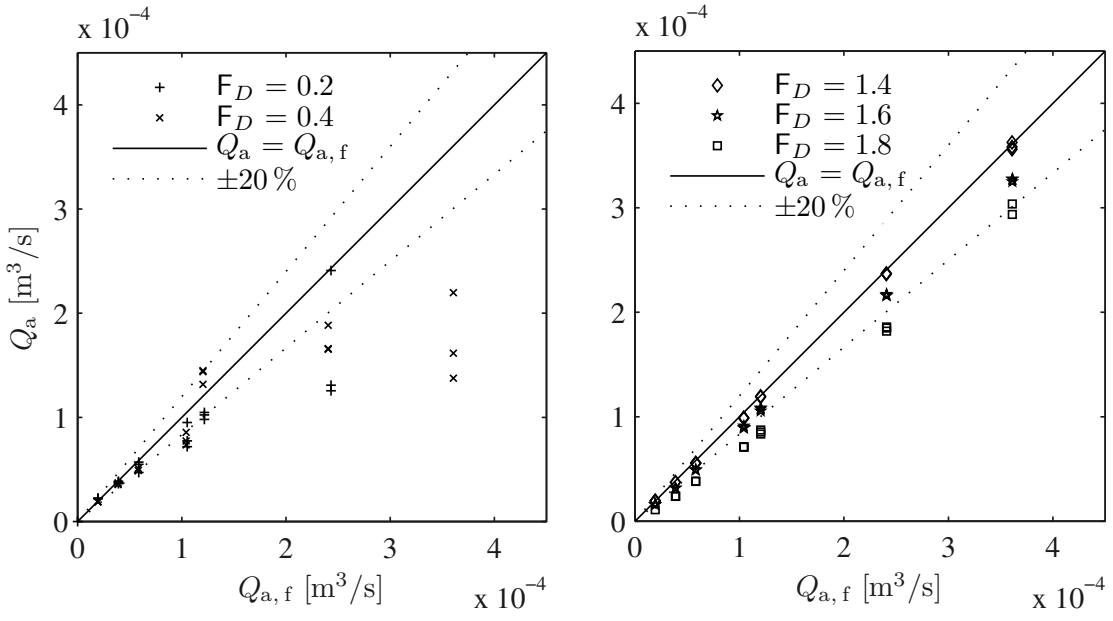

(a) Device #1. (b) Devices #2+#3.

Figure 4.4: Comparison between the measured Q_{a} and the forced aeration due to calibrated air discharge $Q_{\mathrm{a,f}}$.

Fig. 4.4b shows the results for large $\mathsf{F}_D = [1.4,\ 1.6,\ 1.8]$ using devices #2 and #3. These devices are applied simultaneously within a range of $0.4 \leq \mathsf{F}_D \leq 2.2$ in the main tests. The measured Q_{a} has a small statistical dispersion at all $Q_{\mathrm{a,f}}$. The

[2]IQR-median-ratio is used to show the dispersion measured by IQR in relation to the median.

average of the IQR-median-ratio is below 1 %. An upper limit can be derived as follows: Up to $\mathsf{F}_D = 1.4$ the values of Q_a and $Q_{\mathrm{a,f}}$ are in perfect agreement. At $\mathsf{F}_D = 1.6$, Q_a and $Q_{\mathrm{a,f}}$ are within a 20 % range of tolerance, where $Q_\mathrm{a} < Q_{\mathrm{a,f}}$. At $\mathsf{F}_D = 1.8$, $Q_\mathrm{a} < 0.8\,Q_{\mathrm{a,f}}$ independent of $Q_{\mathrm{a,f}}$ within the tested range. The higher the flow velocities, the more air bubbles cannot be caught or are even entrained from the domes and finally pass device #3 without being recorded at all.
To sum up: The present de-aeration system is validated if device #1 is applied for $Q_\mathrm{a} < 1.5 \cdot 10^{-4}$ m^3/s at $\mathsf{F}_D \leq 0.4$, and if devices #2 and #3 are applied for $0.4 \leq \mathsf{F}_D \leq 1.4$ for $Q_\mathrm{a} < 3.6 \cdot 10^{-4}$ m^3/s. For measurements outside of this range, a correction function would have to be applied. However, this was not necessary for the current study as these limits were not exceeded (see chapter **??**).

Validation of Leak Tightness. The de-aeration system had to be tested against probable leaks. Therefore, first the whole model was filled up with water. Next, the inflow and outflow valves were closed to hold $Q_\mathrm{w} = 0$. The rising pipes were filled up completely with water as well. A baseline measurement of the water level was conducted to validate the pressure sensors. The air valves were closed and air was blown into the rising pipes till the water level reached the pipe ridge or the upper edge of the dome. Then, all water levels and pressures were recorded by long term measurements. Fig. 4.5a depicts the resulting time series of the measured pressure in device #2. Three tests had been performed over Δt = [7, 14, 15] h with the use of an air storage as explained above. The repeated tests show a similar behavior in terms of the pressure decrease. The pressure gradient dp decreases linearly with increasing pressure, thus the gradient is small at low pressures (Fig. 4.5b).

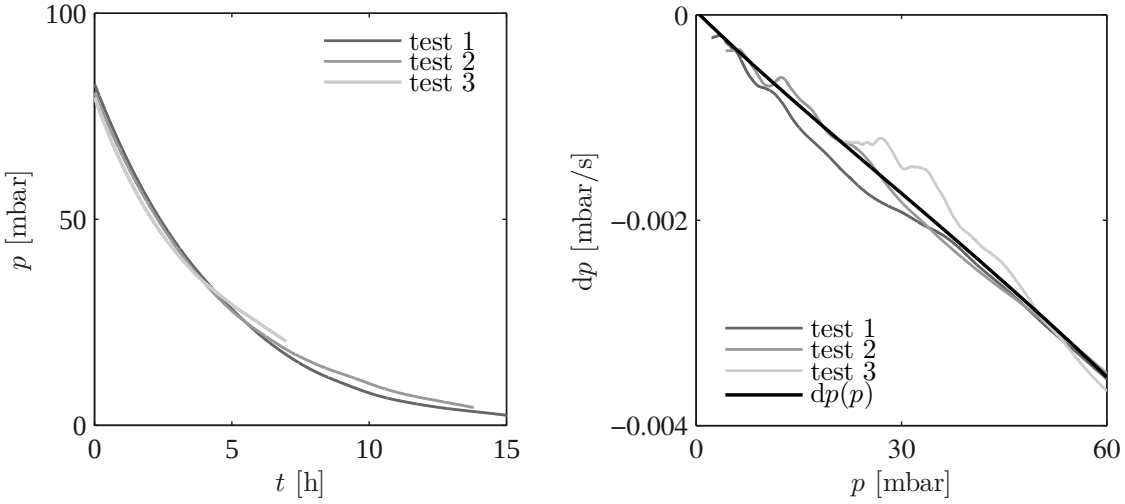

(a) Pressure decrease over time for three leakage tests.

(b) Pressure gradients and their fitted adjustment function dp(p) (see eq. 4.9).

Figure 4.5: Leakage tests of device #2 with one adjoined external air storage.

Fig. 4.5b gives the relation between the pressure gradient dp and the actual pressure p in the range of the experimental runs. The maximum pressure loss is equivalent to $Q_\mathrm{a} = 4$ cm^3/s. This value is quite small in comparison to the measured Q_a of up to 1500 cm^3/s within the experiments. Nevertheless, a correction function d$p(p)$ is derived for each combination of the de-aeration devices to consider small air losses. In the example shown in Fig. 4.5 this is:

$$\mathrm{d}p = -0.001628\, e^{(0.01339p)} + 0.001715\, e^{(-0.04099p)} \,. \tag{4.9}$$

These functions are applied in the analysis of the main experiments later on. In this way an adequate compensation of air losses is reached.

Final Design of the De-aeration System. The de-aeration system was optimized and validated for a broad range of Q_a at different F_D. Three restrictions concerning the measurement duration are still present:

- Q_a is a mean value that covers a variable duration and is determined as a point on the time curve.
- The statistical significance of Q_a is disparate due to varying sample numbers.
- The unsteadiness of Q_a cannot be reflected in a relatively low temporal resolution.

In the final design of the de-aeration system, the data acquisition allows almost continuous Q_a measurements up to a frequency of 1 Hz. The measurement time must be extended to ensure that the full Q_a range is caught. Two external air storages each with a volume of 0.4 m^3 were therefore adjoined to the rising pipe #2 to enlarge the air volume. Fig. 4.6 shows the de-aeration system as installed for the experimental runs.
Before an experimental run is started Q_a is estimated to adjust the configuration of the de-aeration system by preliminary tests. The experimental runs of the main measurement campaign are conducted without device #1, which is applied exclusively for scale family tests. Its rising pipe is dismantled and the dome is closed. Air is de-aerated by devices #2 and #3. Device #2 receives the larger part of air (see chapter 3.5) and thus the air storages are adjoined to this rising pipe. The valid pressure range is unchanged but the required time extension is reached due to the use of the external air storages. Table 4.2 specifies the configuration of the system for each experimental run. It is intended to have roughly the same measurement time for the complete range of Q_a. The air storage at device #2 is variable. For a small amount of air only the rising pipe #2 is applied, for an increased amount one external air storage (#2a) is connected and for a larger amount of air two external air storages (#2a, #2b) are adjoined.

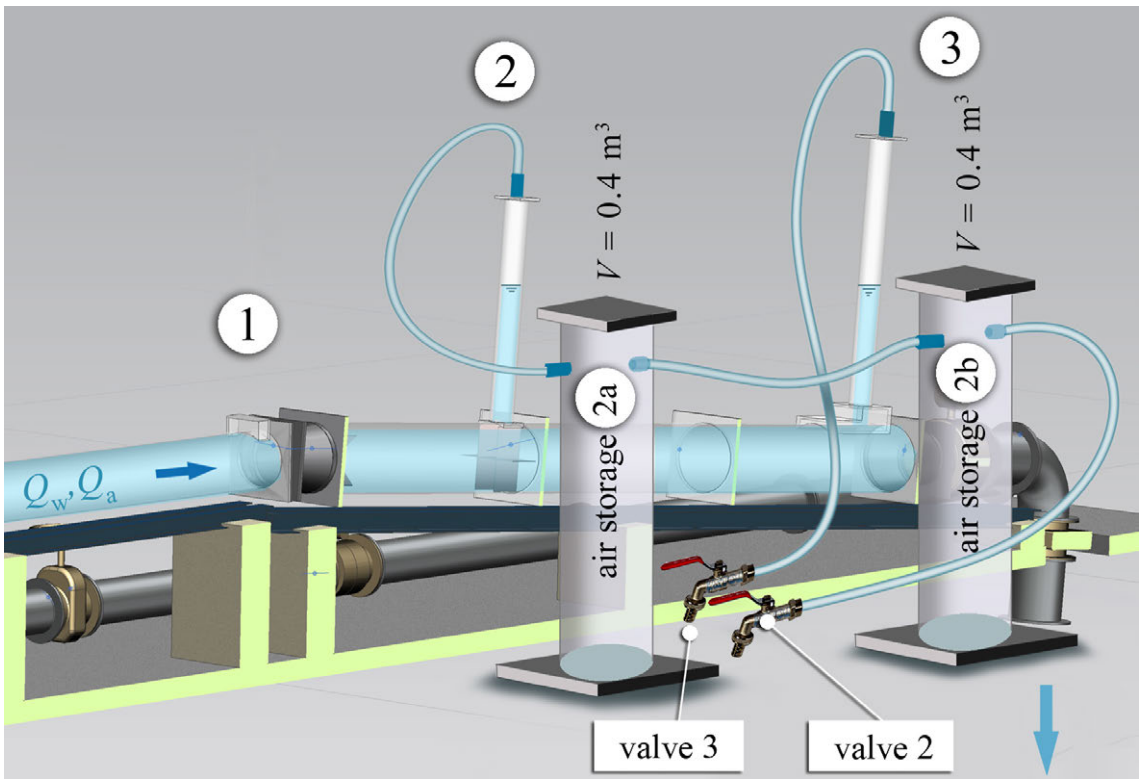

Figure 4.6: Final design of the de-aeration system with two external air storages at device #2.

Required Measurement Duration. The final design of the de-aeration system allows conducting measurements over several hours. The measurement time of an experimental run at constant F_D and h/D has to be optimized: (1) in terms of obtaining a significant mean and maximum Q_a, and (2) in relation to the existing storage capacity of the PIV-system. Tests at $\mathsf{F}_D = [0.8, 0.9, 1.0]$ and $h/D = 2.0$ with a duration of up to eight hours have been conducted to obtain the full range of Q_a fluctuations. Q_a is statistically analyzed, especially its change with respect to different measurement times up to 8 h. Fig. 4.7 shows time series concerning the appearance of the vortex type and the corresponding Q_a and $\hat{Q}_a$ averaged by the actual measurement duration.

The vortex type VT in Fig. 4.7a indicates the presence of an air entraining vortex $VT = 6$ by a black bar. Fluctuations of Q_a (see Fig. 4.7b) during the experimental run are large with respect to time and size. In Fig. 4.7c $\hat{Q}_a$ as air discharge averaged by the actual increasing time is shown. $\hat{Q}_a$ does not change significantly from an average duration of 2 h on. In order to keep the amount of the PIV data usable, the measurement duration for each experimental run is fixed to this duration of 2 h.

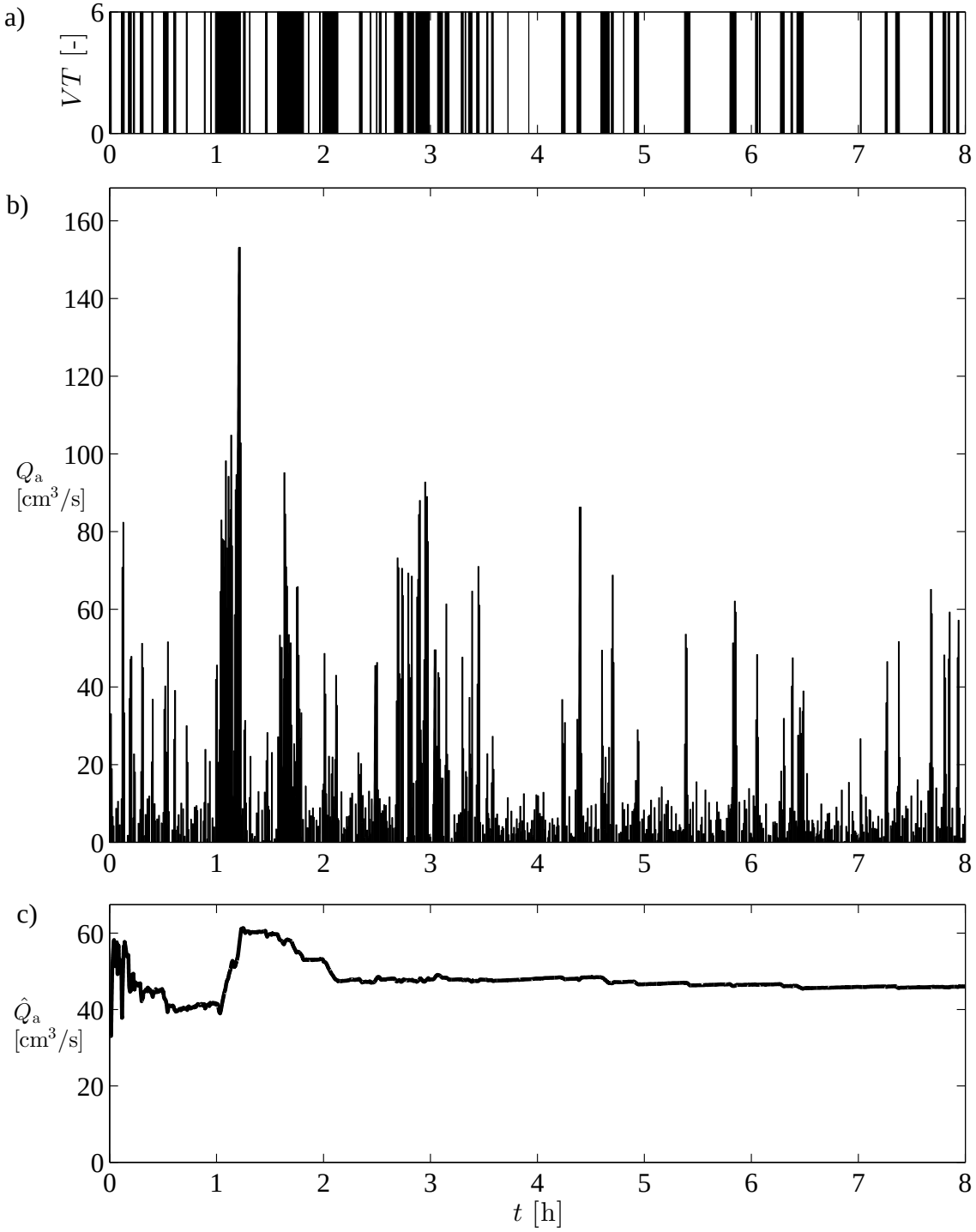

Figure 4.7: Time series of a) vortex type (VT) presence, b) fluctuations of air discharge Q_a, and c) the running average of $\hat{Q}_a$ by increasing measurement duration for $h/D = 2.0$ and $\mathsf{F}_D = 0.9$.

4.3 PIV Application

General. The horizontal velocity field of the vortex is required to determine its circulation Γ via the tangential velocity around the vortex core (see chapter 2.2.3). The measurement principle and setup of the PIV-system as used within this study are explained in chapter 3.4. Special adaptations, the image processing to get velocity vector maps with respect to the air-core, and the situation at the intake pipe are described next.

Fig. 4.8 shows the intake section of the experimental tank during an experimental run, where air is entrained by an air-core vortex. The horizontal laser light sheet is visible at the tank walls parallel to the water surface. The vortex core is emphasized by the laser light sheet. The resulting shadow elongates to the tank wall. From a bottom-up view, as for the PIV camera that is located below the tank, the vortex is behind the intake pipe. Thus, the optical accessibility from the bottom is restricted here.

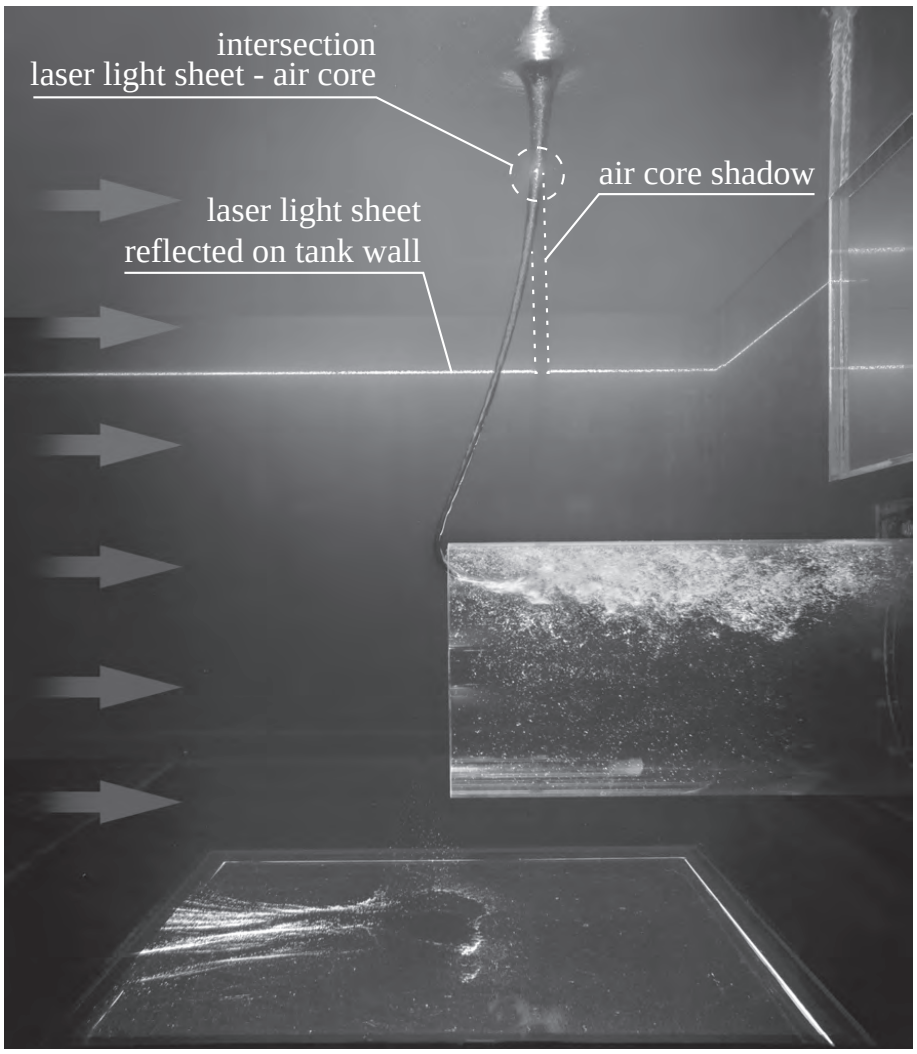

Figure 4.8: Side view of an experimental run with air-core vortex. The operating laser light sheet reflects at the vortex core and the tank walls.

Measurement Plane. A prerequisite to obtain 2D PIV velocity fields that represent the essential velocity components is a small out-of-plane velocity. For the far field of an intake vortex the highest velocities can typically be observed in a horizontal plane and can be classified by the two components of the tangential velocity v_t and the radial velocity v_r. Daggett & Keulegan (1974) showed that v_t is nearly constant with respect to h, i.e. the submergence or the height above the pipe axis, respectively (see chapter 2.3.1). Furthermore, v_r is nearly constant in the upper half of the rotating water body (see chapter 2.3.1). The vertical out-of-plane component v_z corresponds to the axial vortex velocity. Its maximum value is up to 0.1 v_t as measured by Quick (1962) and therefore is negligible. The results from Quick (1962) from basic cylinder experiments with downward inclined intakes are used to define the vertical location of a suitable measurement plane with respect to different tank water levels and various vortex air-core effects (see chapter 2.3.1). Measurements are made at different horizontal planes in a vertical distance from the intake pipe of $h_\mathrm{PIV} = 0.3$–$0.9\ h$. Fig. 4.9 shows the air-core classified by three characteristic zones as introduced in chapter 7. These zones are: ① funnel with variable air-core diameter, ② constant diameter and straight air-core, and ③ bended air-core. These zones are always present, but each section is quite variable in its length.

If the laser sheet is spanned slightly below the water surface at 0.9 h strong reflections occur at the air-core funnel. These reflections disturb the PIV image recordings by blooming effects, i.e. pixels on the CCD camera sensor get over-saturated and can, due to their overload, even disturb their neighbor pixels.

For intermediate horizontal measurement planes between the water surface and the intake pipe at 0.8–0.5 h the blooming effect diminishes. Here the air-core diameter is almost constant. Moreover, the shape of the air tube is nearly vertical and straight.

Horizontal measurement planes that cross the bended section of the air tube record a notable fraction of vertical velocity components, especially at $< 0.3\ h$.

Considering these findings at different heights regarding velocity and optical boundaries, the measurement plane is fixed to 0.8 h for all PIV recordings within this study.

Image Acquisition. The laser energy is set to 100 % and the f-number is chosen to $f_\# = 5.6$. The advantage of smaller $f_\#$ is that more particles are visible, whereas larger $f_\#$ lead to less saturation due to reflections at the air-core vortex and to a larger depth of field δ_z. Thus, a large F-number is chosen. The edge length of the FOV in the object plane of the laser light sheet is $L_\mathrm{FOV} = 1.036$ m and in the image plane $L_\mathrm{CCD} = 0.015$ m. Large-scale PIV ensures to track a wandering vortex in a larger area. The advantage of using a small magnification $M = L_\mathrm{CCD}/L_\mathrm{FOV} = 0.015\ \mathrm{m}/1.036\ \mathrm{m} = 0.014$ is that the depth of field is sufficiently large to focus all

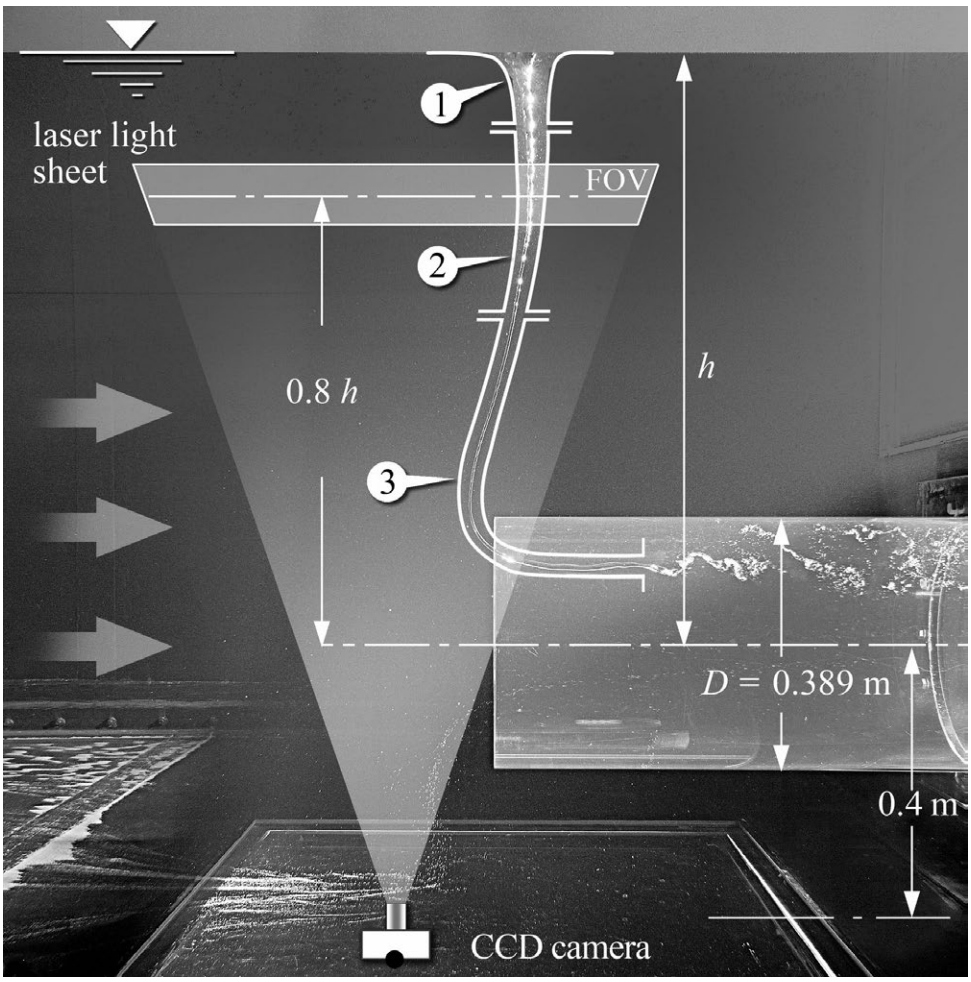

Figure 4.9: Side view snapshot during a typical experimental run with three characteristic zones of an air-core tube: ① air-core funnel, ② straight air-core, and ③ bended air-core. The PIV measurement plane is situated best at 0.8 h above the intake pipe, where the air tube is straight and orientated vertically most of the time.

particles inside the laser light sheet. The laser light sheet thickness is about 4 mm in the center of the FOV. After Raffel et al. (1998) the depth of field is:

$$\delta_z = \frac{2 f_{\#} d_\mathrm{s} (M+1)}{M^2} = 0.4 \text{ m, where} \tag{4.10a}$$

$$d_\mathrm{s} = 2.44 (M+1) f_{\#} \ \lambda_\mathrm{l} = 7.37 \cdot 10^{-6} \text{ m} \tag{4.10b}$$

is the diffraction-limited minimum image diameter (Adrian & Yao, 1985).

The camera is located below the tank and upstream of the intake pipe to enhance optical accessibility from the bottom. Occasionally, the vortex core is above the pipe (see Fig. 4.8). To further improve the optical accessibility tests have been conducted with the camera tilted by an angle of 10° with respect to the usual perpendicular view. However, a larger inclination would have introduced a larger perspective

error, especially near the edges of the FOV. As additional perspective errors appear, the velocity field needs to be dewarped. This was tested by using a calibration plate to obtain an imaging model fit by a direct linear transform (DantecDynamics, 2012a). However, finally the optical accessibility could not be improved significantly. The tests showed clearly that the benefit of tilting is too small compared to the additional errors that are involved by a non-perpendicular view to the measurement plane. Therefore the decision was made to conduct all experimental runs with a perpendicular view to the measurement plane as shown in Fig. 4.9.

Seeding Particles. Griltex® seeding particles from *Ems-Chemie Holding AG* with a mean particle diameter $d_\mathrm{p} = 400\ \mu\mathrm{m}$ in the range of $300\ \mu\mathrm{m} \leq d_\mathrm{p} \leq 500\ \mu\mathrm{m}$ are used. The diffracted particle image diameter d_e of the mean particle diameter of 400 μm is calculated after Adrian & Yao (1985) to:

$$d_\mathrm{e} = \sqrt{(M d_\mathrm{p})^2 + d_\mathrm{s}^2)} = 0.94 \cdot 10^{-6}\ \mathrm{m}. \tag{4.11}$$

The recorded mean particle image diameter on the image plane is $d_\tau \cong \sqrt{d_\mathrm{e}^2 + d_\mathrm{r}^2} = 1.19 \cdot 10^{-5}$ m (Fritz et al., 2003), whereby $d_\mathrm{r} = L_\mathrm{CCD}/2048\ \mathrm{px} = 7.32 \cdot 10^{-6}$ m gives the pixel pitch. This is equivalent to a recorded particle image diameter of:

$$d_\mathrm{px} = d_\tau\ 2048\ \mathrm{px}/L_\mathrm{CCD} = 1.6\ \mathrm{px}. \tag{4.12}$$

Particle diameters ranging from 300 μm to 500 μm result in $1.5\ \mathrm{px} \leq d_\mathrm{px} \leq 1.7\ \mathrm{px}$ on the CCD sensor. Recorded particle diameters have to be larger than 1 px, as otherwise displacement values are biased towards integer values, what is called peak-locking. Aliasing occurs when particles are too small, i.e. the Nyquist sampling theorem is not satisfied (Engelberg, 2008). Under-sampling leads to additional errors. A diameter of $d_\mathrm{px} = 1.6$ px as calculated above is near the optimum recorded particle image diameter of 2.0 px (Raffel et al., 1998) and fulfills the requirements. A possible interaction between the particles and the air bubble formation was neglected within this research project.

Image Analysis. To obtain velocity fields from the particle images an adaptive cross-correlation method is applied. This method typically uses an initial interrogation area (IA). Starting with a window of 512 × 512 px^2, this area is reduced in four refinement steps with two passes each. The final interrogation area size is 32 × 32 px^2. After the 1/4-rule (Keane & Adrian, 1990) and the time delay between two laser pulses of 6 ms, the maximum allowable velocity magnitude is:

$$v_\mathrm{MAG,\,max} = \frac{1}{4}\ \frac{32\ \mathrm{px}}{6\ \mathrm{ms}}\ \frac{1.036\ \mathrm{m}}{2048\ \mathrm{px}} = 0.67\ \mathrm{m/s}. \tag{4.13}$$

An overlap of 50 % between neighboring IAs and deforming windows is used to adapt to the vortical flow structure and to increase the accuracy. To find the correct mean particle displacement per IA, DantecDynamics (2012a) applies a high-accuracy subpixel algorithm that is independent of correlation peak shape (Westergaard et al., 2003). A peak is validated, if the ratio of the highest peak to the second highest peak is > 1.1. A local neighborhood validation with a local median filter and an acceptance factor of 0.2 is chosen. All vectors with a deviation from their neighbors are replaced by an interpolated median value (Westerweel, 1994). A universal outlier detection analysis detects and substitutes false vectors based on a normalized median test on the surrounding vectors (Westerweel & Scarano, 2005). To enhance the calculation speed the described processing is performed in a predefined area of the FOV as illustrated in Fig. 4.10. The location and size of this predefined area depends on vortex wandering and is defined by preliminary test results.

4.4 Vortex Center and Circulation

General. To determine the circulation Γ (see eq. 2.9) the vortex center must be known. Then the radial distance r between each velocity vector and the vortex center can be calculated. The search of the vortex centers' locations is performed using the MATLAB Image Processing Toolbox. Once the vortex centers are located, the spur of the wandering core is tracked as well. For further analysis the origin of the coordinate system of each PIV image is shifted to the vortex center of the current velocity field. This procedure enables an averaging over all instantaneous velocity fields to get a mean vortex related velocity field in the sense of an Eulerian approach. In the following the methodology is explained by using experimental run #7 with $h/D = 1.5$ and $\mathsf{F}_D = 0.6$ (see Table 4.2). Within an experimental run up to 13 PIV runs are conducted as explained in chapter 4.7. The example shown here is run #7.13, i.e. the last PIV run in #7.

Vortex Center. The horizontal velocity field from the PIV processing is analyzed to determine the location of the vortex center. Fig. 4.10 shows a typical PIV result, where the full PIV image is given in the background. The area of the image in which the correlation is performed gives in total 99×74 velocity vectors. The PIV image was taken in bottom-up view (see chapter 3.4). If the rotation is referred to a top-down view, the vortex in Fig. 4.10 rotates counter-clockwise (CCW). Additionally, Fig. 4.11 illustrates the related $v_{\mathrm{MAG}} = \sqrt{v_x^2 + v_y^2}$ as surface plot. As the velocity increases with decreasing distance from the vortex center, the v_{MAG}-surface forms a significant peak (Fig. 4.11). This characteristic property is used next while searching for the vortex center.

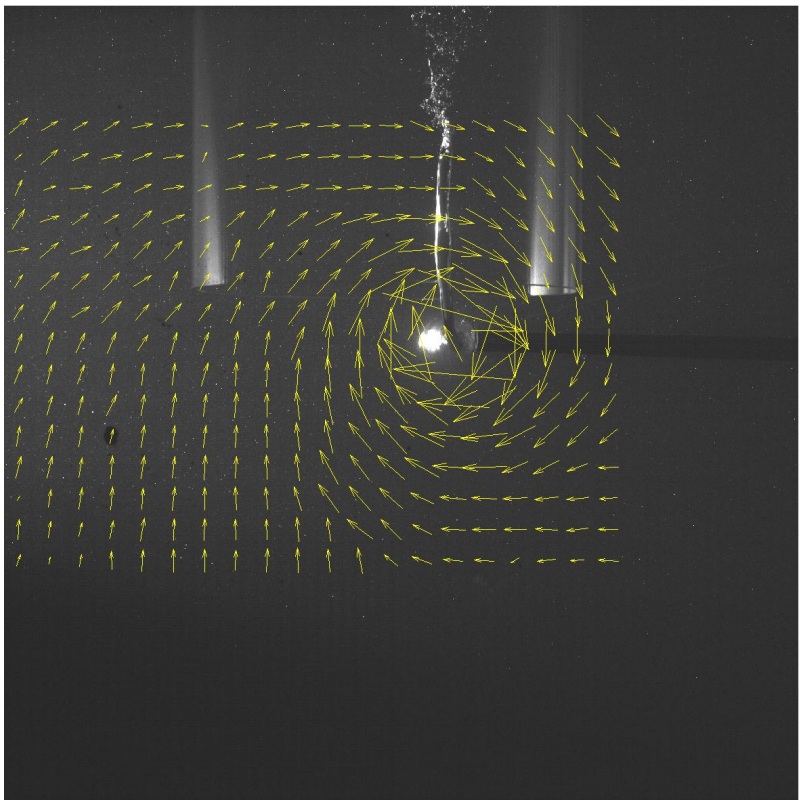

Figure 4.10: PIV image and velocity vector map overlaid (run #7.13).

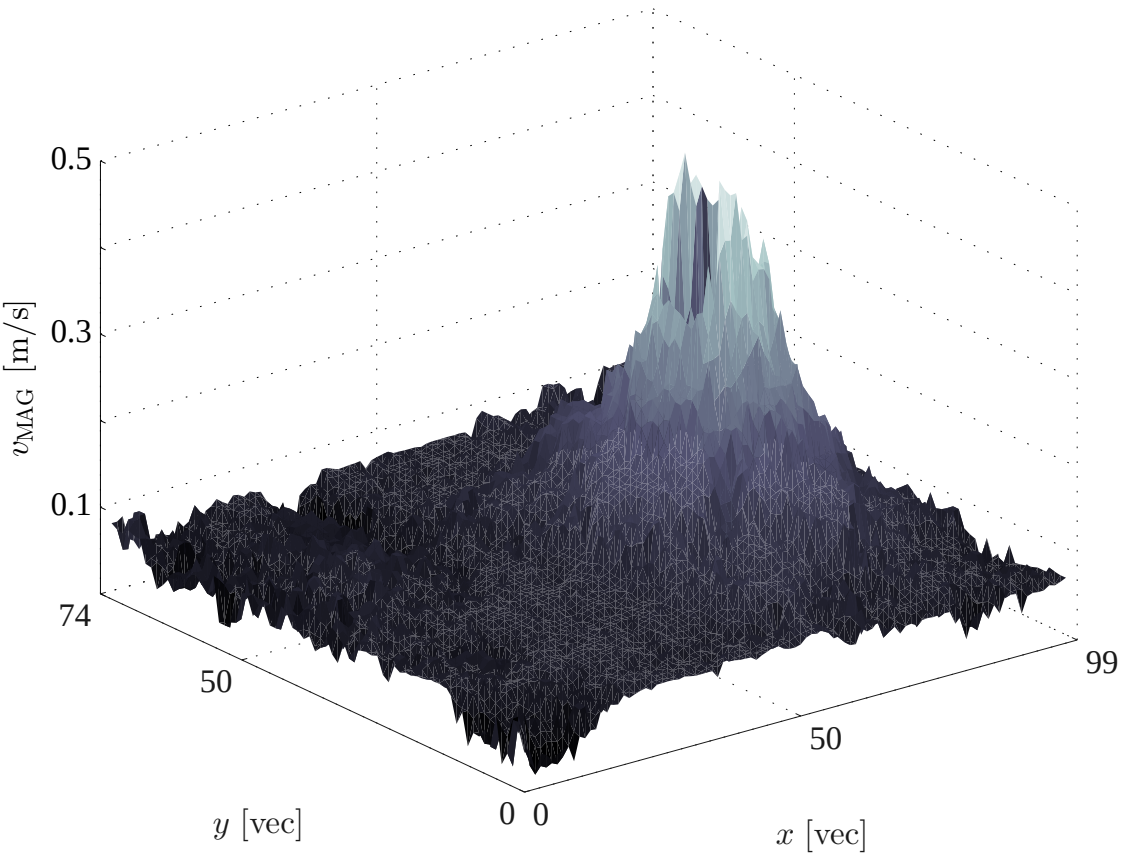

Figure 4.11: Surface plot of the velocity vector map (run #7.13).

Zhang & Sarkar (2012) had a similar problem to detect a vortex center. They investigated the near-ground flow structure of tornadoes and measured the horizontal velocity field of these single-phase air vortices by PIV. The vortex center was determined as the position of the lowest velocity. However, within the current two-phase flow study this method would not apply as the vortex center region cannot be resolved due to the absence of seeding particles and the lack of optical access to the air-core. The phase boundary between the air-core and the surrounding water does not allow to resolve the core of the velocity field.

In the following the methodology to determine the vortex center within the actual study is described in detail. Depending on v_{MAG}, various horizontal layers at $v_{\mathrm{MAG,\,layer}}$ are sliced from the surface plot in the x-y-plane (see Fig. 4.11) and transformed into binary images, where [1] or white is $v_{\mathrm{MAG}} \geq v_{\mathrm{MAG,\,layer}}$ and [0] or black is $v_{\mathrm{MAG}} < v_{\mathrm{MAG,\,layer}}$. Exemplarily, Fig. 4.12a shows a layer sliced at $v_{\mathrm{MAG,\,layer}} = 0.34$ m/s.

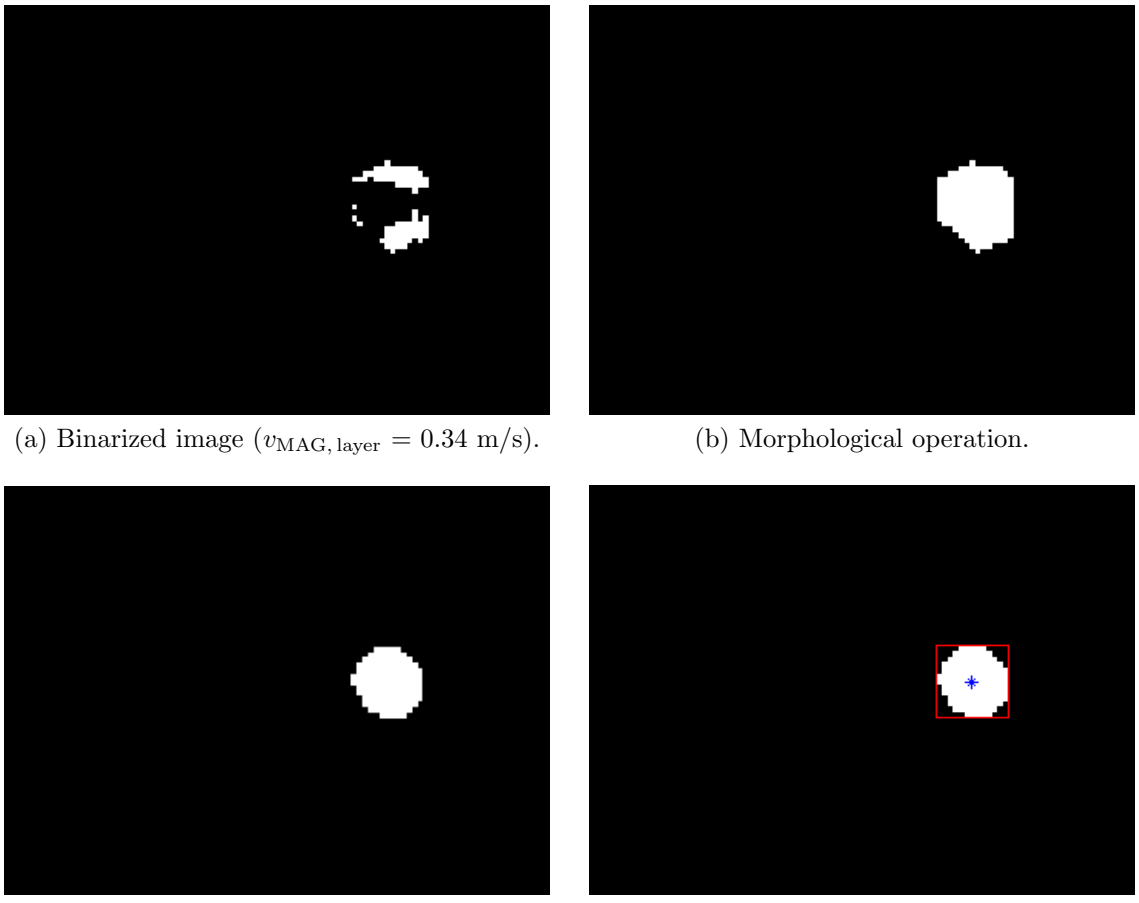

(a) Binarized image ($v_{\mathrm{MAG,\,layer}} = 0.34$ m/s).

(b) Morphological operation.

(c) 2D median filtering.

(d) Bounding box and center.

Figure 4.12: Typical steps while detecting the vortex center. Here, a threshold level at $v_{\mathrm{MAG,\,layer}} = 0.34$ m/s is used.

Within the next step, a morphological closing is performed in order to unite inter-

mediate areas (Leon & Beyerer, 2005). Morphological operations are non-linear, as their sequential arrangement is decisive for the result. For a morphological closing, a dilatation filter and then an erosion filter with a disk-shaped structuring element of radius 12 px has been applied (Fig. 4.12b). Then, a 2D median filtering is performed (Fig. 4.12c). Similar to morphological operations, median filtering is non-linear as well. It is often used in digital image processing to reduce noise. With the last step, a bounding box is laid around the resulting white area that is, in most of the cases, circular-shaped. Other methods were tested to determine the location of the vortex center, e.g. the MATLAB centroid algorithm. However, the bounding box center method was found to be more robust and reliable to match the vortex center, and its center estimation coincides best with the center located by eye.

The procedure described above is repeated for a number of layers that are determined as follows: Tests showed that ten equidistant layers between a lower and upper limit are sufficient to find the vortex center. The lower limit is determined as the maximum of the given threshold value $v_{\mathrm{MAG}} = 0.10$ m/s and the 90^{th}percentile of $\boldsymbol{v}_{\mathrm{MAG}} = 0.17$ m/s, where $\boldsymbol{v}_{\mathrm{MAG}} = v_{\mathrm{MAG}}$-matrix. The upper limit is determined as the minimum of the given threshold value 0.45 m/s and the 99.97^{th}percentile of $\boldsymbol{v}_{\mathrm{MAG}} = 0.48$ m/s. The values within this procedure are based on tests which were conducted to increase the accuracy and the calculation speed. The median of the ten center coordinates in x and y is used to estimate the vortex center at time step $i = 1$ for run #7.13 (Fig. 4.13). The methodology minimizes the influence of misleading findings or outliers at single layers. Finally, a new coordinate system with respect to the radii r_x and r_y is applied, where the vortex center is shifted to $x = 0$ and $y = 0$.

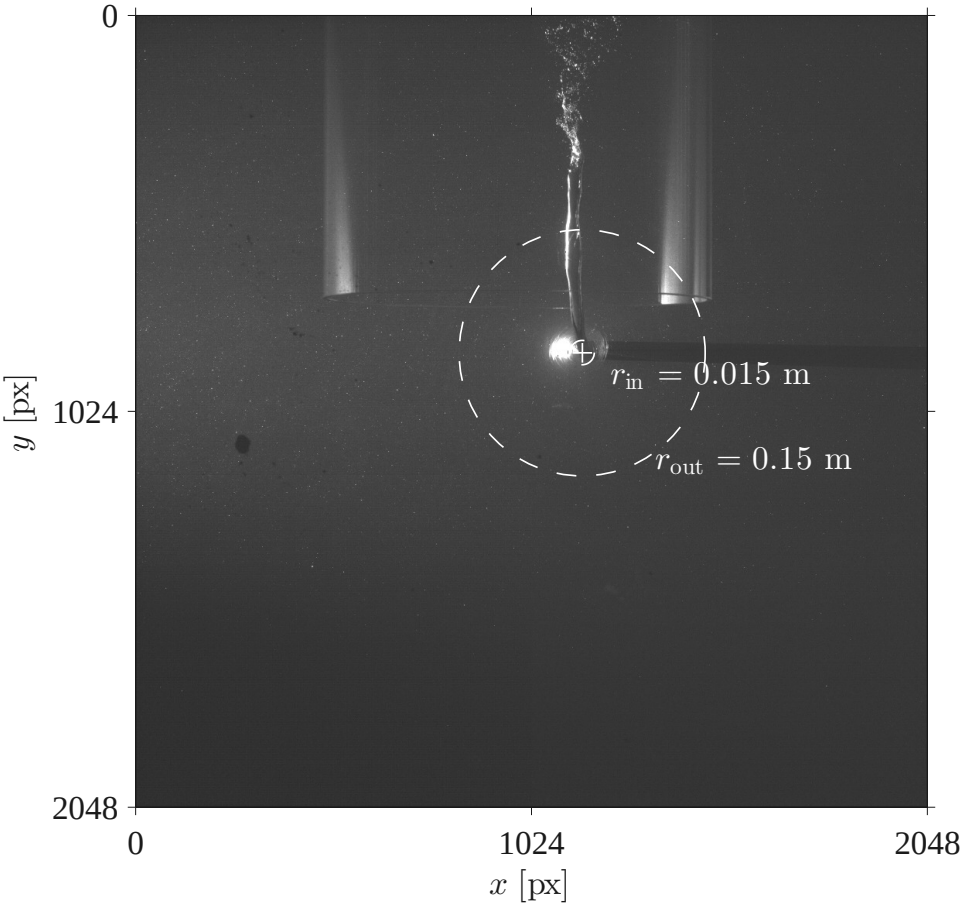

Figure 4.13: Snapshot of a PIV image with the detected vortex center overlaid (run #7.13, $i = 1$). The inner and outer dashed circle give the limits to the area where Γ is calculated. The limits are defined by r_{in} and r_{out}, respectively.

Circulation derived from a Single PIV Image. The circulation Γ is defined from eq. 2.7. Once the horizontal velocity vector map is known from the PIV analysis, a circulation matrix $\boldsymbol{\Gamma}_i$ can be calculated as follows:

$$\boldsymbol{\Gamma}_i = 2\pi \left|\boldsymbol{v}_{\mathrm{t},\,i}\right| \sqrt{\boldsymbol{r}_{x,\,i}^2 + \boldsymbol{r}_{y,\,i}^2}\ , \text{ with} \tag{4.14}$$

$$\boldsymbol{v}_{\mathrm{t},\,i} = \boldsymbol{v}_{x,\,i} \cos(\boldsymbol{\Phi}_i) - \boldsymbol{v}_{y,\,i} \sin(\boldsymbol{\Phi}_i)\ , \text{ and} \tag{4.15}$$

$$\boldsymbol{\Phi}_i = \mathrm{atan2}(\boldsymbol{r}_{x,\,i}, \boldsymbol{r}_{y,\,i})\ , \tag{4.16}$$

where $\boldsymbol{v}_{\mathrm{t},\,i}$ = tangential velocity matrix, $\boldsymbol{r}_{x,\,i}$ and $\boldsymbol{r}_{y,\,i}$ = radius matrices, and $\boldsymbol{\Phi}_i$ = tangential angle matrix. The two-argument function atan2 is a variation of the arctangent function. The angle is positive for counter-clockwise angles (upper half-plane, $y > 0$), and negative for clockwise angles (lower half-plane, $y < 0$).

Next, limits have to be defined to determine the area of $\mathbf{\Gamma}_i$ that is used to calculate the current Γ_i which is the mean of $\mathbf{\Gamma}_i$ and reduces the vortex to a single value. By theory the vortex field of a potential vortex affects an infinitive large area (see chapter 2.2.6). However, this idealization cannot be used if Γ is derived from a measured velocity field, as this effect diminishes exponentially with increasing distance to the vortex center; and, from a certain distance on, it is too small to be resolved by PIV measurements. Therefore an outer circular limit is set by r_{out}. Furthermore, misleading vectors near the vortex core result in noisy areas in $\mathbf{\Gamma}_i$. Therefore, an inner cutout limit r_{in} has to be set as well. Fig. 4.14 shows $\boldsymbol{v}_{\text{t},i}$ by the limits $r_{\text{in}} \geq 0.015$ m and $r_{\text{out}} \leq 0.15$ m (compare Fig. 4.13). These limits of r_{in} and r_{out} have been chosen for the whole analysis procedure of the vector maps gained within the measurement campaign, although changes of r_{in} in the range of $\pm 40\,\%$ showed similar results. However, to determine the outer limit r_{out} a more sophisticated sensitivity analysis had to be performed as given below: In Fig. 4.16 three histograms of Γ_i for $r_{\text{out}} = [0.10, 0.15, 0.20]$ are compared. The median values of $\Gamma = [0.116, 0.120, 0.119]$ m^2/s do not differ much, whereas the total numbers are $n(\sum_{i=1}^{\text{end}} \Gamma_i, r_{\text{out}}) = [544, 1228, 2208]$.

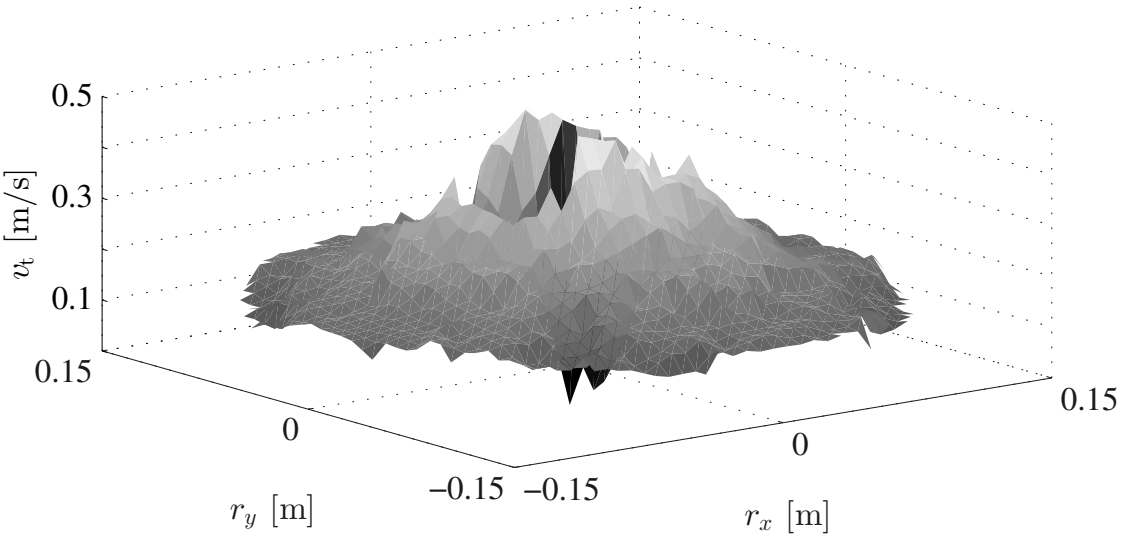

Figure 4.14: Tangential velocity v_{t} [m/s] in an area around the vortex center that has been circularly cut by the limits $r_{\text{in}} \geq 0.015$ and $r_{\text{out}} \leq 0.15$ m.

Fig. 4.15 shows Γ as determined from the methodology described above. Two areas become obvious: (1) an almost constant ring between $0.05 \leq r \leq r_{\text{out}}$ and (2) a decreasing zone for $r \leq 0.05$.

Γ as a mean value should be based on a normally distributed $\mathbf{\Gamma}_i$. However, the Gaussian fits of Fig. 4.16 do not suit properly to the distributions for the skewness γ = [-1.7, -2.2, -1.9]. The decreasing zone for $\Gamma(r_{\text{out}} = 0.10$ m) with 544 values gets more biased than the two other distributions with $n = 1228$ and $n = 2208$ values.

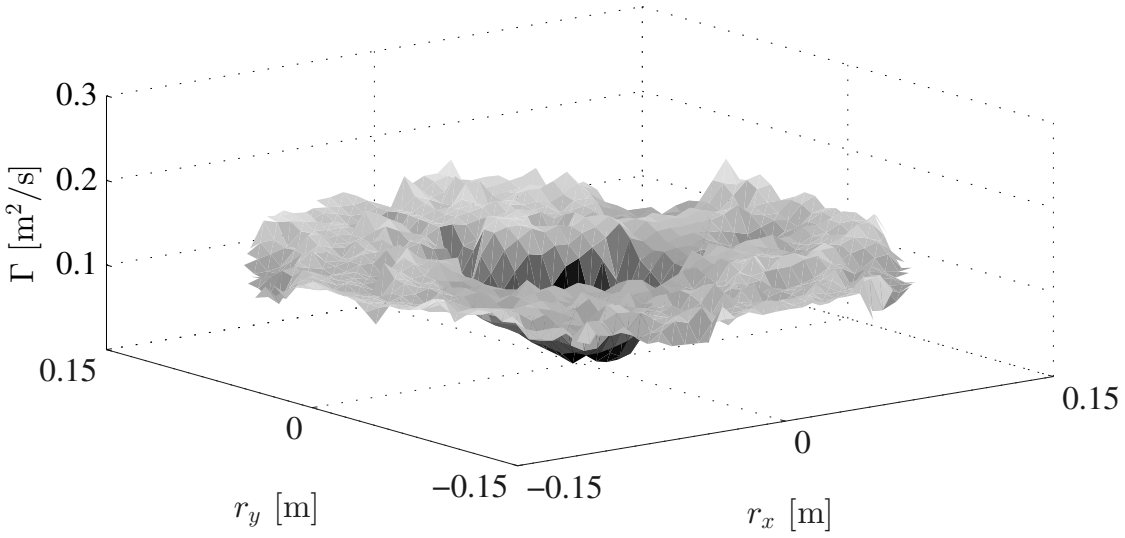

Figure 4.15: Circulation Γ [m^2/s] determined in an area that was cut by the limits $r_{\text{in}} \geq 0.015$ m and $r_{\text{out}} \leq 0.15$ m.

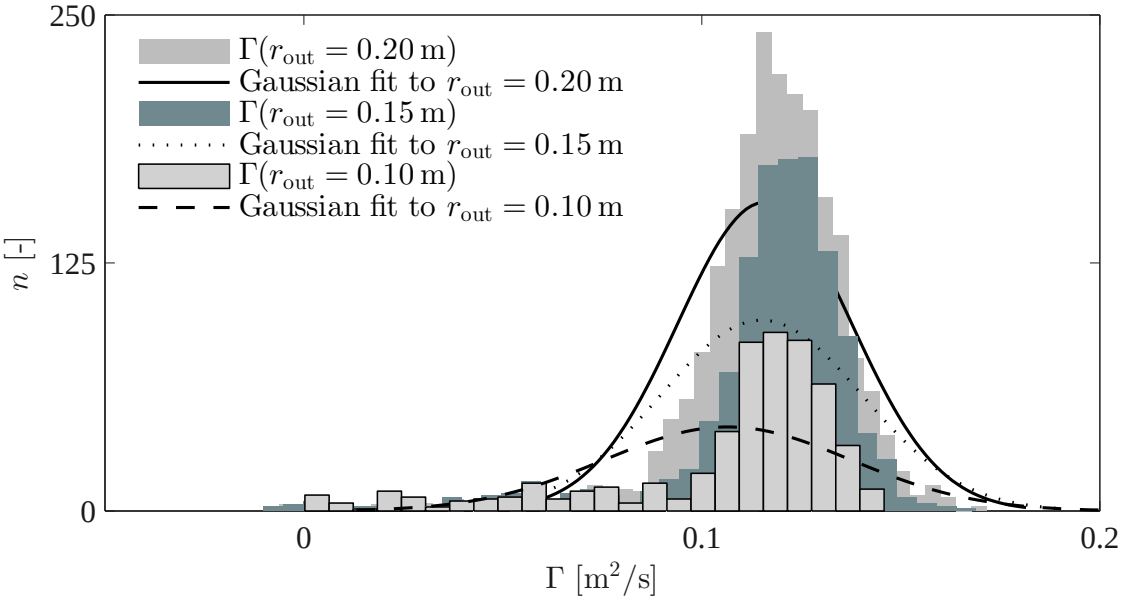

Figure 4.16: Histograms of Γ for $r_{\text{out}} = [0.10, 0.15, 0.20]$ m. Their related Gaussian fits do not suit properly, showing that the distribution is biased.

Similar to the central limit theorem[3] the skewness decreases with increasing n. As the skewness approaches zero, representing a Gaussian distribution, the median becomes equal to the mode and can be used to fix Γ_i. The total number n increases with r_{out}, but for larger r_{out} the velocity field intermixes with secondary currents and the PIV noise is disproportionately high at small velocities. To get a robust statistic[4] the values of the interquartile range IQR are used to determine the optimal value of r_{out}. The corresponding values are IQR(r_{out} = [0.10, 0.15, 0.20] m) = [0.0220, 0.0182, 0.0205] m^2/s. Small IQR refer to for distinct peaks, side effects are negligible small. Thus, the median of Γ within $r_{\text{out}} = 0.15$ m of 0.1204 m^2/s is set to Γ_i. The single number Γ_i represents the whole analyzed velocity field obtained from a single PIV image.
An overview containing the corresponding diagrams and results of determining the mean circulation of one single image Γ_i are saved for each image ($\sum n_{\text{PIVimages}} > 1.6 \cdot 10^5$) to be able to control the process afterwards.

Circulation Time Series. Γ_i can be determined for each time series of a PIV run. However, a continuous and successful determination of Γ_i could not be guaranteed for each PIV image due to the absence of a definitive vortex, e.g. no vortex or more than one vortex, or due to insufficient velocity vector maps, respectively.
Fig. 4.17 shows an example of a Γ_i time series. Deficient values have been detected and smoothed out by a despiking filter. This filter applies a median filter technique to detect the difference of the data points to the filtered time series. As a result, the developed curve $\Gamma_{i,\text{d}}$ equals the Γ_i curve, but does not contain the detected values visible as gaps. An interpolation is applied to supplement the gaps and a moving average filter is used to smooth $\Gamma_{i,\text{d}}$ to get the smoothed curve $\Gamma_{i,\text{s}}$.
Next, the sensitivity of $\Gamma_{i,\text{s}}$ to r_{out} is tested (Fig. 4.18). Again $\Gamma_{i,\text{s}}$ ($r_{\text{out}} = 0.10$ m) has the largest differences compared to curves of $\Gamma_{i,\text{s}}$ ($r_{\text{out}} = 0.15$ m) and $\Gamma_{i,\text{s}}$ ($r_{\text{out}} = 0.20$ m) which do not differ significantly. Therefore, $r_{\text{out}} = 0.15$ m is chosen best to be applied in the time series analysis for determining $\Gamma_{i,\text{s}}$.

[3] After the central limit theorem the mean of a sufficiently large number of values will approximately be normally distributed.

[4] A robust statistic provides estimators for parameters and differs from the standard statistical methods. It is not unduly affected by small departures from model assumptions.

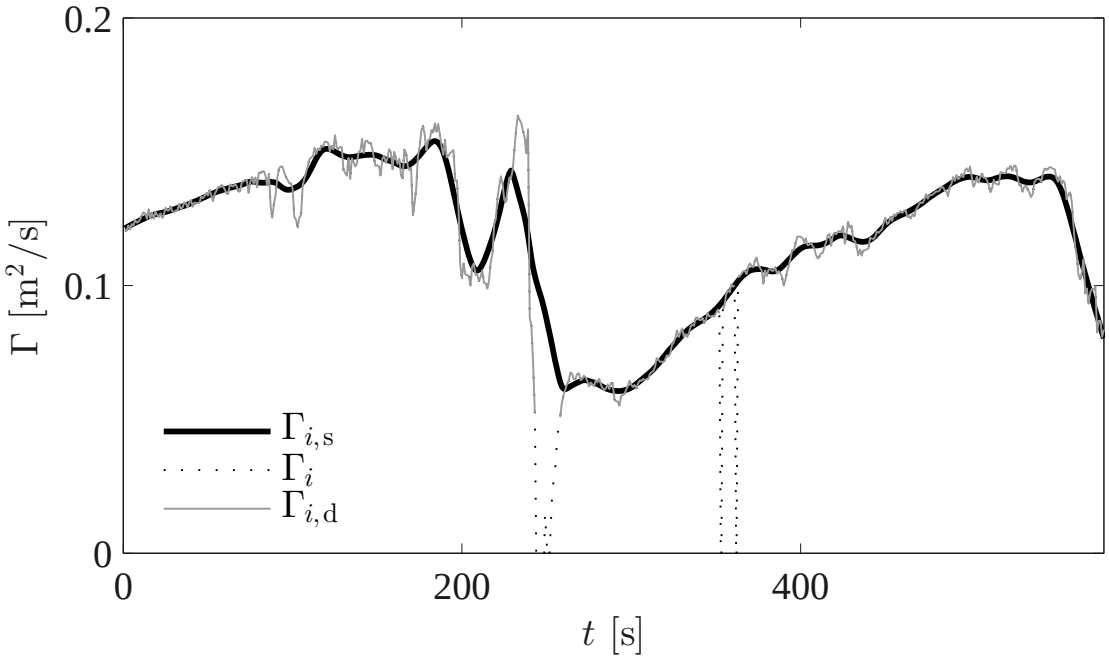

Figure 4.17: Time series of circulation Γ_i, $\Gamma_{i,\mathrm{d}}$ after applying a despiking filter, and $\Gamma_{i,\mathrm{s}}$ smoothed by moving average filter (run #7.13, $i = 1$–579).

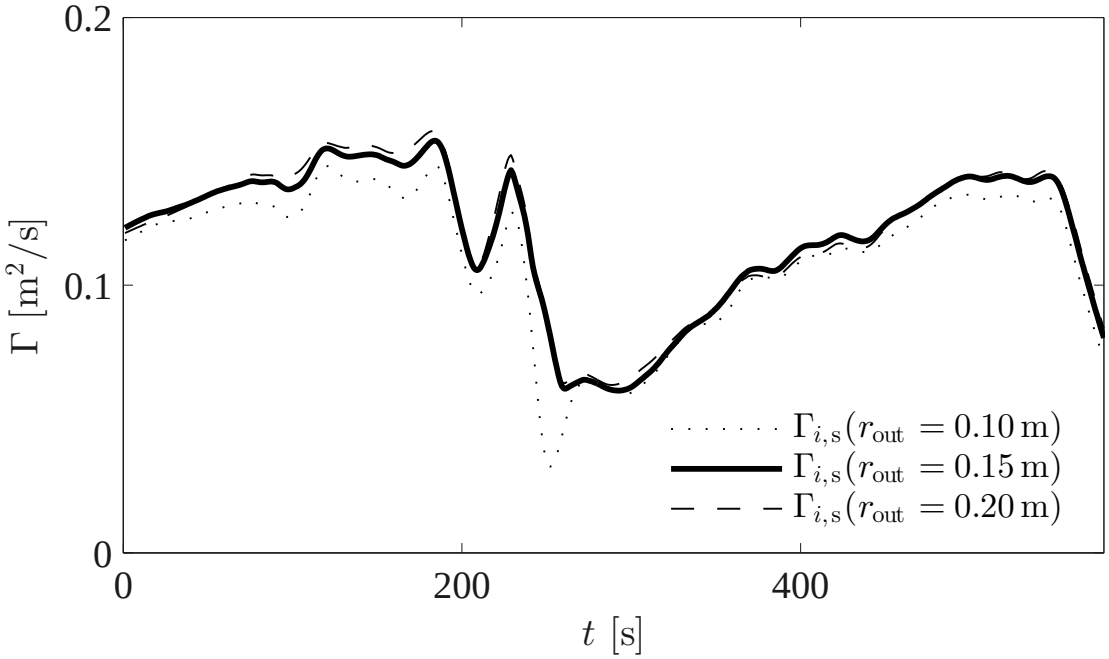

Figure 4.18: Time series of $\Gamma_{i,\mathrm{s}}$ for different r_{out} (run #7.13, $i = 1$–579).

4.5 Air-Core Diameter

The original purpose of PIV is to record and analyze the horizontal velocity field around the vortex core. However, as the laser light sheet hits the air-core a shadow is generated in the lee region. Fig. 4.19 gives a typical example. On the one hand this shadow disturbs the correlation of the PIV double frames. On the other hand the shadow gives a handle to measuring the air-core diameter d_{ac}.

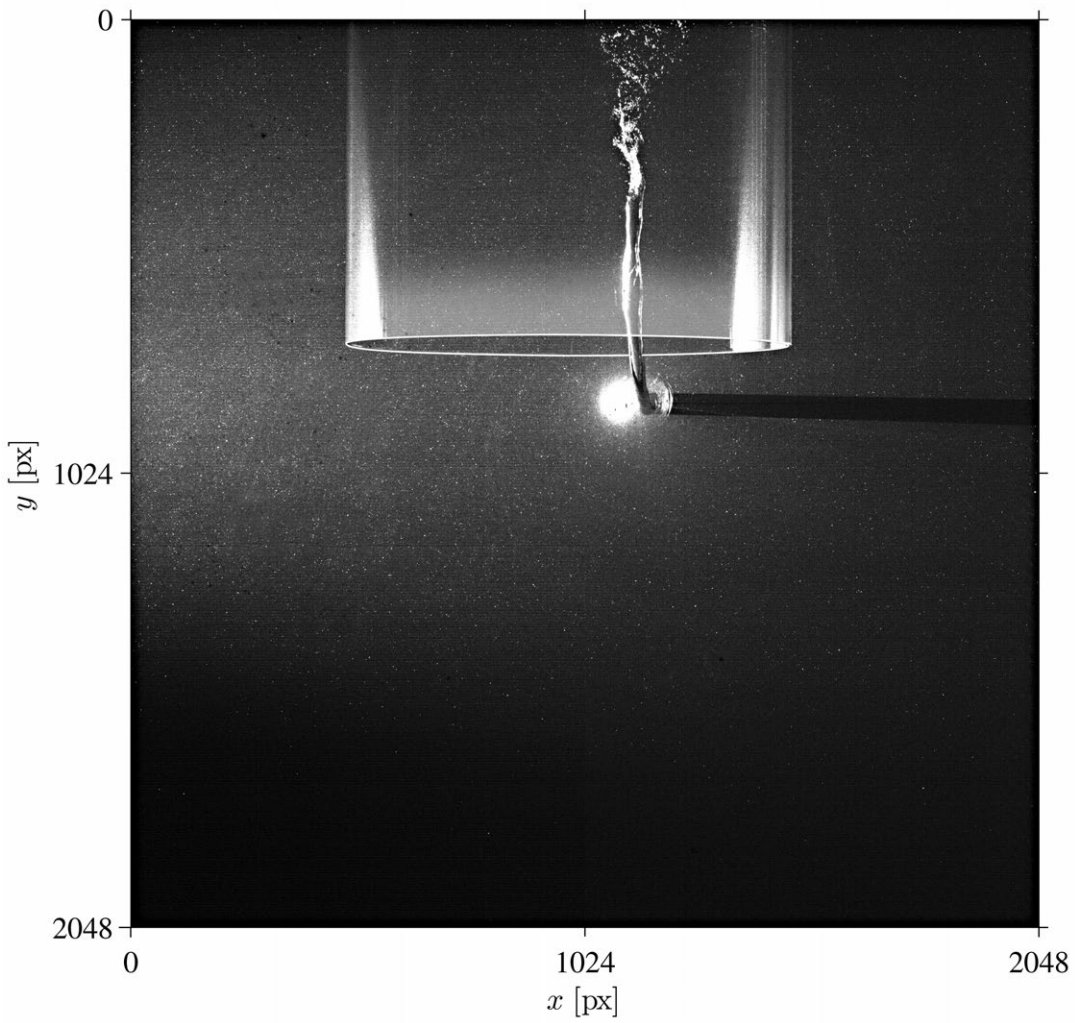

Figure 4.19: Initial PIV image with a prominent air-core shadow.

The shadow is measured via a two-step object detection procedure. The algorithm is implemented in a MATLAB code. Its basic ideas are presented in the following. The first step starts by cropping a stripe of 400 px width from the right margin and over the full height of the PIV image to focus on the region where the shadow is most prominent. A 3×3 px^2 median filter is applied to smooth away the noisy texture due to the PIV particles. Fig. 4.20a shows the resulting partial image. Then a set of functions is applied to get a first estimate of the area of the shadow: The non-uniformly illuminated background is filtered away by a circular averaging filter

with radius of 200 px and the result is transferred to a binary image (Fig. 4.20b). Next, the largest object in the binary image is counted as an indicator of the air-core shadow if the following threshold criteria are fulfilled: (1) at least 100 px have to belong to its area, (2) a maximal inclination of 15° to the horizontal image axis is allowed, and (3) the ratio of the major to the minor axis has to be > 3.0. In case the shadow gets confirmed, it gets elongated along its major axis while the global major diameter is set to the major diameter of the previously detected object plus a boundary dilatation of 4 px. The resulting area of the pre-estimated air-core shadow after the first step of the object detection procedure is given in Fig. 4.20c.

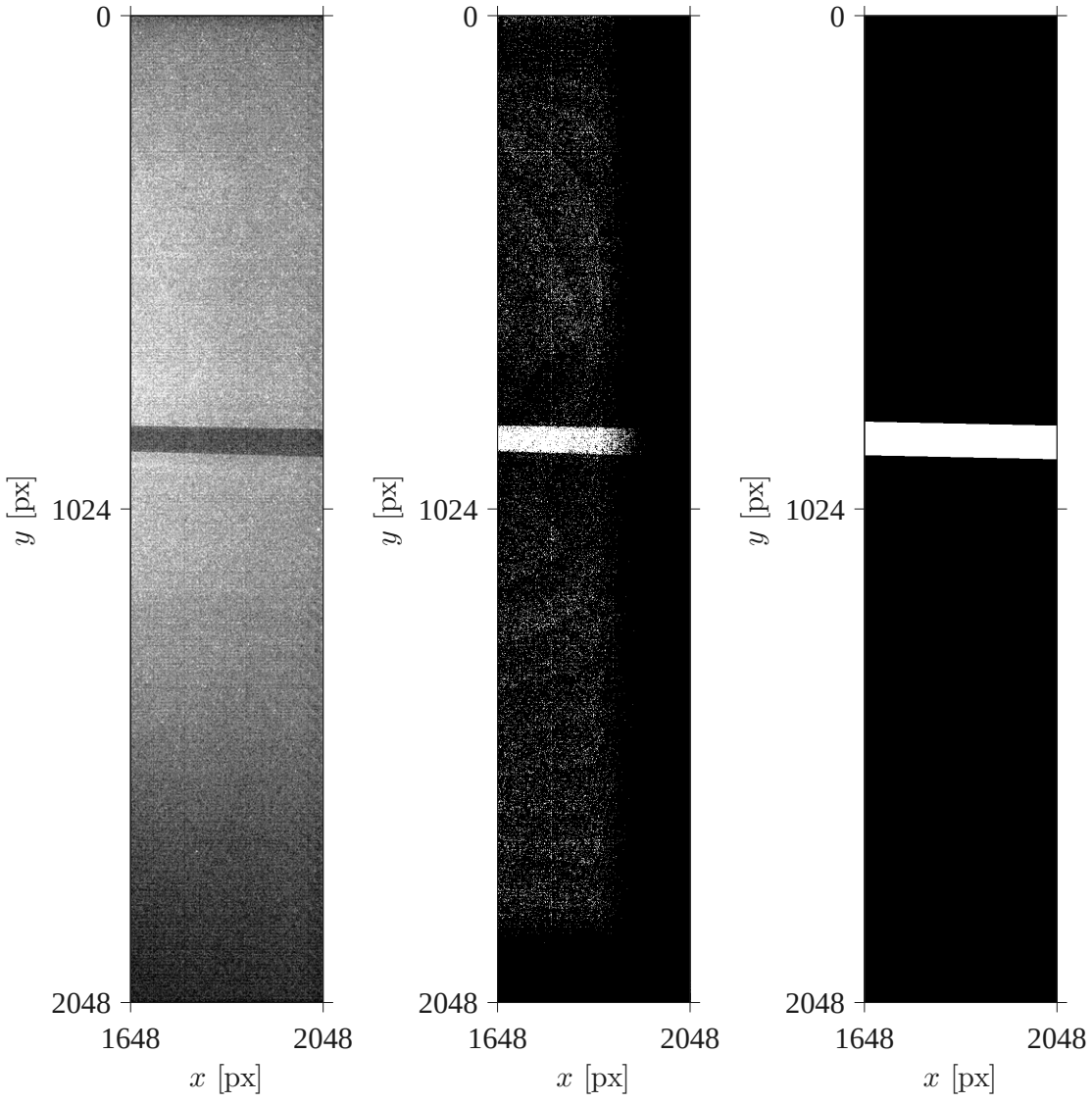

(a) Cropped stripe (b) Filtered binary image (c) Resulting raw estimation of the shadows area

Figure 4.20: First step of measuring the air-core diameter: an image stripe is used for the object detection procedure.

The second step uses Canny edges to find the upper and lower edges of the shadow in detail. In MATLAB (2013) this procedure is explained as follows: *"The Canny method finds edges by looking for local maxima of the gradient of the image. The gradient is calculated using the derivative of a Gaussian filter. The method uses two thresholds, to detect strong and weak edges, and includes the weak edges in the output only if they are connected to strong edges. This method is therefore less likely than the others to be fooled by noise, and more likely to detect true weak edges"*. In Fig. 4.21a a typical result is presented. Beside a noisy and wormy structure a strong indication to the upper and lower edges of the shadows becomes obvious. Next, single edge elements get confirmed in case their ratio major to minor axis is > 3.0 and their inclination to the horizontal image axis is $< 15°$. A confirmed edge is seen to indicate an upper shadow edge in case it is covered by the upper half of the shadow-estimation of the first step, and vice versa for the lower edged. The result looks typically as shown in Fig. 4.21b. The final geometry of the shadow edges is found by fitting linear curves to the edges. In Fig. 4.21c the result is indicated by circles.

Once these edges are known, the upper and lower span angles α_1 and α_2, respectively, as well as distances in between, i.e. the air-core shadow diameter $d_{\mathrm{ac,\,s}}$ at position $x = 1848$ px, can be extracted (see Fig. 4.21c). The determination of the air-core diameter d_{ac} is conducted geometrically using the air-core center coordinates (see chapter 4.4). Depending on the position of the vortex center the difference between the shadow width $d_{\mathrm{ac,\,s}}$ and the air-core diameter d_{ac} varies by -25 % in average. The shadow detection is limited to 7 px in minimum. If two or three air-cores are present the largest shadow is detected. The information of the estimated air-core diameter d_{ac} is used in the analysis of air-core flow (see chapter 7.3).

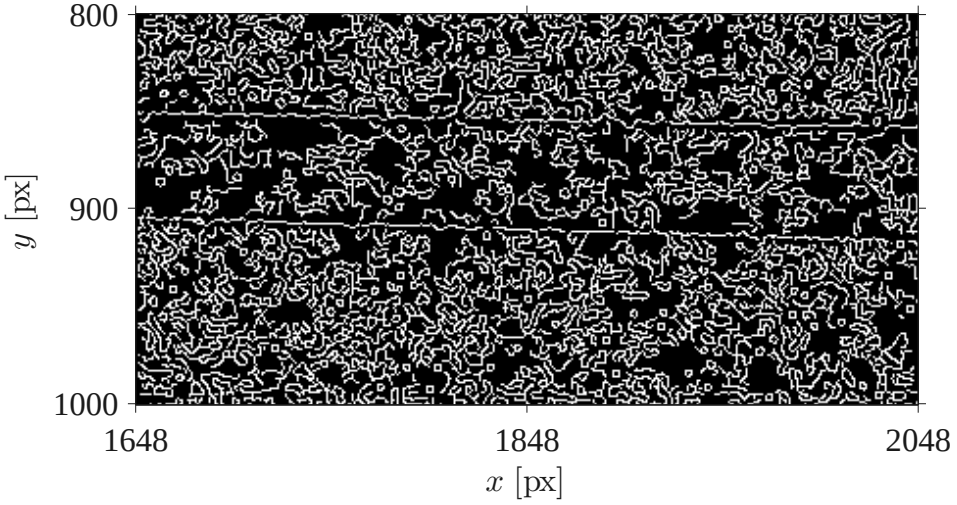

(a) Canny edges

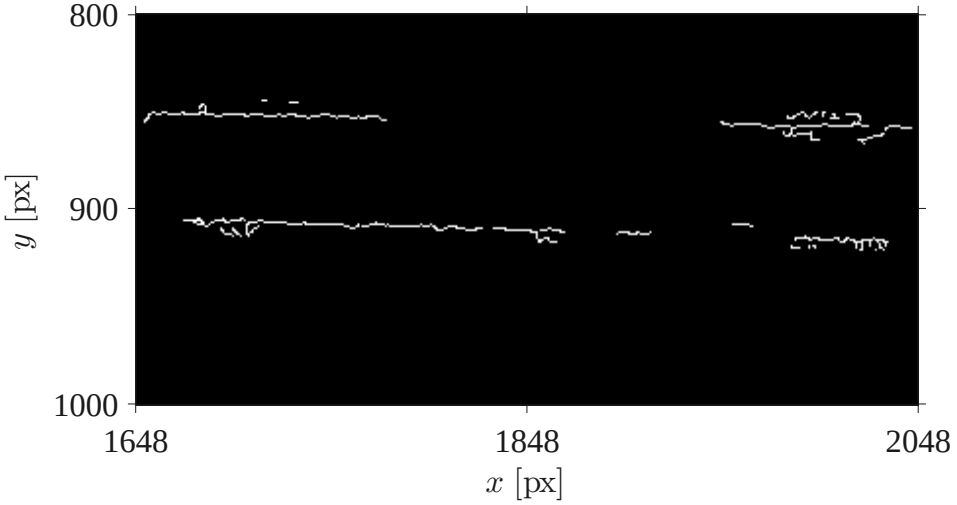

(b) Confirmed Canny edges

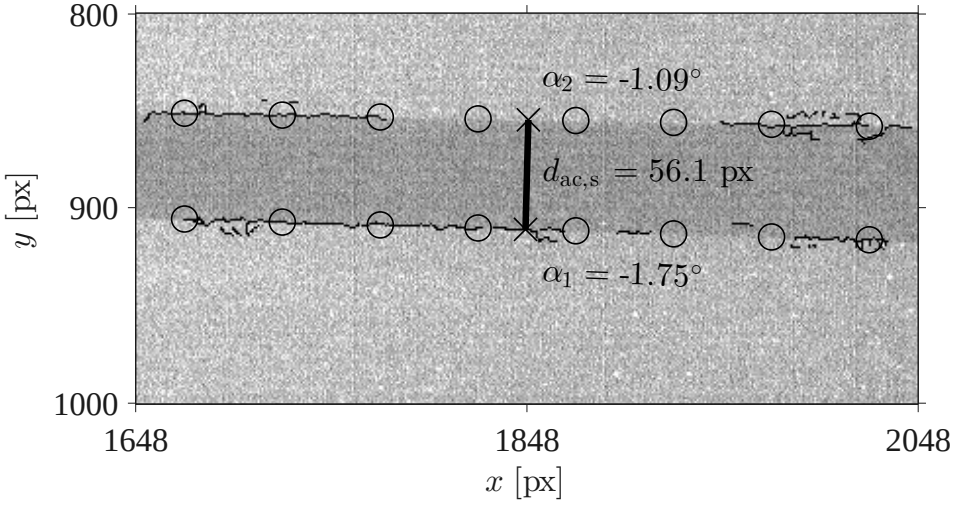

(c) Finally detected shadow edges, where the shadow corresponds to $d_{\mathrm{ac,\,s}} = 2.64$ cm which results in $d_{\mathrm{ac}} = 2.1$ cm.

Figure 4.21: Second step of measuring the air-core diameter: Edge detection in the area of the shadow as proposed after the first step.

4.6 Scale Family Test Setup

The experimental setup to investigate the two-phase flow phenomenon of air-entraining vortices covers a wide range of dimensions. For instance, the reservoir scales in [m], the pipe diameter in [cm], while the diameter of air-core tube is only about a few millimeters. The velocities range from ∼0.1 m/s in the approach flow up to ≥ 3–4 m/s in the intake pipe and ∼10 m/s for the entrained air in the air tube. Consequently, classical scale similarities, e.g. Froude-similarity at high Reynolds numbers may be misleading. Therefore, scale family tests have to be performed to proof the feasibility of the model investigation, with respect to the transferability of the results to larger scales such as prototypes. Unfortunately, no guidelines exist regarding the conduct of those scale family tests. As a rule-of-thumb, three different scales have to be investigated, where the smallest scale should be one third of the largest scale.
Here, the scale factor is defined as the ratio between the intake diameter D_{DN500} and the respective intake diameter $D(\mathrm{DNj})$:

$$\lambda_j = \frac{D(\mathrm{DN500})}{D(\mathrm{DNj})} \ . \tag{4.17}$$

Table 4.1 lists the characteristic parameter of the four different scales that have been investigated, where $\lambda = [1, 1.24, 1.66, 2.55]$ is derived from eq. 4.17. The dynamic similarity is set by assuming the Froude similarity to be valid. The effect of the tank walls and bottom to the flow is assumed to be negligibly small. Therefore, these distances to the intake pipe have not been changed. The intake Froude number F_D and the relative submergence h/D investigated at each of the four scales are identical (see Table 4.1).

Table 4.1: Characteristic parameters of the four scale family test. Empirical limits with respect to the intake cross-section are given by R_D, W_D^2 (see chapter 3.2).

λ [-]	DN [mm]	D [m]	A_D [m^2]	F_D [-]	v_D [m/s]	Q_{w} [m^3/s]	R_D [10^4] > 3.2	W_D^2 [-] > 120
1	500	0.484	0.18	0.4	0.9	0.16	42	5028
				1.4	3.1	0.56	146	61591
1.24	400	0.389	0.12	0.4	0.8	0.09	30	3248
				1.4	2.7	0.33	105	39785
1.66	300	0.291	0.07	0.4	0.7	0.04	19	1817
				1.4	2.4	0.16	68	22264
2.55	200	0.190	0.03	0.4	0.5	0.02	10	775
				1.4	1.9	0.05	36	9491

No reports on former investigations regarding scale effects of air entrainment have been found in literature. In order to have a clue, limits with respect to vortex formation are compared (see Table 4.1). The results of the scale family tests are presented in chapter 5.

4.7 Experimental Program

The experimental program of the main measurement campaign of this study is listed in Table 4.2. All experimental runs are carried out with an inner diameter of the intake pipe of $D = 0.389$[5] m. All experimental runs are performed as follows: Within an initial phase the hydraulic system is tuned to a steady state regarding h/D and F_D as given in Table 4.2. Their range is chosen based on typical HPP conditions (Knauss, 1987c) and is closely related to the working range and capacity of the de-aeration device (see chapter 4.2). Then, the valves of the de-aeration devices are closed and data recording is started simultaneously for all subsystems including the PIV. Experimental runs are performed independently of the occurrence of vortices to avoid statistical bias in the data.
The basic rising pipes [#2, #3], the rising pipes plus one air storage [#2, #2a, #3] as well as the rising pipes plus two air storages [#2, #2a, #2b, #3] are used to determine the volume of entrained air. Table 4.2 lists the devices used for each run. If the water level in the rising pipes falls down to the pipe ridge, the collected air has to be emptied. This procedure lasts about 20 s. Unfortunately, the air discharge cannot be determined within this time slot, resulting in a time lack in the recordings. The whole data acquisition including the PIV recording is performed at a frequency of 1 Hz. After 579 s the PIV data has to be shifted from the RAM to the local hard disk drive. This procedure lasts about 90 s. After this break the acquisition starts again. Unfortunately, this time gap depending on the storage capacity and the transfer rate of the PIV system is inevitable. In total 286 PIV runs with $> 1.6 \cdot 10^5$ double frame images are stored during the experimental runs.
The labeling of an experimental run contains first #, then the experimental number (1–34), separated by a dot the number of a PIV run (up to 13) within an experimental run, for example #7.13.

[5]Note that this diameter has been varied only within the scale family tests.

Table 4.2: Experimental program as performed within this study. h/D = relative intake submergence, F_D = intake Froude number, F_{co} = combined Froude number, h = intake submergence, v_D = intake velocity, Q_{w} = water discharge, L_{FOV} = edge length of field-of-view (FOV). Each run has been conducted with a duration of two hours.

run [no.]	h/D [-]	F_D [-]	F_{co} [-]	h [m]	v_D [m/s]	Q_{w} [m^3/s]	de-aeration by device [-]	L_{FOV} [m]
1	1.25	0.4	0.36	0.486	0.781	0.093	#2, #3	0.9383
2		0.5	0.45	0.486	0.977	0.116	#2, #3	0.9383
3		0.6	0.54	0.486	1.172	0.139	#2, #3	0.9383
4		0.7	0.63	0.486	1.367	0.163	#2, #2a, #3	0.9383
5	1.5	0.5	0.41	0.584	0.977	0.116	#2, #3	0.9645
6		0.55	0.45	0.584	1.074	0.128	#2, #3	0.9645
7		0.6	0.49	0.584	1.172	0.139	#2, #3	0.9645
8		0.7	0.57	0.584	1.367	0.163	#2, #2a, #3	0.9645
9		0.75	0.61	0.584	1.465	0.174	#2, #2a, #3	0.9645
10		0.8	0.65	0.584	1.563	0.186	#2, #2a, #2b, #3	0.9645
11		0.85	0.69	0.584	1.66	0.197	#2, #2a, #2b, #3	0.9645
12		0.9	0.73	0.584	1.758	0.209	#2, #2a, #2b, #3	0.9645
13		0.95	0.78	0.584	1.856	0.221	#2, #2a, #2b, #3	0.9645
14	1.75	0.6	0.45	0.681	1.172	0.139	#2, #3	0.9882
15		0.7	0.53	0.681	1.367	0.163	#2, #3	0.9882
16		0.8	0.60	0.681	1.563	0.186	#2, #3	0.9882
17		0.85	0.64	0.681	1.66	0.197	#2, #2a, #3	0.9882
18		0.9	0.68	0.681	1.758	0.209	#2, #2a, #2b, #3	0.9882
19	2	0.7	0.49	0.778	1.367	0.163	#2, #3	1.0110
20		0.8	0.57	0.778	1.563	0.186	#2, #3	1.0110
21		0.85	0.60	0.778	1.66	0.197	#2, #2a, #3	1.0110
22		0.9	0.64	0.778	1.758	0.209	#2, #2a, #2b, #3	1.0110
23		1	0.71	0.778	1.953	0.232	#2, #2a, #2b, #3	1.0110
24		1.1	0.78	0.778	2.149	0.255	#2, #2a, #2b, #3	1.0110
25	2.25	0.7	0.47	0.875	1.367	0.163	#2, #3	1.0360
26		0.8	0.53	0.875	1.563	0.186	#2, #3	1.0360
27		0.9	0.60	0.875	1.758	0.209	#2, #3	1.0360
28		1	0.67	0.875	1.953	0.232	#2, #2a, #3	1.0360
29		1.1	0.73	0.875	2.149	0.255	#2, #2a, #2b, #3	1.0360
30		1.2	0.80	0.875	2.344	0.279	#2, #2a, #2b, #3	1.0360
31	2.5	0.9	0.57	0.973	1.758	0.209	#2, #3	1.0610
32		1	0.63	0.973	1.953	0.232	#2, #3	1.0610
33		1.1	0.70	0.973	2.149	0.255	#2, #2a, #2b, #3	1.0610
34		1.2	0.76	0.973	2.344	0.279	#2, #2a, #2b, #3	1.0610

Chapter 5

Results of Scale Family Tests

Abstract. *The air entrainment due to intake-vortices as a two-phase flow is analyzed concerning potential scale effects. Scale family tests are decisive to test and to proof the transferability of the achieved experimental findings. The results are used to derive modeling threshold criteria. The main parameter that is varied to investigate four scales is the diameter of the intake pipe D. Its nominal diameter ranges from DN200 to DN500. An overview of the investigated parameter matrix is given with regard to the occurrence of air entraining vortices.*

5.1 Occurrence

Fig. 5.1 shows the parameter matrix that is investigated within the scale family tests. The procedure is described in detail in chapter 4.6. Here, the dots depict the measuring grid. The other markers coding to the nominal diameter DN (see Table 4.1) indicate that air entrainment occurred and could be measured as well. All these markers form a prominent diagonal band through the matrix. The differences between the occurrence of air entrainment of the four scales are small. For a given relative submergence, large pipe diameters tend to have air entrainment at smaller F_D than small ones do. At high F_D the de-aeration system exceeds its capacity at larger scales. Thus a comparison of differences would be misleading here and is therefore omitted. The diagonal band has a characteristic hook at $\mathsf{F}_D = 0.6$–0.8. Here, the smallest scale DN200 is most prominent, although at all scales this hook is present. In contrast to this observation, Knauss (1987b) proposed a linear increase of the critical submergence as shown in Fig. 5.1. The present results generally fit well, except for the mentioned hook. However, it has to be noted that the markers in Fig. 5.1 represent the measurable air entrainment, whereas Knauss (1987b) focused solely on the vortex formation at the state where the air core reached the intake cross-section ($VT6$). In chapter 8.2 a comparison is conducted concerning the common approaches on the one hand (see chapter 2.3.3) and the approach developed in this

research project based on the scale family tests and the main measurement campaign on the other hand. According to the occurrence of vortices with measurable air entrainment no scale effects can be ascertained within the four scales.

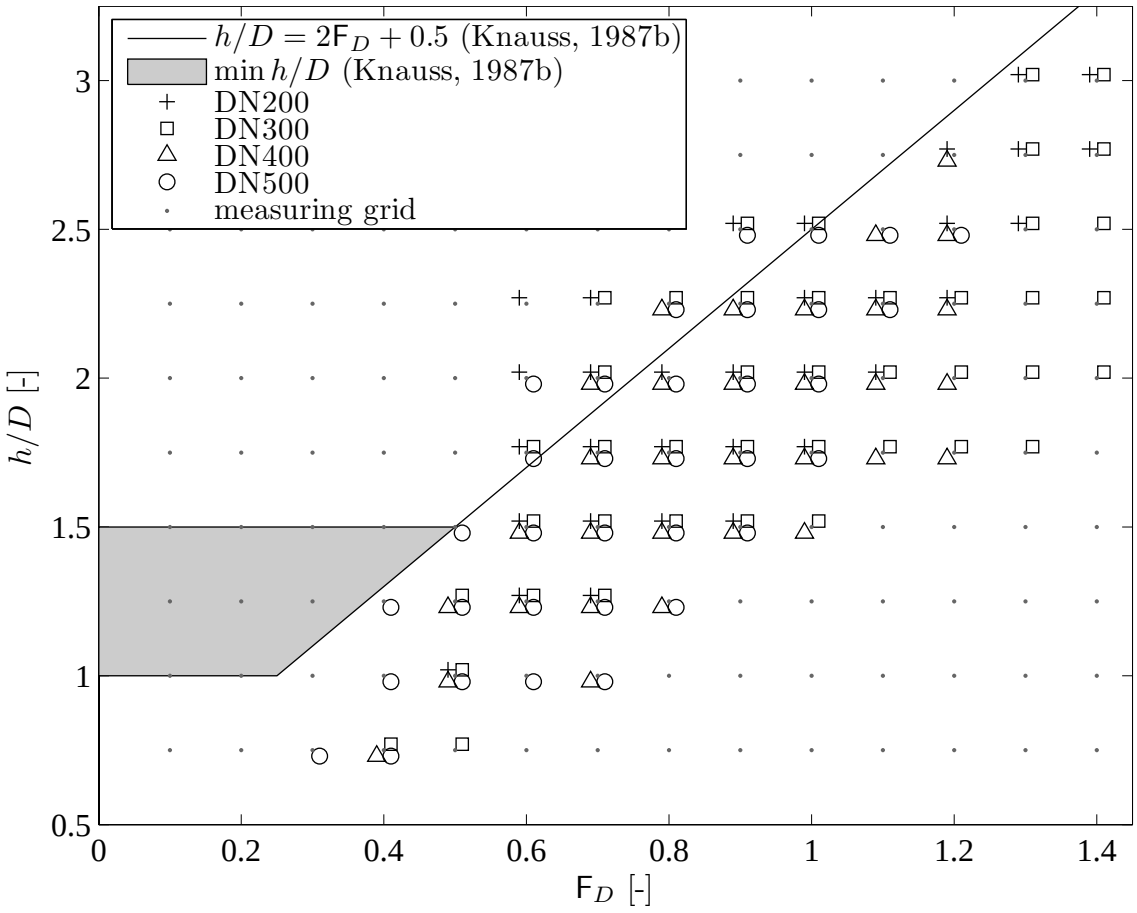

Figure 5.1: Parameter matrix grid and measurable air entrainment of the different scales in comparison to the critical submergence as proposed by Knauss (1987b). The markers indicate that air entrainment occurred and could be measured as well.

5.2 Air Entrainment Rate $\dot{\beta}$

The procedure of air entrainment measurements within the scale family tests slightly differs from the one used for the main measurement campaign, as the de-aeration system with air storages was not developed so far at that time. Here only short time measurement durations have been used to measure air entrainment. To overcome this drawback a visual vortex tracking procedure was performed additionally that accounts for the phases as depicted in Fig. 5.2. Three observed vortex phases, are categorized to formation, constant phase and decay.

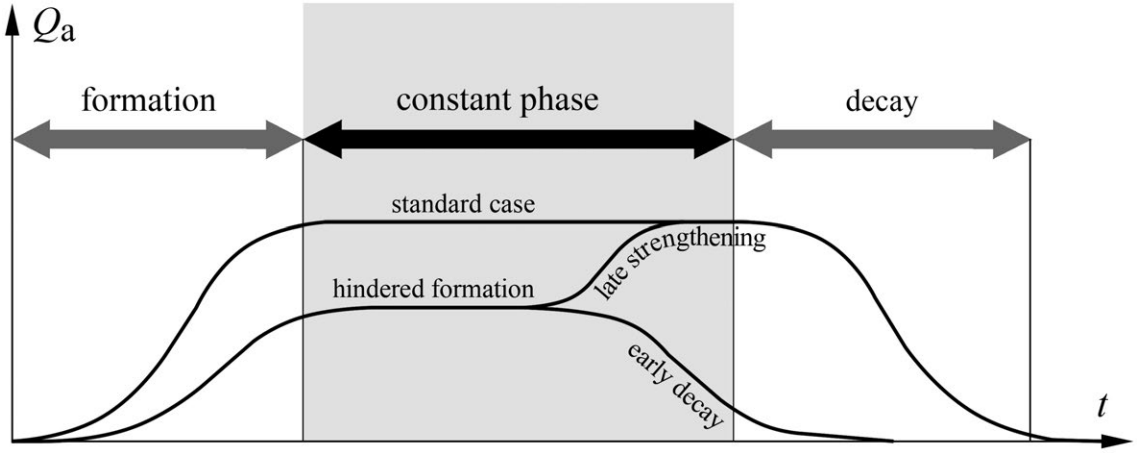

Figure 5.2: Observed vortex phases and corresponding air entrainment (adapted from Meyer (2012)).

In the constant phase a subdivision can been made between a standard case and a hindered vortex formation. At the end of the constant phase the latter may strengthen to a standard vortex or may decay. Measurements of air entrainment were only conducted in the constant phase of the standard case. The resulting air discharge $\dot{Q}_a$ and the air entrainment rate $\dot{\beta}$ refer to this stage, where the dot denotes the measurement within a short duration as explained in chapters 3.5 and 4.2. These punctual measurements are repeated three to five times on the same measurement day. To avoid systematic errors, these measurements are repeated up to three times on another measurement day as well. Thus $\dot{Q}_a$ and $\dot{\beta}$ are based on a minimum of six measurements, where as in average nine to ten measurements have been performed.

Figs. 5.3–5.6 show the results of all scales λ_j, where the subfigures (a) depict the air discharge $\dot{Q}_a$ and the subfigures (b) give the air entrainment rate $\dot{\beta}$. The dimensional air discharge $\dot{Q}_a$ gives the quantity of air entrainment independent of the water discharge Q_w. The non-dimensional air entrainment rate $\dot{\beta}$ is used to compare air entrainment with water discharge. Following the law of similarity (see chapter 3.2), the results of $\dot{\beta}$ for the different scales λ_j have to be identical if no scale effects are present, e.g. air entrainment rate β_{DN200} and β_{DN500} should be similar.

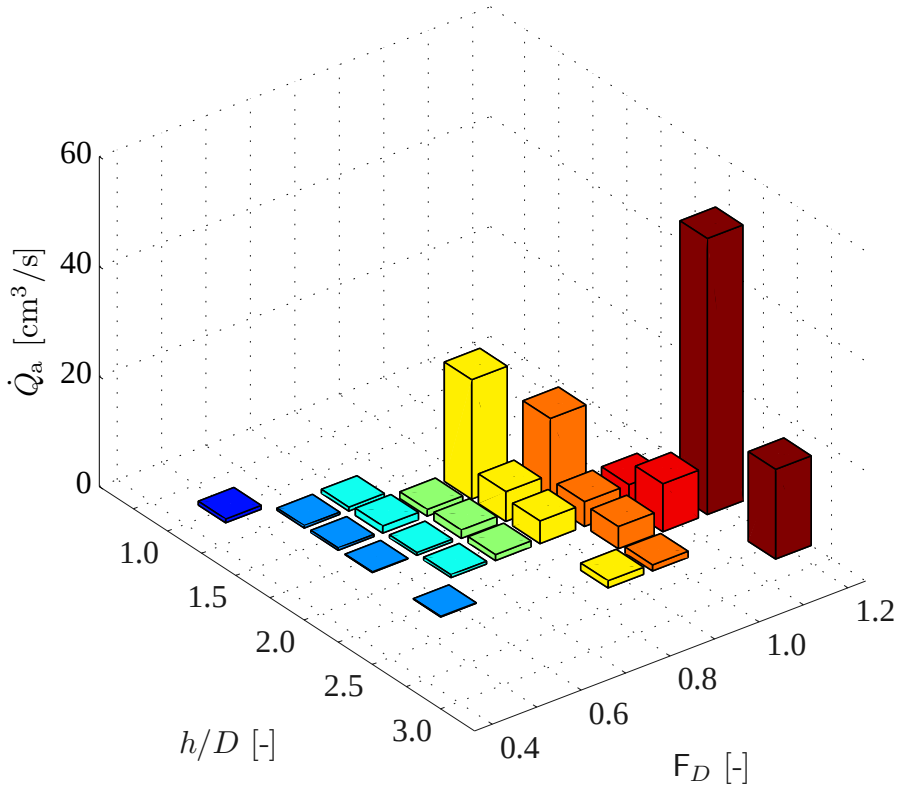

(a) air discharge $\dot{Q}_a$

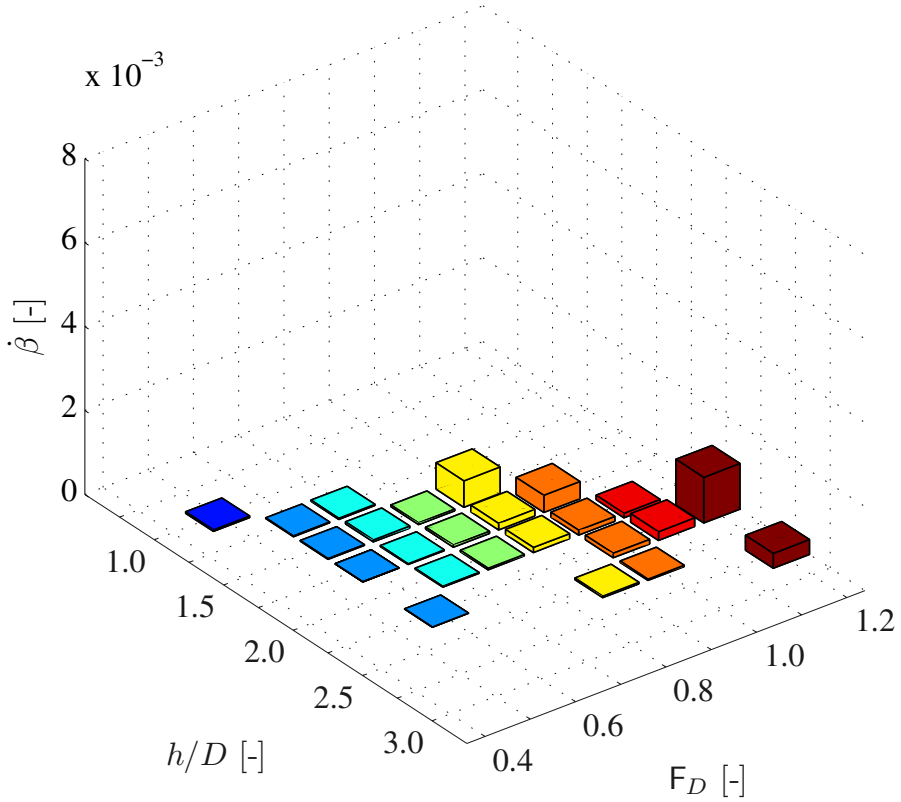

(b) air entrainment rate $\dot{\beta}$

Figure 5.3: Air entrainment at intake pipe diameter DN200, $\lambda_j = 2.55$.

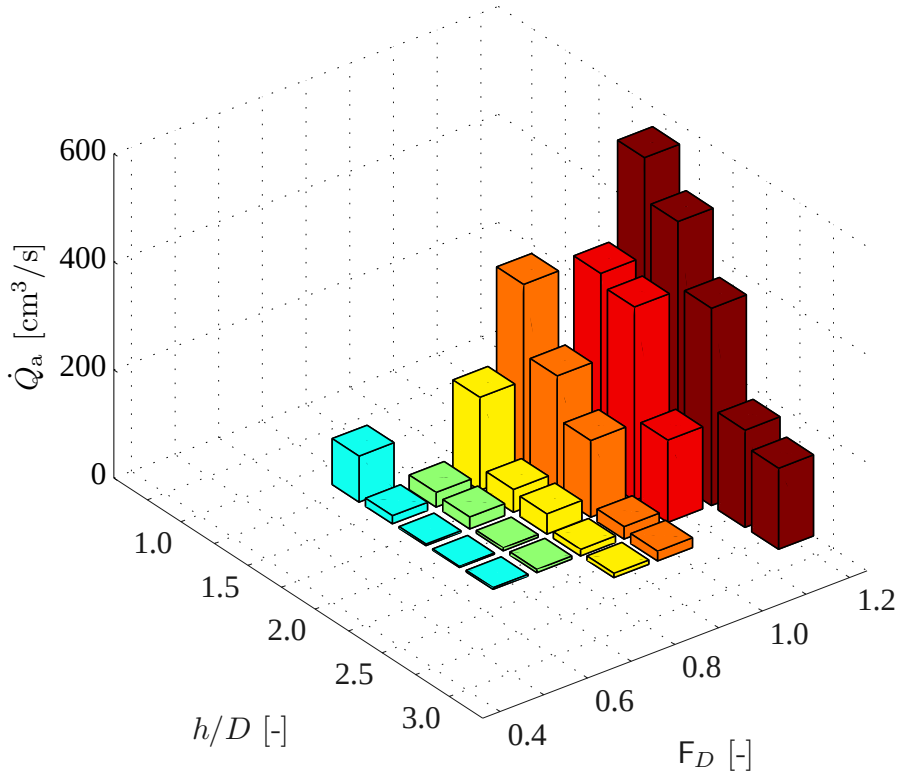

(a) air discharge $\dot{Q}_a$

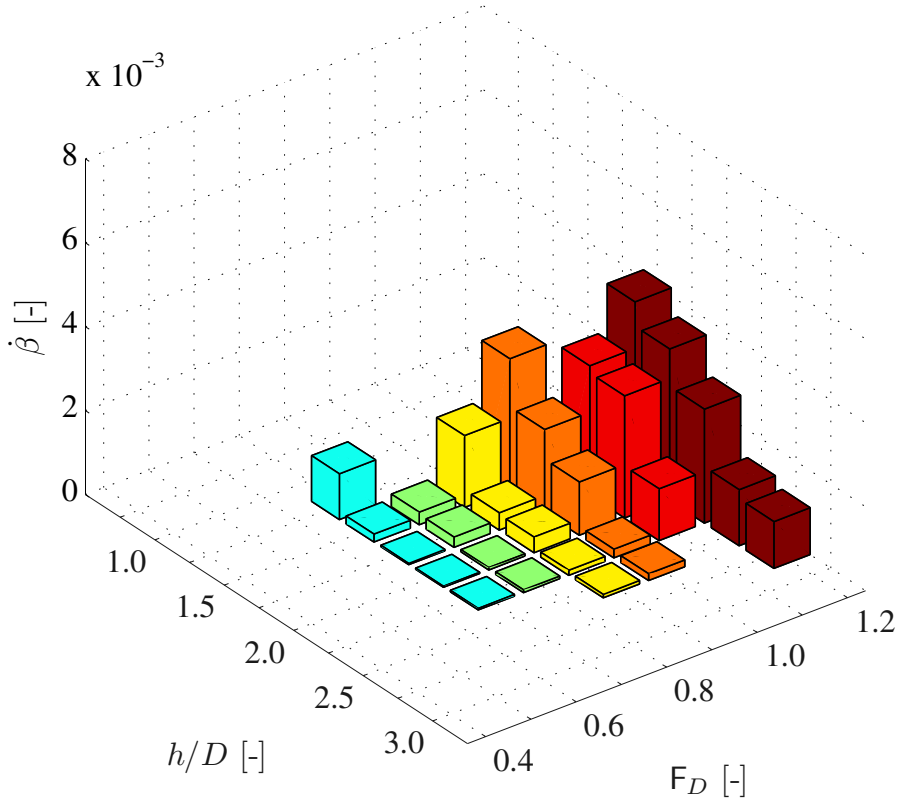

(b) air entrainment rate $\dot{\beta}$

Figure 5.4: Air entrainment at intake pipe diameter DN300, $\lambda_j = 1.66$.

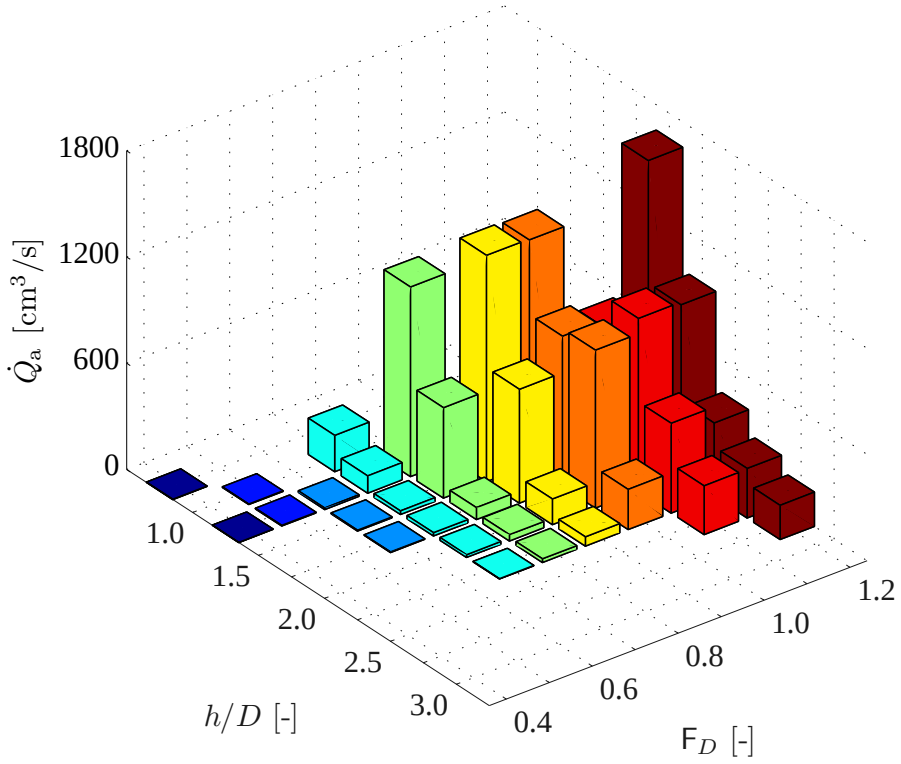

(a) air discharge $\dot{Q}_a$

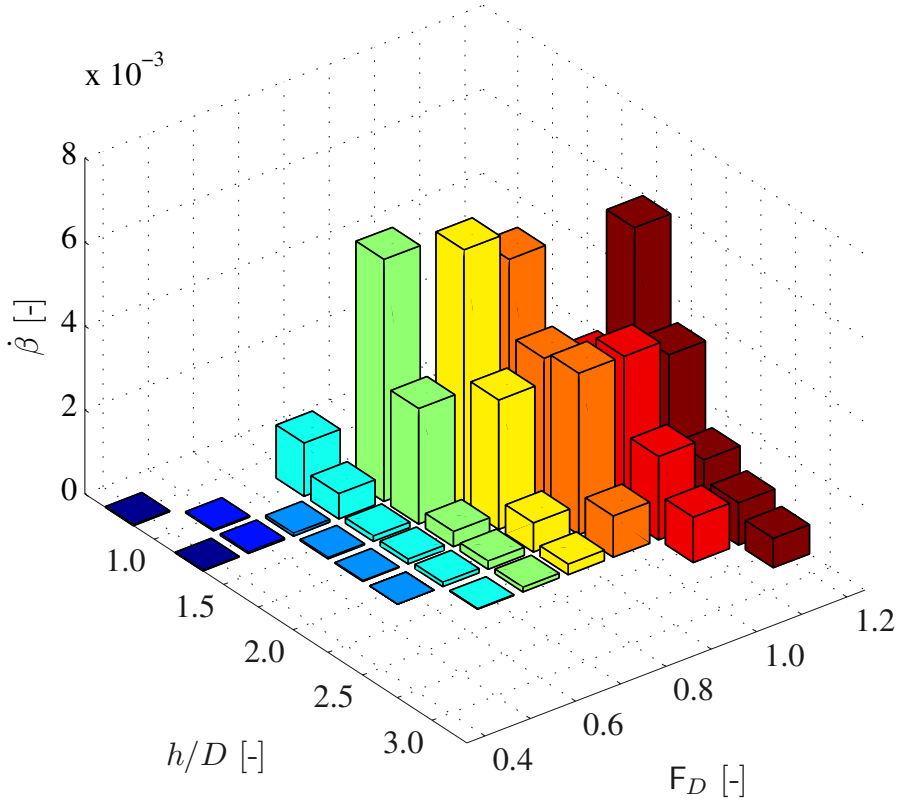

(b) air entrainment rate $\dot{\beta}$

Figure 5.5: Air entrainment at intake pipe diameter DN400, $\lambda_j = 1.24$.

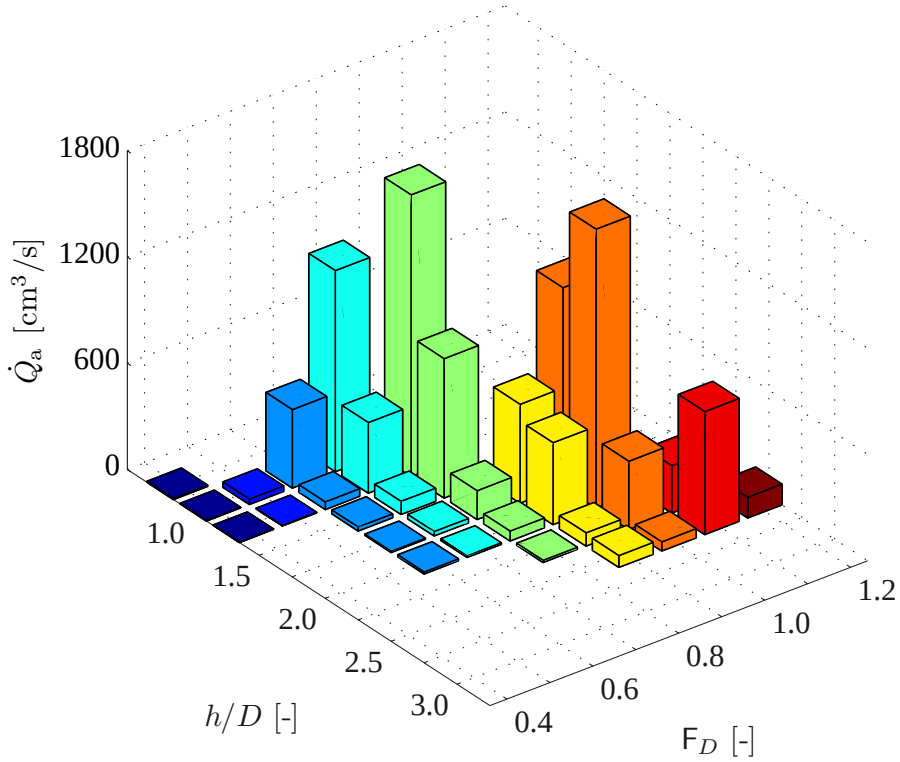

(a) air discharge $\dot{Q}_a$

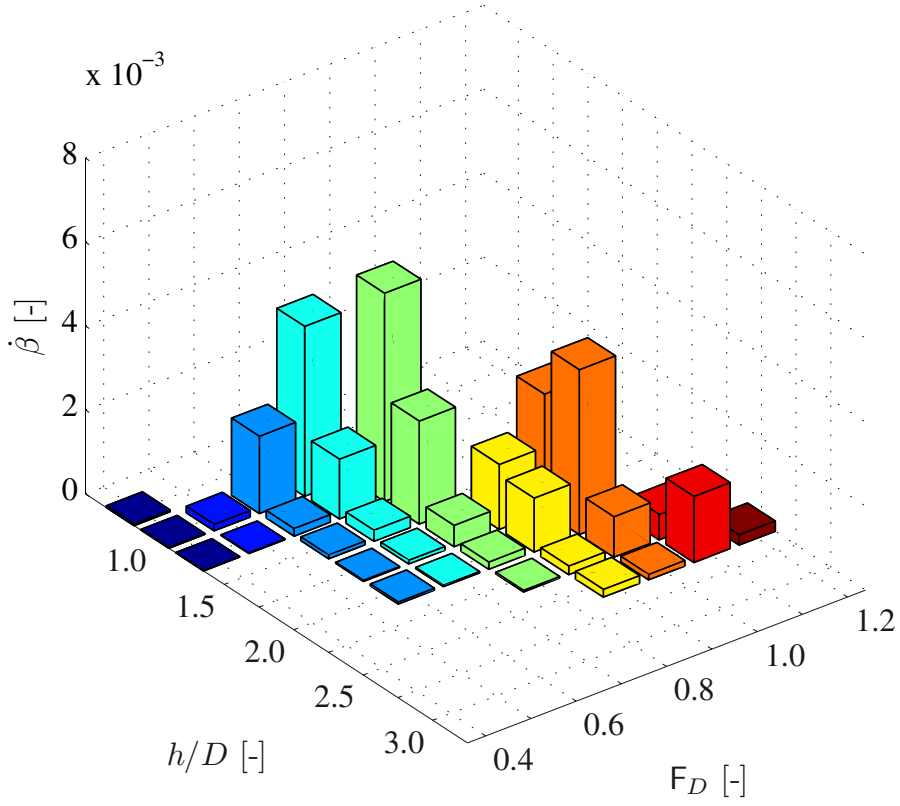

(b) air entrainment rate $\dot{\beta}$

Figure 5.6: Air entrainment at intake pipe diameter DN500, $\lambda_j = 1$.

To compare the results and to detect differences between the scales, a measured air entrainment reduction factor

$$Rf_{DNj} = \frac{\dot{\beta}_i(DN500)}{\dot{\beta}_i(DNj)} \tag{5.1}$$

is introduced to analyze possible scale effects. The variable j denotes different nominal diameter from 200 to 500 mm (scales) and the variable i indicates the measuring grid point as $f(h/D, \mathsf{F}_D)$. If air entrainment has been measured, e.g. for both DN200 and DN500, Rf_{DN200} can be determined by eq. 5.1. For $Rf_{DNj} = 1$ there are no scale effects at all, i.e. the results β_i are independent of the scale. For the comparison of all obtained results, each ratio Rf_{DNj} is calculated in reference to the largest scale of DN500. Fig. 5.7 summarizes the findings of the scale family tests. In this summary Rf-values are only determined for measuring points where air entrainment was measurable in all scales. The box plot depicts the entire set of numerical data of each scale as a group of five basic statistical numbers. The central bold line of each box gives the median. The down and top edges of the box are the inter-quartile range (IQR) from the 25^{th} to the 75^{th} percentile. The whiskers extend to the most extreme data points that are $\leq 1.5\,\mathrm{IQR}$.

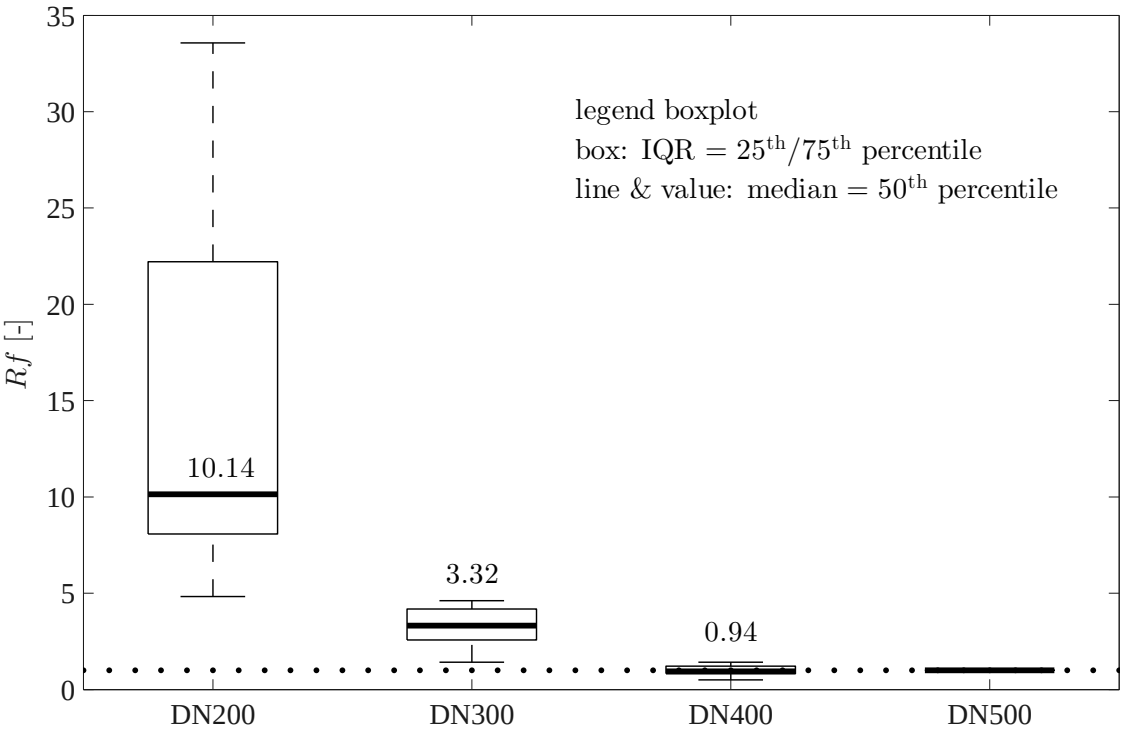

Figure 5.7: Boxplot of analyzed data of the scale family tests for the four scales DN200, DN300, DN400 and DN500. The scales λ are listed in Table 4.1.

The median of Rf_{DN200} is about 10, i.e. the non-dimensional air entrainment rate $\dot{\beta}$ is 10 times smaller than for DN500. The distribution is large and ranges from 5 to 34 Rf. Concerning the intake pipe DN300 the median of Rf_{DN300} is equal to 3.3 and distribution reaches from about 1 to 5 Rf. Thus, scale effects are still present but less intensive than for DN200. At DN400 the median of Rf_{DN400} is almost 1, thus $Rf_{\mathrm{DN400}} \approx Rf_{\mathrm{DN500}}$ holds. The scatter of Rf_{DN400} is negligibly small. In other words, the air entrainment rates match quite well for all runs with DN400, and, consequently, scale effects are insignificantly small.

5.3 Air-Core Diameter of the Four Scales

Fig. 5.8 gives histograms of the measured air core diameter d_{ac} for each of the four scales λ_j.

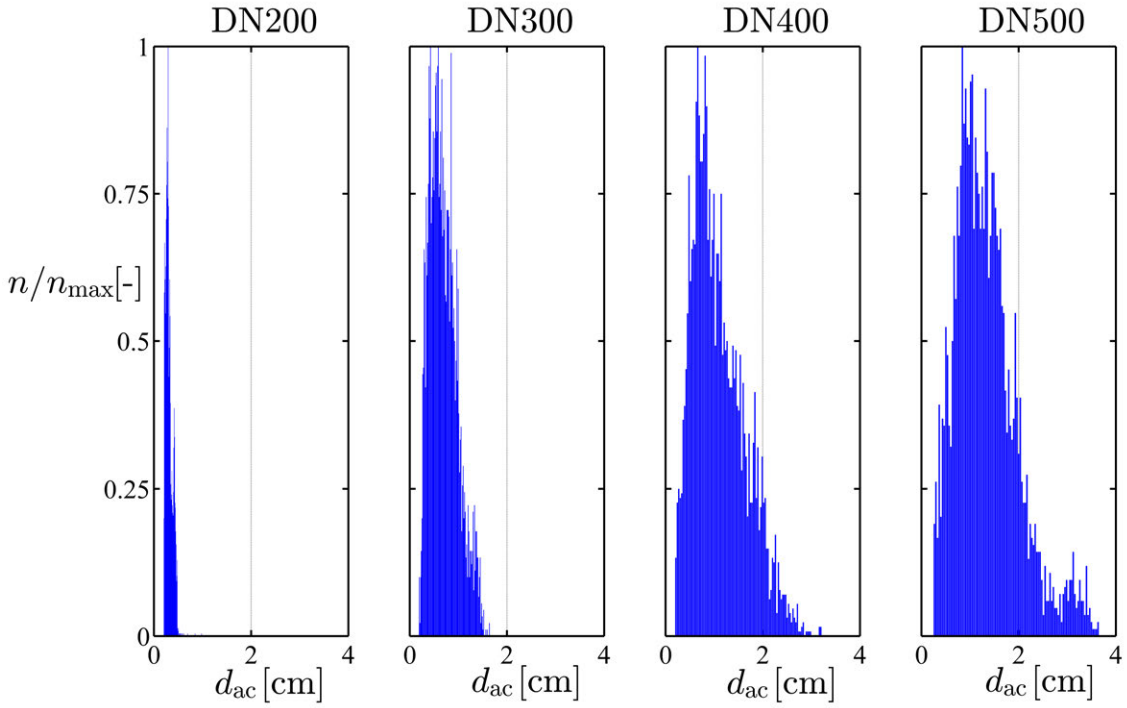

Figure 5.8: Histograms of measured air core diameters d_{ac} for the four scales λ_j. n/n_{max} is used to normalize the ordinates of each histogram.

Obviously, both the histograms of DN200 and DN300 differ from the histograms of DN400 and DN500, whereas the latter two match quite well. The median air-core diameters are $\tilde{d}_{\mathrm{ac}}$([DN200, DN300, DN400, DN500]) = [2.9, 6.7, 9.7, 12.1] mm. The different diameters are regarded to have a strong influence on the air entrainment rate. A detailed analysis concerning d_{ac} determined during the main measurement campaign and the corresponding, indirectly derived air core flow velocity v_{ac} is given in chapter 7.3.

5.4 Scale Effects and Modeling Criteria

Intake Diameter. Scale effects are prominent at the two smallest scales DN200 and DN300, although previous studies (chapter 2.3.5) stated that even much smaller limits would guarantee full scale similarity. For example, the Jain criterion (Jain et al., 1978)

$$\frac{\sqrt{\mathrm{g}D^3}}{\nu} > 5 \cdot 10^4 \,, \tag{5.2}$$

is recommended for Froude models with high Reynolds numbers where no scale effects regarding the vortex formation should occur. Rearranged to the present experimental setup a minimal intake diameter $D \geq 64$ mm is recommended. McCorquodale (1968) suggests a similar minimum intake diameter between 50 mm and 100 mm. This is eight to four times less than the DN400 found in the present study.

Viscosity. In the present study, the process of air entrainment is directly related to vortex formation. The formation, in turn, is highly influenced by the viscosity (see chapter 2.3.5). Fig. 5.9 shows the dependency of air entrainment rate $\dot{\beta}$ and Reynolds number R_D for $h/D = 1.75$. Air entrainment needs a vortex, but the strength of this vortex rules the quantity of air. The resulting air-core diameter reaches from some millimeters up to a few centimeters. For further considerations regarding scale effects the reference scale needs to be changed from the intake pipe diameter, where mainly water flows, to the air core tube diameter, with air flow. The viscosity of air is ten times higher than that of water. Thus a larger boundary layer develops, which, in turn, is responsible for larger head losses. Therefore, the pipe flow itself is assumed to influence the air entrainment rate as well. The difference in length between diameters d_{ac} and D is approximately of one order of magnitude. The difference for the flow cross-sectional areas – with respect to the continuity equation – is of two orders of magnitude.
The sub-proportional size of the air core tube of DN200 and DN300 tests is assumed to cause an over-proportional boundary layer and thus an over-proportional head loss concerning the air-core tube flow. Based on this hypothesis the observed scale effects on the air entrainment rate β are caused by viscous effects.

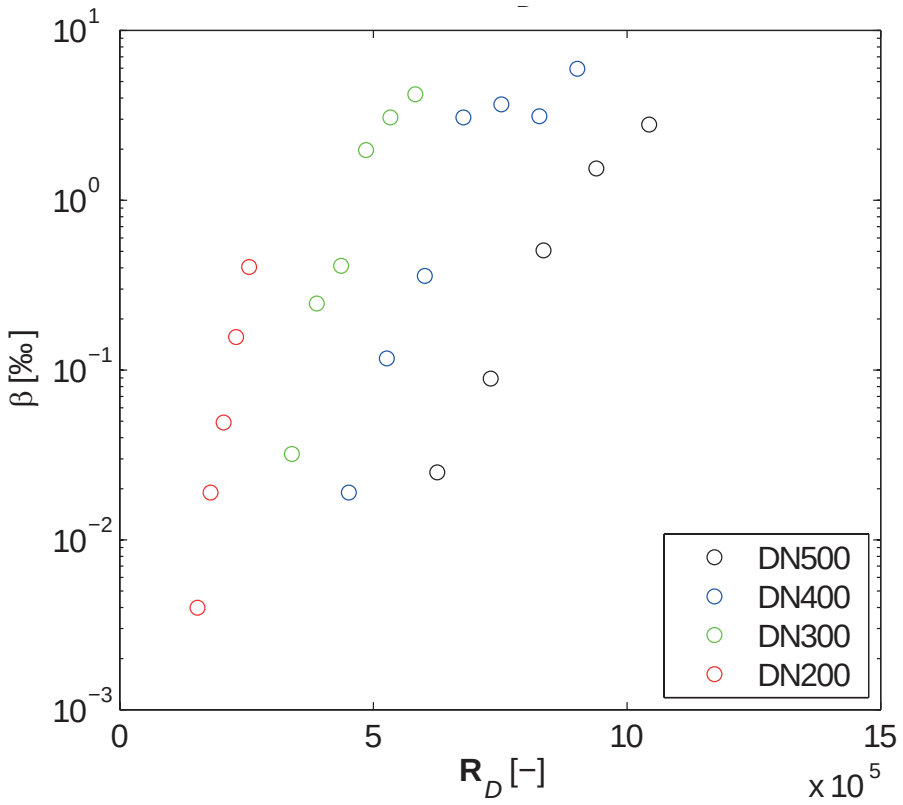

Figure 5.9: Intake Reynolds number R_D and the corresponding air entrainment rate $\dot{\beta}$ for $\mathsf{F}_D = 0.4$–1.2 and $h/D = 1.75$.

Recommendations. Large-scale physical models are necessary to determine the air entrainment of air-core vortices to cope with small scale effects at the air-core tubes with diameters of only a few millimeters. The scale family tests conducted clearly show negligible scale effects for:

- intake pipe diameters $D \geq 400$ mm
- intake Reynolds numbers $\mathsf{R}_D = v_D D/\nu \geq 6 \cdot 10^5$
- intake Weber numbers $\mathsf{W}_D^2 = \rho_\mathrm{w} v_D^2 D/\sigma_\mathrm{w} > 3200 \approx 57^2$.

Chapter 6

Results of Air Entrainment

Abstract. *This chapter presents the data analysis of the experimental campaign in which, for the first time, air entrainment due to intake-vortices has been determined quantitatively. Furthermore, the velocity field obtained by PIV is used to determine its circulation. Finally, air entrainment rates are determined and analyzed. Regression analyses are performed to derive two different approaches enabling the prediction of air entrainment rates. Based on these results, guidelines are given that enable to estimate the amount of air in a pressure system according to the hydraulic conditions at the intake.*

6.1 Air entrainment

6.1.1 General

The air entrainment rate β due to intake vortices is an important parameter for the design of pressure systems (see chapter 1.2). Within a first approach, β is analyzed regarding the standard parameters of the experimental program as given in chapter 4.7, where the quantitative description of air entrainment is structured in three parts. Part 1 considers the air discharge Q_a to be independent of the water discharge Q_w. Q_a is determined by measurements as explained in chapter 4.2. In part 2, the focus is put to the non-dimensional air entrainment rate β allowing upscaling to prototypes. Part 3 deals with the fluctuations of air entrainment.
Figs. 6.1–6.4 exemplarily show typical air entraining vortices that have been observed at the investigated load cases. The photographs have been taken at typical relative intake submergence numbers of $h/D = 1.50$ and $\mathsf{F}_D = [0.6, 0.7, 0.8, 0.9]$. Each subfigure (a) illustrates air entraining vortices from a side view to the experimental tank. Each subfigure (b) shows the according rising pipe #2 to enable a second access to estimate the amount of air qualitatively. F_D as well as the vortex strength increase from Figs. 6.1–6.4. Air entrainment starts at a low level at $\mathsf{F}_D = 0.6$ and

develops to a significant quantity as indicated by the large number of air bubbles separating from the air-core at $\mathsf{F}_D = 0.9$.

Fig. 6.5 shows the occurrence of air entraining intake-vortices within the 34 experimental runs. This parameter matrix overview of the experimental results is spanned by $\mathsf{F}_D = [0.4–1.2]$ and $h/D = [1.25–2.5]$. 34 time series results are given within this matrix (Table 4.2) and each time series is displayed by a subplot. A subplot depicts the measurement duration of two hours and indicates the occurrence of an air entraining vortex $VT6$ (Fig. 2.10) by black bars. This depiction impedes a detailed analysis of the vortex occurrence at the different load cases. However, the plots show a high presence of air entraining vortices within all runs. The diagonal band of the experimental runs in Fig. 6.5 is caused by limits of the air entrainment measurements and was determined in preliminary tests, particularly with regard to scale family tests (chapter 5). At $h/D > 2.25$ and $\mathsf{F}_D < 0.9$ no significant air entraining vortices have been observed and only a few air bubbles have been entrained, causing a negligibly small pressure increase in the rising pipes. Thus, $\beta \to 0$. At $h/D = 1.5$ and $\mathsf{F}_D = [0.85, 0.90, 0.95]$ the amount of entrained air exceeds the capacity of the de-aeration system (chapter 4.2). Air bubbles are still transported in flow direction through the horizontal pipe section (chapter 3.1). At the combined expansion and slope change the bubbles merge to bigger bubbles and finally form to an air pocket (chapter 3.5) for $h/D = 1.50$ and $\mathsf{F}_D = [0.85, 0.90, 0.95]$. Therefore, these three experimental runs have to be truncated after approximately one of hour measurement time. Exemplarily, Fig. 6.6 shows a growing air pocket at $h/D = 1.50$ and $\mathsf{F}_D = 0.9$. Its dimensions mainly increase in length. Thus, the air pocket grows against the flow direction in the horizontal pipe section. Further air is entrained continuously and merges with the present air pocket. At the end of the air pocket the air separates as bubbles to the flow again. A phenomenon akin to a classical hydraulic jump is formed, while the de-aeration is strongly influenced by this air pocket. Furthermore, the water discharge diminishes and thus the water level in the tank increases. Finally, the experimental run had to be aborted.

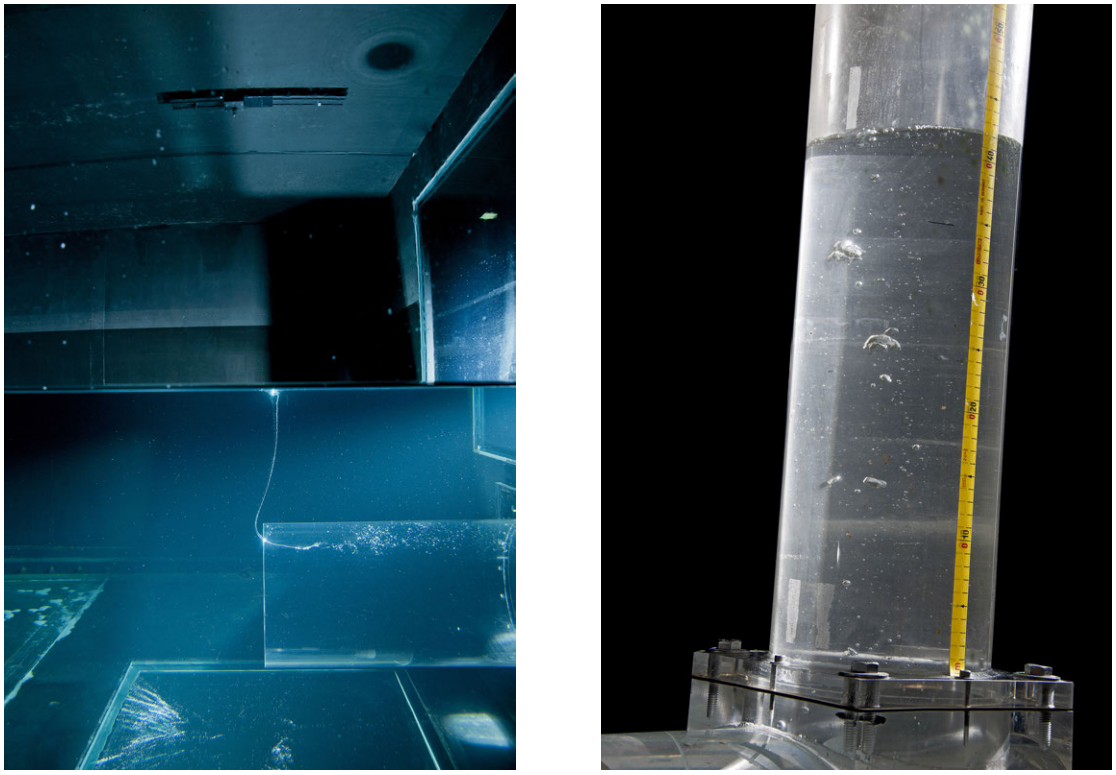

(a) Air entraining vortex (b) De-aeration at rising pipe #2

Figure 6.1: $h/D = 1.50$, $\mathsf{F}_D = 0.6$

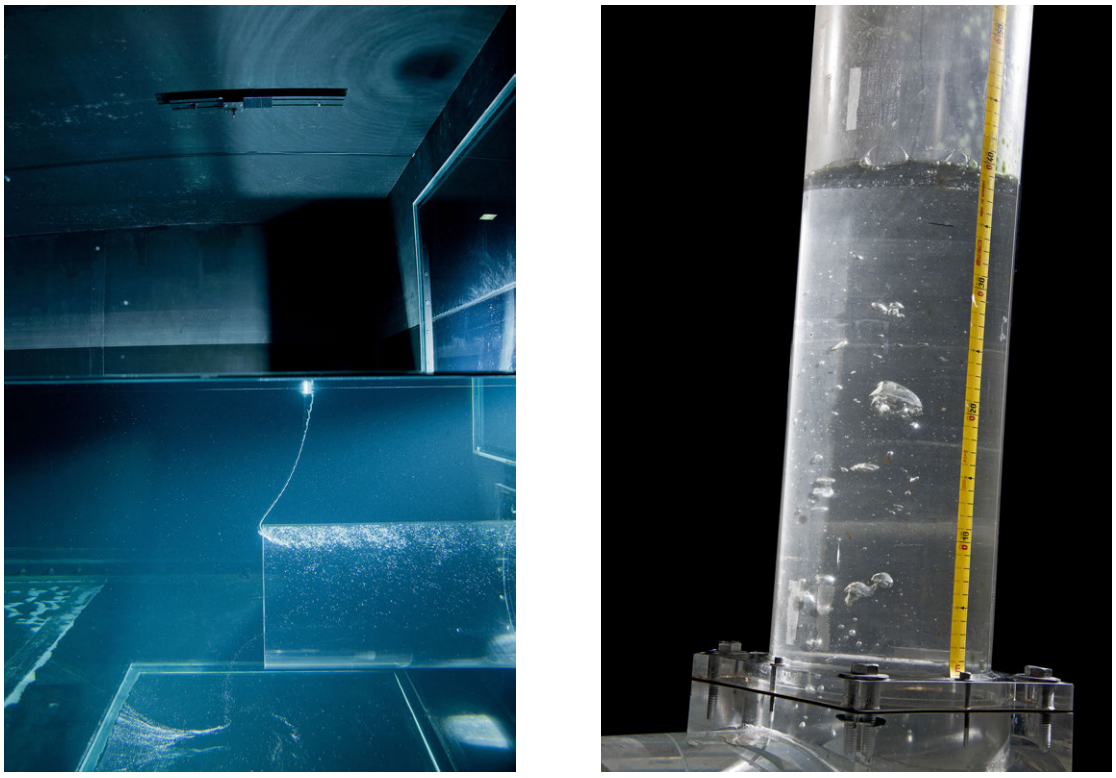

(a) Air entraining vortex (b) De-aeration at rising pipe #2

Figure 6.2: $h/D = 1.50$, $\mathsf{F}_D = 0.7$

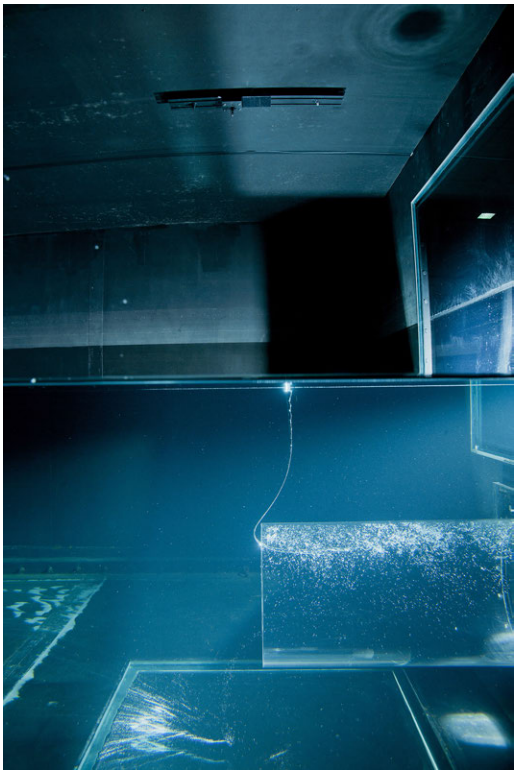

(a) Air entraining vortex

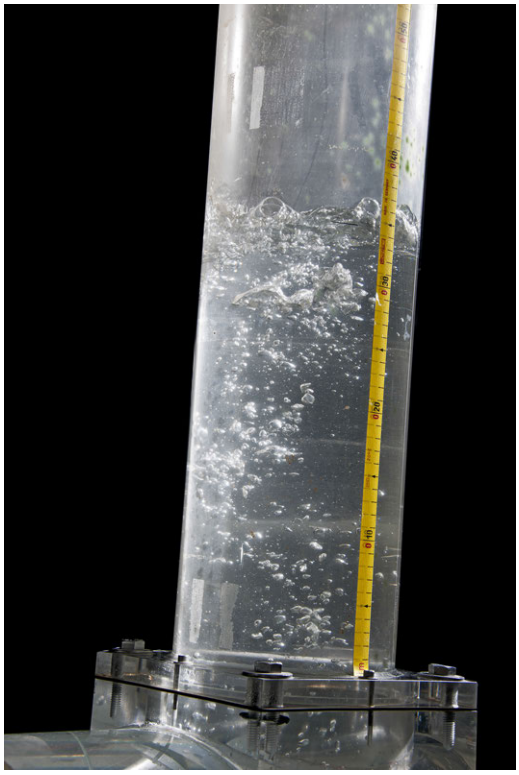

(b) De-aeration at rising pipe #2

Figure 6.3: $h/D = 1.50$, $\mathsf{F}_D = 0.8$

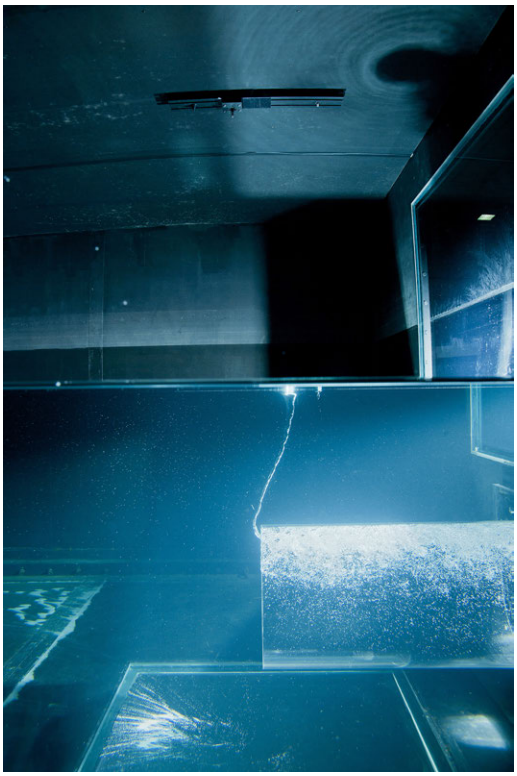

(a) Air entraining vortex

(b) De-aeration at rising pipe #2

Figure 6.4: $h/D = 1.50$, $\mathsf{F}_D = 0.9$

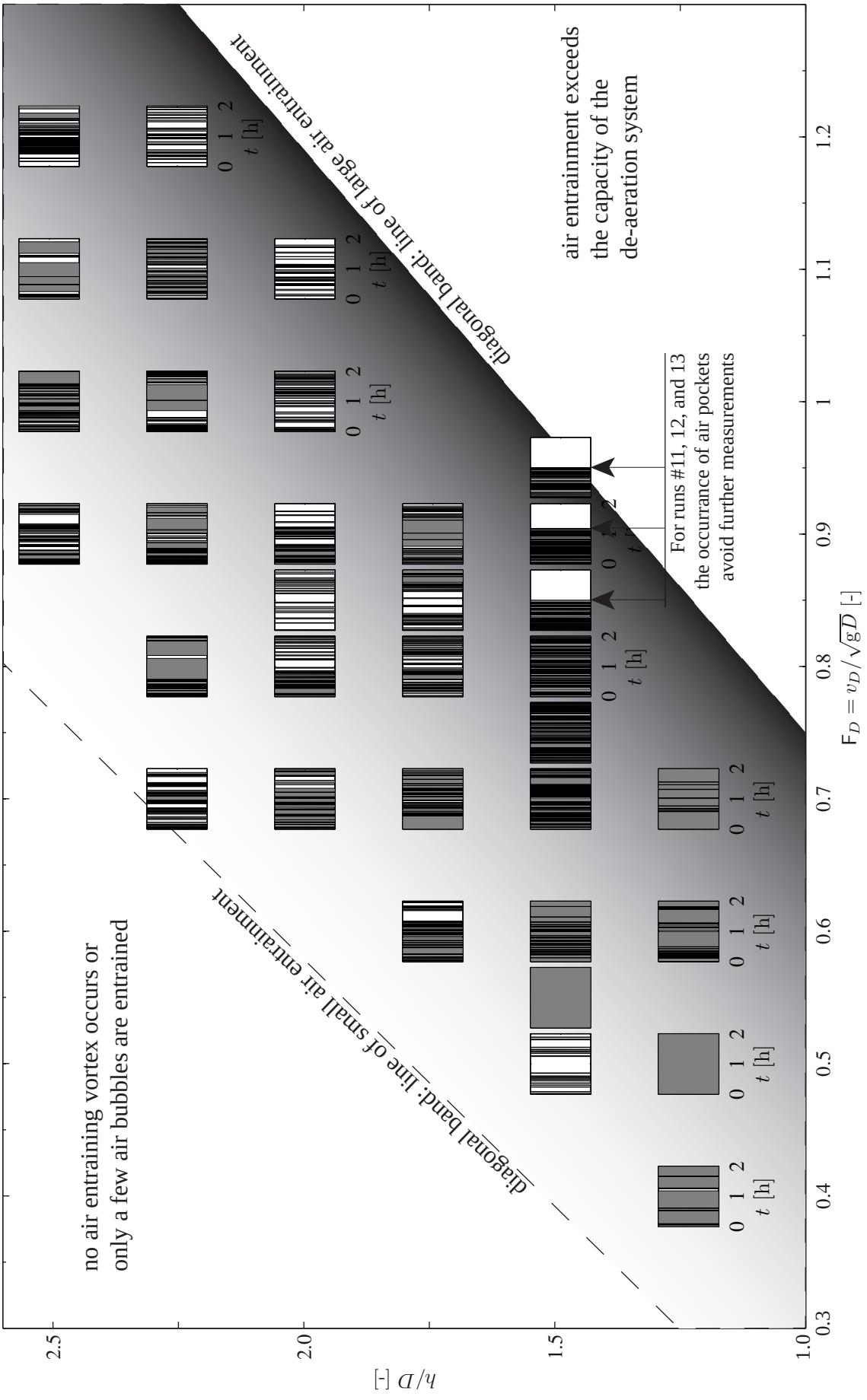

Figure 6.5: Parameter matrix with indicated qualitative air entrainment of 34 experimental runs (see Table 4.2). Each subplot shows the vortex occurrence within the measurement duration $t = 2$ h by black bars = short $VT6$, gray = constant $VT6$ and white $< VT6$.

(a) Air pocket, $t = 0$ s

(b) Increasing air pocket, $t = 120$ s

(c) Developed air pocket equals a hydraulic jump, position and size depends on Q_a, $t = 180$ s

(d) Developed air pocket equals a further developed hydraulic jump, position and size depends on Q_a, $t = 200$ s

Figure 6.6: Development of an air pocket at the slope change (see Fig. 3.1).

6.1.2 Air Discharge Q_a

Definition. The vortex-induced air discharge Q_a is determined by pressure measurements in the rising pipes. The measurement duration was chosen to two hours and the measurement frequency is 1 Hz (see chapter 3.3). The procedure is explained in chapter 4.2. Fig. 6.7 depicts an example of recorded pressure signals within a measurement time $\Delta t = 200$ s. The pressure signal shows some misleading peaks. These peaks are eliminated by using the detrend function of MATLAB. A least-squares data fit of a straight line is computed and afterwards subtracted. The result is a continuous pressure signal. Furthermore, Fig. 6.7 gives the pressure signal smoothed by a moving average with a window length of 30 s and the piecewise median on a window length of 30 s. However, the latter smoothing technique does not have an adequate performance, whereas the difference between the moving average and the detrended signal are small. But occasionally, negative pressure gradients are produced by the moving average method. Finally, Q_a is determined based on the detrended pressure curve.

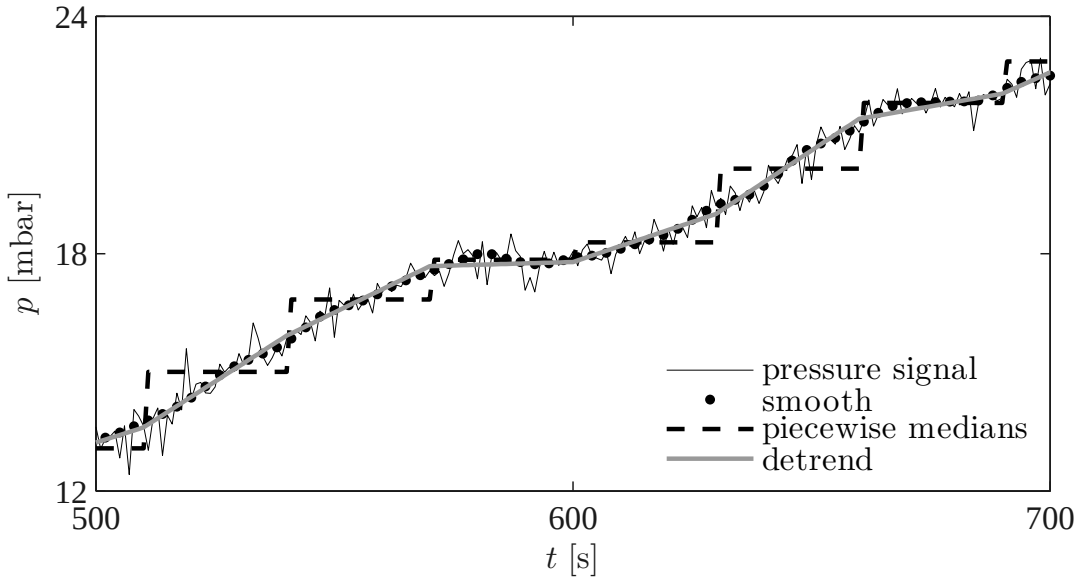

Figure 6.7: Methods used to filter the pressure signal to get a continuous pressure gradient (Bühlmann, 2012).

Next, a definition is given regarding the occurrence of an air-entraining vortex of type $VT6$ and its corresponding entrained Q_a. This definition is a prerequisite to be able to separate and to analyze large air entrainment within an experimental run. A constant phase of air entrainment is defined by three criteria here: (1) $VT6$ must be present for at least 95 % of the phase. (2) The duration is ≥ 600 s, and (3) the vortex interruption duration is < 60 s. In the following, vortex phases are indicated by the index j. Consequently, vortex phases are parts of an experimental run with different, variable durations.

Determination and Analysis of Q_a for selective Experimental Runs.
Figs. 6.8–6.11 present time series of measured Q_a for four exemplary experimental runs at $h/D = 1.5$ and $\mathsf{F}_D = [0.6, 0.7, 0.8, 0.9]$. Each plot contains three subplots. The uppermost subplot illustrates the occurrence of an air entraining vortex by bars, where white corresponds to vortex types $< VT6$, gray denotes $VT6$, and black is used to depict short phases of $VT6$. The middle subplot gives the actual $Q_{a,i}$ for t_i = 1–7200 s (0–2 h) and the median vortex phase related $Q_{a,j}$ is marked by a circle. A vortex phase consists of a variable number n of $Q_{a,i}$ and is generally determined by:

$$Q_{a,j} = \begin{cases} Q_{a,\frac{n+1}{2}} & n \text{ odd} \\ \frac{1}{2}\left(Q_{a,\frac{n}{2}} + Q_{a,\frac{n}{2}+1}\right) & n \text{ even.} \end{cases} \tag{6.1}$$

Thus, $Q_{a,j}$ denotes the median air discharge during a vortex phase. Furthermore, the lower subplots visualize the progress of the running average $\hat{Q}_{a,i}$, that is determined by

$$\hat{Q}_{a,i} = \frac{\sum_{i=1}^{n_i} Q_{a,i}}{n_i} \ . \tag{6.2}$$

The increasing sum of $Q_{a,i}$ is averaged by a likewise increasing time window where $t_i = n_i$ = 1–7200 s.
Fig. 6.8 refers to experimental run #7 (Table 4.2). According to the diagonal band of air entrainment in Fig. 6.5, the air entrainment of this run is rather small. A vortex $VT6$ occurs within 88 % of the measurement duration with a more or less periodical behavior. The fluctuation pattern of Q_a is nearly repetitive. (Note: A frequency analysis will be given in chapter 6.1.4). $Q_{a,i}$ reaches values up to 36 cm^3/s. $\hat{Q}_{a,i}$ shows an asympthotic behavior towards 4 cm^3/s.
Figs. 6.9–6.11 present similar analysis plots as Fig. 6.8. Here, vortices of type $VT6$ occur in experimental runs #[8, 10, 12] by [71, 64, 61] % of the measuring duration of two hours. They reach $\max(Q_{a,i})$ = [52, 220, 550] cm^3/s.
Note that run #12 had to be aborted after a little bit more than one hour. At this time a growing air pocket (compare Fig. 6.6) impeded the measurements (see chapter 4.2). However, experimental runs with growing air pockets, i.e. #[11, 12, 13] (also marked in Fig. 6.5), are used within the analysis shown below. Here, the statistics are exceptionally derived from experiments with one hour duration only.
Figs. 6.8–6.11 have shown characteristic time series of Q_a for a single $h/D = 1.50$. The characteristic time series parallel to the diagonal band as indicated in Fig. 6.5 are given in appendix A, where Figs. A.1–A.6 show time series of experimental runs #[3, 8, 16, 22, 28, 33] (compare Table 4.2).

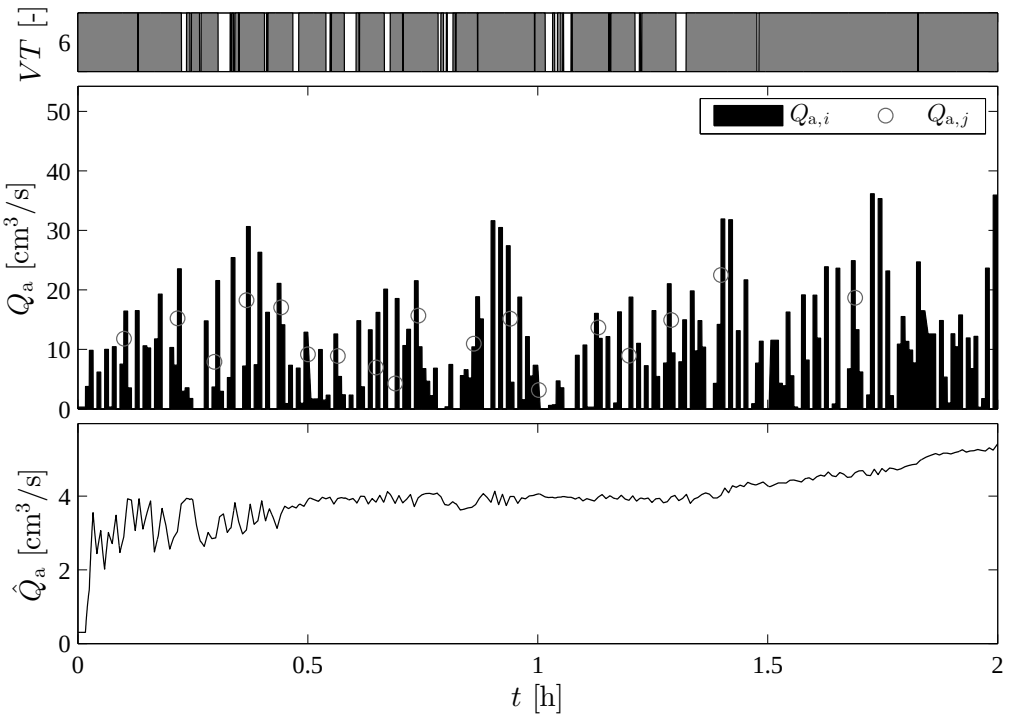

Figure 6.8: Time series of vortex types VT, actual air discharge $Q_{\mathrm{a},i}$ and $VT6$ phase average $Q_{\mathrm{a},j}$, and running average $\hat{Q}_{\mathrm{a},i}$ for run #7 ($h/D = 1.5$, $\mathsf{F}_D = 0.6$, see Table 4.2).

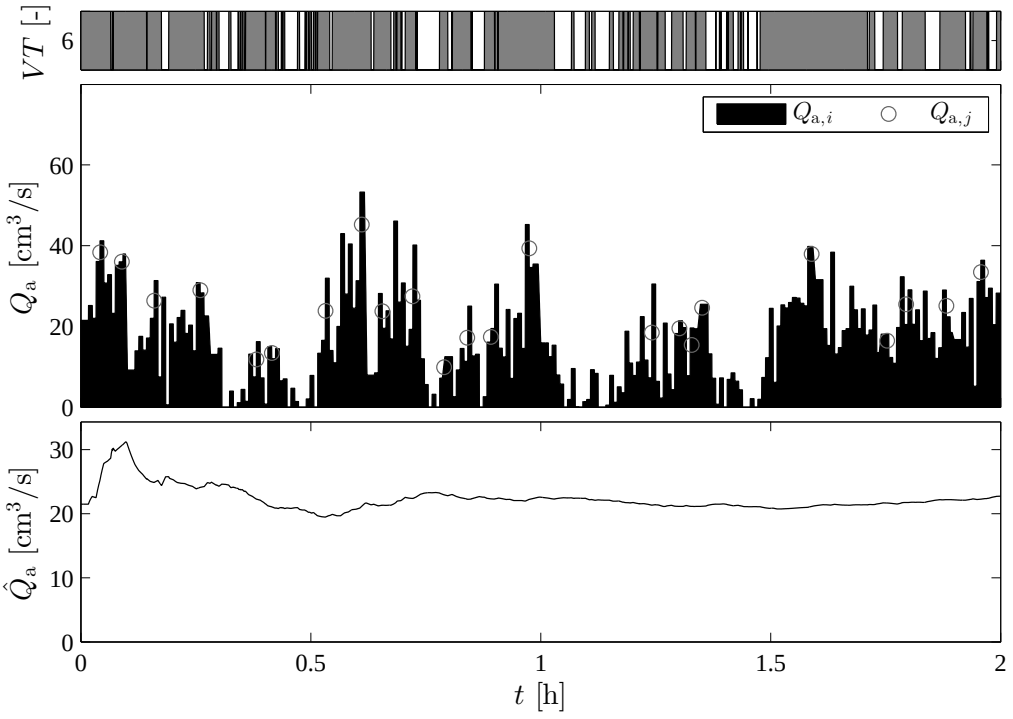

Figure 6.9: Time series of vortex types VT, actual air discharge $Q_{\mathrm{a},i}$ and $VT6$ phase average $Q_{\mathrm{a},j}$, and running average $\hat{Q}_{\mathrm{a},i}$ for run #8 ($h/D = 1.5$, $\mathsf{F}_D = 0.7$, see Table 4.2).

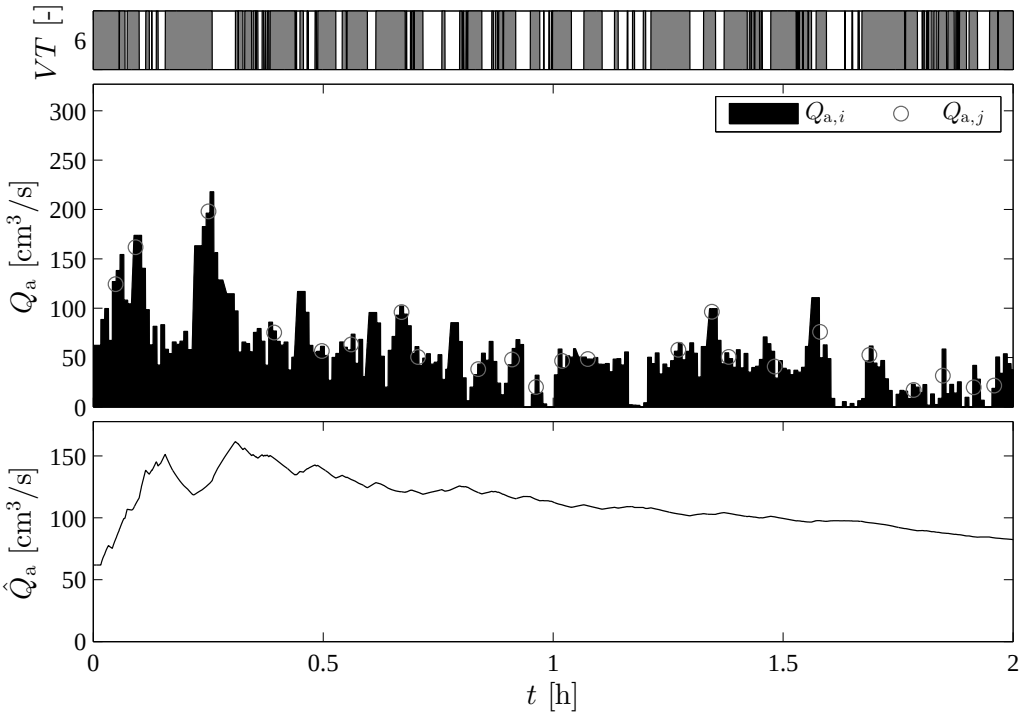

Figure 6.10: Time series of vortex types VT, actual air discharge $Q_{\mathrm{a},i}$ and $VT6$ phase average $Q_{\mathrm{a},j}$, and running average $\hat{Q}_{\mathrm{a},i}$ for run #10 ($h/D = 1.5$, $\mathsf{F}_D = 0.8$, see Table 4.2).

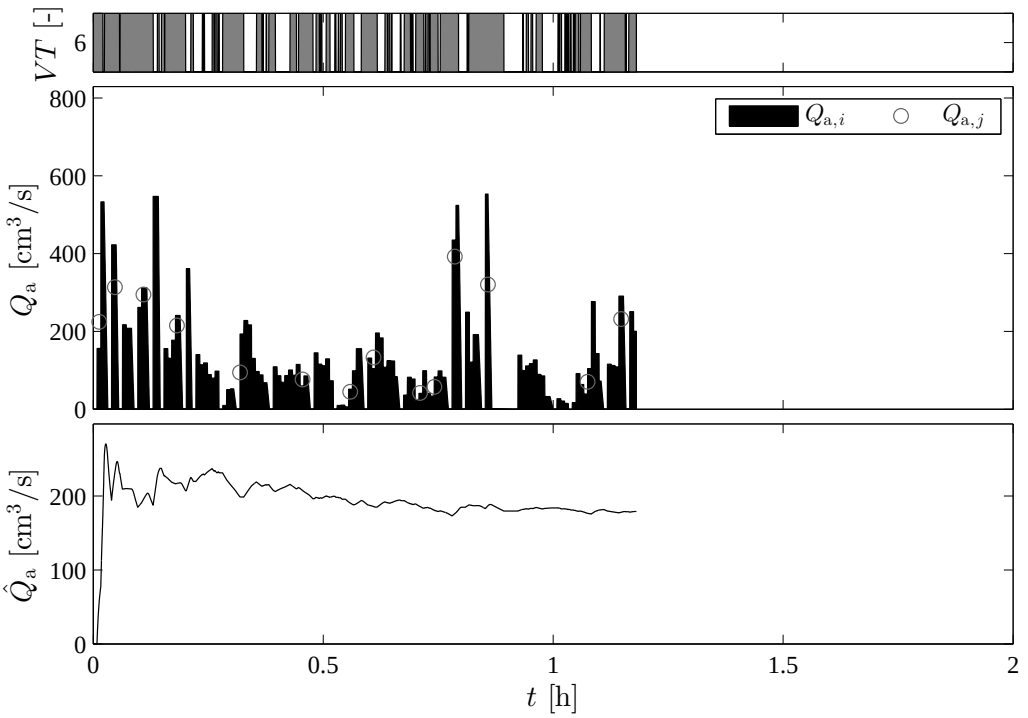

Figure 6.11: Time series of vortex types VT, actual air discharge $Q_{\mathrm{a},i}$ and $VT6$ phase average $Q_{\mathrm{a},j}$, and running average $\hat{Q}_{\mathrm{a},i}$ for run #12 ($h/D = 1.5$, $\mathsf{F}_D = 0.9$, see Table 4.2).

Determination and Analysis of Q_a for all Experimental Runs. The results of all 34 experimental runs have been determined and analyzed statistically. Two average values are used to characterize the measured air entrainment: $\bar{Q}_\mathrm{a}$ gives a characteristic mean value related to the air entrainment and $\check{Q}_\mathrm{a}$ denotes a characteristic maximum value[1] related to the vortex phases. Their definitions read:

$$\bar{Q}_\mathrm{a} = \frac{\sum_{1}^{n_{VT6}} Q_{\mathrm{a},\,i,VT6}}{n_{VT6}} \tag{6.3a}$$

$$\check{Q}_\mathrm{a} = \frac{\sum_{1}^{n_j} Q_{\mathrm{a},\,j}}{n_j}\,. \tag{6.3b}$$

In Fig. 6.12 the air discharge is plotted against the mean water discharge $\bar{Q}_\mathrm{w}$ for all 34 experimental runs. Fig. 6.12a gives the mean values $\bar{Q}_\mathrm{a}$ and Fig. 6.12b gives the mean of the vortex phases $\check{Q}_\mathrm{a}$. The trend of $\bar{Q}_\mathrm{a}$ and $\check{Q}_\mathrm{a}$ is quite similar, but the scale of the y-axis of the former is 2.5 times higher.

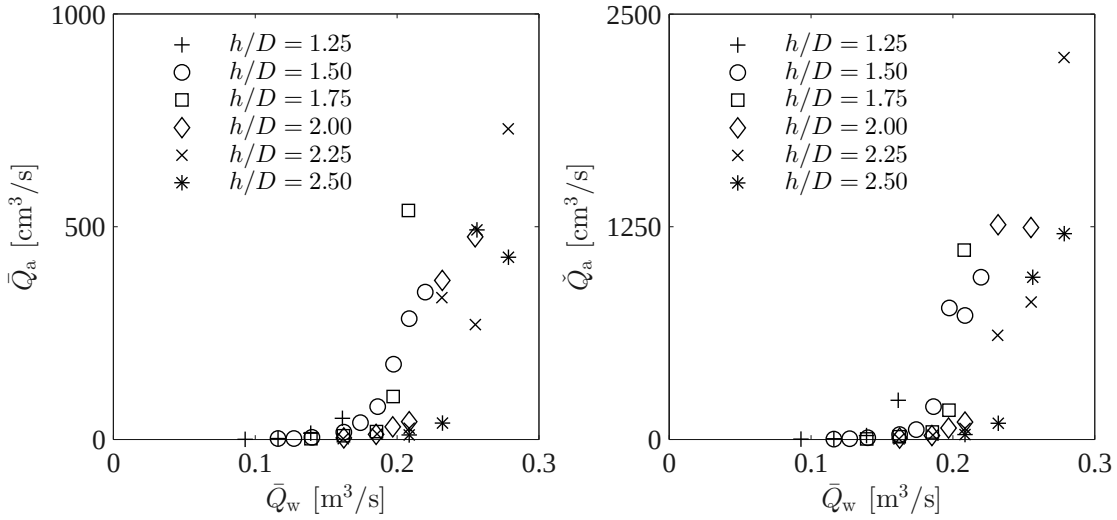

(a) Mean air discharge

(b) Mean air discharge of the vortex phases

Figure 6.12: Mean air discharges vs. water discharge $\bar{Q}_\mathrm{w}$ of the 34 experimental runs.

In Fig. 6.13 a combination of all h/D is given by plotting $\bar{Q}_\mathrm{a}$ and $\check{Q}_\mathrm{a}$ against $\bar{Q}_\mathrm{w}/\sqrt{h/D}$. The exponential trend becomes clearly obvious. By applying a regression analysis with robust least squares fit[2] the following relationship can be

[1]The characteristic maximum value equals not the maximum of an experimental run. Instead it is a two times averaged value, first within the vortex phase and second over all vortex phases average values in an experimental run. This value is related to the vortex phases where high air discharge is measured and is therefore called characteristic maximum.

[2]Robust least squares fitting is non-linear. It is assumed that the response errors follow a normal distribution, and that extreme values are rare. Extreme values or outliers are less weighted.

found:

$$\bar{Q}_\mathrm{a} = 0.005\, e^{64\bar{Q}_\mathrm{w}/\sqrt{h/D}} \quad \text{and} \tag{6.4a}$$

$$\check{Q}_\mathrm{a} = 0.003\, e^{72\bar{Q}_\mathrm{w}/\sqrt{h/D}}\,, \tag{6.4b}$$

with $\mathrm{R}^2 = 0.97$ and $\mathrm{R}^2 = 0.98$, respectively. The high coefficients of determination R^2 indicate a clear dependency of the inserted parameters.

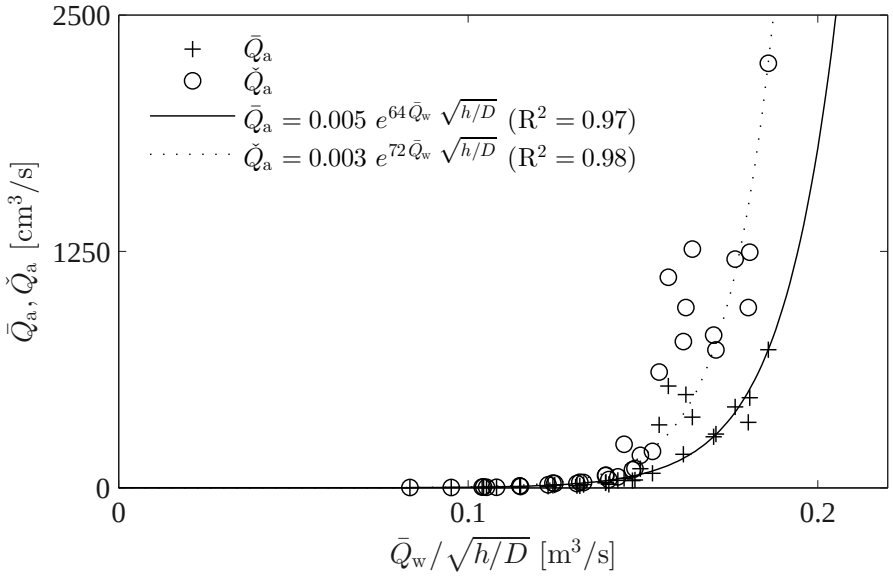

Figure 6.13: Mean air discharge $\bar{Q}_\mathrm{a}$ and mean air discharge $\check{Q}_\mathrm{a}$ for all h/D, versus $\bar{Q}_\mathrm{w}/\sqrt{h/D}$.

The results of air discharge Q_a averaged for the experimental runs, using different criteria, show a good correlation between the three parameters Q_w and h/D. Therefore, the physical air entrainment is seen to be determined. The air entrainment rate β is the ratio of Q_a and Q_w. This dimensionless parameter is discussed in relation to h/D in the next section.

6.1.3 Air Entrainment Rate β

The maximum detected air entrainment rate of $\check{\beta} = \check{Q}_\mathrm{a}/\bar{Q}_\mathrm{w} = 0.81\,\%$ was measured at $h/D = 2.25$ and $\mathsf{F}_D = 1.2$ (run #30, see Table 4.2). However, by visual observation, the white water in the pressure pipe is expected to give even higher rates. Compared to the published air entrainment rates as listed in Table 2.2, the indications of Hattersley (1965) are in the same range, whereas the indications from Iversen (1953), Denny & Young (1957), and Padmanabhan (1984) are about one order of magnitude higher. Fig. 2.39 shows the air entrainment rate after Iversen (1953) at $D_\mathrm{Prototype} = 464$ mm and $Q_\mathrm{w,\,Prototype} = 164$ l/s. The air entrainment

rate (air to water ratio-%[3]) generally approaches zero at h/D >1–1.2. The h/D-range in this research project are $1.25 \leq h/D \leq 2.5$, except for the scale family tests which were conducted in a range of $0.75 \leq h/D \leq 3.0$. The lowest setup of Fig. 2.39 is slightly comparable with the setup used in this research project and gives $\beta \approx 6.25 \cdot 10^{-4}$ at $h/D = 0.75$. Scale family test results give $\dot{\beta}$(DN500)$= 0.43 \cdot 10^{-4}$ and $\dot{\beta}$(DN400)$= 0.22 \cdot 10^{-4}$. These values are 15–30 times smaller. A reasonable comparison based on one data point is not feasable. Most data points of Padmanabhan (1984) are in the range $\beta < 1\,\%$ (Fig. 2.40), what confirms the present results better. Incipient air entrainment starts at about $0.4\,\mathsf{F}_D$ (Fig. 6.14) which is also in good agreement with Padmanabhan (1984). Another accordance can be found to Padmanabhan (1984), where air entrainment starts slightly below $0.4\,\mathsf{F}_{\mathrm{co}}$ as well (see chapter 6.3).

Originally, the experimental runs have been performed by following a parameter matrix spanned via F_D and h/D. In Fig. 6.14

$$\bar{\beta} = \frac{\bar{Q}_{\mathrm{a}}}{\bar{Q}_{\mathrm{w}}} \tag{6.5a}$$

$$\text{and } \check{\beta} = \frac{\check{Q}_{\mathrm{a}}}{\bar{Q}_{\mathrm{w}}} \tag{6.5b}$$

are plotted against the intake Froude number F_D in a similar manner as in Fig. 6.12.

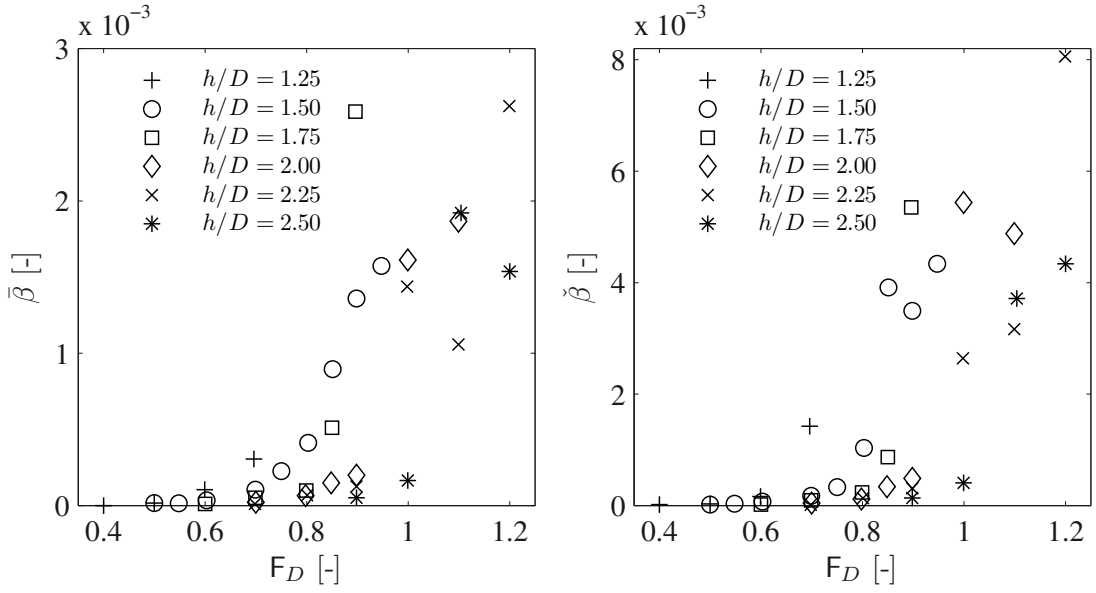

(a) Mean air entrainment rate

(b) Mean air entrainment rate of singular vortex phases

Figure 6.14: Mean air entrainment rates of the 34 experimental runs.

[3]It is assumed that the indication of "%" is incorrect, otherwise the values have to be divided by 100.

The air entrainment rate β of the measured intake-vortices is analyzed in detail in chapter 6.3 for a combination of the parameters F_D and h/D. Furthermore, a similar analysis is performed in chapter 6.4 for parameters that are related to the rotating flow field.

6.1.4 Air Entrainment Fluctuations

In the following the fluctuations of air entrainment are analyzed regarding two aims. The first aim is to be able to determine an appropriate mean air entrainment rate β that accounts for the frequency and the amount of entrained air adequately. The second aim is to understand the characteristics of formation and decay of a vortex in an unsteady or periodical manner.
Fluctuations of the vortex types have been described already by Durgin & Hecker (1978) and Hecker (1987) (see chapter 2.3.4). They used the recorded vortex types to assess an intake design. In this research project the vortex type box is used to record the fluctuations (see chapter 3.3). The investigation of air entrainment due to vortices implies a large vortex strength, i.e. $VT6$. Within the investigated parameter range the speed of vortex formation is quite high and a differentiation between $VT0$ and $VT6$ was omitted. Instead a binary signal $VT0/VT6$ is recorded. During preliminary tests at the incipient of air entrainment it was possible to record the entire range of vortex types.
A first analysis of vortex duration as shown in Fig. 6.5 did not show any coherence at all. To analyze the data for a possible periodicity of air entrainment a frequency analysis was carried out. Fig. 6.15 shows the power spectra of air-entraining intake-vortices within the 34 experimental runs. This parameter matrix overview of the experimental results is spanned by $\mathsf{F}_D = [0.4\text{–}1.2]$ and $h/D = [1.25\text{–}2.5]$. 34 time series are analyzed and given in this matrix (Table 4.2), while each time series is displayed by a subplot. Each subplot depicts the frequency on the horizontal axis and the related duration of the vortex presence on the vertical axis. Typically, power spectra of these kind are used to analyze distinctive peaks of energy in a time series by showing the amplitude squared on the vertical axis. Here, the vortex duration gives a proxy of energy. Thus dominating frequencies would become obvious by distinctive peaks in the spectra – in case they were present. However, as can be seen in the subplots, no distinct frequency could be isolated clearly. The maximum occur at a recurrence period of $\gg 10^2$ s with increasing tendency to 10^3 s, indicating that the process of vortex generation and its recurrence could not be analyzed adequately within the standardized measurement duration of two hours. Vice versa, from a recurrence period of $< 10^2$ s, the dominance is decreasing logarithmically. More detailed findings with respect to dominating frequencies of air-entraining vortices could not be given.

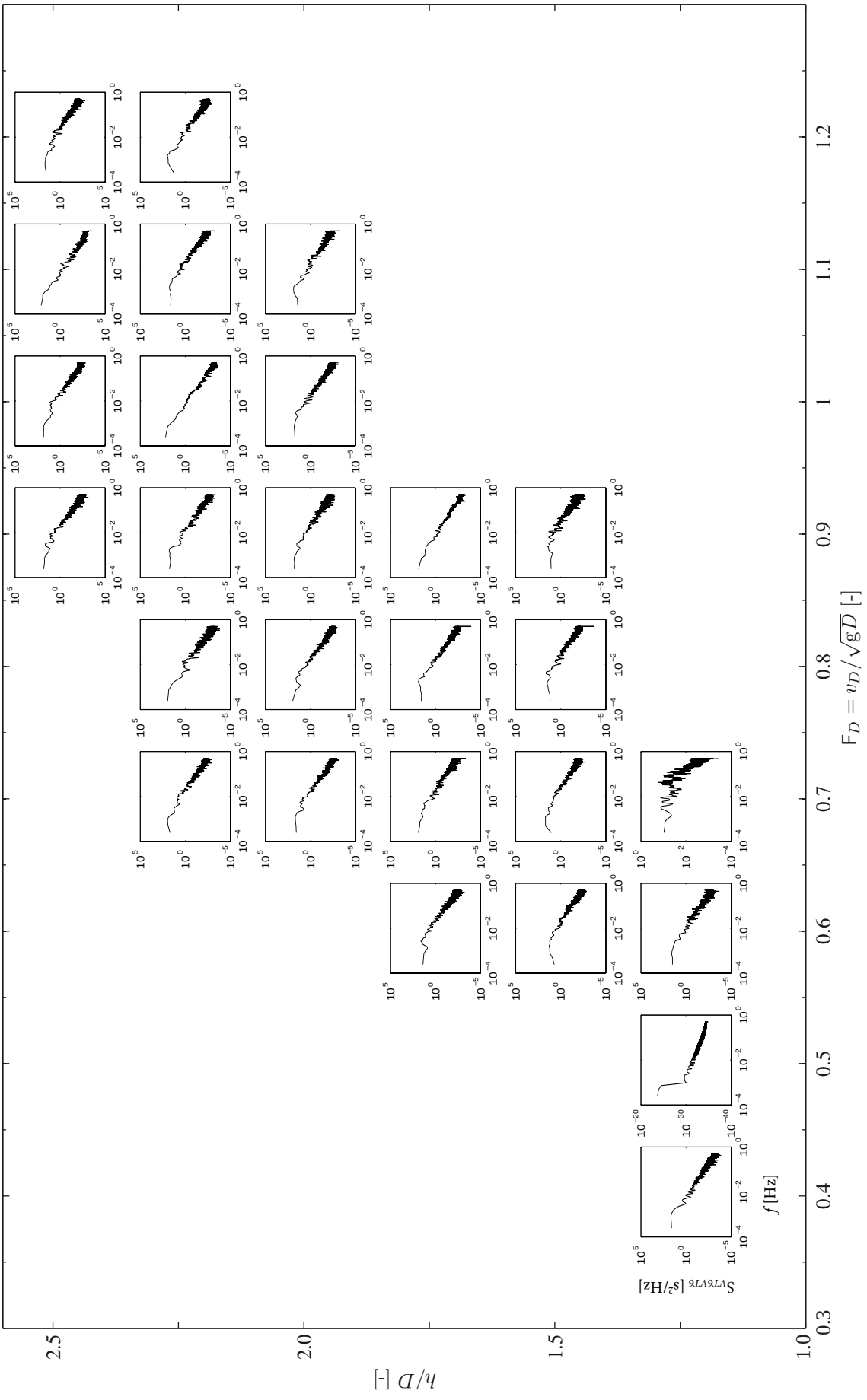

Figure 6.15: Parameter matrix with frequency analysis of air entrainment of each 34 experimental runs (see Table 4.2).

6.2 Circulation Γ

6.2.1 Horizontal Velocity Field of the Vortex

The horizontal velocity field of the vortex in a horizontal plane has been measured by means of a 2D PIV system as explained in chapters 3.4 and 4.3. The image size at the measurement plane is approximately 1×1 m^2 (see Table 4.2). Fig. 6.16 shows an exemplary velocity field. This is a section of the PIV image which is specified for a PIV run based on an optimization between the vortex wandering (see chapter 8.1) and the calculation speed of the PIV processing. The vectors visualize the direction in the 2D plane and the velocity magnitude v_{MAG} by their arrow lengths. The contour plot in the background depicts the velocity magnitude v_{MAG}. Further examples are given in appendix B, where Fig. B.1 and Fig. B.2 show the subsequent next three time steps of the velocity field from Fig. 6.16.

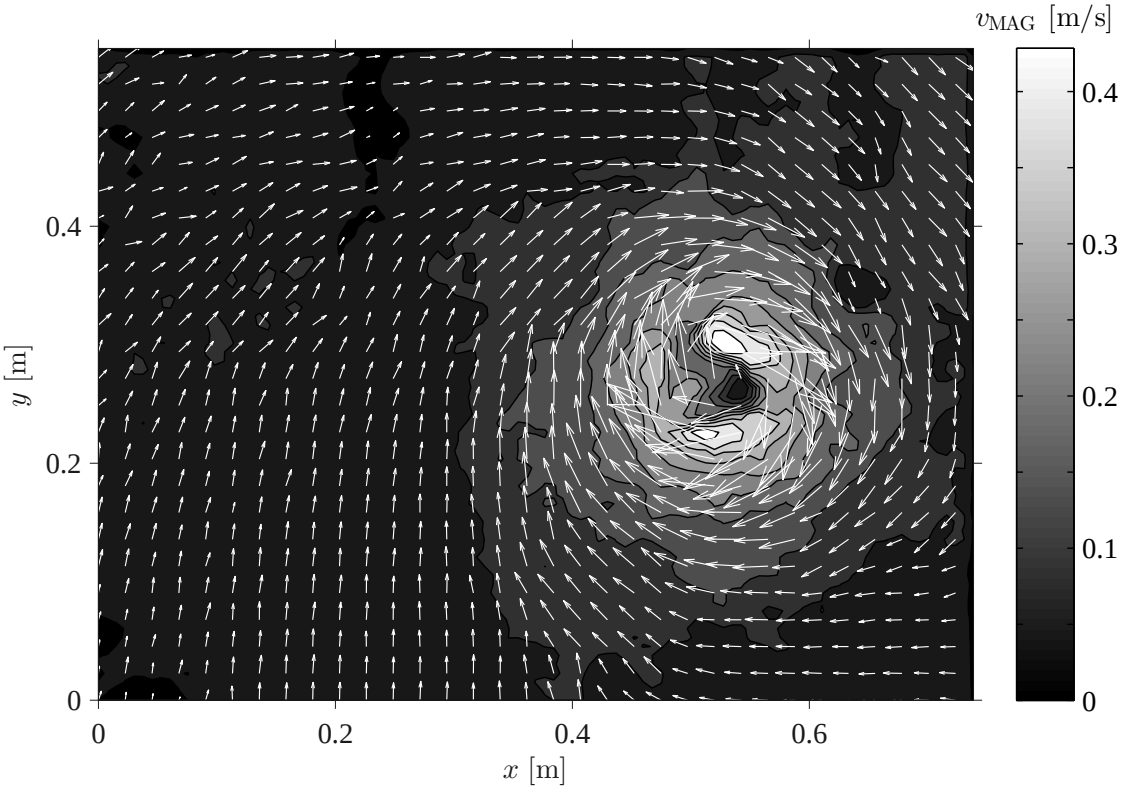

Figure 6.16: Bottom upwards view to the velocity field of an intake vortex (run #8.13.1).

In the following subsections the horizontal velocity field surrounding an intake-vortex is analyzed to determine the circulation Γ.

6.2.2 Circulation of Exemplary Experimental Runs

The circulation Γ of the intake-vortices is determined via the horizontal velocity fields as gained by 2D PIV (see chapter 4.4) as exemplary shown in Fig. 6.16. If a free vortex is assumed, Γ describes the surrounding velocity field by a single quantity (see chapter 2.2.3). Figs. 6.17 and 6.18 show the circulation Γ of the exemplary run shown in chapter 7.3.1. Within the measurement duration of experimental run #2 the circulation Γ is determined by in total 10 PIV runs. Consequently, nine breaks become obvious due to the PIV procedure (see chapter 4.4). During the whole experimental run the vortex type $VT6$ is present and the circulation Γ could be computed successfully at every time step. A fluctuating signal quite similar to the time series of the air-core diameter (Fig. 7.9) is determined.

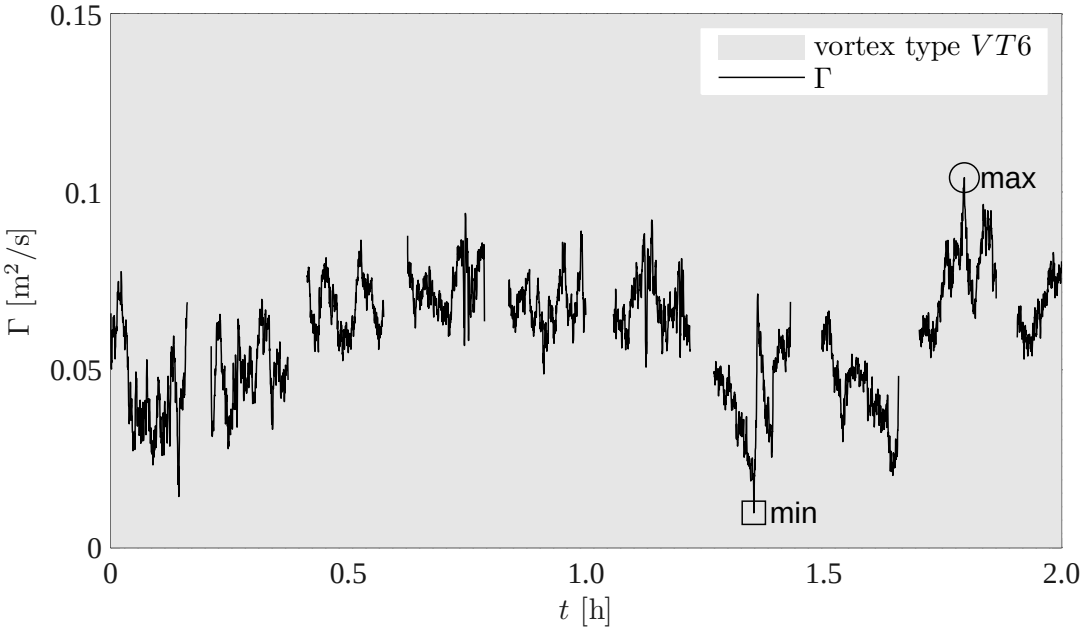

Figure 6.17: Circulation within experimental run #2. This time series consists of PIV run #2.1–#2.10. Nine gaps are due to inevitable interruptions while conducting the PIV recordings.

The computed circulation Γ of a second exemplary run (#28) is shown in Fig. 6.18. A different signal shape becomes obvious. Here, the vortex is present only at 64 % of the measurement time and the unsteadyness of the signal is quite higher. Furthermore, the absolute values of Γ have a broader range from zero up to the doubled maximum as computed for run #2. When the minimum circulation approaches zero this indicates the absence of any vortex. Vice versa, with the formation of a vortex a Γ-value is present und increases rapidly. For run #28 the obtained range of Γ and its fluctuations are large.
The resulting distributions for both run #2 and run #28 are depicted in Fig. 6.19, giving quite different shapes of their histograms. Run #2 shows a more narrow

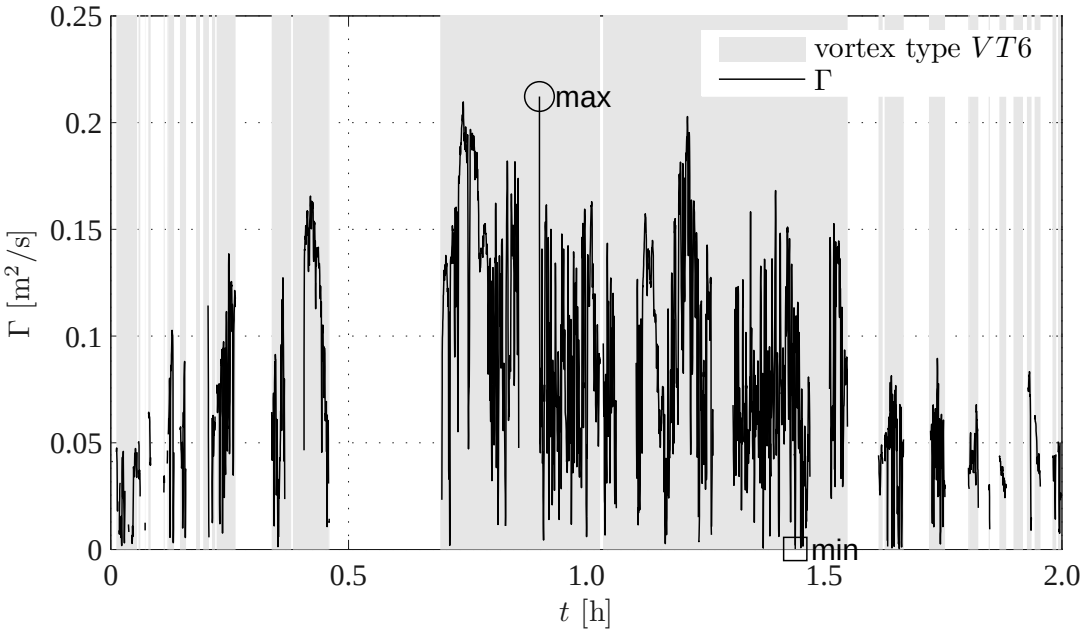

Figure 6.18: Circulation within experimental run #28. This time series consists of PIV run #28.1–#28.10. Values of Γ are blanked out in case of vortex type $< VT6$.

distribution with a distinct peak. In contrast to run #2, run #28 has a wider, almost doubled distribution that starts at zero. However, the median circulations $\tilde{\Gamma}$ of both exemplary runs differ only by 25 %. To achieve a single representable value that significantly describes the circulation within an experimental run can not be given.

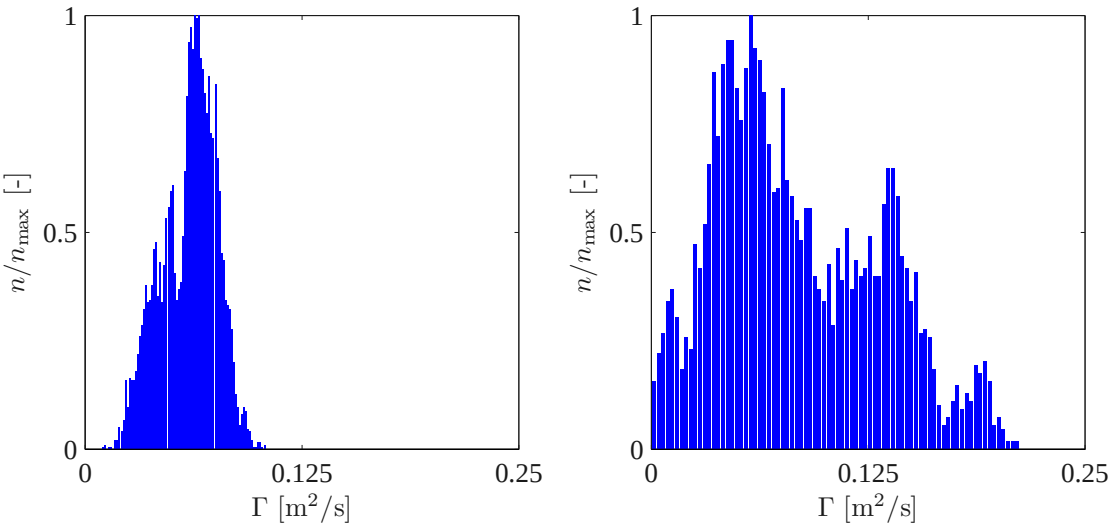

(a) Run #2, $\tilde{\Gamma} = 0.062$ m^2/s.

(b) Run #28, $\tilde{\Gamma} = 0.078$ m^2/s.

Figure 6.19: Histograms for circulation within the example runs.

6.2.3 Circulation of all Experimental Runs

The circulation Γ within all 34 experimental runs differs concerning its range and absolute values. This section focuses on an average circulation number to compare the experimental runs. The median circulation $\tilde{\Gamma}$ and the median circulation number $\tilde{N}_\Gamma$

$$\tilde{N}_\Gamma = \frac{\tilde{\Gamma} D}{Q_\mathrm{w}} \,, \tag{6.6}$$

respectively, is considered in the following. The comparison is conducted as function of the combined Froude number F_co, as given in Fig. 6.20. The runs are separated regarding the relative submergence h/D.

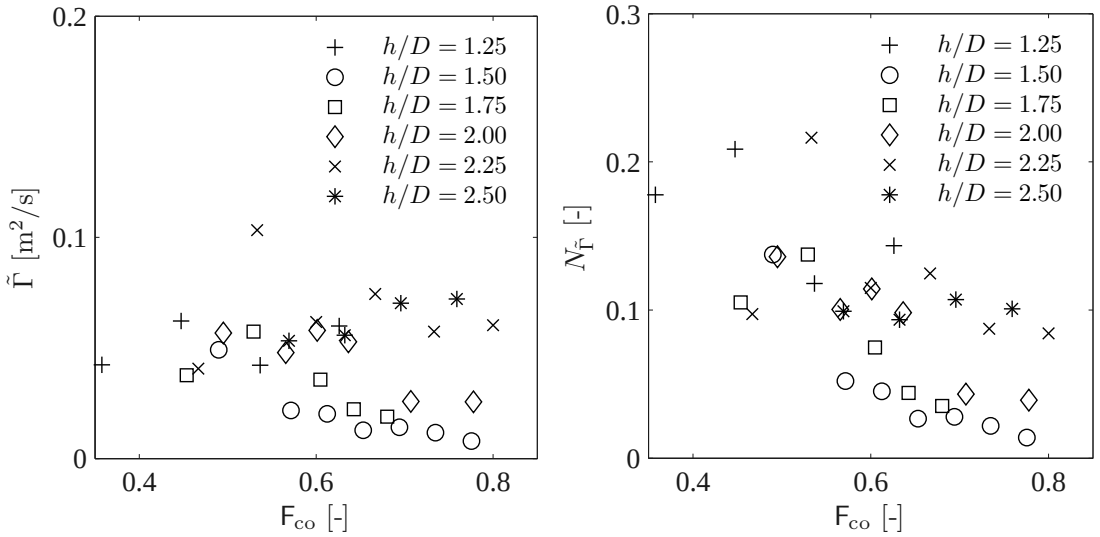

(a) Median circulation $\tilde{\Gamma}$

(b) Median Circulation number $N_{\tilde{\Gamma}}$

Figure 6.20: Circulation of the experimental runs versus combined Froude number F_co.

Fig. 6.20a shows no clear significant relationship, thus the median circulation is mostly independent of the combined Froude number. For the linear correlation coefficient[4] $\rho_{X,Y}$ = -0.22 holds. Regarding the dimensionless median Circulation number $N_{\tilde{\Gamma}}$ the combined Froude number F_co has a correlation coefficient $\rho_{X,Y}$ = -0.66. This high correlation is a result of the inclusion of Q_w in eq. (6.6) which is also included in F_co. Moreover, it can be noticed that no clear relationship can be revealed for the circulation $\tilde{\Gamma}$ to common flow parameters, e.g. h/D, F_D and F_co.

[4]Correlation coefficient $\rho_{X,Y}$ after Pearson: $\rho_{X,Y} = \frac{\mathrm{cov}(X,Y)}{\sigma_X \sigma_Y} = \frac{E[(X-\mu_X)(Y-\mu_Y)]}{\sigma_X \sigma_Y}$.

6.3 Air Entrainment vs. Common Flow Parameters

6.3.1 Linear Regression Analysis

A correlation of the air entrainment rate β to common flow parameters has already been briefly analyzed in chapter 6.1.3. As indicated by the diagonal band in Fig. 6.5, β depends on F_D and h/D. Several multivariate correlations have been tested as well, but no clear relationship could be found.
A different approach is applied hereafter to identify the influence of various parameters. Chapter 6.1.3 showed that F_D has a higher influence on β than h/D. As both parameters F_D and h/D contain the intake pipe diameter D in the denominator, β must be influenced mainly by h and v_D. Therefore, a linear regression analysis[5] with β and the combined Froude number $\mathsf{F}_{\mathrm{co}} = v_D/\sqrt{\mathrm{g}h}$ has been carried out. In Fig. 6.21 the mean air entrainment rate during vortex phases $\breve{\beta}$ is plotted against the combined Froude number F_{co}.

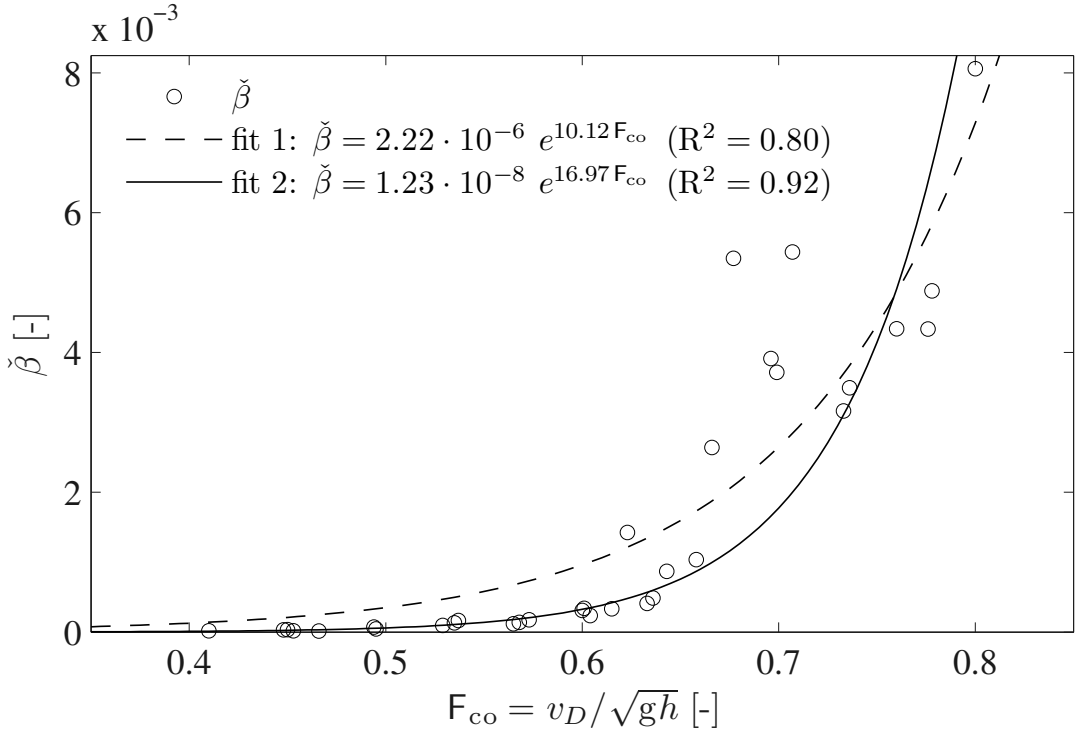

Figure 6.21: Correlation $\breve{\beta}$ vs. F_{co}. Difference of using robust least squares (fit 2) compared to least squared method (fit 1).

[5]Note that a linear regression model assumes that the relationship between the response variable and the predictor variable is linear. The model is termed to be linear because of the linearity of the parameter of the predictor variable.

Two linear regression curves are drawn as well, given by

$$\check{\beta} = 2.22 \cdot 10^{-6}\, e^{10.12\,\mathsf{F}_{\mathrm{co}}} \ (\mathrm{R}^2 = 0.80) \tag{6.7a}$$

$$\check{\beta} = 1.23 \cdot 10^{-8}\, e^{16.97\,\mathsf{F}_{\mathrm{co}}} \ (\mathrm{R}^2 = 0.92). \tag{6.7b}$$

Eq. 6.7a is derived by using an ordinary least squares regression. The result is strongly influenced by high $\check{\beta}$-values at $\mathsf{F}_{\mathrm{co}} = 0.66$–$0.71$, where β starts to increase significantly. A comparison to the scale family test results shows similar high $\check{\beta}$-values in this range of F_{co} (chapter 6.3.4). Therefore, a robust regression[6] is applied as well, resulting in eq. 6.7b. Here, the weight of outliers within the regression is reduced. Consequently, $\mathrm{R}^2 = 0.80$ for eq. 6.7a is lower than $\mathrm{R}^2 = 0.92$ for eq. 6.7b. Applying the robust regression analysis also to the mean air entrainment rate $\bar{\beta}$ during the whole time series, if a vortex type $VT6$ is present, of each experimental run, the correlation becomes $\mathrm{R}^2 = 0.91$. Fig. 6.22 shows the air entrainment rates $\bar{\beta}$ and $\check{\beta}$ with fitted robust regression curves in a semi-logarithmic plot to facilitate the interpretation of smaller values.

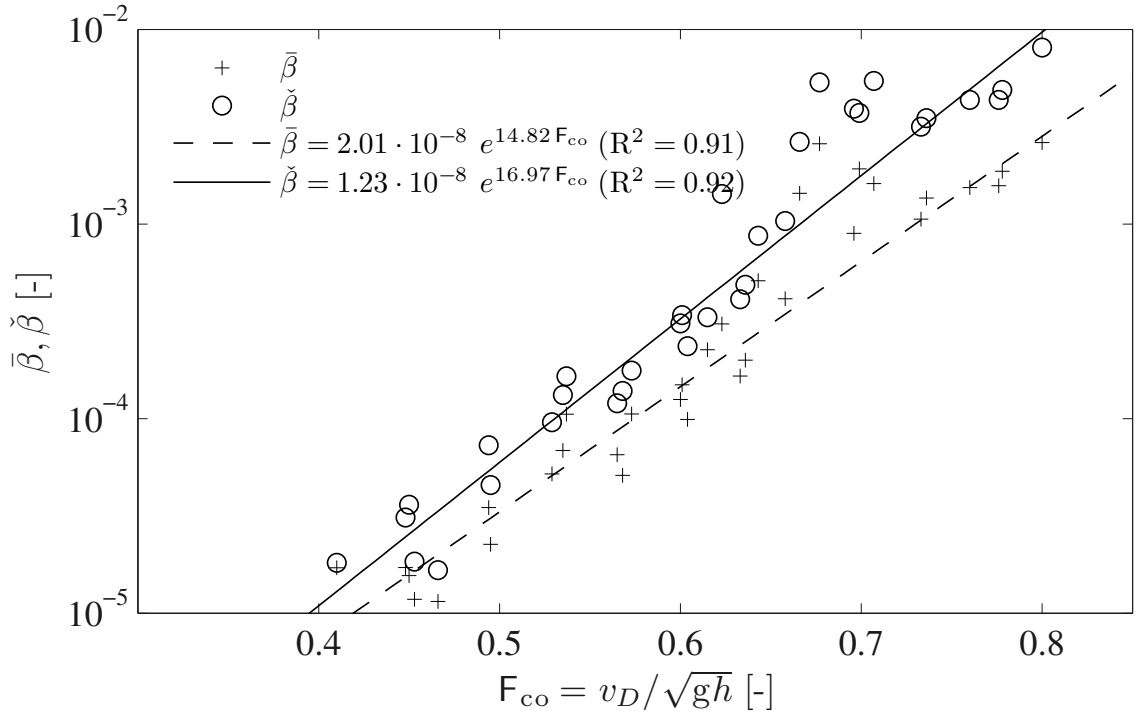

Figure 6.22: Robust regression curves of $\bar{\beta}$ and $\check{\beta}$ given in semi-log plot.

[6] A robust regression model is designed to be not overly affected by disregards of the made assumptions. Outliers were treated separately.

In analogy to eq. 6.7b, the exponential relationship is clearly obvious as a straight line by:

$$\bar{\beta} = 2.01 \cdot 10^{-8}\, e^{14.82\,\mathsf{F}_{\mathrm{co}}}\ (\mathrm{R}^2 = 0.91). \tag{6.8}$$

The plotted curves of eq. 6.8 and eq. 6.7b are almost parallel, indicating a linear relationship between $\bar{\beta}$ and $\check{\beta}$. The plotted fits only have slight differences.
A prerequisite for an applicable guideline is a simple equation that gives robust air entrainment estimations. To develop a simple and coherent correlation, eq. 6.8 and eq. 6.7b are reshaped to be parallel. Fig. 6.23 depicts the resulting curves, where the prefactor within the exponent is fixed to 16 while maximizing R^2. Different prefactors between 10–17 have been tested as well resulting in slightly lower R^2.

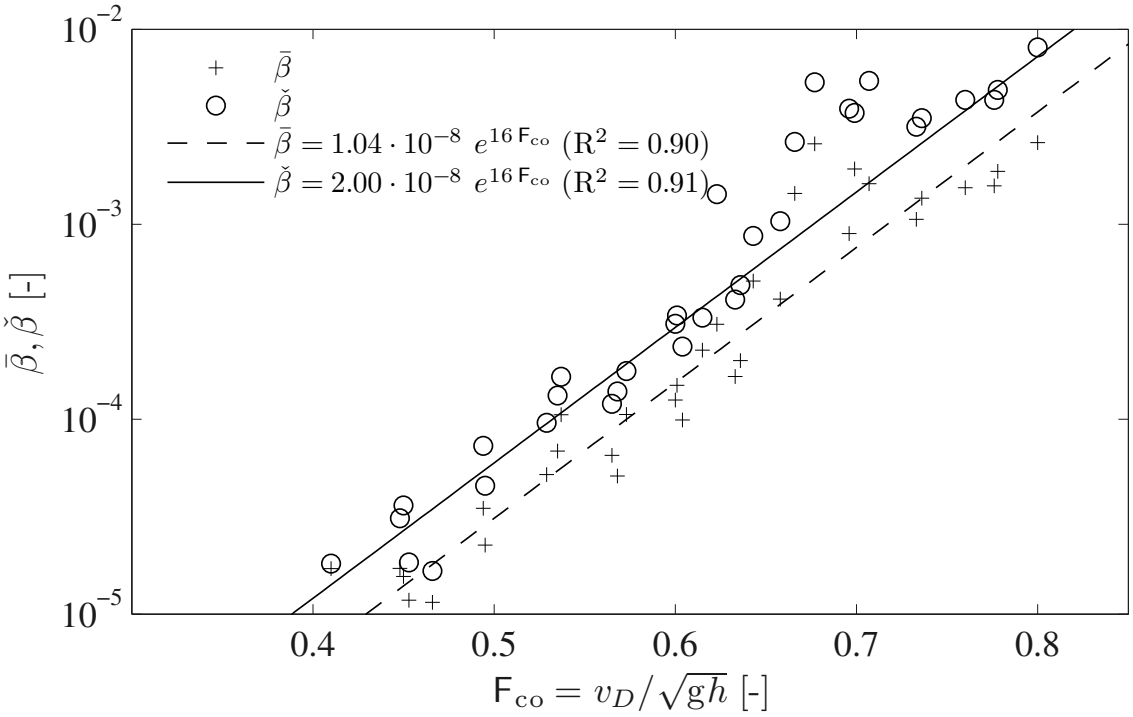

Figure 6.23: Final correlation of $\bar{\beta}$ and $\check{\beta}$ with respect to a linear relationship.

The final equations are

$$\bar{\beta} = 1.04 \cdot 10^{-8}\, e^{16\,\mathsf{F}_{\mathrm{co}}}\ (\mathrm{R}^2 = 0.90) \tag{6.9a}$$

$$\check{\beta} = 2.00 \cdot 10^{-8}\, e^{16\,\mathsf{F}_{\mathrm{co}}}\ (\mathrm{R}^2 = 0.91) \tag{6.9b}$$

$$\check{\beta} = 1.92 \cdot \bar{\beta} \tag{6.9c}$$

validated within the boundaries: $0.3 \leq \mathsf{F}_{\mathrm{co}} \leq 0.8$. These relationships can be used to determine the mean of the measured data on air entrainment rate β. Fig. 6.24 depicts

the residuals of $\bar{\beta}$ and $\check{\beta}$ against F_{co}. Except for some outliers, their distributions are almost uniform, between -0.6 and +0.6, so that the chosen exponential regression model can be judged to be valid.

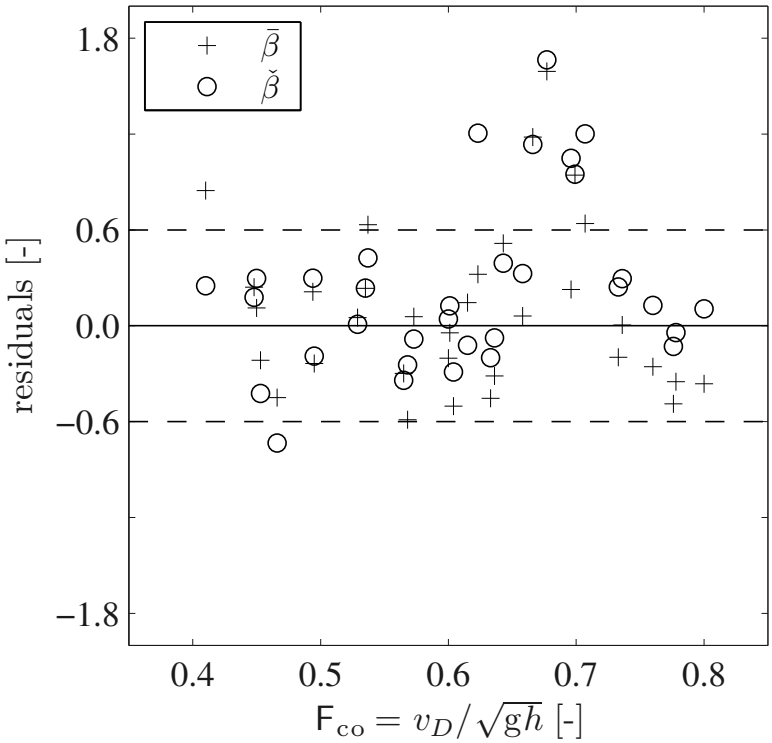

Figure 6.24: Residuals of $\bar{\beta}$ and $\check{\beta}$.

Furthermore, the mean air entrainment rate of the vortex phases $\check{\beta}$ are approx. two times the mean air entrainment rate $\bar{\beta}$ (Fig. 6.23).
Eqs. 6.9) describe the average of the expected quantities. By applying these equations a mean value of β can be estimated. The residual analysis shown in Fig. 6.24 is used to validate the chosen regression model. The distribution of the residuals can be assumed to be normally distributed. Additionally, a confidence band can be calculated, giving a boundary in which the expected value lies. Statements based on the confidence band for prospective observations cannot be made, however.

6.3.2 Comparison to Results of Padmanabhan (1984)

The literature review regarding air entrainment due to intake-vortices (see chapter 2.4) showed that very few data sets are available. Padmanabhan (1984) gives the most detailed data set, as has been shown graphically in Fig. 2.40. Although all achieved data were plotted, no regression analysis was conducted. Fig. 6.25 shows the lower section of Padmanabhan's figure superimposed by the air entrainment rate $\check{\beta}$ as determined within this research project.

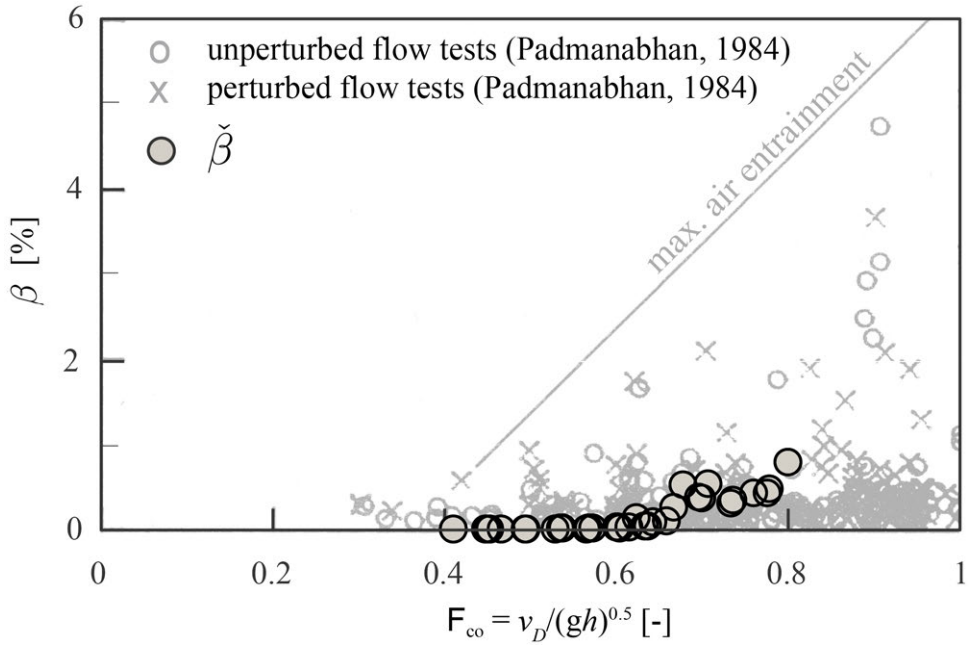

Figure 6.25: Comparison of Padmanabhan's data (1984) and mean air entrainment rate according to single vortex phases $\check{\beta}$ as gained within this research project.

The measured air entrainment rates $\check{\beta}$ within the parameter range of F_{co} are in a good agreement with the plotted data of Padmanabhan. The initial point of air entrainment matches quite well at $\mathsf{F}_{co} \approx 0.3$ for Padmanabhan (1984) and at 0.4 as determined within the present research project. Note, that the measurement accuracy of Padmanabhan's data amounts to $\beta = \pm 1\,\%$. This wide range of accuracy may lead to the conclusion, that almost all data are within this range. Neglecting this fact, the data of both studies are comparable regarding the rate of air entrainment. A more precise comparison, e.g. a semi logarithmic plot of the data, is skipped here as the original data cloud remains unrecoverable. However, the given line of "max. air entrainment" (Padmanabhan, 1984) can be used for a rough comparison (Fig. 6.26). The line can be approximated by

$$\beta = 0.12\,\mathsf{F}_{co} - 0.044\ . \tag{6.10}$$

The maximum air entrainment shown in Fig. 6.8 has larger values than the developed mean values of this research project. In particular, the amplitude of air entrainment within an experimental run of this research project never reach the entrainment level as indicated by Padmanabhan's data points. Eq. 6.10 leads to a clear conservative overestimation of the initial air-entrainment. Nevertheless, Padmanabhan's data are helpful to confirm the data achieved within this research project.

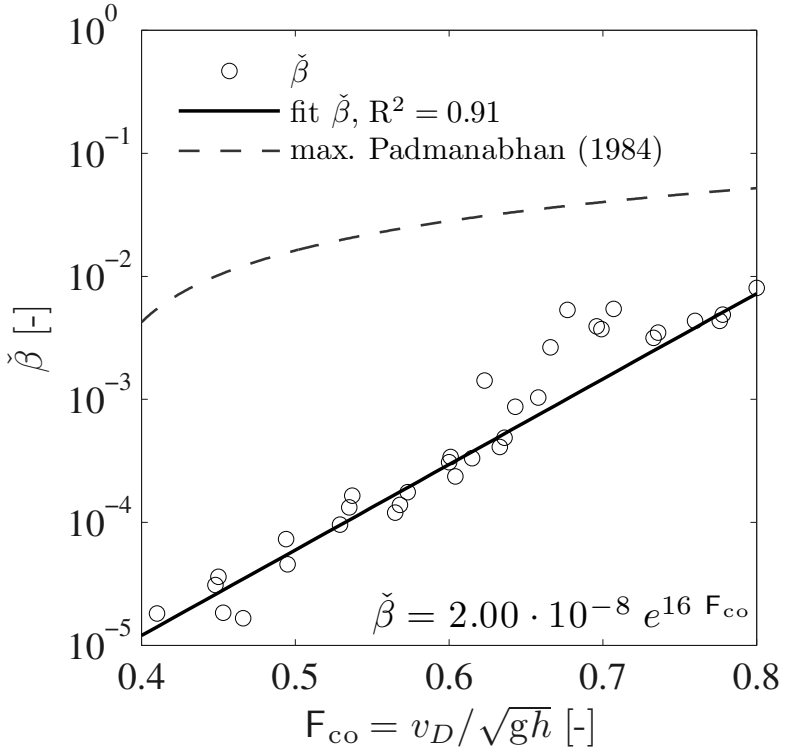

Figure 6.26: Semi-logarithmic plot of the max. air entrainment given by Padmanabhan (1984) and the obtained air entrainment rate $\breve{\beta}$ including the function found by a regression analysis.

6.3.3 Prediction Band

Stahel (2008) suggests a prediction band to calculate boundaries for prospective observations. This methodology enables a statement about a stochastic variable. Principally, the prediction band has to be distinguished from the confidence band. The confidence band does not contain the random deviation and is therefore smaller. For example, if 95 % of prospective observations should be below a certain value, a statistically based boundary can be determined by the prediction band Pr:

$$Pr = \pm q\,\hat{\sigma}\sqrt{1 + \frac{1}{n} + \frac{(x_0 - \bar{x})^2}{SS_X}} \tag{6.11a}$$

$$SS_X = \sum_{i=1}^{n} (x_i - \bar{x})^2\ , \tag{6.11b}$$

where q is the parameter of the chosen quartile of the distribution, $\hat{\sigma}$ is the standard deviation of the residuals, x_0 input variable, x_i output variable and the $\bar{x}$ the mean output variable. For $n \geq 30$, typically a normal distribution can be used. SS_X considers the distribution of the x-values. The farther they are apart, the more

accurate is the specified regression curve and thus the prediction band.
In the present case, the x-values correspond to F_{co}. The prediction band is determined and shown in Fig. 6.27. At $\mathsf{F}_{\mathrm{co}} = 0.66$ the data set is subdivided in two ranges to account for the values that could not have been judged as outliers in the regression analysis (see chapter 6.3.1). Therefore, the prediction bands have a different width. For $\mathsf{F}_{\mathrm{co}} < 0.66$ estimations are more accurate.
The present statistical analysis is based on an exceedance probability of 95 % and is equal to two times the standard deviation. The estimation of β via common flow parameters can be done in an band that is given by the following equations:

$$\bar{\beta} = \text{limit} \cdot 10^{-8} \mathrm{e}^{16 \cdot \mathsf{F}_{\mathrm{co}}} \tag{6.12a}$$

$$\check{\beta} = \text{limit} \cdot 10^{-8} \mathrm{e}^{16 \cdot \mathsf{F}_{\mathrm{co}}} \tag{6.12b}$$

The limits are given in detail in Table 6.1 below.

Table 6.1: Limits of the prediction band of air entrainment rate β appropriate to eqs. 6.12a and 6.12b.

F_{co}	limit	$\bar{\beta}$	$\check{\beta}$
<0.66	upper	2.08	4.09
	lower	0.52	0.97
≥0.66	upper	4.36	6.80
	lower	0.25	0.60

The regression analysis regarding the air entrainment rate β and the combined Froude number F_{co} results in a valuable prediction band. Thus, for the first time guidelines are given to estimate the air entrainment rate due to intake-vortices by common flow parameters.

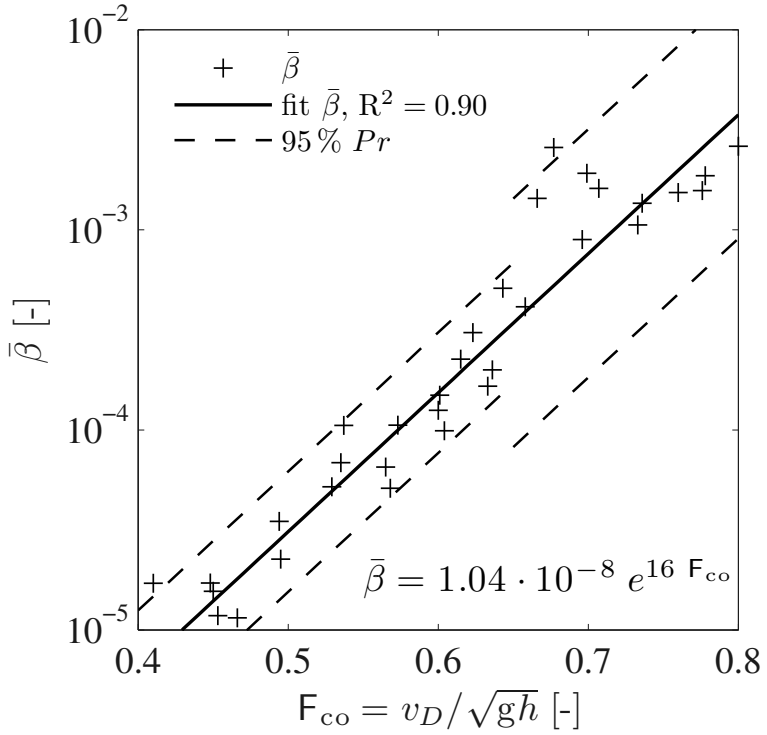

(a) Mean air entrainment

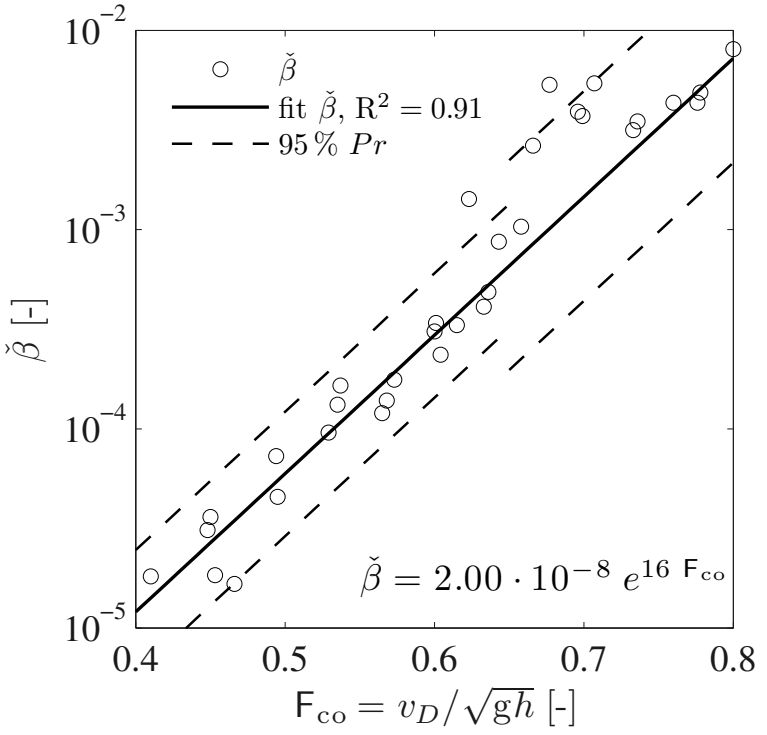

(b) Mean air entrainment according to single vortex phases

Figure 6.27: Prediction bands to estimate the air entrainment rate β. A subdivision is made at $\mathsf{F}_{co} = 0.66$ to account for varying prediction widths.

6.3.4 Comparison to Scale Family Test Results

The methodology of measuring the entrained air was developed to enhance accuracy and measurement duration. The manual selection of the standard case of air entrainment as explained in chapter 5 needs to be compared to the achieved results by the final designed de-aeration system (see chapter 4.2). Table 4.2 gives Fig. 6.28 shows the short-time air entrainment rates $\dot{\beta}$ determined at DN400 within the scale family tests in comparison to the mean air entrainment rate of the vortex phase $\check{\beta}$ both plotted against F_{co}.

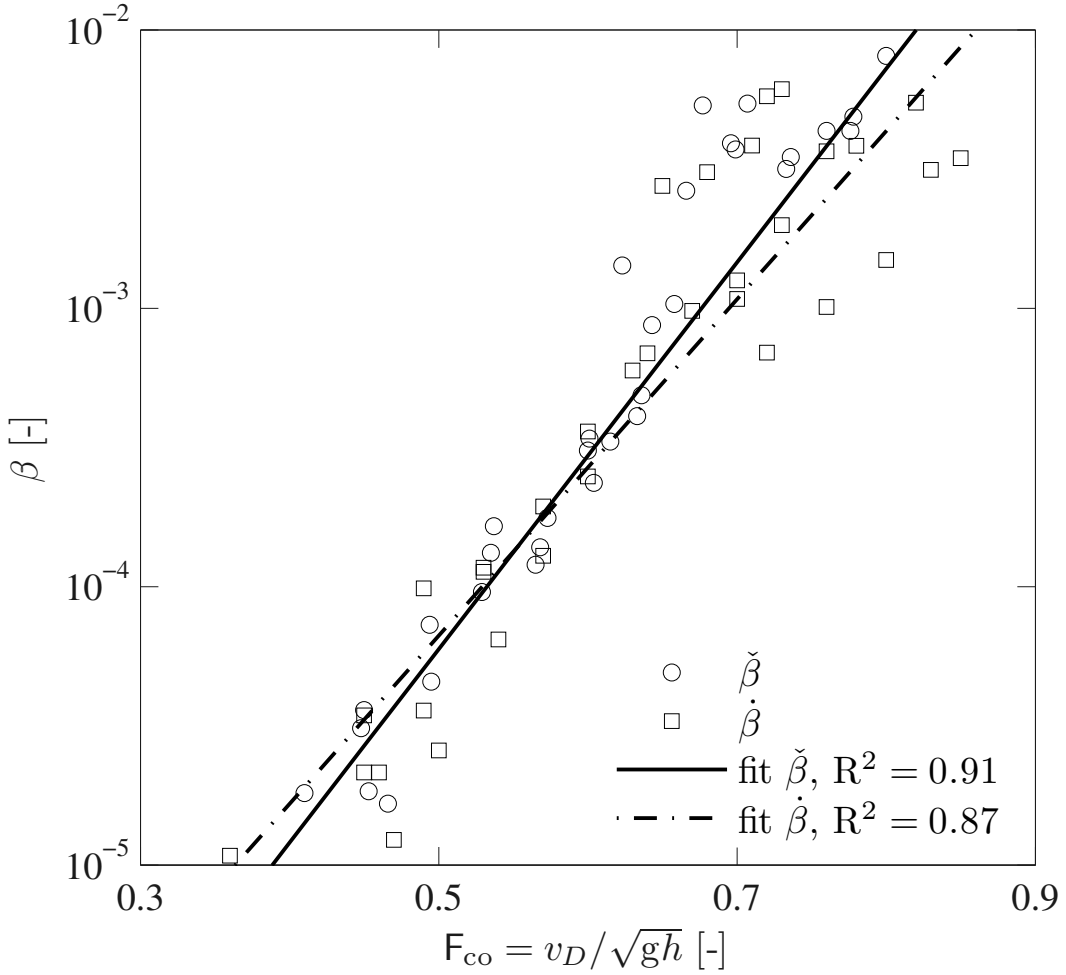

Figure 6.28: Comparison of air entrainment rate of the scale family tests $\dot{\beta}$(DN400) and the mean air entrainment rate of the vortex phases $\check{\beta}$ determined during the main measurements.

The matching of $\dot{\beta}$(DN400) and $\check{\beta}$ is quite well. Especially in the central region at $\mathsf{F}_{\mathrm{co}} = 0.5$–$0.7$ the air entrainment rates agree notably well. Furthermore, the high β show at least a similar scatter, as already discussed in chapter 6.3.1. The regression lines almost match as well. Consequently the results of both methodologies can be considered as validated.

6.4 Air Entrainment vs. Circulation

A coherence of air entrainment and rotational flow parameters has to be proven to give a second approach to estimate the air entrainment rate β. The circulation Γ is a measure of the rotational flow. At first sight, it is hypothesized that Γ gives a more direct handle to the characteristics of the air-entraining vortex as it can be done by basic parameters as described in chapter 6.3. Furthermore, it is assumed that these characteristics affect the air discharge Q_a and especially the air entrainment rate β. For this second approach a more precise regression model and thus a small prediction band is expected.

Fig. 6.29 shows the data of the air entrainment rate β versus the related circulation Γ of exemplary run #2. The vertical appearance of the data lines are due to the fact that Γ is determined by separate time steps of 1 s, but Q_a and thus β have to be determined by detrending the pressure signal of the rising pipes covering a time window of several seconds length (see chapter 6.1.2). An averaging of the vertically distributed data results more or less in a horizontal line for run #2. This would indicate an independency of β from Γ. A clear trend of the presented data of run #2 does not become obvious.

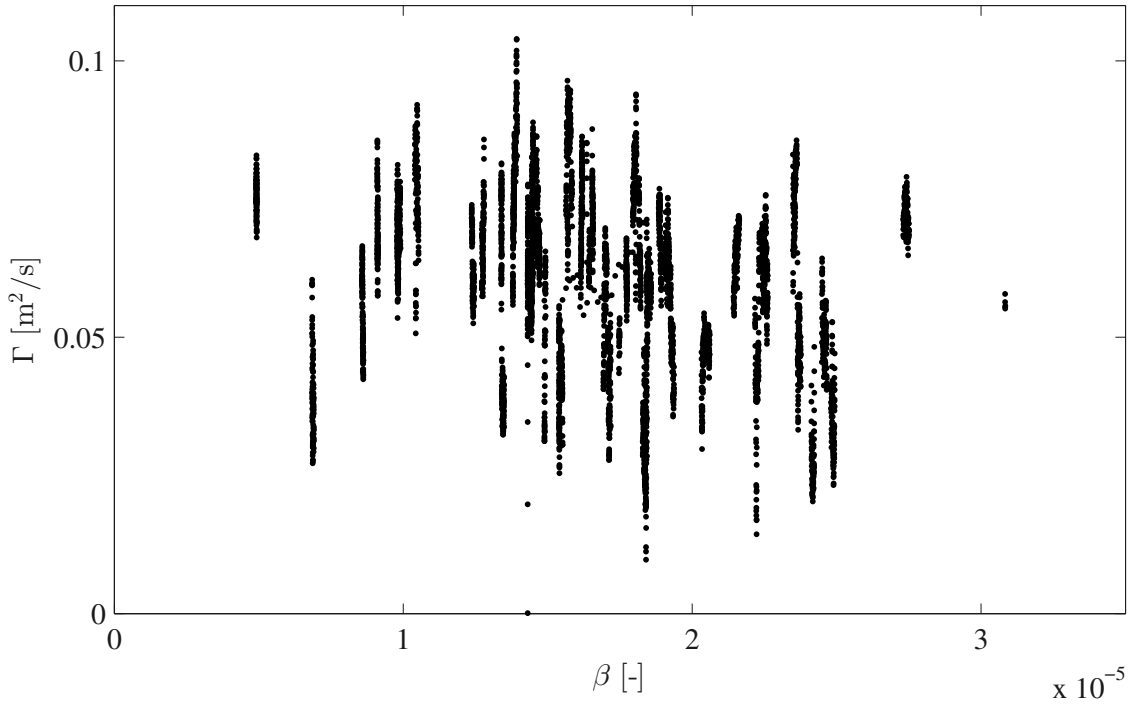

Figure 6.29: Comparison of air entrainment rate β and circulation Γ of exemplary run #2.

Fig. 6.30 shows the data of the air entrainment rate β versus the related circulation Γ of exemplary run #28. The vertical data lines are prominent as well compared to

Fig. 6.29. A slightly increasing trend can be guessed if the vertical lines of the data are averaged.

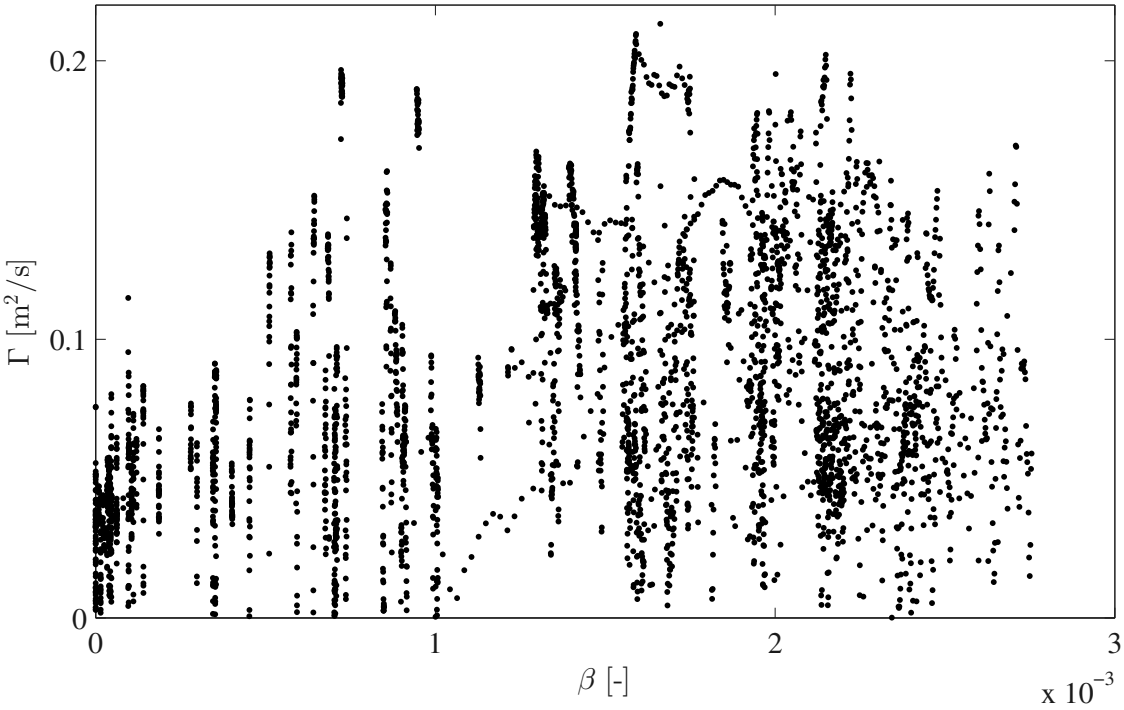

Figure 6.30: Comparison of air entrainment rate β and circulation Γ of exemplary run #28. Note that in comparison to Fig. 6.29 the vertical axis is doubled and the horizontal axis is nearly two orders of magnitude larger.

The air entrainment rate β and the circulation Γ data are analyzed one by one within all experimental runs. However, a clear relationship is not found. Next, the mean values of the air entrainment rate β and the circulation Γ are analyzed.
The median circulation $\tilde{\Gamma}$ has already been analyzed in chapter 6.2. The correlation of $\tilde{\Gamma}$ to the known common flow parameter, e.g. the combined Froude number F_{co}, is small. Instead, the correlation of the circulation number $\tilde{N}_\Gamma$ to F_{co} shows a slight statistical significance.
In Figs. 6.31a–6.31d $\tilde{\Gamma}$ is plotted against $[\bar{Q}_{\mathrm{a}}, \check{Q}_{\mathrm{a}}]$ and $[\bar{\beta}, \check{\beta}]$, respectively. Regarding $\tilde{\Gamma}$, both the dimensional Q_{a} and the non-dimensional β have small correlation coefficients $\rho_{X,Y}$ = [-0.19, -0.24, -0.26, -0.31]. Furthermore, in Figs. 6.32a–6.33b $\tilde{N}_\Gamma$ is plotted against $[\bar{Q}_{\mathrm{a}}, \check{Q}_{\mathrm{a}}]$ and $[\bar{\beta}, \check{\beta}]$, respectively. The plots depict a certain dependency of the non-dimensional circulation number $\tilde{N}_\Gamma$. The correlation coefficients $\rho_{X,Y}$ are $\rho_{X,Y}$ = [-0.47, -0.49, -0.52, -0.54]. Generally the strength of linear dependence between each analyzed parameter pair is rather small and their negative values imply that all data points lie on a line for which Y decreases as X increases.

Depending on the size of $\rho_{X,Y}$ the correlation can be divided in the following groups (Stahel, 2008): $|\rho_{X,Y}| = 0$–0.1 can be interpreted as no correlation, $|\rho_{X,Y}| = 0.1$–0.3 as small correlation, $|\rho_{X,Y}| = 0.3$–0.5 as medium correlation, and $|\rho_{X,Y}| = 0.5$–1.0 as strong correlation. Consequently, the correlations of the dimensional circulation $\tilde{\Gamma}$ and the air entrainment are assessed to be small. However, the correlations of the non-dimensional circulation numbers $\tilde{N}_\Gamma$ are at the threshold to a strong correlation.

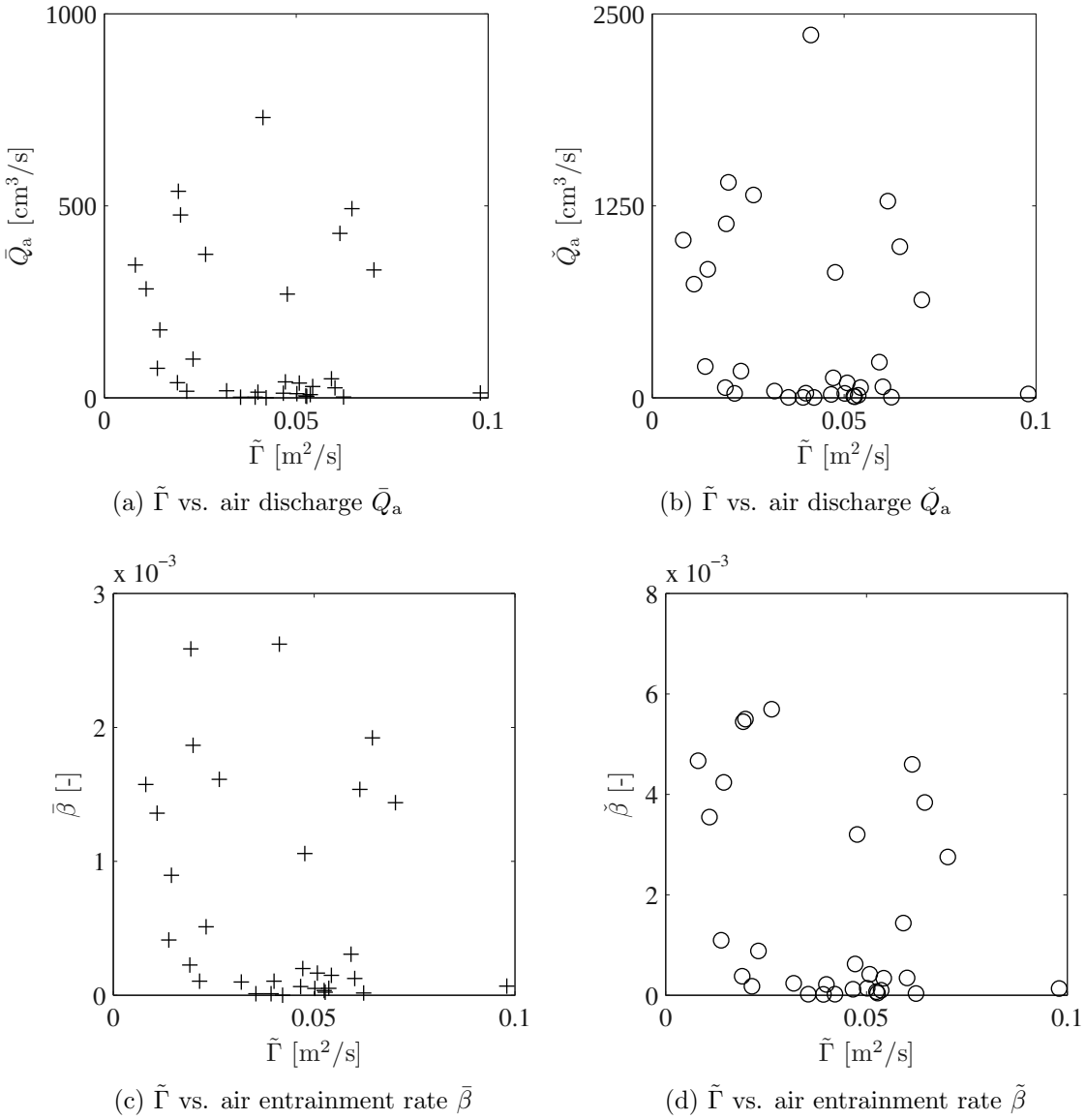

(a) $\tilde{\Gamma}$ vs. air discharge $\bar{Q}_a$

(b) $\tilde{\Gamma}$ vs. air discharge $\check{Q}_a$

(c) $\tilde{\Gamma}$ vs. air entrainment rate $\bar{\beta}$

(d) $\tilde{\Gamma}$ vs. air entrainment rate $\tilde{\beta}$

Figure 6.31: Median circulation $\tilde{\Gamma}$ plotted against (a, b) dimensional parameters of air discharge and (c, d) non-dimensional air entrainment rate.

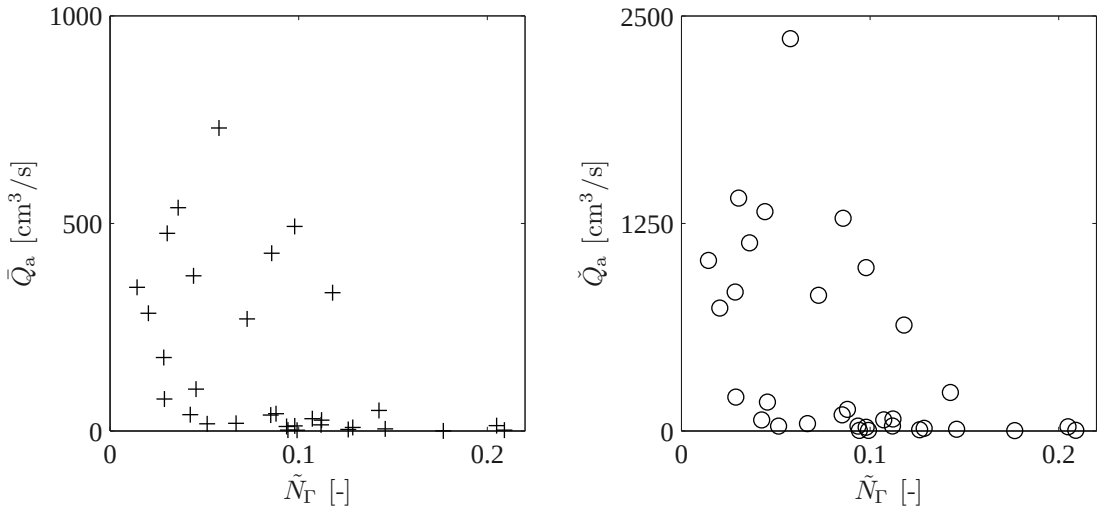

(a) $\tilde{N}_\Gamma$ vs. air discharge $\bar{Q}_a$ (b) $\tilde{N}_\Gamma$ vs. air discharge $\check{Q}_a$

Figure 6.32: Median circulation number $\tilde{N}_\Gamma$ plotted against air discharge Q_a.

The correlations of the non-dimensional parameters $\tilde{N}_\Gamma$ and $\bar{\beta}/\tilde{\beta}$ shown in Fig. 6.33a and Fig. 6.33b are strong. Several regression models are tested in the corresponding regression analyses. An exponential regression model fits the data best. However, the residual analysis do not support these exponential regression models. Fig. 6.33 shows the two exponential equations found. The coefficients of determination are small for

$$\bar{\beta} = 0.0027\, e^{-22.85\,\tilde{N}_\Gamma} \ (\mathrm{R}^2 = 0.24) \tag{6.13a}$$

$$\check{\beta} = 0.0076\, e^{-22.88\,\tilde{N}_\Gamma} \ (\mathrm{R}^2 = 0.29). \tag{6.13b}$$

Further analyses regarding a more suitable regression is omitted here. Instead, conclusions concerning the minor influence of the circulation on the air entrainment process can be derived from the small correlation coefficients and the small coefficients of determination. Moreover, the development of a prediction model to estimate the air entrainment by rotational parameters is considered to be misleading.

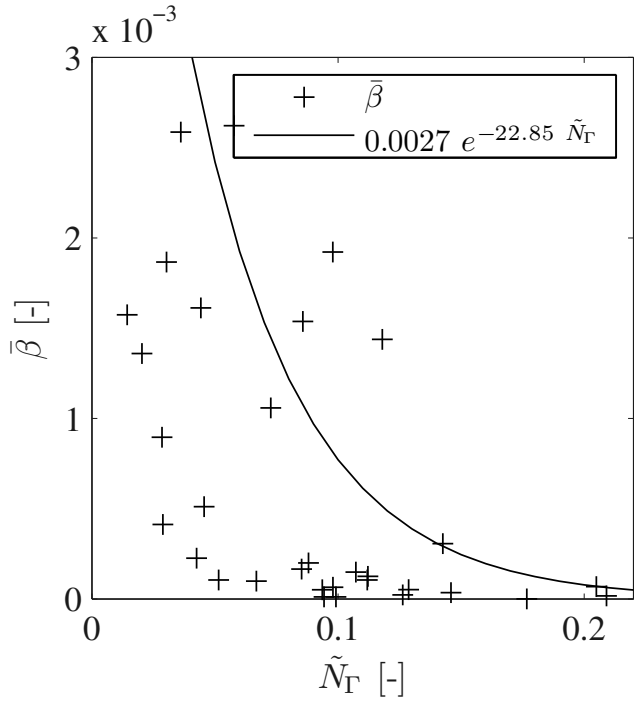

(a) $\tilde{N}_\Gamma$ vs. air entrainment rate $\bar{\beta}$

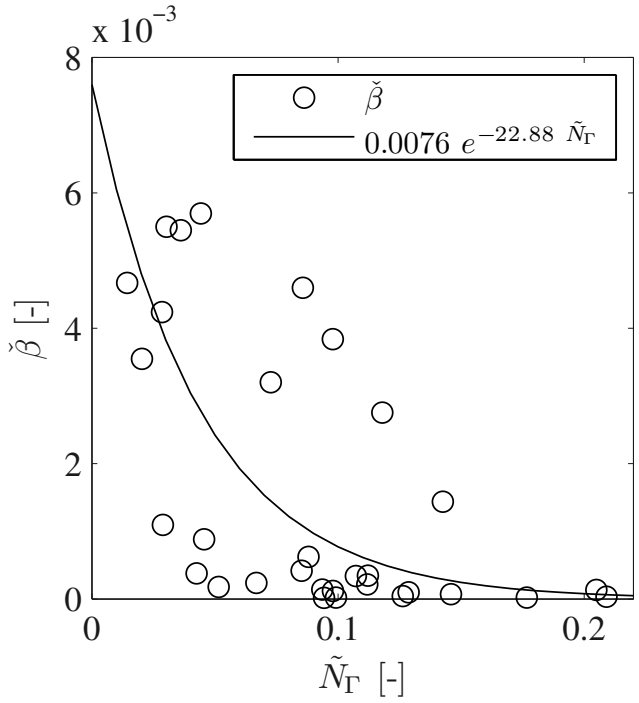

(b) $\tilde{N}_\Gamma$ vs. air entrainment rate $\tilde{\beta}$

Figure 6.33: Median circulation number $\tilde{N}_\Gamma$ plotted against non-dimensional parameters of air entrainment rate.

Chapter 7

Results of Air-Core Flow

Abstract. *Intake-vortex induced air entrainment into pressure systems takes place through the fully developed air-core tube. The air-core diameter is measured by image processing techniques, enabling an analysis of the air-core flow. A crude model that describes the air flow hydraulics in the tube is developed. The air flow velocity is determined based on the measured air discharges. Finally, the findings concerning the air-core flow are analyzed with respect to the driving processes.*

7.1 General

Air entrainment into pressure systems takes place through the entirely developed air-cores. Type $VT5$ and $VT6$ intake vortices have an air-core (see Fig. 2.10). If the circulation of the vortex reaches a sufficient size, air is entrained and the air flows through the pipe of the air-core tube.

Fig. 7.1 shows an air-core vortex. The decisive geometric parameters are the air-core diameter d_{ac} and the air-core length l_{ac}. The path between the surface and the intake depends on the approach flow; a possible air flow field in the core is visualized in Fig. 7.1. Some general considerations and descriptions of the flow in an air-core of a vortex are given next. They provide an important part in understanding the whole air entrainment process, with the air flowing from the free surface through the air-core to its end, where the core is separated to bubbles entering the pressure system.

The driving physical processes in the core of the vortex are unknown. In the following, three conceivable processes are explained. Their order depends on its weight of influence.

The first process considers bubble separation. Bubble separation takes place at the end of the core as shown in Fig. 7.1. The bubbles detach from the air-core after they have been guided into the pipe. The sharp edged circular cross-sectional pipe intake induces a contraction at the beginning in which the flow cross-section is reduced

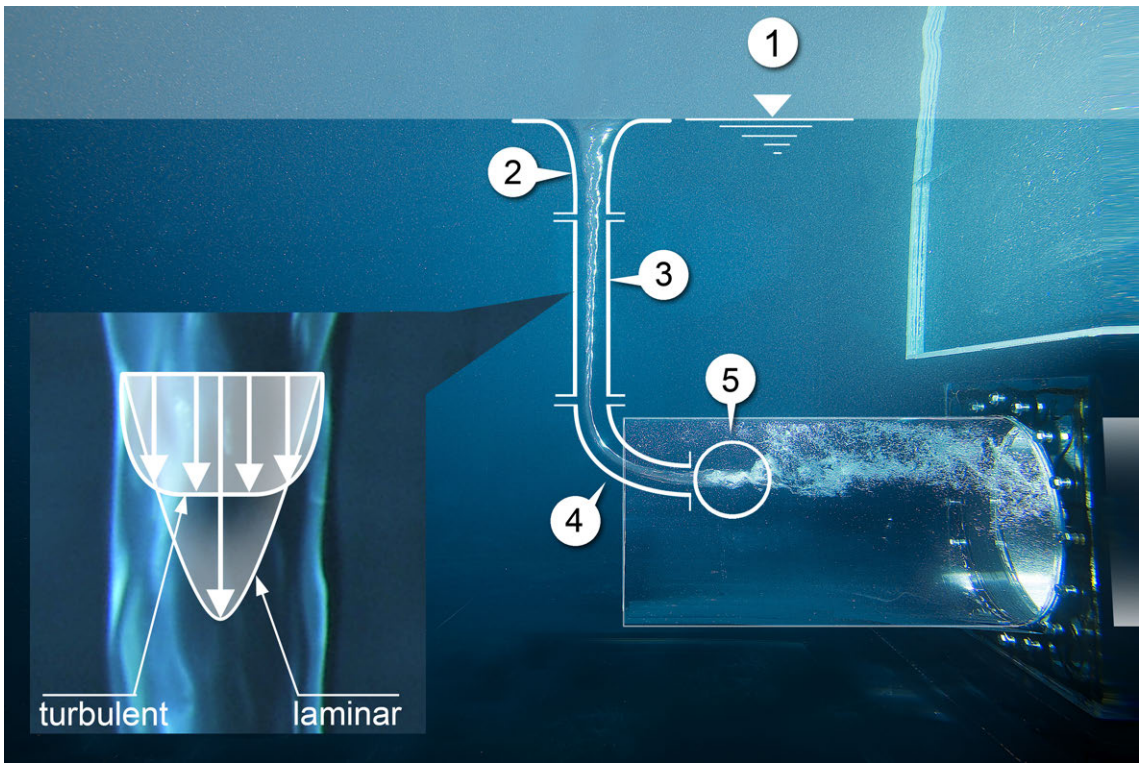

Figure 7.1: Air-core vortex at a horizontal sharp-edged and circular pipe intake: ① Free surface, ② Sinkhole, ③ Straight air-core, ④ Bent air-core, ⑤ Bubble separation.

(Fig. 7.1). Downstream the flow spreads throughout the whole pipe cross-section. The mean velocity of water decreases at this location, resulting in a slight hydraulic loss. This may reduce the spin of the vortex and makes the core tube unstable. The current surrounding turbulence leads ultimately to the bubble separation. This process involves a lack of air that has to be filled up to have a state of equilibrium. Thus, air has to flow from the free surface through the core.

The second process considers the core pressure. The reduction of the pressure in the core due to rotation reaches a value below atmospheric pressure. Consequently, air flows from the high to the low pressure region.

The third process focuses on the air-water interface of the air-core tube. The water surface of the air-core and the inside wall of this pipe, respectively, are being moved by the surrounding water body. This surface is rough, similar to other highly turbulent flows. Therefore, the adjoining air is dragged along.

The path of the air flow in the core can be straight or spiral according to its axis. The velocity distribution is fairly unknown till today. The compressibility of air depends on several parameters. It is important to know when a change in the compressibility must be taken into account. Next, some considerations are given concerning the hydrodynamics.

In some cases, the flow calculation, especially while regarding air flow, has to be

adapted to the change in density and viscosity. The density ρ of gases depends on the pressure p and the temperature ϑ. The ideal gas assumption is valid for air. The ideal gas law is $p = \rho R_\mathrm{s} T$, with $R_\mathrm{s} \cong 287.058$ J/(kg K). The change of density is proportional to the pressure p and inversely proportional to the temperature T. The relative changes of the density can be calculated via the Mach number M that gives the relationship between the air velocity v_a and the speed of sound c_a by

$$\mathsf{M} = \frac{v_\mathrm{a}}{c_\mathrm{a}}\,, \tag{7.1}$$

$$\text{with } c_\mathrm{a} = \sqrt{\kappa R_\mathrm{s} T}\,. \tag{7.2}$$

The heat capacity ratio or adiabatic index κ, respectively, is a measure of the resistance to compression. It is the ratio between the pressure increase and the resulting decrease in volume. For instance, $\kappa = 1.4$ holds for dry air at 20 °C. The according value of water is approximately four magnitudes larger. The speed of sound in air is approx. 345 m/s. At a certain limit compressibility plays a crucial role in determining the flow velocity. The following considerations are used to decide whether the compressibility should be taken into account, or is to be disregarded. The flow in the core can be described by adiabatic pipe flow. If $\mathsf{M} > 0.2$, the compressibility of air must be considered (Clift et al., 1978). The relative change of the density can be calculated from M by

$$\frac{\Delta\rho}{\rho} \approx \frac{\mathsf{M}^2}{2}. \tag{7.3}$$

That means, for instance, that a change of 1 % of the density takes place at air velocities of about 50 m/s. Compressibility should be considered above air velocities v_a of about 70 m/s ($\mathsf{M} = 0.2$). Underneath this limit, the air velocity can be calculated approximately by the standard incompressible formulas. Furthermore, in most cases, water can be assumed to be incompressible. The temperature is only of slight influence on its density. The pressure influence is negligible.
The viscosity of air and water is different. For example, the kinematic viscosity ν_a at 20 °C is $15.23 \cdot 10^{-6}\mathrm{m}^2/\mathrm{s}$ and hence nearly 15 times greater than water. The pressure influence is negligible, but the temperature has a strong impact. For gases, the viscosity increases with increasing temperature, whereas the viscosity of liquids decreases with a temperature increase.

7.2 Flow Visualization

General. The questions mainly concerning the driving process and the flow regime of the air-core flow discussed above are still unanswered. Especially the path and the turbulence of the air in the air-core tube are of great interest to enhance the understanding of the physical process of air entrainment. Velocity measurements within the air-core tube are extremely difficult to conduct due to a various number of reasons, e.g. the vortex wandering and the high fluctuations of the air-core diameter, respectively. Next, two test setups are described. Their results should give clues for further investigations.

By Smoke. Fig. 7.2 shows a snapshot of air flow visualization during an experiment. The smoke is provided by a flow proof tube[1] that enables the production of a small amount of grey smoke.

Figure 7.2: Smoke experiment at $h/D = 2.0$, $\mathsf{F}_D = 0.9$ to visualize the air flow through the tube of an air-core intake vortex.

[1]The flow proof tube is from *Drägerwerk AG & Co. KGaA*, Germany.

Vortex wandering is smaller at small submergences, whereas the highest air entrainment rate is measured at $h/D = 2.25$, $\mathsf{F}_D = 1.2$ (run #30, see chapter 6.1.3). For the experiment shown in Fig. 7.2 a parameter combination of $h/D = 2.0$, $\mathsf{F}_D = 0.9$ is chosen. This enables to follow the vortex wandering at the water surface, to have a sufficient air-core diameter and to have a high air entrainment rate.
Fig. 7.2 shows that the smoke has a slightly smaller density than the surrounding air, thus it rises. Moreover, due to the vortex wandering (see chapter 8.1) the smoke supply has to be conducted manually. If the smoke is placed near the sinkhole of the vortex it is strongly sucked in. The smoke is entrained similar to air. Due to the large turbulence of the air-core tube flow the mixing of air and smoke is done very quickly. Fig. 7.3 shows a snapshot with a zoom into the air-core tube. This view is restricted due to reflections on the air-core. Furthermore, the smoke is already mixed and cannot be identified clearly based on the recorded photographs. The observations lead to assume that this flow is most probably driven by viscous forces.

Figure 7.3: Detail of the air-core tube near the sinkhole while using smoke to visualize the flow through the tube.

In summary it can be said that the visualization by smoke failed due to the following reasons:

- The provided amount of smoke was too small to visibly fill the air-core.
- The density is slightly smaller than the one of air and thus the smoke rises before it is sucked in.

By Dry Ice. A basic substance which fulfills the wanted requirements is dry ice. It is the solid form of carbon dioxide. The direct sublimation to a gas is very useful to produce a large amount of fog. When dry ice is placed in water sublimation is accelerated, and low-sinking, dense clouds of smoke-like fog are created. This property is used to visualize the air-core tube flow successfully. Fig. 7.4 shows a photograph where dry ice fog is used. A tub is filled with dry ice and water from the experimental tank is used to assemble both substances. A huge amount of white fog covers the water surface. This stratification provides sufficient fog for the visualization of the air-core tube flow. Moreover, the problem due to vortex wandering is solved automatically. For security reasons, the duration of the manually provided fog was limited by the concentration of toxic carbon dioxide between the water surface and the experimenter.

Figure 7.4: Provision of sufficient gas above the water surface by dry ice fog to visualize the flow through the air-core.

The air-core tube, especially the air flow inside the tube is of great importance. Visualization by a photograph needs to freeze the whole structure. Difficulties regarding the high velocities and the large distance between camera and the air-core, that is permanently changing due to vortex wandering of the air-core, have to be

handled properly. To solve this, the depth of field[2] has to be enlarged. This is done by using flash generators and external lights which provide sufficient light energy during short flash durations. Therefore, the depth of field was enlarged to approximately 0.70 m. A plate camera[3] is used with an image resolution of 40 Mpx. Fig. 7.5 shows a photograph that unifies all enhancements. The air-core is filled by dry ice fog and its structure is frozen in this picture. The wall structure of the air-core tube characterized by capillary waves becomes clearly visible.
Figs. 7.6–7.8 show three details which are cut out from Fig. 7.5: the sinkhole, the straight air-core and the bent air-core. A closer look to the layer between that encapsulated air-core leads to the assumption that this layer has a certain thickness. Especially near the sinkhole its size is bigger. Furthermore, two main results can be derived from these photographs. First, the velocity of the tube wall increases with decreasing air-core diameter. This can be seen by the sharpness of the air-core in Fig. 7.6 compared to the unsharpness of the air-core in Fig. 7.8. The tangential velocity of a free vortex increases while the radius is decreasing (chapter 2.2.6). The assumption that the circulation is constant along the air-core tube can be affirmed. Second, the concentration of fog is decreasing along the air-core tube. This is an indication that the velocity of the gas mixture through the air-core tube increases. Nevertheless, the magnitude of their acceleration, which depends on the path through the tube, remains unknown.

[2]The depth of field is the distance between the nearest and farthest objects in a scene that appear acceptably sharp in an image.

[3]The lens is mounted at one side of the plate. At the other side of the plate is the digital camera back. This system is used for large format photography.

Figure 7.5: Air-core intake vortex tube flow visualization by dry ice fog.

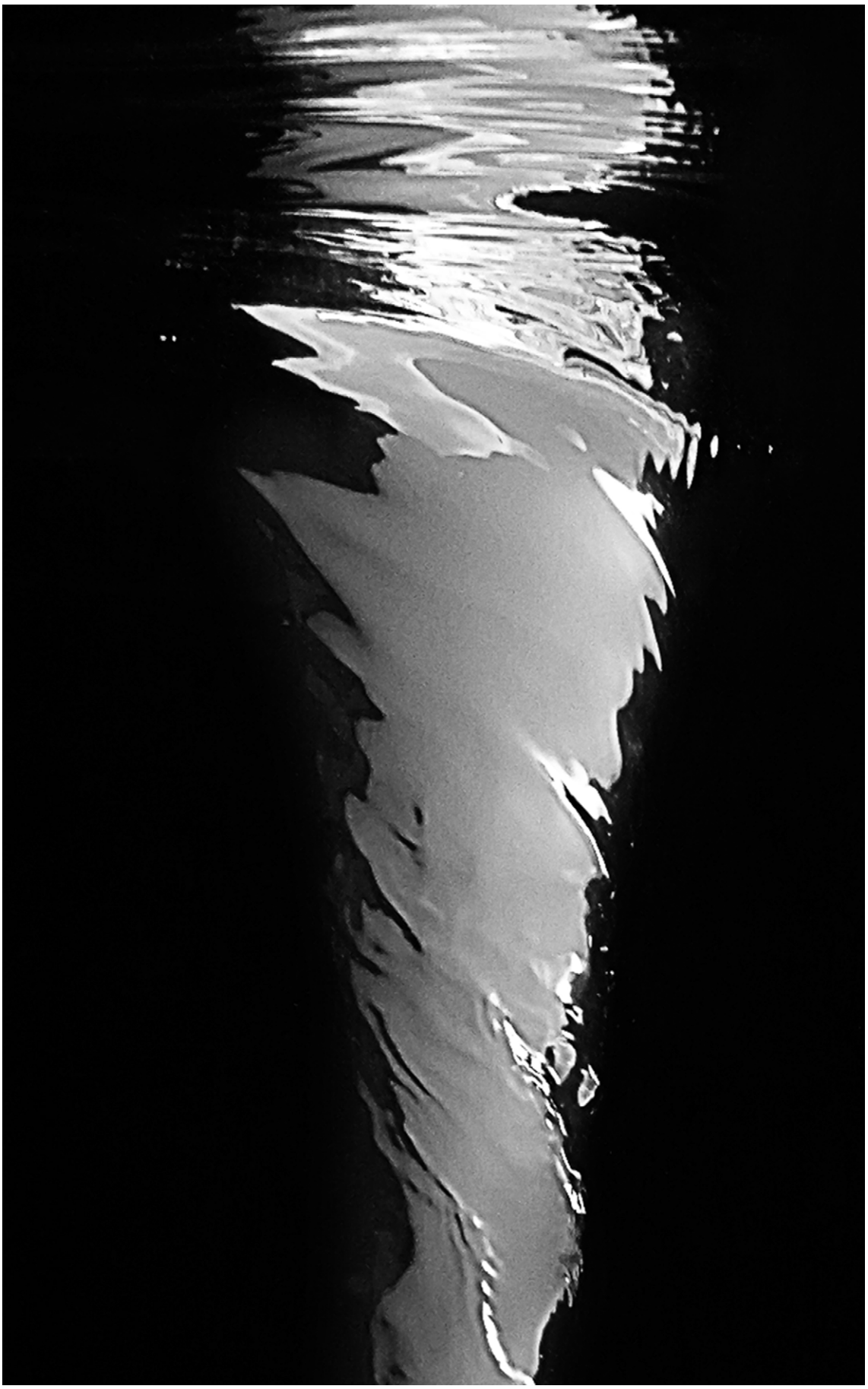

Figure 7.6: Detail (sinkhole) of the air-core tube flow filled up with dry ice fog.

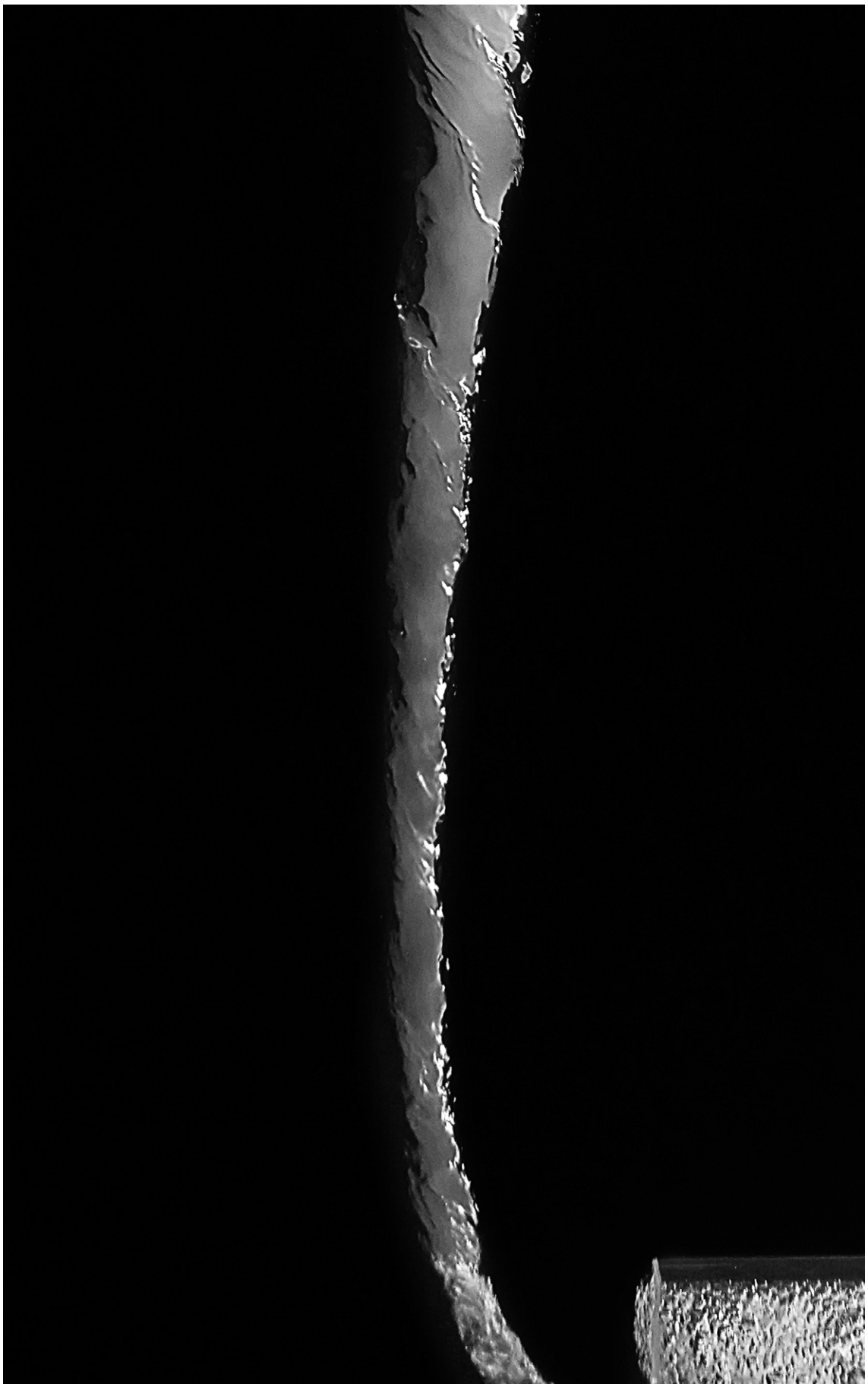

Figure 7.7: Detail (straight air-core) of the air-core tube filled up with dry ice fog.

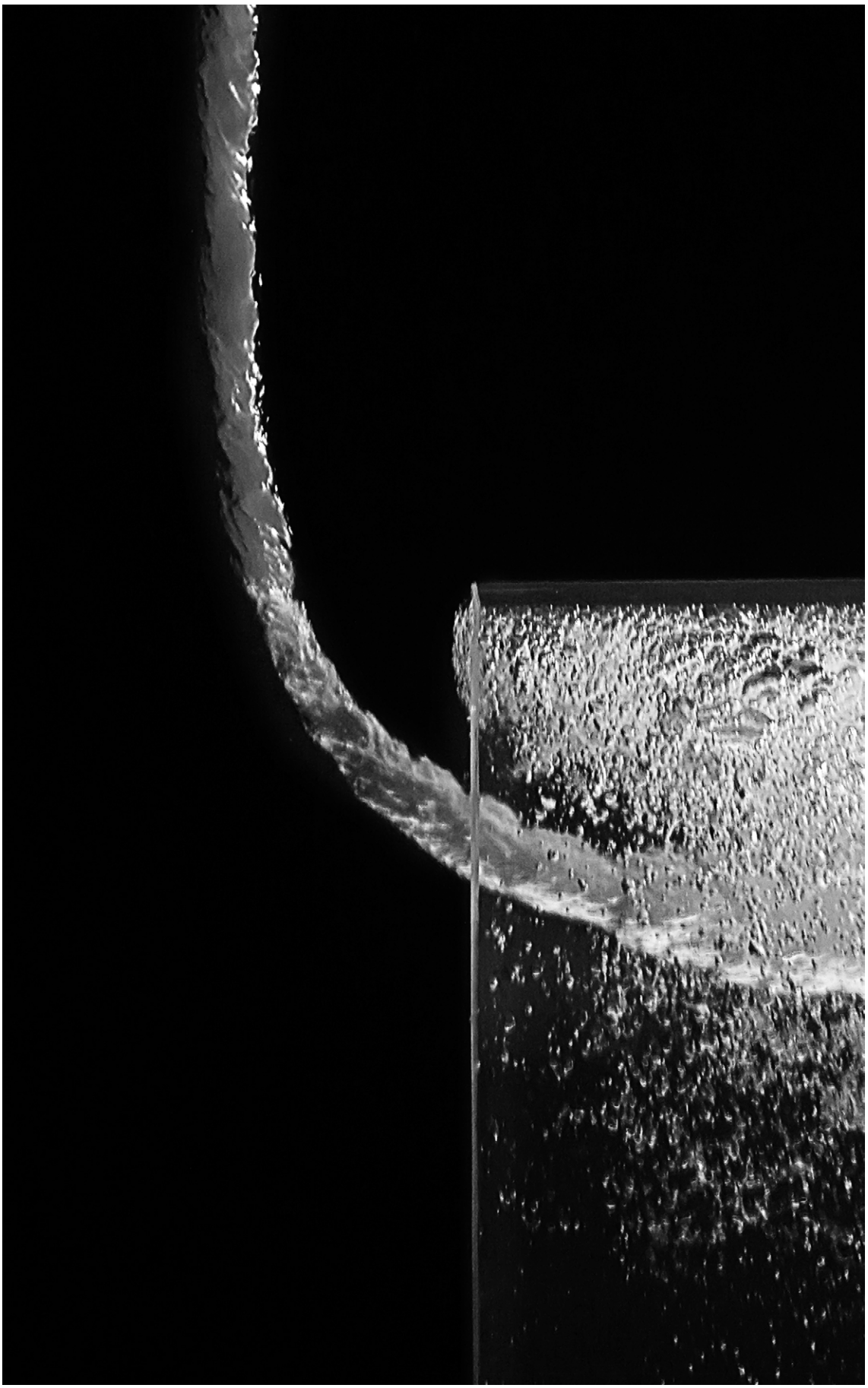

Figure 7.8: Detail (bent air-core) of the air-core tube filled up with dry ice fog.

7.3 Air-Core Diameter d_{ac}

7.3.1 Air-Core Diameter of Exemplary Experimental Runs

The air-core diameter d_{ac} of the intake-vortices is determined by object detection techniques applied to the PIV images (see chapter 4.5). The lower limit of the detectable air-core diameter is given by

$$d_{\mathrm{ac,\,min}} = \frac{L_{\mathrm{FOV}}\; d_{\mathrm{px,\,min}}}{L_{\mathrm{CCD}}}, \tag{7.4}$$

where $d_{\mathrm{px,\,min}} = 5.6$ px is depending on the object detection algorithm and the distance between the shadow area, where the air-core is detected indirectly to the air-core itself ($d_{\mathrm{px,\,min}} = 7.0$ px/1.25, see chapter 5.3), $L_{\mathrm{CCD}} = 2048$ px (see chapter 3.4) and L_{FOV} varies from 938.3–1061 mm (Table 4.2). Consequently, the smallest diameters that are detectable vary between $d_{\mathrm{ac,\,min}} = 2.6$–$2.9$ mm. Additionally, similar to the circulation data processing, despiking and filtering algorithms are applied to the detected air-core data. Fig. 7.9 shows the determined air-core diameter d_{ac} of run #2 exemplarily.

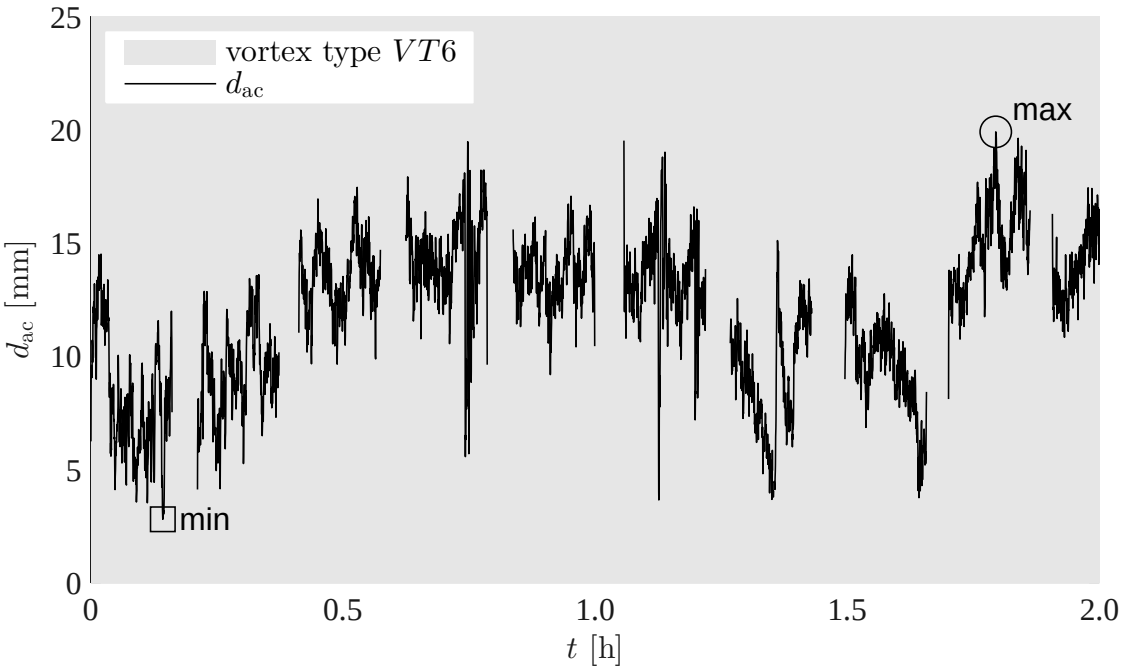

Figure 7.9: Time series of measured air-core diameter d_{ac} within experimental run #2, where in total ten PIV runs #2.1–#2.10 have been carried out. The gray area indicates that vortex type $VT6$ was present over the entire measurement duration.

The gray background indicates the presence of vortex type $VT6$. Ten PIV runs were conducted within this experimental run. Breaks between these runs become

obvious and occur mainly due to the PIV procedure (see chapter 4.4). However, if no vortex $VT6$ is present or if the object detection procedure works incorrectly, smaller breaks evolve as well. Regarding the latter shortcoming, the threshold values were chosen to achieve only valuable and robust results. For the example given in Fig. 7.9 they range between $d_{\mathrm{ac}} = 2.8$–19.9 mm. Both kinds of air-core vortices, the smallest and the largest one within run #2, are shown in Fig. 7.10 to give an impression on the range of there size.

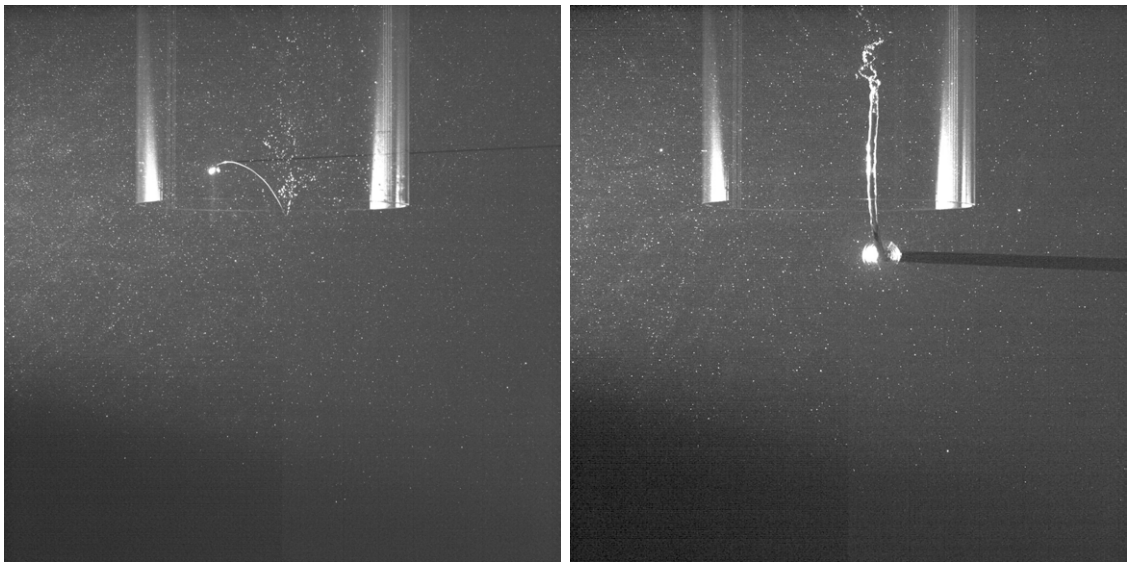

(a) Minimal $d_{\mathrm{ac}} = 2.8$ mm (7 px), image at $t = 515$ s.

(b) Maximal $d_{\mathrm{ac}} = 19.9$ mm (51.7 px), image at $t = 6461$ s.

Figure 7.10: Examples of air-core diameter d_{ac} within run #2.

In contrast to run #2 where $VT6$ was present over the whole measurement duration, in many runs the occurrence of $VT6$ showed an unsteady behavior or d_{ac} was too small to be detected. A typical example is given in Fig. 7.11 for experimental run #28, where additionally the largest range of $2.8 \leq d_{\mathrm{ac}} \leq 34.8$ mm within an experimental run was observed. Obviously, the number of detected air-cores is smaller than in run #2. The PIV images of both the smallest and the largest detected air-core diameter are shown separately in Fig. 7.12. Generally, the determined air-core diameter have a larger range and strong variations within short times. The range over all runs is $2.6 \leq d_{\mathrm{ac}} \leq 34.8$ mm. To inspect the nature of the air-core diameters' variability a histogram analysis was performed. Fig. 7.13 shows the normalized histograms of runs #2 and #28. It becomes obvious that the mean, the median and the mode of these distributions are different. To give a single characteristic value of air-core diameter would be misleading. However, the median gives an idea. Here, $\tilde{d}_{\mathrm{ac}} = 12.5$ mm holds for run #2 and an almost doubled $\tilde{d}_{\mathrm{ac}} = 20.0$ mm results for run #28.

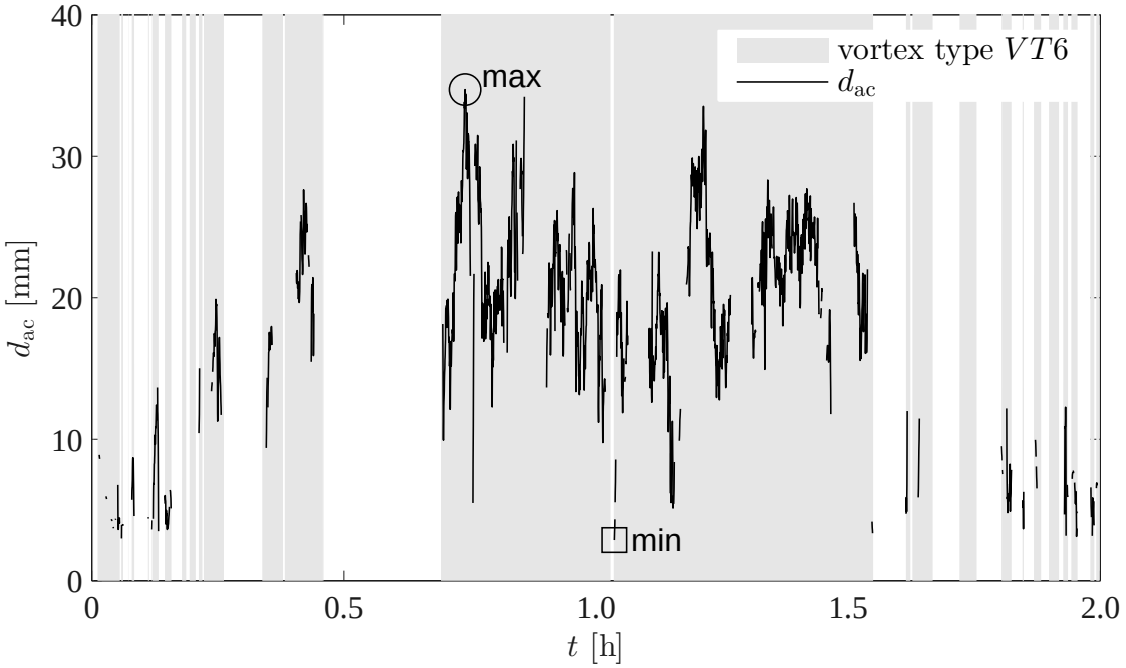

Figure 7.11: Time series of measured air-core diameter d_{ac} within experimental run #28, where in total ten PIV runs #28.1–#28.10 have been carried out. The gray areas indicates the presence of a vortex type $VT6$.

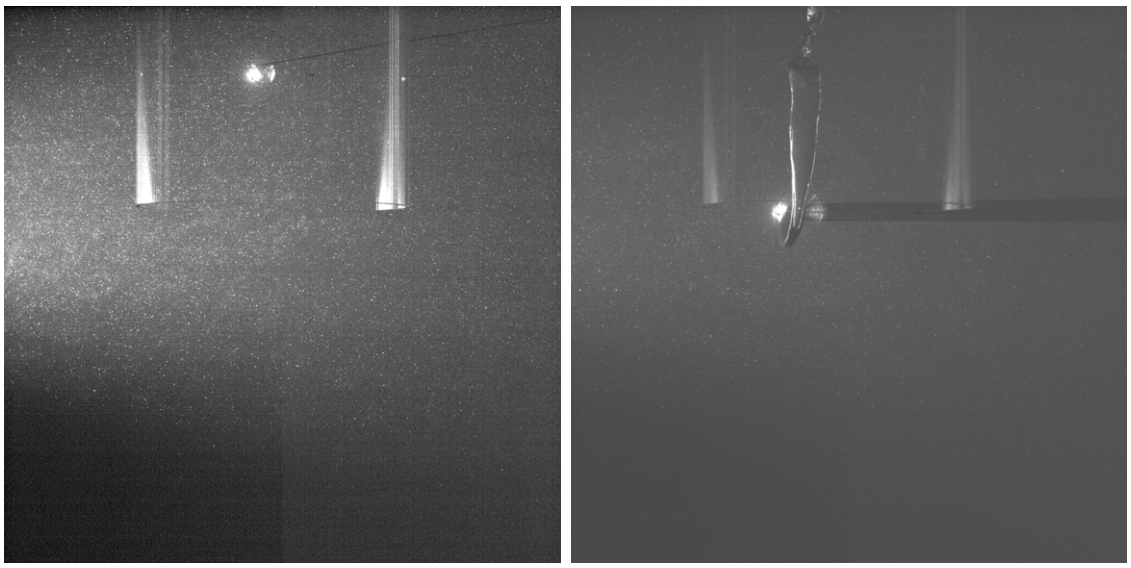

(a) Minimal $d_{ac} = 2.8$ mm (7 px), image at $t = 3731$ s.

(b) Maximal $d_{ac} = 34.8$ mm (86.0 px), image at $t = 2666$ s.

Figure 7.12: Examples of air-core diameter d_{ac} within run #28.

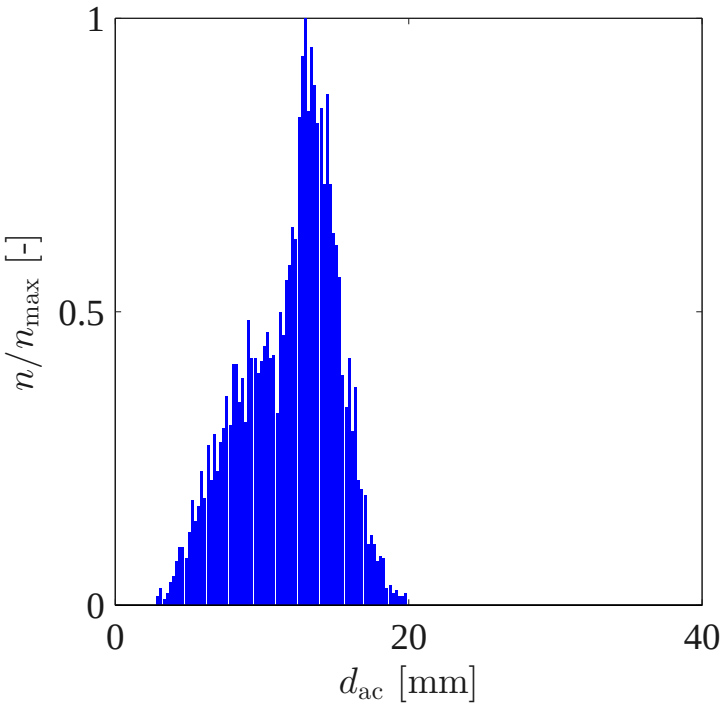

(a) Run #2, $\tilde{d}_{\mathrm{ac}} = 12.5$ mm.

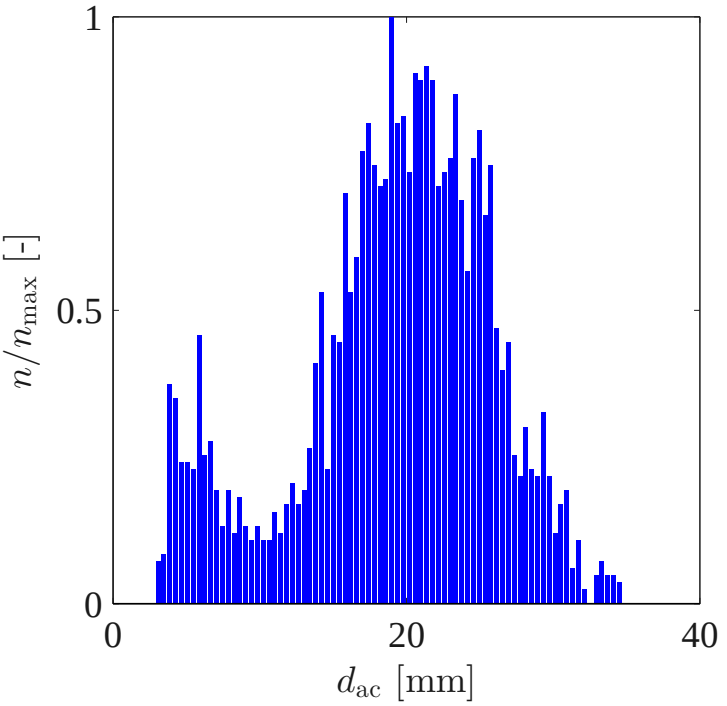

(b) Run #28, $\tilde{d}_{\mathrm{ac}} = 20.0$ mm.

Figure 7.13: Histograms for air-core diameter d_{ac} within the example runs.

7.3.2 Air-Core Diameter of all Experimental Runs

The air-core diameter d_{ac} determined with a frequency of 1 Hz is unevenly distributed as shown above. The relation $\tilde{d}_{\mathrm{ac}} = f(h/D, \mathsf{F}_{\mathrm{co}})$ is analyzed hereafter, however.
Fig. 7.14 gives a comparison of the combined Froude number F_{co} to the median air-core diameter $\tilde{d}_{\mathrm{ac}}$. No significant relationship becomes obvious. The linear correlation coefficient[4] of all runs is $\rho_{X,Y} = 0.25$ and therefore the correlation is small.

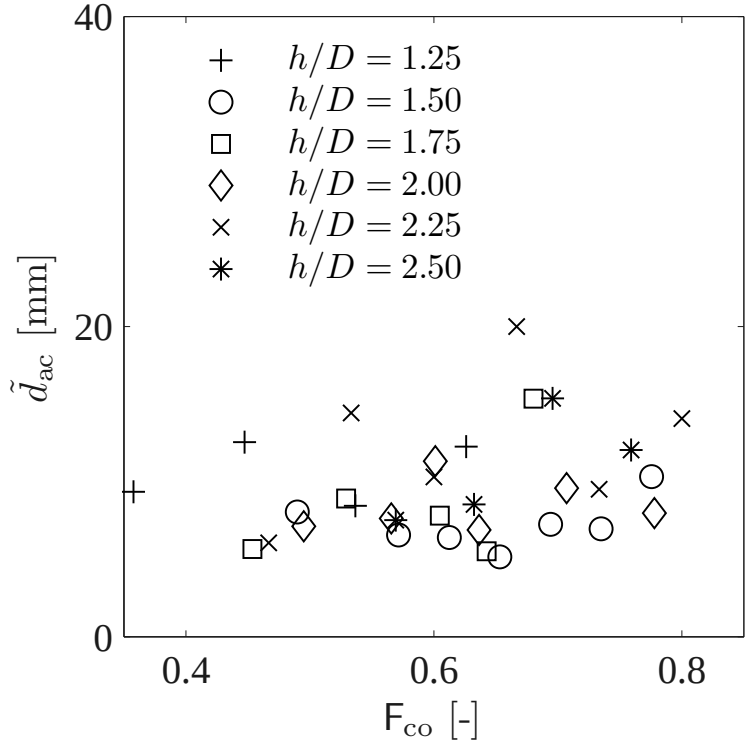

Figure 7.14: Median air-core diameter $\tilde{d}_{\mathrm{ac}}$ of the experimental runs compared to the combined Froude number F_{co}.

Regarding the different relative submergences h/D shown in Fig. 7.14 a slightly varying trend can be determined. However, a robust relationship concerning the intake flow conditions is not recognizable. Based on several regression analyses no significant relationship could be found. Therefore it is assumed, that the air-core diameter and the common flow parameter are not significantly related.

[4]Correlation coefficient $\rho_{X,Y}$ after Pearson: $\rho_{X,Y} = \frac{\mathrm{cov}(X,Y)}{\sigma_X \sigma_Y} = \frac{E[(X-\mu_X)(Y-\mu_Y)]}{\sigma_X \sigma_Y}$. The correlation coefficient between two variables is defined as the covariance of the two variables divided by the product of their standard deviations. Here, no regression analysis is necessary. In contrast to the correlation coefficient the coefficient of determination R^2 is used to describe how well a regression line fits a set of data.

7.4 Air-Core Diameter vs. Circulation

The air-core diameter d_{ac} and the circulation Γ are processed from the same PIV images. Thus in opposite to the comparison of the air entrainment measurements vs. the PIV results, no time lack has to be considered. Recordings were made at a frequency of 1 Hz.

Fig. 7.15 shows both time series of the determined air-core diameter d_{ac} and the circulation Γ within run #2. Both signals show a quite similar shape within this run indicating a strong positive correlation. Due to a continuous presence of an air-core vortex during the whole run, Γ is clearly above zero. The computed air-core diameter falls at no time below the minimal detectable air-core diameter of 2.8 mm. However, this implies not per se that a vortex was present, as a smaller vortex or no vortex, i.e. $< VT6$ would have been possible as well.

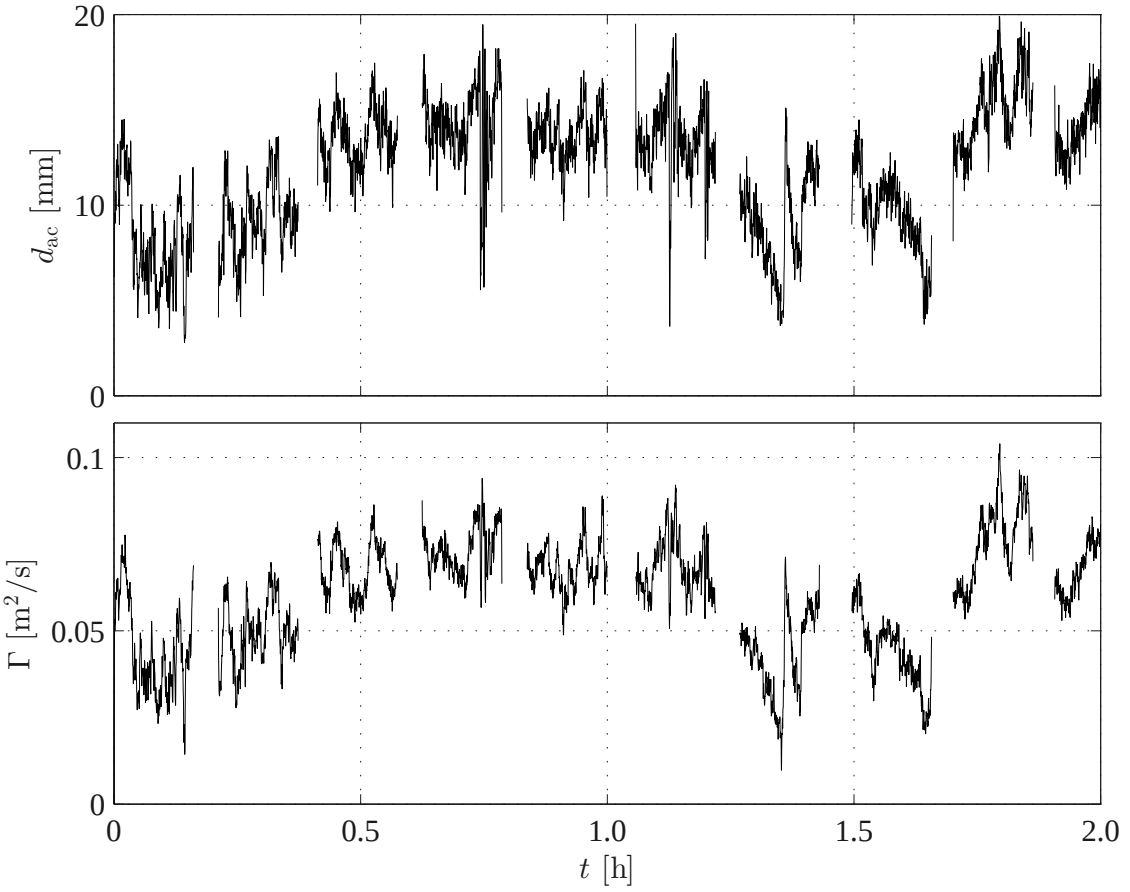

Figure 7.15: Time series of run #2 with determined air-core diameter d_{ac} and circulation Γ. An air-core vortex was present during the whole experimental run over 2 h.

Next, the obvious matching of both time lines is inspected via a scatter plot as given in Fig. 7.16. To achieve equal dimensions the air-core diameter is multiplied by the

mean intake velocity v_D to result in [m^2/s]. A linear trend of all 6400 data points becomes obvious. A regression analysis that applies a least squares fit results in

$$\Gamma_{\#2l} = 5.1\, d_{ac} v_D \ (\mathrm{R}^2 = 0.84) \tag{7.5a}$$

$$\text{and } \Gamma_{\#2lo} = 4.7\, d_{ac} v_D + 0.0054 \ (\mathrm{R}^2 = 0.84)\ , \tag{7.5b}$$

where the index #2l indicates a linear approach without and #2lo indicates a linear approach with an offset. The coefficients of both equations are found by a regression analysis while applying the method of least squares. The findings are quite similar. Eq. 7.5a and 7.5b are given in Fig. 7.16 as well. As the gradient of both lines is similar the offset in eq. 7.5b is relatively small, indicating a small initial Γ being necessary to get an air-core at the height of the PIV laser sheet. The coefficients of determination $\mathrm{R}^2 = 0.84$ for both equations confirm this analogy.

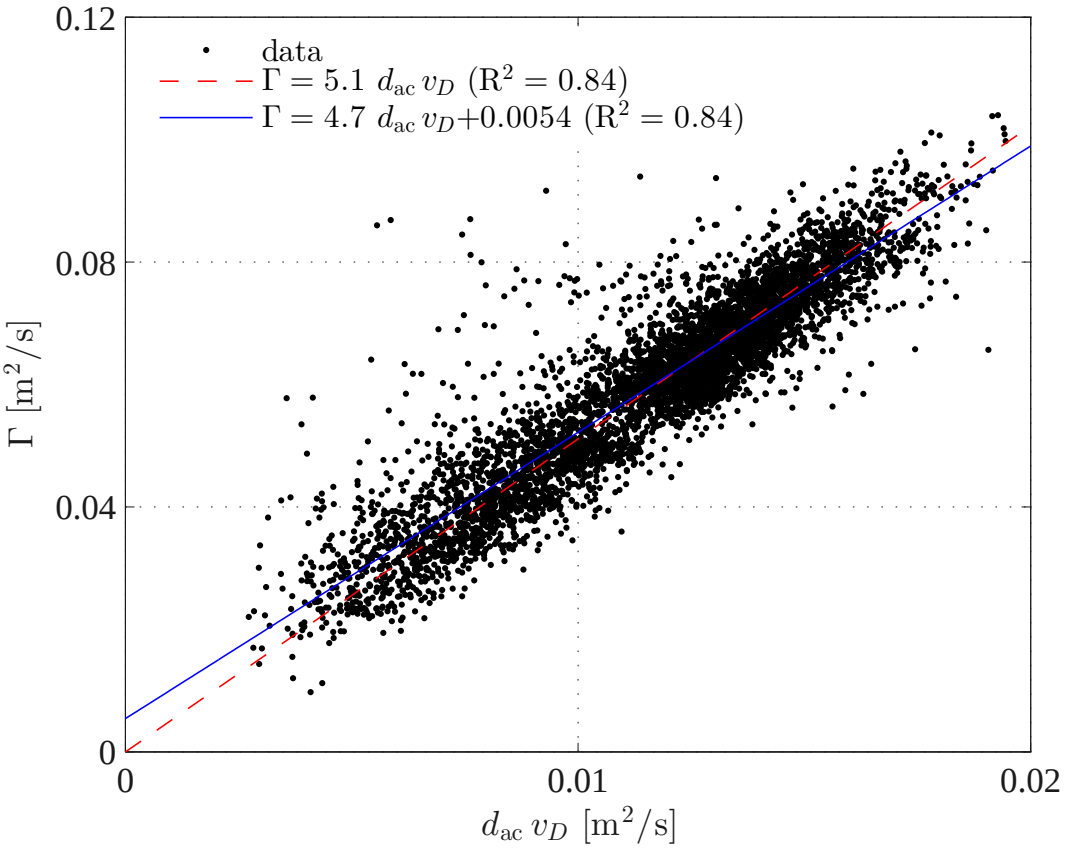

Figure 7.16: Comparison of actual air-core diameter d_{ac} multiplied by v_D and the corresponding circulation Γ within experimental run #2.

A physical reason of the noticed offset has to be checked. As mentioned above small d_{ac} are filtered out, and consequently the data points do not reach the origin. That

means the cluster of data is thinned out while approaching the lower limit of possible air-core diameter detection. This could be affirmed by the approach that a minimal circulation must be necessary to generate an initial air-core vortex. In other words: an offset is physically based and the offset gives an initial $\Gamma_{\min,VT6}$.
Fig. 7.17 shows the time series of the second exemplary run #28.

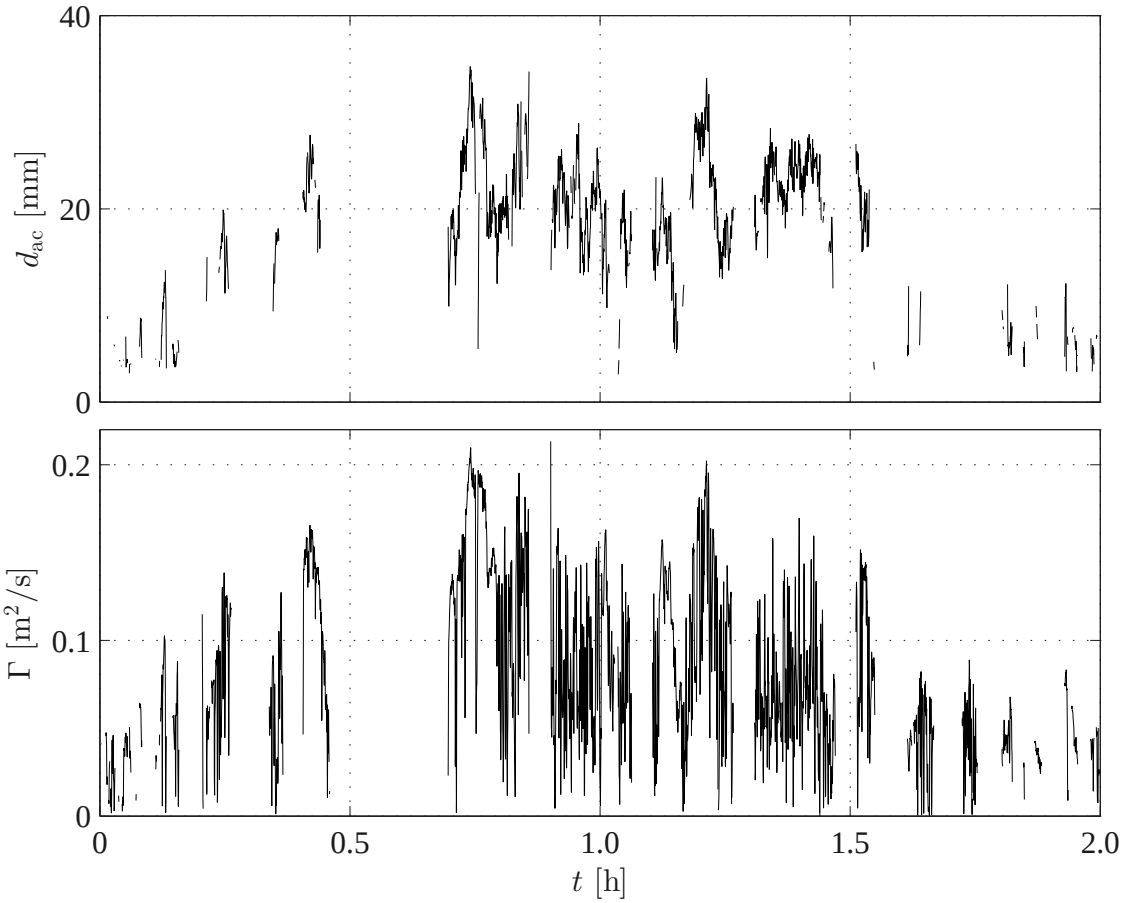

Figure 7.17: Time series of run #28 with determined air-core diameter d_{ac} and circulation Γ. An air-core vortex was present 64 % of the run. Note that both vertical axes are doubled in comparison to Fig. 7.15.

As assessed in the previous sections, the fluctuations of air-core diameter d_{ac}, circulation Γ and also the presence of vortex type $VT6$ during the whole experimental run are higher than in example run #2. Hence, the data in Fig. 7.18 could not be expected to have a clear relationship as for the data of first exemplary run #2. A regression analysis that applies a least squares fit results in

$$\Gamma_{\#28l} = 2.4\, d_{ac} v_D \ (R^2 = 0.18) \tag{7.6a}$$

$$\text{and } \Gamma_{\#28lo} = 1.7\, d_{ac} v_D + 0.0278 \ (R^2 = 0.21) \tag{7.6b}$$

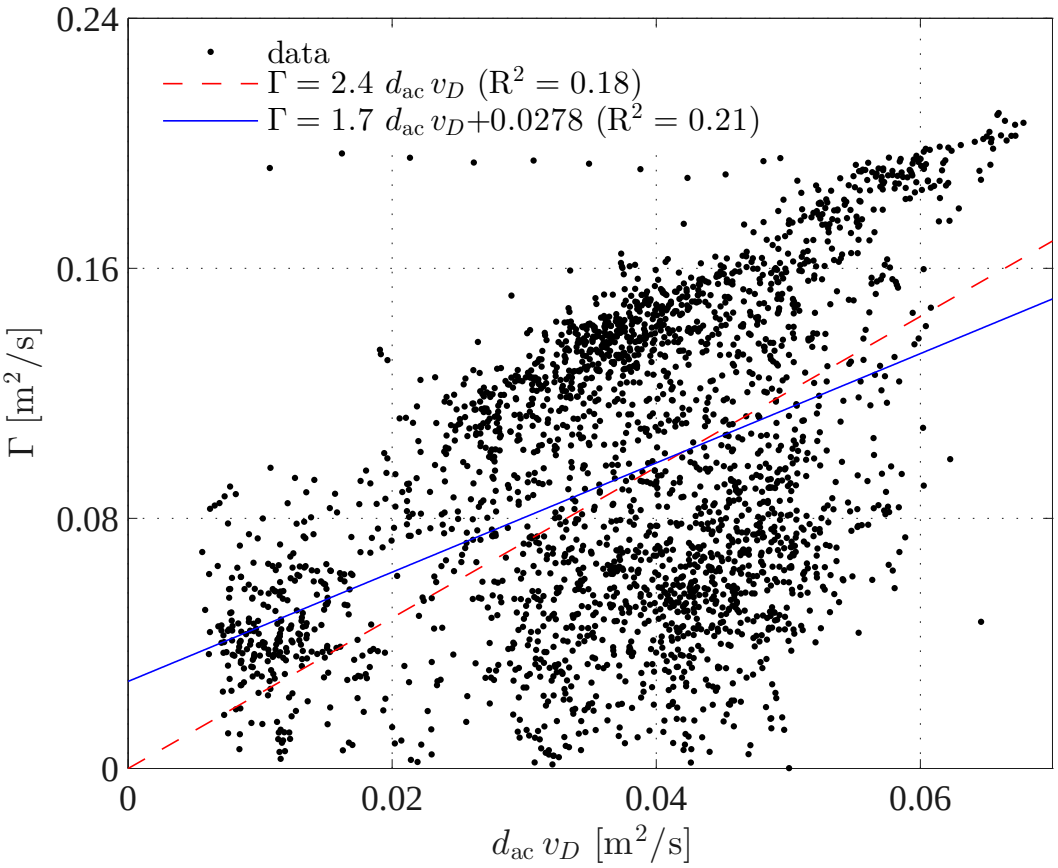

Figure 7.18: Comparison of actual air-core diameter d_{ac} multiplied by v_D and the corresponding circulation Γ within experimental run #28.

Whereas run #2 showed robust values of R^2 for a linear regression of Γ and d_{ac}, this is obviously not the case for run #28. For exemplary run #2 the correlation coefficient of the data shown in Fig. 7.16 is $\rho_{X,Y} = 0.92$. Fig. 7.19 shows the correlation coefficients for runs #[1–34]. A common interpretation of the magnitude of this coefficient is follows: A medium correlation is present holds for $|0.3 \leq \rho_{X,Y} \leq 0.5|$ and a strong correlation if $|0.5 \leq \rho_{X,Y} \leq 1.0|$.

23 of 32 runs (72 %) have at least a medium correlation. A strong correlation has been found for 17 of 32 runs (53 %). Runs with lower correlation coefficients near the upper border of the diagnal band are shown in Fig. 6.5. The runs in Fig. 7.19 are sorted after h/D and than after F_D (see Table 4.2). Additionally, this information is given in Fig. 7.19 by the normalized values $(h/D)/\max(h/D)$ and $\mathsf{F}_D/\max \mathsf{F}_D$. The air entrainment increases from the upper to the lower border of this diagonal band which is a function of h/D and F_D.

A large air-core vortex and air bubbles in the intake pipe are strongly affecting the data processing of the velocity vector maps. Thus, the circulation is not determined unambiguously in runs with large air entrainment rates. At the same h/D the air entrainment is increasing with F_D. The influence on the performance to compute

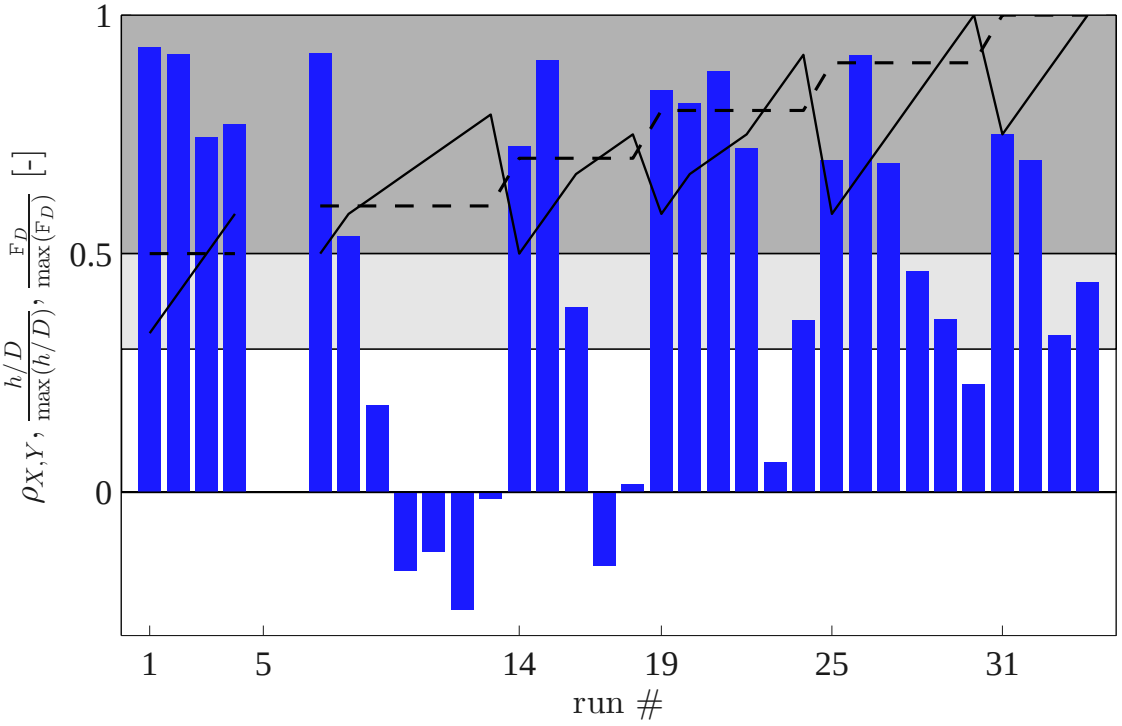

Figure 7.19: Correlation coefficient $\rho_{X,Y}(\Gamma, d_{\mathrm{ac}} v_D)$ for runs #[1–34] indicated by bars. The abscissa indicates each first run of h/D similar to Table 4.2. Additionally, $(h/D)/\max(h/D)$(dashed line) and $\mathsf{F}_D/\max \mathsf{F}_D$ (solid line) are delineated. A strong correlation is indicated by a dark gray background and a medium correlation by a light gray background. Small or none correlation is indicated in white. Note: run #[5, 6] could not be correlated at all due to an infrequent occurrence of a vortex type $VT6$.

the circulation can be seen by a decreasing $\rho_{X,Y}$ in Fig. 7.19 in each case after run = [1, 5, 14, 19, 25, 31]. On this basis, it can be assumed that the runs with a strong correlation can be used to describe the physical process adequately.
A regression analysis, including runs with strong correlation coefficients, concerning the coefficients *gradient* and *offset* results in a simple approximation:

$$\Gamma = \widetilde{gradient}\; d_{\mathrm{ac}}\, v_D\,, \tag{7.7}$$

where the median gradient $\widetilde{gradient} = 4.5$ implies a relatively small IQR = 1.3.
By eq. 7.7 a valuable correlation between the circulation Γ and the air-core diameter d_{ac} times v_D is found. These parameters describe the surrounding velocity field of the vortex and the developed air-core independent of the remaining parameters. The intake velocity v_D is used to achieve the same units.

7.5 Air-Core Flow Velocity

Figs. 7.20 and 7.21 show the data of the air discharge Q_a plotted against the air-core diameter d_{ac} of the exemplary runs #2 and #28. Fig. 7.20 depicts a stage of air entrainment, where the air-core diameter d_{ac} has a considerable size, but the air entrainment quantified by the air discharge Q_a is very small and slightly above the minimum measurable Q_a. A first interpretation is that a common air-core can be present without a considerable air entrainment. The vertical data lines in Fig. 7.20 are due to the fact that d_{ac} is detected second by second separately, but Q_a has to be determined by detrending the pressure signal of the rising pipes covering a time window of several seconds length (see chapter 6.1.2). An averaging of the vertically distributed data results more or less in a horizontal line for run #2. This indicates that, in the present case, the air discharge Q_a is independent of the air-core diameter d_{ac}. No trend of the presented data of run #2 is obvious.

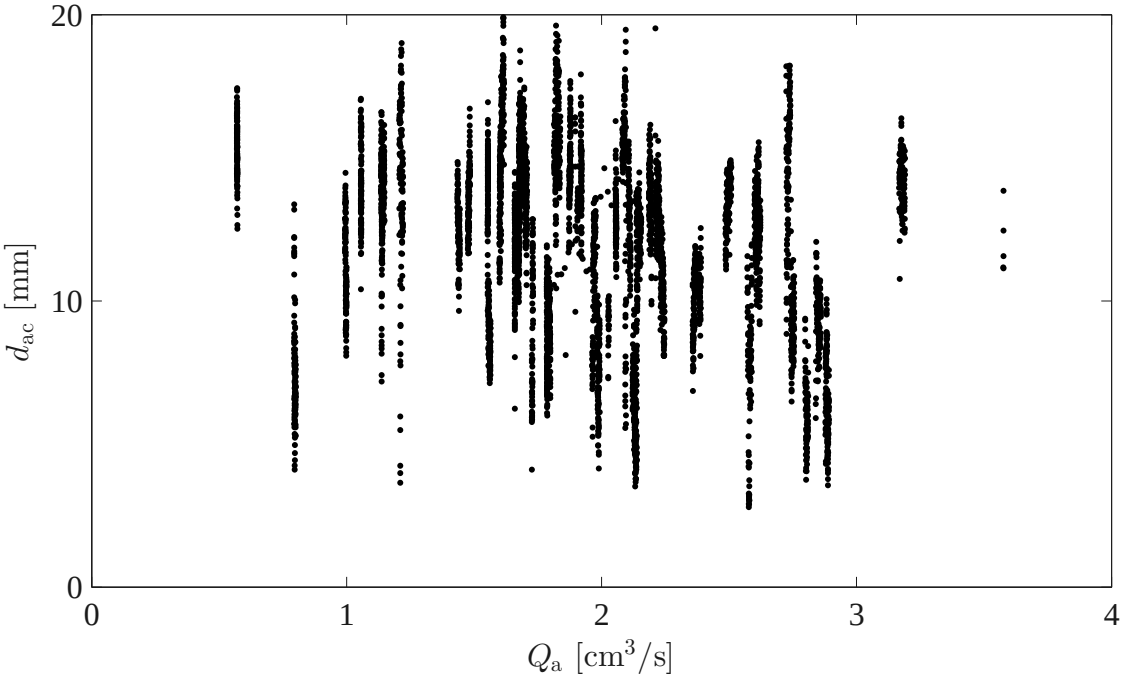

Figure 7.20: Comparison of air discharge Q_a and the air-core diameter d_{ac} data of exemplary run #2.

Fig. 7.21 presents the data of the second exemplary run. Although, the vertical lines are still prominent, an increase of Q_a with increasing d_{ac} becomes obvious. Generally, compared to the first exemplary run shown in Fig. 7.20, considerably higher air discharges Q_a of more than two orders of magnitude are based on air-core diameters d_{ac} which are only twice as large. The hypothesis that Q_a and d_{ac} are independent appears still reasonable.

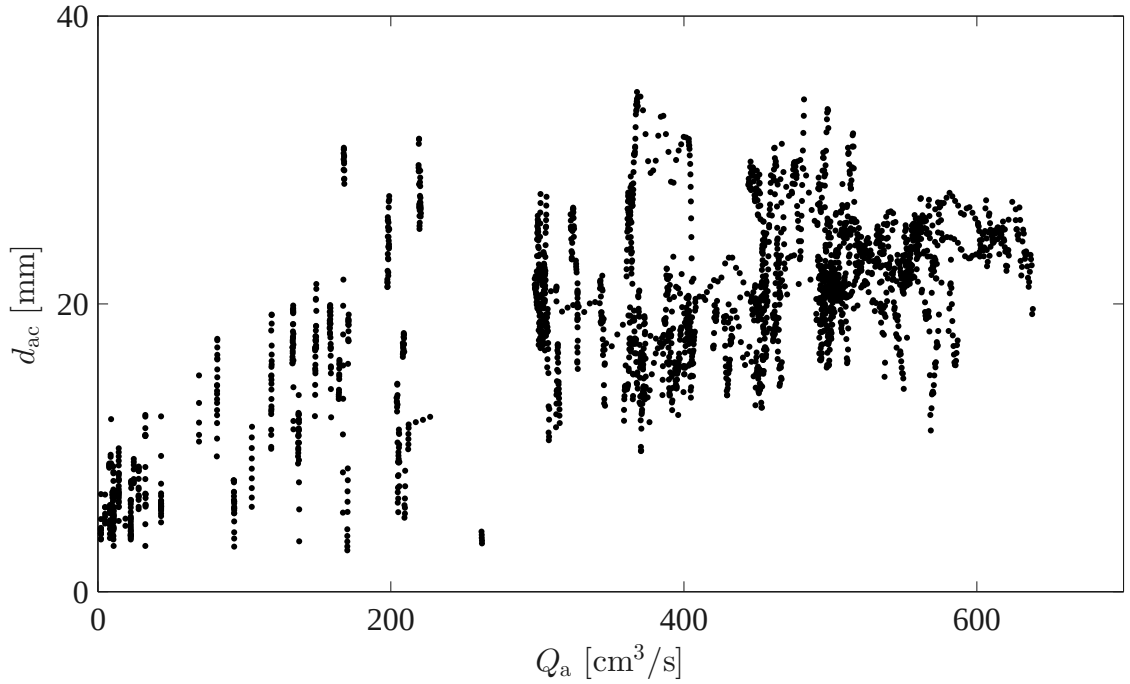

Figure 7.21: Comparison of air discharge Q_a and the air-core diameter d_{ac} data of exemplary run #28. Note that in comparison to Fig. 7.20 the vertical axis is doubled and the horizontal axis is upscaled by factor 175.

The air-core flow velocity v_{ac} can be determined using the continuity equation as a function of the air discharge Q_a (see chapter 6.1.2) and the air-core diameter d_{ac} (see chapter 7.3):

$$v_{ac} = \frac{Q_a}{A_{ac}} = \frac{4\,Q_a}{\pi d_{ac}^2}\,, \tag{7.8}$$

where A_{ac} is the cross sectional area of the air-core tube. Based on eq. 7.8 the average air flow velocity in the air-core tube v_{ac} is determined. Fig. 7.22 shows the dependency of v_{ac} and d_{ac} for both exemplary runs. The air-core flow velocity v_{ac} as a function of the air-core diameter d_{ac} behaves quite similar in all experimental runs. Generally, a characteristic decrease of d_{ac} for increasing v_{ac} can be observed. Hence, small velocities occur while large tube diameters are present. Vice versa, large velocities occur at small diameters. These velocities are one or two magnitudes larger than the intake pipe velocity v_D. The obtained overall range is $v_{ac} = 0$–90 m/s, where as the mean air-core velocity is $\bar{v}_{ac} = 1.4$ m/s.

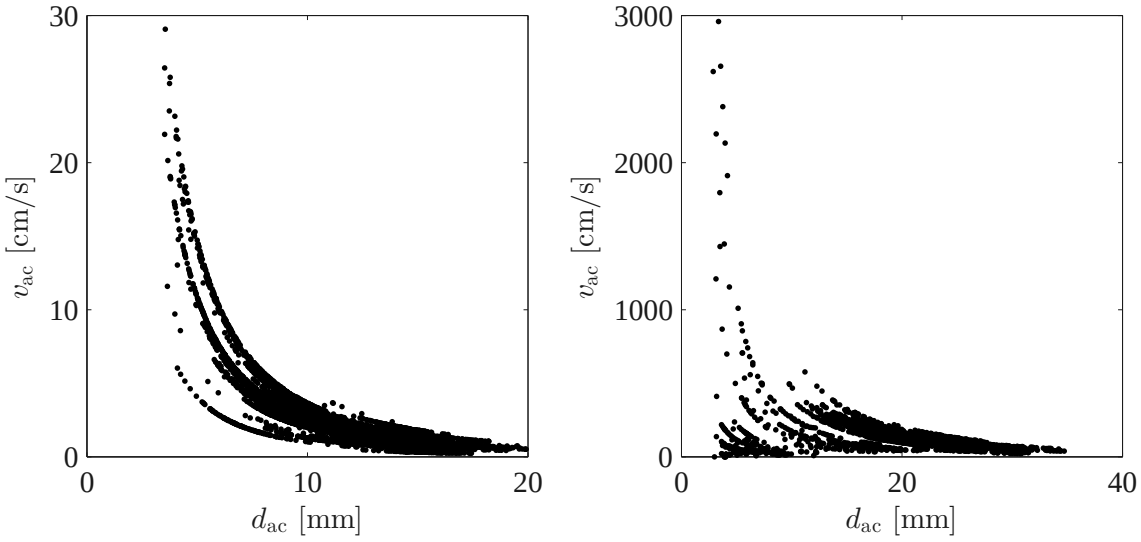

(a) run #2 (b) run #28

Figure 7.22: Air-core flow velocity v_{ac} depending on d_{ac} for two exemplary runs.

The kinematic viscosity of air ν_a is nearly 15 times greater than water (see chapter 9.2). Therefore, it can be assumed that the boundary layer of the air flow velocity profile has a dominant effect on the head loss while air is passing through the air-core tube. The size and shape of the boundary layer depends mainly on the degree of turbulence.

The characterization of pipe or tube flow is usually made by the Reynolds number. Therefore, the air-core tube Reynolds number can be written as

$$\mathsf{R}_{ac} = \frac{v_{ac}\, d_{ac}}{\nu_a}. \tag{7.9}$$

Generally, for fully developed flow in a pipe of diameter D, experimental observations conducted by Osborne Reynolds[5] show that laminar flow occurs for $\mathsf{R}_D < 2300$ and turbulent flow occurs for $\mathsf{R}_D > 4000$. For $2300 \leq \mathsf{R}_D \leq 4000$, laminar and turbulent flows are possible. Consequently, this flow is called transition flow and is affected by the pipe roughness and flow uniformity. However, laminar flow can also occur at higher Reynolds numbers and, vice versa, turbulent flow for lower Reynolds number. Fig. 7.23 shows the air-core tube Reynolds number determined from eq. 7.9 for both exemplary runs in log-log-plots. The air-core diameter d_{ac} is normalized by the intake pipe diameter D. The transition zone from laminar flow to turbulent flow is highlighted by vertical lines. Both runs feature both laminar and turbulent flows.

[5]Osborne Reynolds (⋆23 August 1842 in Belfast, †21 February 1912 in Watchet) was a prominent Anglo-Irish innovator in the understanding of fluid dynamics.

In almost every experimental run the transition zone has been reached. Runs with large air entrainment rates tend to have rather high Reynolds numbers and thus the flow is mainly turbulent according to the common classification of Reynolds.

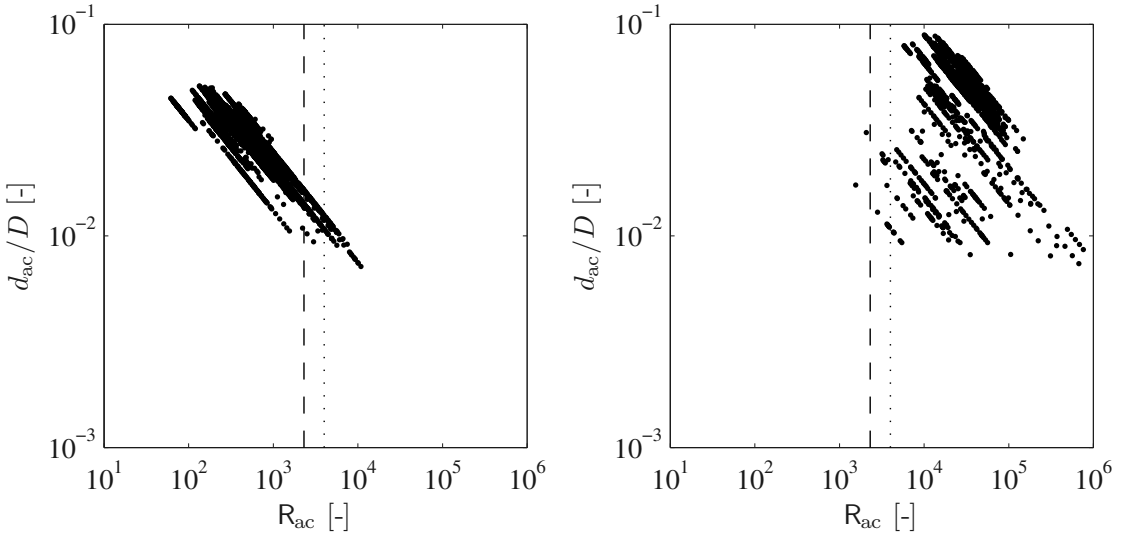

(a) run #2 (b) run #28

Figure 7.23: Air-core tube Reynolds number R_{ac} vs. the relative air-core diameter d_{ac}/D for both exemplary runs, with transition zone between laminar flow $\mathsf{R}_{ac} < 2300$ (dashed line) and turbulent flow $\mathsf{R}_{ac} > 4000$ (dotted line).

An analysis of all experimental run data regarding the air-core tube Reynolds number is made as function of the combined Froude number F_{co}. A distinction is made between the median air-core tube Reynolds number $\tilde{\mathsf{R}}_{ac}$ and the mean air-core tube Reynolds number $\bar{\mathsf{R}}_{ac}$. Fig. 7.24 shows the air-core tube Reynolds number R_{ac} vs. the combined Froude number F_{co} of all experimental runs.
As expected the mean value is in average for each experimental run approximately 40 % larger as it is strongly affected by single large values of an experimental run dataset. To find a general relationship the regression analysis is conducted while using all data as shown in Fig. 7.24. Note that here a robust least-squares regression is applied to reduce the sensitivity to outliers. Additionally, the coefficient of determination R^2 is computed while less considering the outliers (MATLAB, 2013). The relationship of the turbulence characteristics in the air-core tube and the common flow parameter can be described by

$$\mathsf{R}_{ac} = 4.4\, e^{13.7\,\mathsf{F}_{co}} \ (\mathrm{R}^2 = 0.99). \tag{7.10}$$

Surprisingly, the air-core flow velocity is quite high and occasionally one or two orders of magnitude higher than the actual intake pipe velocity. During the formation

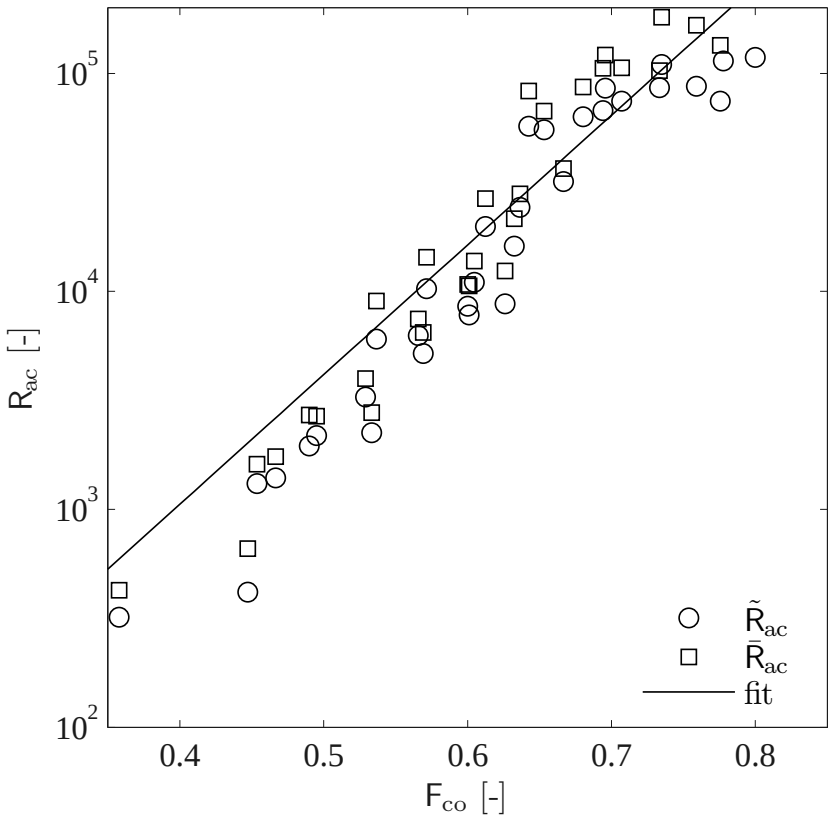

Figure 7.24: Air-core tube Reynolds number R_{ac} vs. the combined Froude number F_{co} averaged for each experimental run. The median air-core tube Reynolds number $\tilde{R}_{ac}$ and the mean air-core tube Reynolds number $\bar{R}_{ac}$ are depicted separately. The frequently fit is achieved with all data shown and can be described by eq. 7.10.

and decay of an air-core vortex the air-core diameter, the air discharge and thus the air-core flow velocity change in a wide range. Consequently, the turbulence characteristics change frequently from laminar to turbulent flow and vice versa. It is assumed, however, that this crucial change in flow has no effect on the surrounding water flow due to the large difference in density between air and water.

It is further assumed that the driving process of air entrainment is the pressure drag flow. This flow entrains air bubbles from the air-core. The demand of air is delivered by air from the free surface. Physically expressed, pressure compensation occurs due to the low pressure at the air-core tail.

The size of the air-core tube is of secondary importance regarding the quantity of air entrainment. If pressure compensation takes place, the air-core cross-section is influencing the head losses. Therefore, considerable air-core diameters may occur while almost no air entrainment is observed.

7.6 Vortex Formation and Air-Core Flow Process

As already mentioned in chapter 2.2 the vortex formation at intakes is strongly related to the vorticity. Especially vorticity tubes and their solenoidal nature provide the key to understand the vortex formation at intakes.
Fig. 7.25 shows a vorticity tube approaching a horizontal intake. Due to the acceleration of the flow towards the intake the tube is stretched, while both ends are still connected to the boundaries. Vorticity tubes as depicted in Fig. 2.6b, where both ends are at the free surface, behave in a similar manner. The stretching in the vicinity of the intake induces a faster rotation of the tube. Once the tube is caught in the intake, the basis is given for a free surface and a subsurface vortex, respectively. At the free surface these ends occur as $VT1$–$VT2$ (see Fig. 2.10). The large vorticity within the intake pipe energizes the rotation at tube ends. If the rotation reaches a sufficient value regarding the rotational velocity the pressure in the center of the tube decreases significantly down to atmospheric pressure. This leads to a free surface vortex with an air-core tube down to the intake cross-section. However, a subsurface vortex can develop simultaneously at the same time, but this vortex needs a higher rotational velocity to occur. If present, this core is visible by water steam due to cavitation. The position of both occurring vortices relative to the intake has been confirmed by a large number of observations within this research project.

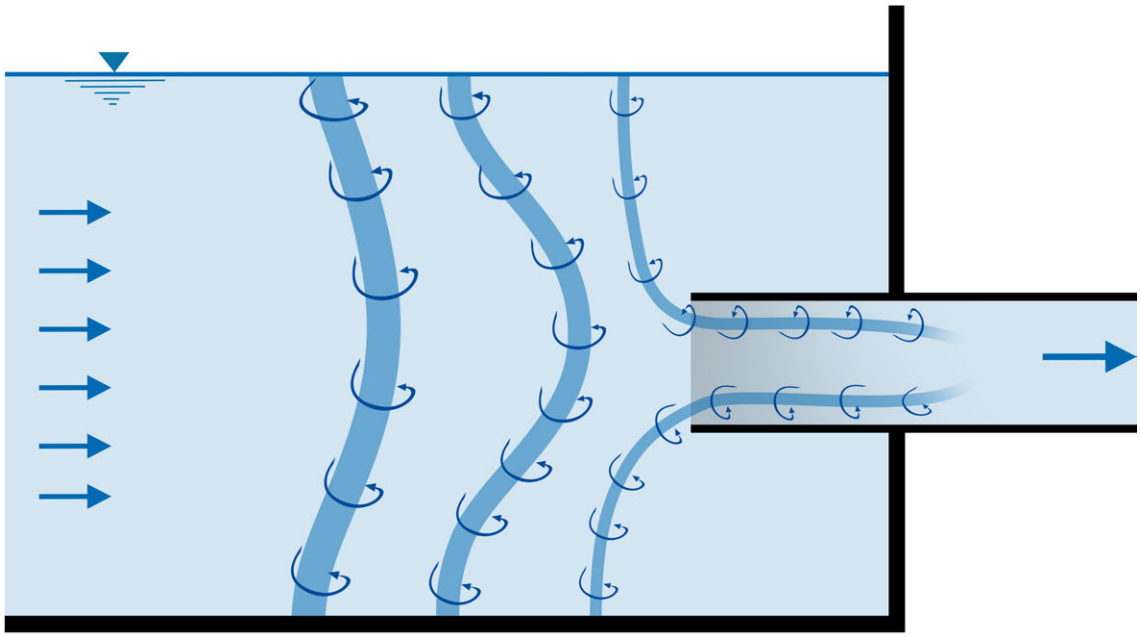

Figure 7.25: Vortex formation due to stretching of vorticity tubes towards the horizontal intake.

Due to the complex flow field that causes a number of vorticity tubes, several vor-

tices at an intake can happen at the same time. Some impressions are shown in appendix D.

The driving process of the air-core flow can be derived from the influencing parameters regarding the quantitative air entrainment. The circulation is not the dominating process in this respect. As has been shown in chapter 7.4 the circulation is strongly correlated to the air-core diameter. Therefore, a strong circulation can be seen to be a necessity to provoke an air-core tube. Once the air-core is developed and reaches the faster flowing water in the vicinity of the intake bubbles are entrained and separated from the air-core. Consequently, it is hypothized that the air-core flow is mainly influenced by the magnitude of intake velocity v_D, and the circulation provokes merely the generation and shape of the tube.

Chapter 8

Results of Vortex Wandering and Critical Intake Submergence

Abstract. *The horizontal movement of a vortex core in relation to the intake section is determined by an algorithm that uses PIV processed velocity fields and object detection methods. Moreover, a new approach is presented to predict the critical submergence with respect to the air entrainment rate.*

8.1 Vortex Wandering

Due to its unsteady behavior an intake-vortex is wandering with respect to its horizontal position. The center coordinates determined within the circulation procedure (see chapter 4.4) are used to track the vortex path. Figs. 8.1–8.3 show six runs exemplarily. Here the point of origin is defined by the intake pipe axis. The scatter depicts the particular positions within the two hours measurement duration by a frequency of 1 Hz. The scatter consists of in maximum 7200 points in total. Their distribution related to the x-axis and the y-axis, respectively, is given as well in Figs. 8.1–8.3. The black rectangle indicates the 2D IQR regarding the x-axis and the y-axis. Note, that the example series is continued by Figs. C.1–C.3 in appendix C.
At low water levels the spread is small (Fig. 8.1). If the water level and, consequently, the distance between intake pipe and free surface is increased, the spread increases as well (Figs. 8.2–8.3). The air-core tube length is more or less the same at larger distances. A large amplitude results in small changes of the angle of the air-core tube with respect to the vertical axis. In a bottom upwards view the vortex occurs mainly left above the intake pipe at higher water levels for the current example, possibly indicating a slight inhomogeneity in the approach flow.

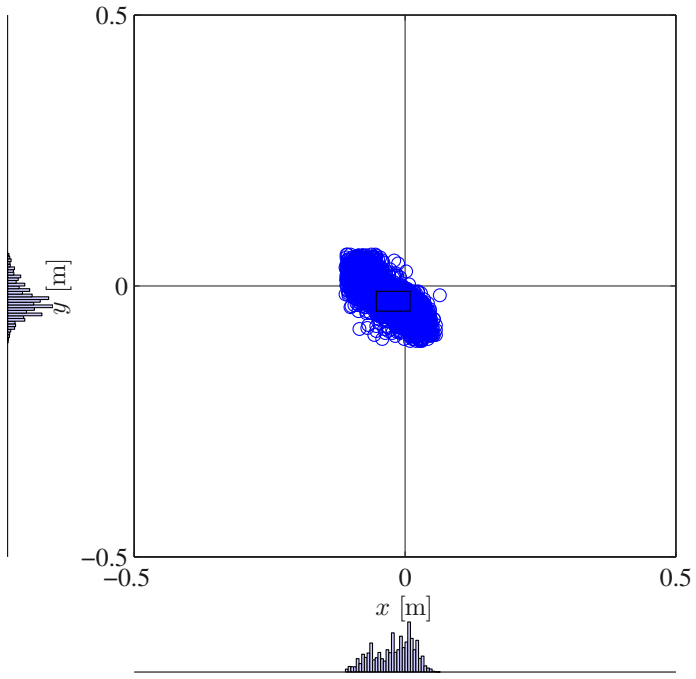

Figure 8.1: Center coordinates determined within the circulation procedure which enables to track the vortex path. The black rectangle indicates the 2D IQR that can be derived by the distributions shown next to the x-axis and the y-axis (Run #2, $h/D = 1.25$, $\mathsf{F}_D = 0.5$).

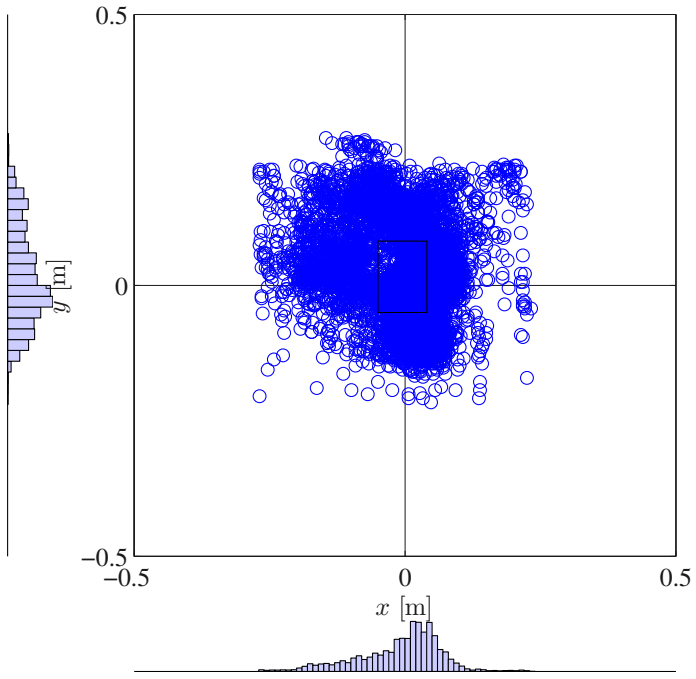

Figure 8.2: Center coordinates determined within the circulation procedure which enables to track the vortex path. The black rectangle indicates the 2D IQR that can be derived by the distributions shown next to the x-axis and the y-axis (Run #7, $h/D = 1.50$, $\mathsf{F}_D = 0.6$).

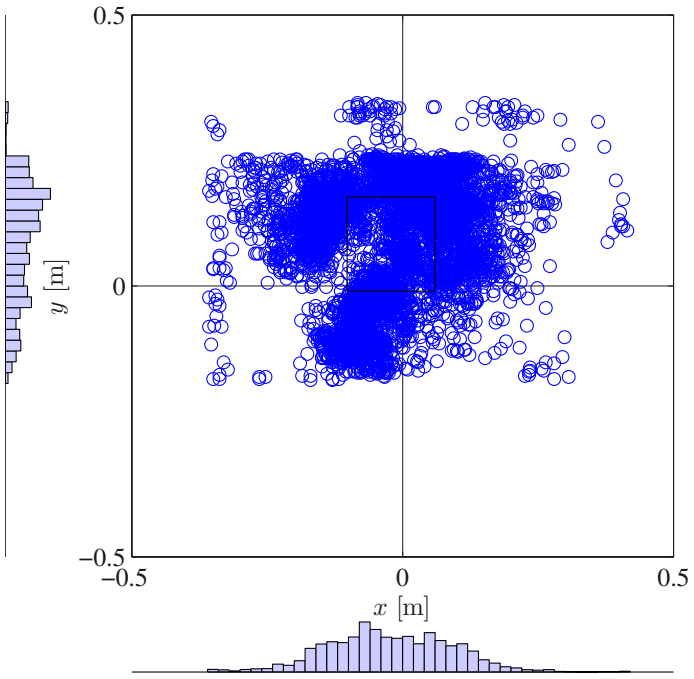

Figure 8.3: Center coordinates determined within the circulation procedure which enables to track the vortex path. The black rectangle indicates the 2D IQR that can be derived by the distributions shown next to the x-axis and the y-axis (Run #15, $h/D = 1.75$, $\mathsf{F}_D = 0.7$).

8.2 Critical Intake Submergence

Nowadays, the critical submergence h_{cr} is the most widely used design criteria to avoid air entrainment due to intake-vortices (chapter 2.3.3). The existing equations, which are frequently used in design practice, are presented in chapter 2.3.3. All published knowledge depends on observations of the vortex formation at intakes. Thus h_{cr} and therefore the critical situation concerning air entrainment was determined without any air entrainment measurements at all.

The quantitative air entrainment measurements of this study enable a completely new approach. By applying the findings of the present study h_{cr} can be determined for the first time in direct correlation to the air entrainment rate β. A minimum air entrainment rate of $\beta = 1 \cdot 10^{-5}$ could be measured within this study. The critical submergence is the submergence at the point when air is entrained. Therefore, a relative critical intake submergence can be newly estimated at the point when the smallest air entrainment rate β_{cr} becomes measurable. This reads

$$\left(\frac{h}{D}\right)_{\mathrm{cr}} = f(\beta_{\mathrm{cr}} = 1 \cdot 10^{-5}) \ , \tag{8.1}$$

while smaller rates of β are assumed to be negligible. In chapter 6.3 the relationship of the air entrainment rate β and the combined Froude number F_{co} was found and

described by eqs. 6.9a and 6.9b. If β_{cr} is inserted into eqs. 6.9a and 6.9b, the critical combined Froude number becomes $\mathsf{F}_{co,\,cr}(\bar{\beta}) = 0.43$ and $\mathsf{F}_{co,\,cr}(\check{\beta}) = 0.39$, respectively. Based on the intake Froude number F_D and the critical combined Froude number $\mathsf{F}_{co,\,cr}$ the relative critical intake submergence $(h/D)_{cr}$ can be derived as follows. The critical combined Froude number $\mathsf{F}_{co,\,cr} = v_D/\sqrt{g h_{cr}}$ and the intake Froude number $\mathsf{F}_D = v_D/\sqrt{gD}$ can be recast to

$$\left(\frac{h}{D}\right)_{cr} = \frac{\mathsf{F}_D^2}{\mathsf{F}_{co,\,cr}^2} \,. \tag{8.2}$$

Fig. 8.4 shows the developed approach for air entrainment rates $\bar{\beta}$ (Fig. 8.4a) and $\check{\beta}$ (Fig. 8.4b) in comparison to the two classical approaches of Knauss (1987b) and Gordon (1970). Eq. 8.2 enables the determination of the critical submergence for $1.25 \leq (h/D)_{cr} \leq 2.5$, while statements outside of this range remain undefined and thus plotted by dotted lines. Based on the scale family tests (SFT) presented in chapter 5 this range can be extended to $0.75 \leq (h/D)_{cr} \leq 3.0$. The envelope curve of the SFT results shown in Fig. 5.1 gives an idea how the critical submergence behaves outside of the range of the main measurements. However, it can be assumed, that the dotted curve, i.e. the upper extension of the developed approach, is misleading. The curve which increases over-proportionally the curve of Knauss (1987b) for large F_D-values.

Based on the developed approach the critical submergence can be determined. This approach is limited to a relatively small range of $1.25 \leq h/D \leq 2.5$. The envelope curve of the scale family tests can be used to extend the range to $0.75 \leq h/D \leq 3.0$. This curve is shown in Fig. 8.4 and can approximated by:

$$(h/D)_{cr} = -2.5\ \mathsf{F}_D^{-0.45} + 5.3 \tag{8.3}$$

This power equation is in contrast to the linear dependencies as suggested by Gordon (1970) and Knauss (1987b). Mainly affecting is the characteristic hook (see Fig. 5.1). The trend outside the given range remains undefined.

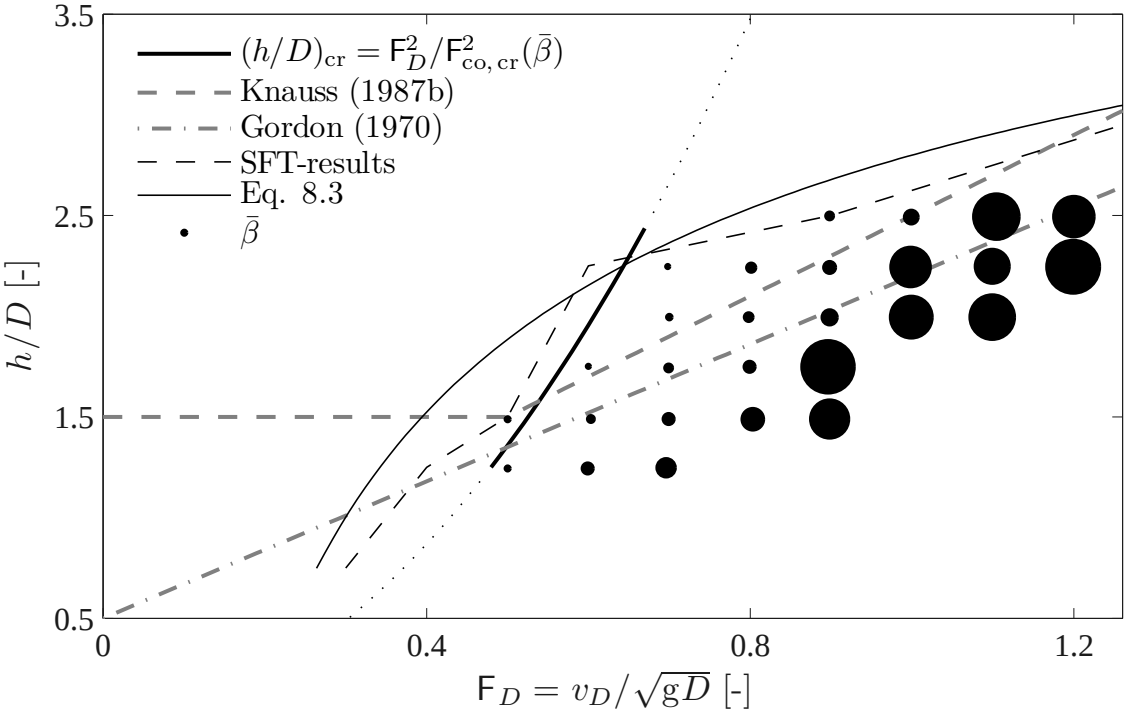

(a) Mean air entrainment rate $\bar{\beta}$ with $\mathsf{F}_{\mathrm{co,\,cr}}(\bar{\beta}) = 0.43$

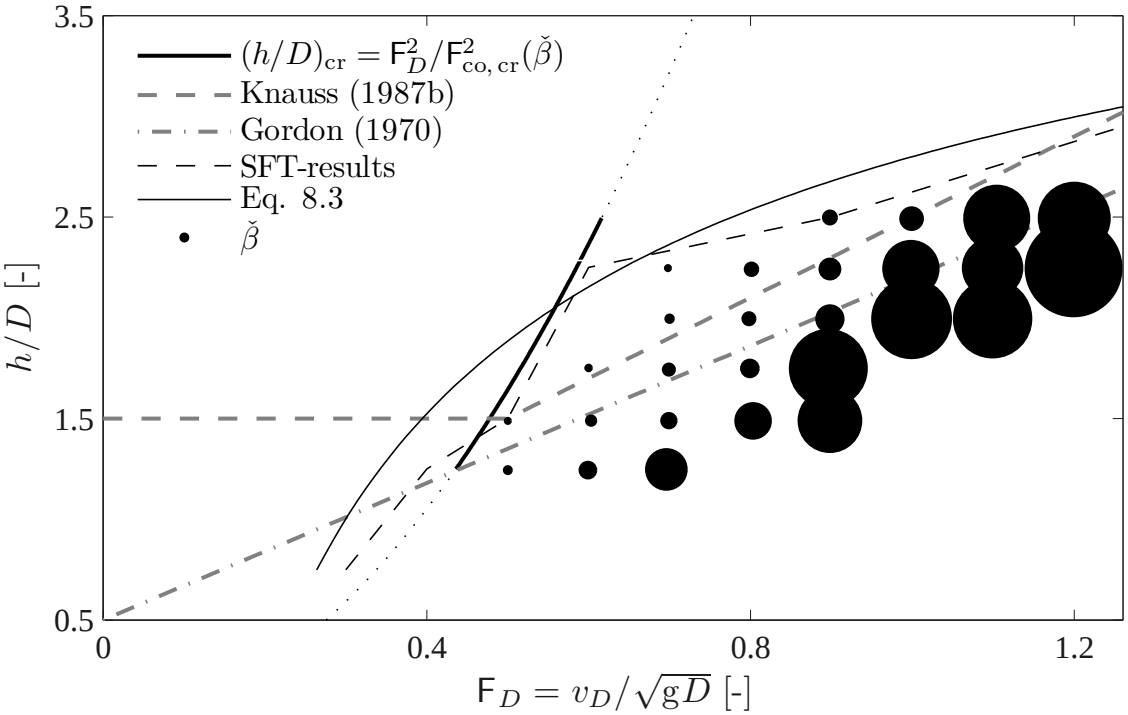

(b) Mean air entrainment rate according to single vortex phases $\check{\beta}$ with $\mathsf{F}_{\mathrm{co,\,cr}}(\check{\beta}) = 0.39$

Figure 8.4: Critical relative intake submergence defined at an air entrainment rate $\beta = 1 \cdot 10^{-5}$ (solid curve) in comparison with approaches from Knauss (1987b) and Gordon (1970). The newly developed approach is valid for $1.25 \leq (h/D)_{\mathrm{cr}} \leq 2.5$. Scale family tests (SFT) results are indicated with an envelope curve (dashed) and an approximation (Eq. (8.3), thin solid curve) is given to extend this range to $0.75 \leq (h/D)_{\mathrm{cr}} \leq 3.0$. The black circles present the parameter matrix. Their size is correlated to the measured air entrainment rate.

Chapter 9

Case Studies

Abstract. *The enhancement of the common practical design procedure regarding intakes is one of the main aims of the present research project. In this chapter the achieved results and the developed guidelines are utilized to cope with prototype conditions. First, a general case is discussed in which the application of the results regarding the prediction of air entrainment by common flow parameters is shown. Then, this procedure is applied to two prototype examples located in Switzerland and in Ethiopia, respectively.*

9.1 Overview

Table 9.1 shows a summary of the chosen case study examples. To compare the results a relative submergence of $h/D = 2$, which represents a typical encountered case when operating a HPP, is chosen. Within the following prototype examples (chapters 9.4 and 9.5) different ratios of h/D are used.

Table 9.1: Characteristics of case study examples. Air discharge Q_a is computed for a chosen $h/D = 2$, air volume V_a is given after an operation of 1 h.

example	D, D_H [m]	Q_w [m^3/s]	v_D [m/s]	F_D [-]	F_{co} [-]	$Q_a(\check{\beta})$ [10^{-3} m^3/s]	$V_a(\check{\beta})$ [m^3]
General	5.0	100	5.1	0.73	0.51	7.0	26.9
Handeck II (section 4)	4.4	65	3.3	0.5	0.37	0.5	1.7
Gibe III (section 5)	7.0	283	7.3	0.89	0.57	128	460

9.2 General

The "General" case gives a fictitious, simple example where the intake cross-section is circular. No bellmouth or further geometric specifications have to be taken into account.

Air Entrainment Rate. Due to its geometric simplification the "General" example shows how easily air entrainment can be determined by the developed guidelines. The intake velocity v_D represents the flow at the intake section, while the submergence h stands for the influence of the water body above the intake. Both are summarized to the combined Froude number F_{co}. Eqs. 6.9 give the relationship of F_{co} to the air entrainment rate β. The determination process gives the following results:

$$
\begin{aligned}
v_D &= \frac{Q_{\mathrm{w}}}{\frac{\pi}{4}D^2} = \frac{100\,\mathrm{m}^3/\mathrm{s}}{\frac{3.14}{4}(5\,\mathrm{m})^2} = 5.1\,\mathrm{m/s} \\
h &= (h/D)\cdot D = 2\cdot 5\,\mathrm{m} = 10\,\mathrm{m} \\
\mathsf{F}_{\mathrm{co}} &= \frac{v_D}{\sqrt{\mathrm{g}h}} = \frac{5.1\,\mathrm{m/s}}{\sqrt{9.81\,\mathrm{m/s}^2\cdot 10\,\mathrm{m}}} = 0.51
\end{aligned}
$$

$$
\begin{aligned}
\bar{\beta} &= 1.04\cdot 10^{-8}\, e^{16\,\mathsf{F}_{\mathrm{co}}} = 3.89\cdot 10^{-5} \\
\check{\beta} &= 2.00\cdot 10^{-8}\, e^{16\,\mathsf{F}_{\mathrm{co}}} = 7.48\cdot 10^{-5}\,.
\end{aligned}
$$

A prediction band as introduced in chapter 6.3.3 should be considered to take into account the probability of air entrainment. Limits are given in Table 6.1. The band of probable air entrainment has an upper limit (ul) and a lower limit (ll) which are determined using eq. 6.12:

$$
\begin{aligned}
&\mathsf{F}_{\mathrm{co}} < 0.66 \\
&\bar{\beta}_{\mathrm{ul}} = 2.08\cdot 10^{-8}\, e^{16\,\mathsf{F}_{\mathrm{co}}} = 7.78\cdot 10^{-5} \\
&\bar{\beta}_{\mathrm{ll}} = 0.52\cdot 10^{-8}\, e^{16\,\mathsf{F}_{\mathrm{co}}} = 1.95\cdot 10^{-5} \\
&\check{\beta}_{\mathrm{ul}} = 4.09\cdot 10^{-8}\, e^{16\,\mathsf{F}_{\mathrm{co}}} = 1.53\cdot 10^{-4} \\
&\check{\beta}_{\mathrm{ll}} = 0.97\cdot 10^{-8}\, e^{16\,\mathsf{F}_{\mathrm{co}}} = 3.63\cdot 10^{-5}\,.
\end{aligned}
$$

This dimensionless air entrainment rate is converted to dimensional parameters to give estimation about the size of entrained air.

The air discharge Q_a and the related air volume V_a that is entrained within one hour of operation become:

$$\begin{aligned}
\bar{Q}_{a,\,ul} &= 0.0078\,m^3/s \Rightarrow 28\,m^3 \\
\bar{Q}_{a,\,ll} &= 0.0019\,m^3/s \Rightarrow \;\; 7\,m^3 \\
\check{Q}_{a,\,ul} &= 0.0153\,m^3/s \Rightarrow 55\,m^3 \\
\check{Q}_{a,\,ll} &= 0.0036\,m^3/s \Rightarrow 13\,m^3\,.
\end{aligned}$$

With a known quantitative air entrainment a basis is given for forthcoming decisions towards or against counter measures. Chapter 2.4 gives an overview of the possibilities.

Critical Submergence. Typically, the critical submergence is determined by the intake Froude number F_D (eq. 2.16). Commonly used approaches give $(h/D)_{cr} = 1.7$ for symmetrical flow conditions and $(h/D)_{cr} = 2.2$ for asymmetrical flow conditions (Gordon, 1970), and a value of $(h/D)_{cr} = 2.0$ (Knauss, 1987b), respectively. The critical submergence $(h/D)_{cr}(\check{\beta})$ as developed in chapter 8.2 gives $(h/D)_{cr}(\bar{\beta}) = 2.9$ and $(h/D)_{cr}(\check{\beta}) = 3.5$. Additionally, the envelope as described by eq. (8.3) gives a critical submergence $(h/D)_{cr} = 2.5$.

Conclusion. This "General" example shows how to determine the air entrainment from the developed guidelines. However, an application to prototype examples requires a more complex determination procedure. Then, two main points have to be analyzed: (1) the load case depending on the discharge Q_w and the submergence h and (2) the geometrical boundaries of the intake flow. Furthermore, the behavior of air bubbles or air pockets depending on the geometry and the flow condition in the pressure system have to be analyzed.

9.3 Introduction to Prototype Examples

Concerning the intake design, the focus is usually put on three main aspects: 1) reduction of head loss, 2) avoidance of intake-vortices, and 3) control of sediment entrainment. Typically, the intake cross-section is located above the reservoir bottom, is equipped with a trash rack and is inclined. Adjoining to intake cross-sections that are rectangular in most of the cases a transition to the circular pressure tunnel (bellmouth intake) is necessary.
During the design process of the intake especially the "avoidance of intake-vortices" has to be changed by the proposed guidelines. By focussing on the air entrainment itself and not on the critical submergence, as done previously, the intake design can

be improved. By default, the critical submergence h_{cr} is estimated after Gordon (1970) and Knauss (1987b). In chapter 6.3 new equations have been derived that provide a tool to estimate the critical submergence as well, although the main finding of this research project is the predictability of the air entrainment.

As mentioned above, the discharge Q_w and the submergence h are the guiding parameters. A sensitivity analysis regarding these two input parameters has to be conducted first. Rarely, the maximum discharge or the minimum submergence, respectively, gives the determining load case. Several combinations must be checked.

To define, the location and the geometry of the controlling cross-section the considerations regarding air entrainment and critical submergence have to be applied to more than one cross-section. To verify if a possible intensification within the intake section takes place. This procedure is recommended because the intake cross-section is not decisive per se. Moreover, an equivalent diameter of the rectangular cross-section has to be defined. Knauss (1987b) suggests to substitute the pipe diameter D by the intake section height H. Another method may is to use the hydraulic diameter $D_H = 4A/P$, where A is the cross-sectional area and P is the wetted perimeter of the cross-section.

Two examples that have been recently investigated at VAW, i.e. the intake of the HPP Handeck II and the middle outlets of the Gibe III dam, are used to show the adaption to specific intake boundary conditions in the following.

9.4 Example 1: HPP Handeck II (Switzerland)

Fig. 9.1 shows the intake situation at the Räterichsboden reservoir in Switzerland. The existing drawdown level at full load of the hydraulic machinery is defined at 1720 m asl. Below this level and down to 1712 m asl. the discharge Q_w has to be decreased from a maximum of 42.5 to 24 m^3/s. Below 1712 m asl. the hydraulic machinery is switched off.

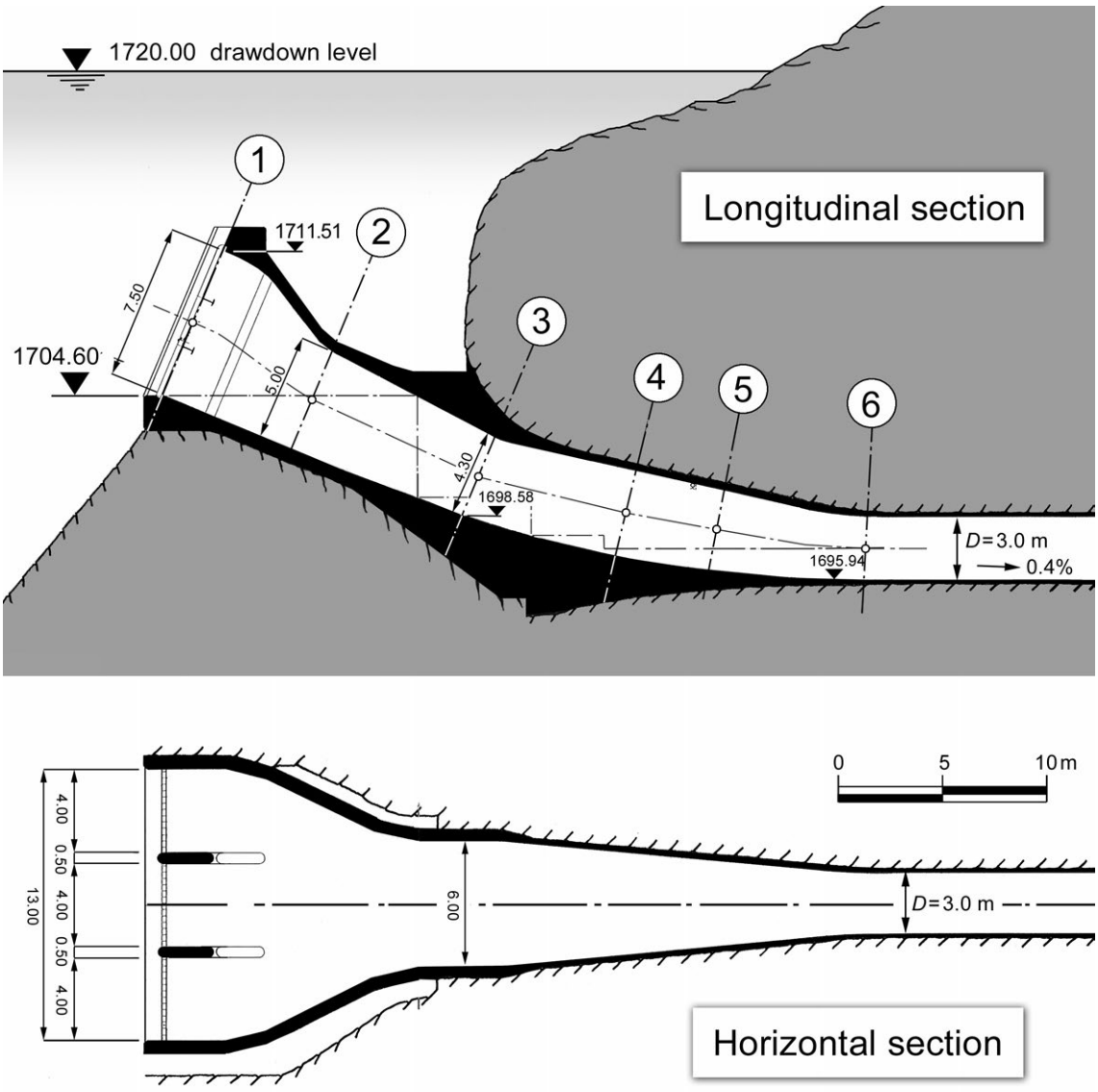

Figure 9.1: Longitudinal and horizontal sections of the intake of HPP Handeck II (VAW, 2010). Note that here the conditions previous to the retrofitting measures have been chosen to provide a typical design process situation.

The intake has a rectangular intake cross-section of 12 m width and 7.5 m height. An increase of power production is planned while using the present hydraulic structure.

Hence the water discharge will increase from $Q_w = 42.5$ to 65 m^3/s. The drawdown level is set to 1720 m asl. The stagnation zone above the intake gives a similar intake situation as investigated in this research project. Note that the rectangular shaped intake leads to two intake vortices, one in each upper corner. Based on specific hydraulic model studies a vortex quenching as described in chapter 2.2.6 is not to be expected at rectangular intake cross-sections. The average intake velocity v_D in cross-section ① is 0.72 m/s, and, consequently, the intake Froude number F_D is low.

Air Entrainment Rate. The determination of the air entrainment rate needs to be adapted to the different load cases and the controlling cross-sections. The flow conditions described by the common flow parameters are given in Table 9.2 for six cross-sections.

Table 9.2: Determined parameters regarding the chosen cross-sections as indicated in Fig. 9.1 at a water level of 1720 m asl. For rectangular cross-sections (①–⑤) the hydraulic diameter D_H is given. Numbers in parentheses refer to D_H substituted by the intake section height H.

		cross-section					
	unit	1	2	3	4	5	6
length on tunnel axis	[m]	0	5.1	15.6	22.9	27.3	34.5
tunnel axis elevation	[m asl.]	1708.1	1704.6	1702.3	1698.9	1698.1	1697.0
D, D_H, H	[m]	9.2 (7.5)	6.6	5.0	4.4	3.9	3.0
A	[m^2]	90.0 (44.2)	48.3	25.8	19.8	15.4	7.1
$v_D = Q_w/A$	[m/s]	0.72 (1.47)	1.35	2.52	3.28	4.22	9.20
$\mathsf{F}_D = v_D/\sqrt{gD}$	[-]	0.08 (0.17)	0.19	0.39	0.52	0.68	1.70
$\mathsf{F}_{co} = v_D/\sqrt{gh}$	[-]	0.12 (0.14)	0.16	0.26	0.29	0.36	0.77
$\bar{\beta} = 1.04 \cdot 10^{-8}\, e^{16\,\mathsf{F}_{co}}$	[10^{-5}]	*0.003 (0.009)*	*0.006*	*0.022*	*0.040*	0.105	20.522
$\check{\beta} = 2.00 \cdot 10^{-8}\, e^{16\,\mathsf{F}_{co}}$	[10^{-5}]	*0.006 (0.018)*	*0.012*	*0.043*	*0.077*	0.201	39.465

The intake velocity v_D and thus F_{co} are decisive for the air entrainment rate. Due to the presence of two simultaneous intake-vortices it can be assumed that the intake diameter D_H can be substituted by the intake height (Knauss, 1987b). To take into account the rectangular intake section the intake section area is determined by the intake height $H = 7.5$ m to $A_H = \pi/4 \cdot H^2 = 44.2$ m^2. This consideration is based on rectangular intakes where the width is extended and the height remains constant. Due to energetic reasons it is assumed that the intake width becomes independent from the height. Consequently, the resulting cross-sectional flow might be adequately considered by the intake height H.
Air entrainment rates are determined by eqs. 6.9 based on common flow parameters (see chapter 6.3). The values of F_{co}, and the mean air entrainment rate $\bar{\beta}$ and the mean air entrainment rate during the vortex phases $\check{\beta}$ are given at six exemplary

cross-sections in Table 9.2. Due to the limited validity of $0.3 \leq \mathsf{F}_{\mathrm{co}} \leq 0.8$ the approach given in eqs. 6.9 is not applicable for cross-sections ①–④ and marked italic in Table 9.2. However, cross-sections ⑤+⑥ fulfill this criteria. At a drawdown level of 1720 m asl the mean air entrainment rate in cross-section ⑤ can be estimated to $\bar{\beta} = 1.1 \cdot 10^{-6}$ and for cross-section ⑥ to $\bar{\beta} = 2.1 \cdot 10^{-4}$. The determination of the mean air entrainment rate in cross-section ⑤ results in $\check{\beta} = 2.0 \cdot 10^{-6}$ and for cross-section ⑥ $\check{\beta} = 3.9 \cdot 10^{-4}$. Due to the position of cross-sections ⑤ and ⑥ inside the tunnel their significance concerning the intake situation is uncertain.
This procedure has to be repeated for different load cases.

Critical Submergence. Approaches based on F_D indicate a low critical submergence. Knauss'(1987b) approach gives a minimal relative submergence $h/D = 1$–1.5. A critical submergence $(h/D)_{\min} = 1.5$ is chosen. The approaches using the air entrainment rate (eqs. 6.9) are not valid in all cross-sections due to the small F_D and F_{co}, respectively. They would underestimate a critical submergence.
Based on hydraulic model investigations the critical submergence in this example was investigated by physical model tests with a scale of 1:25 and 1:35 (VAW, 2010). Vortices with a dye core ($VT3$) occurred up to a water level of 1734 m asl. It was assumed that a vortex type $VT3$ in the model equals a vortex type $VT5$–6 in the prototype. Both all existing and newly developed (eq. 8.2) approaches underestimate the critical submergence, giving a high level of uncertainty. Anti-vortex canopy-shaped devices were investigated and a minimum area of 250 m^2 was found. An additional de-aeration device after Wickenhäuser (2008) was suggested as a valuable solution. Probable air entrainment can be collected and discharged through rising pipes. At the time of the model study the air entrainment could not be estimated adequately.
The definition of a drawdown level based on a zero-air-criterion is not straight forward here. All approaches give lower elevations than 1734 m asl. based on hydraulic model study.

Conclusion. The approach to estimate the critical submergence and thereby the prediction of the air entrainment rate itself can be applied for combined Froude numbers $\mathsf{F}_{\mathrm{co}} \geq 0.3$, i.e. about from cross-section ④. The quantitative air entrainment is given for a reservoir level of 1720 m asl. For cross-section 4, an air volume $\check{V}_{\mathrm{a}}$ of 0.18 m^3 after one hour operation is expected. Although this volume is quite small, it should be taken into account.

9.5 Example 2: Gibe III Dam (Ethiopia)

Gibe III is a 243 m high roller compacted concrete (RCC) dam which is currently under construction in Ethiopia. Fig. 9.2 shows the intake section of one of the two middle outlets through the dam body. The intake is formed by a rounded and overhanging invert at an elevation of 749.76 m asl. The rectangular intake has a width of 7 m and a height of 13 m. The straight 10.7 m long, bellmouth shaped transition stretches from the rectangular cross-section to the circular cross-section of $D = 7$ m, followed by a 10 m long contraction to $D = 6$ m. Both outlets are designed with a discharge capacity of approximately 735 m^3/s at a reservoir level of 875 m asl.

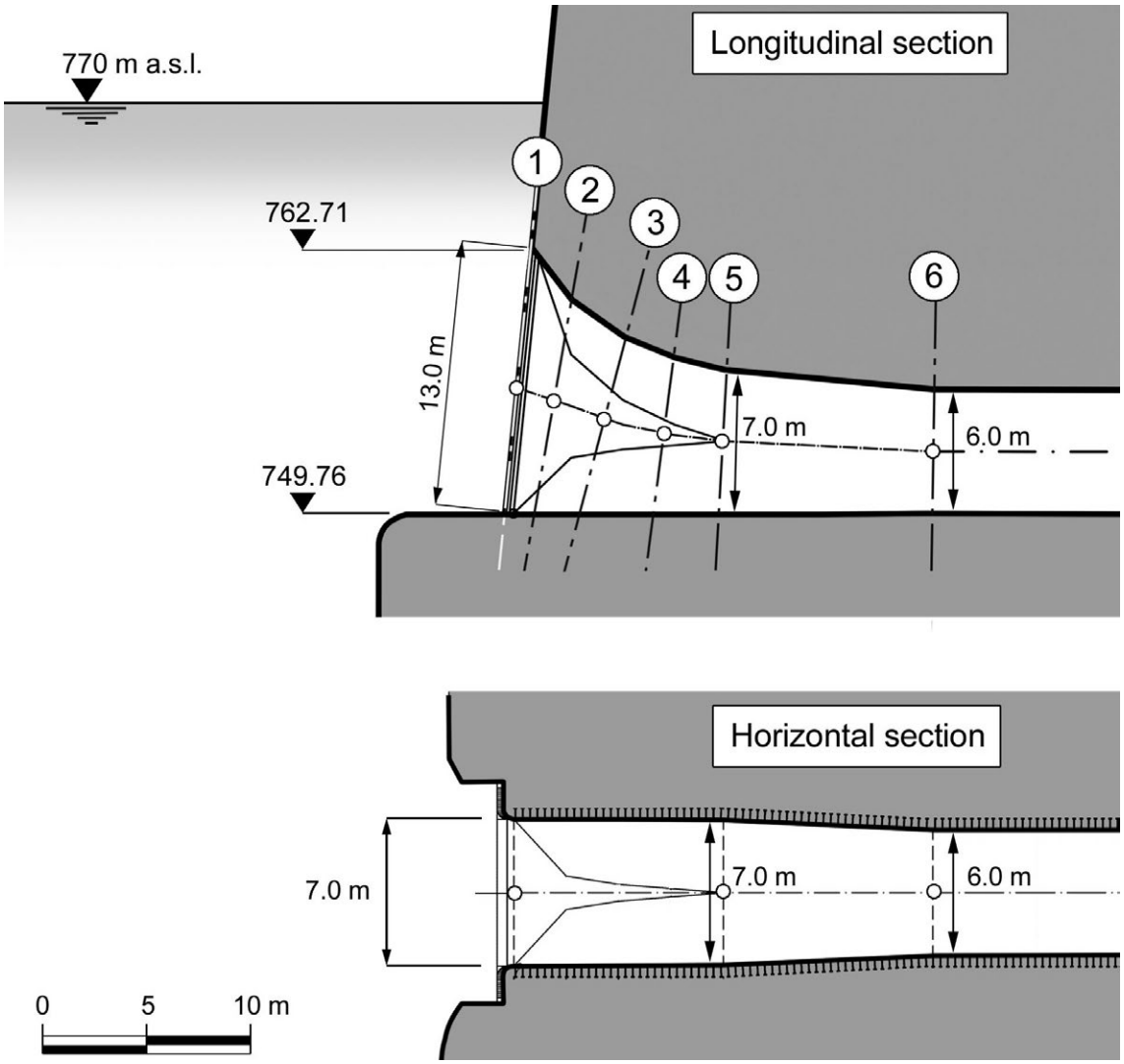

Figure 9.2: Longitudinal and horizontal sections of the middle outlet of Gibe III dam (VAW, 2013b).

The middle outlet can optionally be used during the impounding process with a discharge of approximately 184 m^3/s at a reservoir level of 760 m asl. The load case

analyzed in the following is a water level of 770 m asl. and a discharge of 283 m^3/s. Comparing the stagnation zone above the intake it is significantly smaller than in example 1. But note that the rectangular shaped intake leads to two intake vortices, one in each upper corner. This is favored by the niches at the intake (see Fig. 9.2) and within the hydraulic model investigation a vortex quenching as described in chapter 2.2.6 was not observed.

Air Entrainment Rate. Air entrainment is estimated by eqs. 6.9 based on common flow parameters (see chapter 6.3). The values of F_{co} based on the mean air entrainment rate $\bar{\beta}$ and on the mean air entrainment rate during the vortex phases $\check{\beta}$ are given at six exemplary cross-sections in Table 9.3.

Table 9.3: Determined parameters regarding the chosen cross-sections as indicated in Fig. 9.2 at a water level of 770 m asl. For rectangular cross-sections (①–④) the hydraulic diameter D_H is given. Numbers in parentheses refer to D_H substituted by the intake section height H.

		cross-section					
	unit	1	2	3	4	5	6
length on tunnel axis	[m]	0	1.9	4.2	7.4	10.7	20.7
tunnel axis elevation	[m asl.]	756.23	755.37	754.53	753.69	753.26	752.76
D, D_H, H	[m]	9.1 (13.0)	8.4	7.9	7.3	7.0	6.0
A	[m^2]	91 (133)	74.1	63.6	54.1	38.5	28.3
$v_D = Q_w/A$	[m/s]	3.1 (2.1)	3.8	4.5	5.2	7.3	10.0
$\mathsf{F}_D = v_D/\sqrt{gD}$	[-]	0.28 (0.19)	0.37	0.47	0.60	0.89	1.30
$\mathsf{F}_{co} = v_D/\sqrt{gh}$	[-]	0.27 (0.18)	0.32	0.36	0.41	0.57	0.77
$\bar{\beta} = 1.04 \cdot 10^{-8}\, e^{16\,\mathsf{F}_{co}}$	[10^{-5}]	*0.07 (0.02)*	0.17	0.34	0.77	9.99	228.2
$\check{\beta} = 2.00 \cdot 10^{-8}\, e^{16\,\mathsf{F}_{co}}$	[10^{-5}]	*0.14 (0.04)*	0.33	0.64	1.48	19.20	438.8

Approximately at all given cross-sections the application of the approach given in eqs. 6.9 is valid. At a drawdown level of 1720 m asl. the mean air entrainment rate ranges from $\bar{\beta} = 7.5 \cdot 10^{-7}$ in cross-section ① up to $\bar{\beta} = 2.3 \cdot 10^{-3}$ in cross-section ⑤ and from $\check{\beta} = 1.4 \cdot 10^{-6}$ up to $\check{\beta} = 4.4 \cdot 10^{-3}$.
The estimated air entrainment rates are exemplified by the volume of air which accumulates after one hour of operation, $V_a(\bar{\beta})$ = 0.8–2322 m^3 and $V_a(\check{\beta})$ = 1.5–4465 m^3.

Critical Submergence. The example is computed using the reservoir level of 770 m asl. (Fig. 9.2) and a water discharge of 283 m^3/s. The average intake velocity v_D in cross-section ① is 3.1 m/s, and, consequently, the intake Froude number F_D is 0.28. Approaches based on F_D indicate a low critical submergence. Knauss'(1987b) approach gives a minimal relative submergence h/D = 1–1.5, $(h/D)_{min}$ =

1.5 is chosen. The approaches using the air entrainment rate (eqs. 6.9) are computed in all cross-sections, but for cross-sections 1–3 they would underestimate the critical submergence as compared to the Knauss'1987b approach.

Conclusion. The approach to estimate the critical submergence and thus the prediction of the air entrainment rate itself can be applied for combined Froude numbers $\mathsf{F}_{co} \geq 0.3$. The quantitative air entrainment is given for a water level of 770 m asl. For cross-section 5, an air volume V_a of 195 m^3 after one hour of operation is expected.

9.6 Conclusion of Prototype Examples

Both examples show a difficulty to determine a reliable critical submergence, as the differences between the approaches are significant. For this reason, an air-allowance-criterion is suggested, i.e. for given reservoir levels the amount of entrained air can be determined and counter-measures can be designed to handle the range of probable air entrainment.

Chapter 10

Summary and Outlook

10.1 Summary

Air in pressure systems of hydropower plants (HPP) has in general negative consequences such as reductions in turbine efficiency and flow rate as well as pulsations and pressure surges. Vortices at intakes are a major source of air entrainment. Typically the occurrence of this phenomenon is avoided by operating the HPP's upper water level above a threshold value of the critical submergence that has been pre-determined via ungainly empirical approaches. Significant reserves are required consequently. Often, the postulated large submergence results in a loss of flexibility, of storage volume, and of efficiency of the plant. However, with many storage plants being newly built or upgraded in the course of an increasing regulating energy demand, a precise tool is needed to predict the air entrainment rate.

To analyze the air entrainment rate due to intake vortices systematically, large-scale physical model tests have been conducted at VAW in a 50 m^3 laboratory steel tank. Two pumps provided a flow discharge of up to 510 l/s in a closed loop. The intake pipe has a diameter of 0.4 m and the tank has a maximum water level of 2.2 m. The full range of typical load cases at power intakes have been investigated, while the unsteady nature of the hydraulic phenomena of vortex formation was undisturbed by complying with certain geometric boundary conditions. The horizontal velocity field around the vortex is measured by 2D Particle Image Velocimetry (PIV) on a total area of 1 m^2. A de-aeration system enabled continuous measurements of the air entrainment rate at a frequency of 1 Hz. Shadows of air-cores on the PIV images have been used to determine their diameter indirectly to enable an estimation of the air velocity in the core via the continuity equation. The transferability of the results from model scale to prototype conditions has been validated via scale family tests.

Air entrainment due to intake vortices initiates at an intake Froude number $\mathsf{F}_D = v_D/\sqrt{\mathrm{g}D} = 0.4$ and low submergence. The air entrainment rate increases up to 0.8 % with increasing F_D and decreasing relative submergence h/D. An increase of

the circulation of the intake vortex is not directly related to the air entrainment rate. Results show that air entrainment occurs by a considerable unsteadiness over time within different load cases. The probability of occurrence of intake vortices, the size of the air-core, the velocity field, and the air entrainment rate are compared and analyzed towards two practical design approaches. The first one is intrinsic. It is based on parameters F_D and h/D that are known when a HPP is operated, thus a forecast to the air entrainment rates is possible. The second approach is extrinsic, as it is based on the circulation Γ of the far flow field upstream of the intake. Surprisingly, this approach does not enable a more precise determination of the air entrainment rate, as the circulation Γ showed to be of minor important influence the air entrainment rate.

10.2 Principle Findings

The final outcome of this research project can be outlined as follows:

- Sophisticated measuring techniques have been developed and successfully applied in a newly constructed laboratory tank.
- The experimental facility enables the modeling and investigation of air entraining intake-vortices that are undisturbed by boundary conditions, e.g. tank walls or superimposed flow fields.
- Quasi-continuous air entrainment rates β of up to 0.8 % have been measured successfully.
- The scale similarity of the conducted experiments has been proven. Investigations of vortex-induced air entrainment based on a Froude model approach should apply intake diameters $D \geq 400$ mm with regard to scale effects in the air-core diameter. Viscosity and surface tension effects of the flow can be neglected if $\mathsf{R}_D = v_D D/\nu \geq 6 \cdot 10^5$, and $\mathsf{W}_D^2 = \rho_\mathrm{w} v_D^2 D/\sigma_\mathrm{w} > 3200 \approx 57^2$, respectively.
- The velocity magnitude of air tube flow is of one order higher than the surrounding water flow.
- The intensity of vortex wandering increases with increasing submergence h/D, or, in other words, the lower the submergence, the more stable is the center of the intake-vortex.
- An approach to determine the critical intake submergence h_cr based on the air entrainment rate measurements is developed. The relation reads

  $(h/D)_\mathrm{cr} = \mathsf{F}_D^2/\mathsf{F}_{\mathrm{co,\,cr}}^2$

- Two guidelines have been derived to estimate the air entrainment rate β at a simple intake prototype.

  The first approach is intrinsic. It takes advantage of common parameters that are known during the operation of a HPP. The relationship is given by

  $\bar{\beta} = 1.04 \cdot 10^{-8} e^{16 \cdot \mathsf{F}_{\mathrm{co}}}$,
  $\check{\beta} = 2.00 \cdot 10^{-8} e^{16 \cdot \mathsf{F}_{\mathrm{co}}}$,
  where $\bar{\beta}$ denotes the mean air entrainment rate, $\check{\beta}$ denotes the mean air entrainment rate of the vortex phases and $\mathsf{F}_{\mathrm{co}} = v_D/\sqrt{\mathrm{g}h}$ is the combined Froude number. The boundaries are given by $\mathsf{F}_{\mathrm{co}} = [0.3\text{–}0.8]$. A rule of thumb can be given by $\check{\beta} = 2\bar{\beta}$. An application of this guideline requires a prediction band – which is seen to be a prerequisite for a proper guideline – to consider the probability of air entrainment.

  The second approach is extrinsic. It uses characteristic parameters of the rotating flow field. The relationship reads $\check{\beta} = 0.0076\, e^{-22.88 N_{\tilde{\Gamma}}}$, where $N_{\tilde{\Gamma}} = \tilde{\Gamma} D/\bar{Q}_{\mathrm{w}}$ is the mean circulation number.

10.3 Outlook

From a hydraulic point of view, intake-vortices are fascinating and highly complex. During this research project many additional research topics where arising, that should be investigated in separate studies in more detail. The itemized points are not in order of their importance.

- Air entrainment at non-circular and non-sharp-edged intake pipes.
- Air entrainment at rectangular intakes with transition to circular cross-section.
- Air entrainment at intakes with trash racks.
- 3D velocity measurements of the air-core tube surrounding flow.
- Air flow measurements in an air-core tube.
- Pressure distribution along the air-core tube.
- Formation of more than one simultaneous air-core intake-vortices.
- Physical explanation of the "air entrainment hook" at $\mathsf{F}_{\mathrm{co}} \approx 0.7$.

These items can be divided into two groups: the practice-orientated and the physically process understanding aspects. However, a clear separation of the different items is difficult:
Thus, this research project has given a conceptual framework in investigating air entrainment at intake that evolves several recommendations for further studies.

Bibliography

Ackeret, J. (1952). Exact solutions of the Stokes-Navier equations for incompressible fluids with modified boundary conditions. *Zeitschrift fur Angewandte Mathematik und Physik*, 3(4), 259–271.

Adrian, R. J. & Yao, C. S. (1985). Pulsed laser technique application to liquid and gaseous flows and the scattering power of seed materials. *Applied Optics*, 24(1), 44–52.

Amphlett, M. B. (1976). *Air-entraining vortices at a horizontal intake.* Technical report, HRS Wallingford, Wallingford, UK.

Andersen, A., Bohr, T., Stenum, B., Rasmussen, J. J., & Lautrup, B. (2006). The bathtub vortex in a rotating container. *Journal of Fluid Mechanics*, 556, 121–146.

Anwar, H. O. (1965). Flow in a free vortex. *Water Power*, 17(4), 153–161.

Anwar, H. O. (1966). Formation of a weak vortex. *Journal of Hydraulic Research*, 4(1), 1–16.

Anwar, H. O. (1967). Vortices at low-head intakes. *Water Power*, 19(11), 455–457.

Anwar, H. O. (1968a). Prevention of vortices at intakes. *Water Power*, 20(10), 393–401.

Anwar, H. O. (1968b). Vortices in a viscous fluid. *Journal of Hydraulic Research*, 6(1), 1–15.

Anwar, H. O. (1983). The non-dimensional parameters of free-surface vortices measured for horizontal and vertically inverted intakes. *La Houille Blanche*, 38(1), 11–25.

Anwar, H. O. & Amphlett, M. B. (1980). Vortices at vertically inverted intake. *Journal of Hydraulic Research*, 18(2), 123–134.

Anwar, H. O., Weller, J. A., & Amphlett, M. B. (1978). Similarity of free-vortex at horizontal intake. *Journal of Hydraulic Research*, 16(2), 95–105.

Ball, E. B. (1933). Free vortices. *The Engineer*, 155(June 30), 666.

Berge, J.-P. (1966). A study of vortex formation and other abnormal flow in a tank with and without a free surface. *La Houille Blanche*, 21(1), 9–40.

Binnie, A. M. (1964). Some experiments on bath-tub vortex. *Journal of Mechanical Engineering Science*, 6(3), 256–257.

Bohling, L., Andersen, A., & Fabre, D. (2010). Structure of a steady drain-hole vortex in a viscous fluid. *Journal of Fluid Mechanics*, 656(1), 177–188.

Borghei, S. M. & Kabiri-Samani, A. R. (2010). Effect of anti-vortex plates on critical submergence at a vertical intake. *Scientia Iranica Transaction - Civil Engineering*, 17(2), 89–95.

Bowden, R. C. & Hassan, I. G. (2009). Modeling the onset of gas entrainment in a single downward discharge from a stratified gas - liquid region with liquid crossflow. *Journal of Fluids Engineering - Transactions of the ASME*, 131(3), 031304 –1–8.

Bretschneider, H. (1981). Massnahmen zum Vermeiden des Lufteintags bei Einlaufbauwerken. *Wasserwirtschaft*, 71(5), 125–128 [in German].

Brix, S. C. M. (2004). *Untersuchungen zur Entstehung und Stärke von Triebwerkseinlaufwirbeln*. RWTH Aachen, Aachen, Germany [in German].

Bühlmann, M. (2012). *Lufteintrag durch Einlaufwirbel*. Master Thesis, VAW, ETH Zurich, Switzerland [unpublished, in German].

Burgers, J. M. (1948). A mathematical model illustrating the theory of turbulence. *Advances in Applied Mechanics*, 1(1), 171–199.

Chang, E. (1977). *Review of literature on the formation and modelling of vortices in rectangular pump sumps*. Technical Report TN1414, British Hydromechanics Research Association (BHRA), Cranfield, UK.

Chang, E. (1979). *Experimental data on the hydraulic design of intakes and rectangular pump sumps*. Technical Report RR1518, British Hydromechanics Research Association (BHRA), Cranfield, UK.

Chang, E. & Prosser, M. J. (1978). Intake design to prevent vortex formation. In *Proc. of the ASCE, IAHR, and ASME Joint Symposium on Design and Operation of Fluid Machinery* (pp. 393–402).

Clift, R., Grace, J. R., & Weber, M. E. (1978). *Bubbles, Drops and Particles*. New York: Academic Press.

Constantinescu, G. S. & Patel, V. C. (2000). Role of turbulence model in prediction of pump-bay vortices. *Journal of Hydraulic Engineering*, 126(5), 387–391.

Cotel, A. J. & Breidenthal, R. E. (1999). Turbulence inside a vortex. *Physics of Fluids*, 11(10), 3026–3029.

Daggett, L. L. & Keulegan, G. H. (1974). Similitude in free-surface vortex formations. *Journal of the Hydraulics Division*, 100(HY11), 1565–1581.

DantecDynamics (2012a). *DynamicStudio v3.31 User's Guide.* Dantec Dynamics, Skovlunde, DK.

DantecDynamics (2012b). Measurement principles of PIV. url: `http://www.dantecdynamics.com/Default.aspx?ID=1049` (downloaded 12.9.2012).

Davis, P. A. (2012). Personal communication.

De Siervi, F., Viguier, H. C., Greitzer, E. M., & Tan, C. S. (1982). Mechanisms of inlet-vortex formation. *Journal of Fluid Mechanics*, 124(11), 173–207.

Denny, D. F. (1956). An experimental study of air-entraining vortices in pump sumps. *Proc. of the Institution of Mechanical Engineers*, (pp. 106–125).

Denny, D. F. & Young, G. A. J. (1957). The prevention of vortices and swirl at intakes. *IAHR Seventh General Meeting*, (pp. Paper C1).

Durgin, W. W. & Hecker, G. E. (1978). The modeling of vortices at intake structures. *Proc. of the ASCE, IAHR, and ASME Joint Symposium on Design and Operation of Fluid Machinery*, (pp. 381–391).

Dyment, A. (1998). Finite amplitude hydraulic jumps in partly filled conduits of arbitrary shape. *Comptes Rendus de l'Acadámie des Sciences - Series IIB - Mechanics-Physics-Chemistry-Astronomy*, 326(3), 179–184.

Einstein, H. A. & Li, H. (1955). Steady vortex flow in a real fluid. *La Houille Blanche*, 10(4), 483–496.

Engelberg, S. (2008). *Digital Signal Processing: An Experimental Approach.* Springer, London, UK.

Falvey, H. (1980). *Air-water flow in hydraulic systems.* Technical report, Bureau of Reclamation, Denver, USA.

Fischer, H. B. (1979). *Mixing in inland and coastal waters.* New York: Academic Press.

Fritz, H. M., Hager, W. H., & Minor, H. E. (2003). Landslide generated impulse waves. 1. Instantaneous flow fields. *Experiments in Fluids*, 35(6), 505–519.

Göckler, G. (2012). Personal communication.

Gorbachev, S. I., Maksimovich, V. A., & Saranchev, V. O. (2007). Hybrid modelling of vortex formation at the Boguchany intake. *Hydropower and Dams*, (3), 64–68.

Gordon, J. L. (1970). Vortices at intakes. *Water Power*, 22(4), 137–138.

Granger, R. (1966). Steady 3-dimensional vortex flow. *Journal of Fluid Mechanics*, 25(3), 557–576.

Gulliver, J. S. & Rindels, A. J. (1985). Vortices at vertical intakes. *Proc. of the ASCE Hydraulics Division Specialty Conference, Lake Buena Vista, USA*, (pp. 973–978).

Gulliver, J. S. & Rindels, A. J. (1987). Weak vortices at vertical intakes. *Journal of Hydraulic Engineering*, 113(9), 1101–1116.

Gulliver, J. S., Rindels, A. J., & Lindblom, K. C. (1986). Designing intakes to avoid free-surface vortices. *International Water Power and Dam Construction*, 39(9), 24–28.

Haindl, K. (1959). Contribution to air entrainment by a vortex. *Proc. IAHR 8th Congress, Montreal, Canada*, 2, 16.D 1–17.

Hattersley, R. T. (1965). Hydraulic design of pump intakes. *Journal of the Hydraulics Division*, 91(2), 223–249.

Hecker, G. E. (1981). Model-prototype comparison of free-surface vortices. *Journal of the Hydraulics Division*, 107(10), 1243–1259.

Hecker, G. E. (1987). *Fundamentals of vortex intake flow*, (pp. 13–38). Swirling flow problems at intakes, IAHR Hydraulic Structures Design Manual 1, Taylor & Francis: Balkema, Rotterdam, NL.

Hite, J. E. & Mih, W. C. (1994). Velocity of air-core vortices at hydraulic intakes. *Journal of Hydraulic Engineering*, 120(3), 284–297.

Hodkinson, B. (1933). Free vortices. *The Engineer*, 156(Aug. 18), 656.

Hutter, K., Wang, Y., & Chubarenko, I. P. (2011). *Physics of Lakes*. Foundation of the Mathematical and Physical Background. Springer-Verlag Berlin Heidelberg.

Iversen, H. W. (1953). Studies of submergence requirements of high-specific-speed pumps. *Transactions of the ASME*, 75(4), 635–641.

Jain, A. K., Raju, K. G. R., & Garde, R. J. (1978). Vortex formation at vertical pipe intakes. *Journal of the Hydraulics Division*, 104(10), 1429–1445.

Karassik, I. J., Messina, J. P., Cooper, P., & Heald, C. C. (2008). *Pump Handbook - Guidlines for design of intakes for hydraulic plants*, volume 4. McGraw - Hill, New York, USA.

Keane, R. D. & Adrian, R. J. (1990). Optimization of paricle image velocimeters. 1. Double pulsed systems. *Measurement Science & Technology*, 1(11), 1202–1215.

Knauss, J. (1972). *Wirbel an Einläufen zu Wasserkraftanlagen.* Technical report, Versuchsanstalt für Wasserbau der Technischen Hochschule München, Germany [in German].

Knauss, J. (1983). *Wirbelbildung an Einlaufbauwerken (Luft- und Dralleintrag).* Technical report, Deutscher Verband für Wasserwirtschaft und Kulturbau e. V. (DVWK) [in German].

Knauss, J. (1987a). *Introduction*, (pp. 1–11). Swirling flow problems at intakes, IAHR Hydraulic Structures Design Manual 1, Taylor & Francis: Balkema, Rotterdam, NL.

Knauss, J. (1987b). *Prediction of critical submergence*, (pp. 57–76). Swirling flow problems at intakes, IAHR Hydraulic Structures Design Manual 1, Taylor & Francis: Balkema, Rotterdam, NL.

Knauss, J. (1987c). *Swirling flow problems at intakes.* IAHR Hydraulic Structures Design Manual. Taylor & Francis, Balkema/ Rotterdam, NL.

Kobus, H. (1974). Anwendung der Dimensionsanalyse in der experimentellen Forschung des Bauingenieurwesens. *Die Bautechnik*, 51(3), 88–94 [in German].

Kohlhase, S. (1973). *Über den Vordrall an Pumpeneinläufen im Wirbelfeld.* Mitteilungen 38, Franzius-Institut für Wasserbau und Küsteningenieurwesen, TU Hannover, Germany [in German].

Kolf, R. C. & Zielinski, P. B. (1959). The vortex chamber as an automatic flow-control device. *Journal of the Hydraulics Division*, 12, 1–8.

Krüger, D. A. V. (2009). *Iguassu river diversion for construction of segredo hydropower scheme.* Diversion of large Brazilian rivers, Brazilian Committee on Dams (C. Piasentin, ed.) & ICOLD.

Leon, F. P. & Beyerer, J. (2005). Surface characterization by morphological filtering. *Technisches Messen*, 72(12), 663–670.

Levi, E. (1972). Experiments on unstable vortices. *Journal of the Engineering Mechanics Division*, (EM3), 539–559.

Li, H. F., Chen, H. X., Ma, Z., & Zhou, Y. (2008). Experimental and numerical investigation of free surface vortex. *Journal of Hydrodynamics*, 20(4), 485–491.

Lugt, H. J. (1983). *Vortex flow in nature and technology.* Wiley, New York, USA: Wiley.

Lugt, H. J. (1985). Vortices and vorticity in fluid-dynamics. *American Scientist*, 73(2), 162–167.

Lugt, H. J. (1996). *Introduction to Vortex Theory.* Vortex Flow Press, Potomac, Maryland, USA.

Ma, J. M., Liang, Y. B., & Huang, J. T. (2000). Minimum submergence before double - entrance pressure intakes. *Journal of Hydraulic Engineering*, 126(8), 628–631.

Ma, J. M., Oberai, A. A., Drew, D. A., Lahey, R. T., J., & Moraga, F. J. (2010). A quantitative sub-grid air entrainment model for bubbly flows - plunging jets. *Computers & Fluids*, 39(1), 77–86.

Martin, H. & Pohl, R. (2009). *Technische Hydromechanik 4: Hydraulische und numerische Modelle.* Verlag Bauwesen, Berlin, Germany [in German].

MATLAB (2013). *MATLAB 8.1 (R2013a) User's Guide.* The MathWorks, Natick, Massachusetts, USA.

McCorquodale, J. A. (1968). Scale effects in swirling flow. *Journal of the Hydraulics Division*, 94(HY1), 285–300.

Meyer, A. (2012). *Modellfamilie zum Lufteintrag durch Einlaufwirbel.* Master Thesis, VAW, ETH Zurich, Zurich, Switzerland [unpublished, in German].

Möller, G., Detert, M., & Boes, R. (2012). Air entrainment due to vortices - state-of-the-art. *Proc. 2nd IAHR Europe Congress 2012*, (pp. paper B16).

Möller, G., Pinotti, M., & Boes, R. (2010). Einlaufwirbeluntersuchung am Kraftwerk Handeck 2 - Kritische Überdeckungshöhe und Wirbelunterdrünkungsmassnahmen. *Proc. Internationales Symposium Wallgau, Lehrstuhl und Versuchsanstalt für Wasserbau und Wasserwirtschaft, TU München*, (Bericht 124), 407–416 [in German].

Nagarkar, P. K. (1986). Submergence criteria for hydroelectric intake.

Nakayama, A. & Hisasue, N. (2010). Large eddy simulation of vortex flow in intake channel of hydropower facility. *Journal of Hydraulic Research*, 48(4), 415–427.

Odgaard, A. J. (1986). Free-surface air core vortex. *Journal of Hydraulic Engineering*, 112(7), 610–620.

Okamura, T., Kamemoto, K., & Matsui, J. (2007). CFD prediction and model experiment on suction vortices in pump sump. *Proc. of 9th Asian International Conference on Fluid Machinery*, (pp. AICFM9–053).

Padmanabhan, M. (1984). Air ingestion due to free-surface vortices. *Journal of Hydraulic Engineering*, 110(12), 1855–1859.

Padmanabhan, M. (2008). Personal communication.

Papillon, B., Kirejczyk, J., & Sabourin, M. (2000). Atmospheric air admission in hydroturbines. *Proc. Hydro Vision*, (pp. 1–11).

Pennino, B. J. & Hecker, G. E. (1979). A synthesis of model data for pumped storage intakes. *Proc. of the joint ASME/CSME applied mechanics, fluidsengineering and bioengineering conference*, (pp. 103–112).

Poullikkas, A. (2000). Effects of entrained air on the performance of nuclear reactor cooling pumps. *Proc. of Melecon 2000: Information Technology and Electrotechnology for the Mediterranean Countries*, (pp. 1028–1031).

Prosser, M. J. (1977). *The hydraulic design of pump sumps and intakes*. Technical report, British Hydromechanics Research Association (BHRA)/Construction Industry Research and Information Association (CIRIA).

Prosser, M. J., Paterson, I. S., & Noble, R. M. (1986). Pump intake design - the right approach. *Proc. of the Institution of Civil Engineers Part 1-Design and Construction*, 80, 832–836.

Quick, M. C. (1962). Scale relationships between geometrically similar free spiral vortices (part I). *Civil engineering and public works review*, (9), 1135–1138.

Quick, M. C. (1970). Efficiency of air-entraining vortex formation at water intake. *Journal of the Hydraulics Division*, 96(7), 1403–1416.

Raffel, M., Willert, C., & Kompenhans, J. (1998). *Particle Image Velocimetry*. Springer, Berlin, Germany.

Rajendran, V. P., Constantinescu, S. G., & Patel, V. C. (1999). Experimental validation of numerical model of flow in pump-intake bays. *Journal of Hydraulic Engineering*, 125(11), 1119–1125.

Rajendran, V. P. & Patel, V. C. (2000). Measurement of vortices in model pump-intake bay by PIV. *Journal of Hydraulic Engineering*, 126(5), 322–334.

Raju, K. G. R. & Garde, R. J. (1987). *Modelling of vortices and swirling flows.*, (pp. 77–90). Swirling flow problems at intakes, IAHR Hydraulic Structures Design Manual 1, Taylor & Francis: Balkema, Rotterdam, NL.

Rankine, W. J. M. (1861). *A manual of applied mechanics.* Griffin, Bohn and Company, London, UK: Griffin, Bohn and Company, London, UK.

Reddy, Y. R. & Pickford, J. A. (1972). Vortices at intakes in conventinal sumps. *Water Power*, 24(3), 108–109.

Reddy, Y. R. & Pickford, J. A. (1974). Vortex suppression in stilling pond overflow. *Journal of the Hydraulics Division*, 100(NHY11), 1685–1698.

Rindels, A. & Gulliver, J. S. (1983). *An experimental study of critical submergence to avoid free-surface vortices at vertical intakes.* Technical Report 224, St. Anthony Falls Hydraulic Laboratory, Mineapolis, Minnesota, USA.

Rohan, K. (1966). Conditions of similarity for a drain vortex. In *Modern trends in hydraulic engineering research*, volume 2 (pp. 89–93).

Rott, N. (1958). On the viscous core of a line vortex. *Zeitschrift fur Angewandte Mathematik und Physik*, 9b(5-6), 543–553.

Rutschmann, P., Volkart, P., & Vischer, D. L. (1987). *Design recommendations.*, (pp. 91–100). Swirling flow problems at intakes, IAHR Hydraulic Structures Design Manual 1, Taylor & Francis: Balkema, Rotterdam, NL.

Shapiro, A. H. (1962). Bath-tub vortex. *Nature*, 196(4859), 1080–1081.

Stahel, W. A. (2008). *Statistische Datenanalyse.* Vieweg, Wiesbaden, Germany [in German].

Suerich-Gulick, F., Gaskin, S., Villeneuve, M., Holder, G., & Parkinson, E. (2008). Experimental and numerical analysis of free surface vortices at a hydropower intake. *Proc. of the 7. Int. Conference on Hydroscience and Engineering (ICHE - 2006)*, (pp. 1–11).

Sulzer (2012). Personal communication.

Tastan, K. & Yildirim, N. (2010). Effects of dimensionless parameters on air entraining vortices. *Journal of Hydraulic Research*, 48(1), 57–64.

Tietjens, O. (1960). *Strömungslehre - Physikalische Grundlagen vom technischen Standpunkt.* Springer, Berlin, Germany.

Tokyay, T. E. & Constantinescu, S. G. (2006). Validation of a large-eddy simulation model to simulate flow in pump intakes of realistic geometry. *Journal of Hydraulic Engineering*, 132(12), 1303–1315.

Travis, Q. B. & Mays, L. W. (2011). Prediction of intake vortex risk by nearest neighbors modeling. *Journal of Hydraulic Engineering*, 137(6), 701–705.

Trefethen, L. M., Bilger, R. W., Fink, P. T., Luxton, R. E., & Tanner, R. I. (1965). Bath-tub vortex in southern hemisphere. *Nature*, 207(5001), 1084–1085.

Tritton, D. J. (1988). *Physical fluid dynamics*. Oxford Universiy Press, New York, USA: Oxford Universiy Press, New York, USA.

Uni-KL (2012). Url: `http://www.uni-kl.de/SAM/data/fotos/pr_einlauf.jpg` (downloaded 10.1.2012), University Kaiserslautern, Germany.

VAW (2006). *Kopswerk II, Peltonturbinen im Gegendruckbetrieb, Hydraulische Modellversuche zur Entlüftungsproblematik*. Technical Report 4212, Laboratory of Hydraulics, Hydrology and Glaciology (VAW), Zurich, Switzerland [unpublished, in German].

VAW (2010). *Kraftwerk Handeck 2 - Physikalische Modellversuche zum Einlaufbauwerk*. Technical Report 4280, Laboratory of Hydraulics, Hydrology and Glaciology (VAW), Zurich, Switzerland [unpublished, in German].

VAW (2013a). *F.M. Hongrin-Léman, Hydraulic investigation of the pumped-storage scheme Veytaux 2*. Technical Report 4296, Laboratory of Hydraulics, Hydrology and Glaciology (VAW), Zurich, Switzerland [unpublished].

VAW (2013b). *Gibe III Hydroelectric Project - Middle Outlets of Gibe III dam*. Technical Report 4294, Laboratory of Hydraulics, Hydrology and Glaciology (VAW), Zurich, Switzerland [unpublished].

Wang, Y. K., Jiang, C. B., & Liang, D. F. (2011). Comparison between empirical formulae of intake vortices. *Journal of Hydraulic Research*, 49(1), 113–116.

Wang, Z. & Gursul, I. (2012). Unsteady characteristics of inlet vortices. *Experiments in Fluids*, 53(4), 1015–1032.

Westergaard, C., Madsen, B., Marassi, M., & Tomasini, E. (2003). Accuracy of PIV signals in theory and practice. *Proc. of the 5th International Symposium on Particle Image Velocimetry*, (pp. paper 3301).

Westerweel, J. (1994). Efficient detection of spurious vectors in particle image velocimetry data. *Experiments in Fluids*, 16(3-4), 236–247.

Westerweel, J. & Scarano, F. (2005). Universal outlier detection for PIV data. *Experiments in Fluids*, 39(6), 1096–1100.

Wickenhäuser, M. (2008). Zweiphasenströmung in Entlüftungssystemen von Druckstollen. *VAW-Mitteilung 205 (H.-E. Minor, ed.) ETH Zurich, Switzerland [in German].*

Yildirim, N. (2004). Critical submergence for a rectangular intake. *Journal of Engineering Mechanics*, 130(10), 1195–1210.

Yildirim, N. & Jain, S. C. (1979). Effect of a surface layer on free surface vortex. In *Proc. of XVIII Congress IAHR, Delft, Netherlands* (pp. 411–418).

Yildirim, N. & Kocabas, F. (1995). Critical submergence for intakes in open-channel flow. *Journal of Hydraulic Engineering*, 121(12), 900–905.

Yildirim, N. & Kocabas, F. (1998). Critical submergence for intakes in still-water reservoir. *Journal of Hydraulic Engineering*, 124(1), 103–104.

Yildirim, N., Kocabas, F., & Gulcan, S. C. (2000). Flow-boundary effects on critical submergence of intake pipe. *Journal of Hydraulic Engineering*, 126(4), 288–297.

Yildirim, N. & Tastan, K. (2009). Critical submergence for multiple pipe intakes. *Journal of Hydraulic Engineering*, 135(12), 1052–1062.

Yildirim, N., Tastan, K., & Arslan, M. M. (2009). Critical submergence for dual pipe intakes. *Journal of Hydraulic Research*, 47(2), 242–249.

Zhang, W. & Sarkar, P. P. (2012). Near - ground tornado-like vortex structure resolved by particle image velocimetry (PIV). *Experiments in Fluids*, 52(2), 479–493.

Zielinski, P. B. & Villemonte, J. R. (1968). Effect of viscosity on vortex-orifice flow. *Journal of the Hydraulics Division*, 94(HY3), 745–752.

Acknowledgements

I would like to express my gratitude to all people who contributed in different ways to this work. In particular I would like to acknowledge the following persons:

- Prof. Dr. R.M. Boes, Director of VAW, who was the supervisor of this work. Many thanks for giving me the opportunity to conduct this work.
- Prof. Dr. A. Schleiss (EPF Lausanne, CH) kindly took on the duty of a co-examiner. I would like to thank him very much.
- Prof. Dr. J.S. Gulliver (University of Minnesota, USA) I would like to thank for thoroughly reviewing this doctoral thesis and being a co-examiner.
- I would like to thank my advisor Dr. Martin Detert for his excellent ideas, for the fruitful and interesting discussions and for the continuous motivation.
- I want to thank Andreas Meyer, Jens Keller, and Marius Bühlmann for their commitment in our vortex research group. You all did a great research job.
- Thanks to all the colleagues and friends from VAW who created a great working atmosphere.
- I am especially grateful to my wife Berit who gave me love, motivation and encouragement to always look on the bright side of life. Many thanks go to our two daughters Mette and Grete, who are truly amazing.
- I would like to thank my parents Ulrike-Sabine and Peter Möller as well as my grandparents Ingeborg and Heinz Möller who made everything possible.
- I am very grateful to my friends Dr. Martin Wickenhäuser and Dr. Volker Weitbrecht for sharing their knowledge, their great ideas, many helpful inputs and discussions. Guys, now I'm looking forward to many joint ski tours again!
- The fantastic images of the air-core were arranged and taken by my friend Christian (www.christianriisruggaber.com). Thank you for your dedication!
- Thank you Prof. K. Hutter for the gainful discussions regarding vorticity!
- I have also appreciated the excellent work of all the staff in the mechanics workshop, the laboratory, and the electronics workshop of VAW.
- Drawings, graphics, and photographs in the present work were most carefully made by Mr. W. Thürig and Mr. A. Schlumpf. Thank you!
- I would like to thank swiss*electric* research and the Swiss Federal Office of Energy (SFOE) for their financial support as well as Arnoldo Baumann, Pöyry Energy AG Zurich, for their technical supervision.

Appendix A

Air Discharge Q_{a}

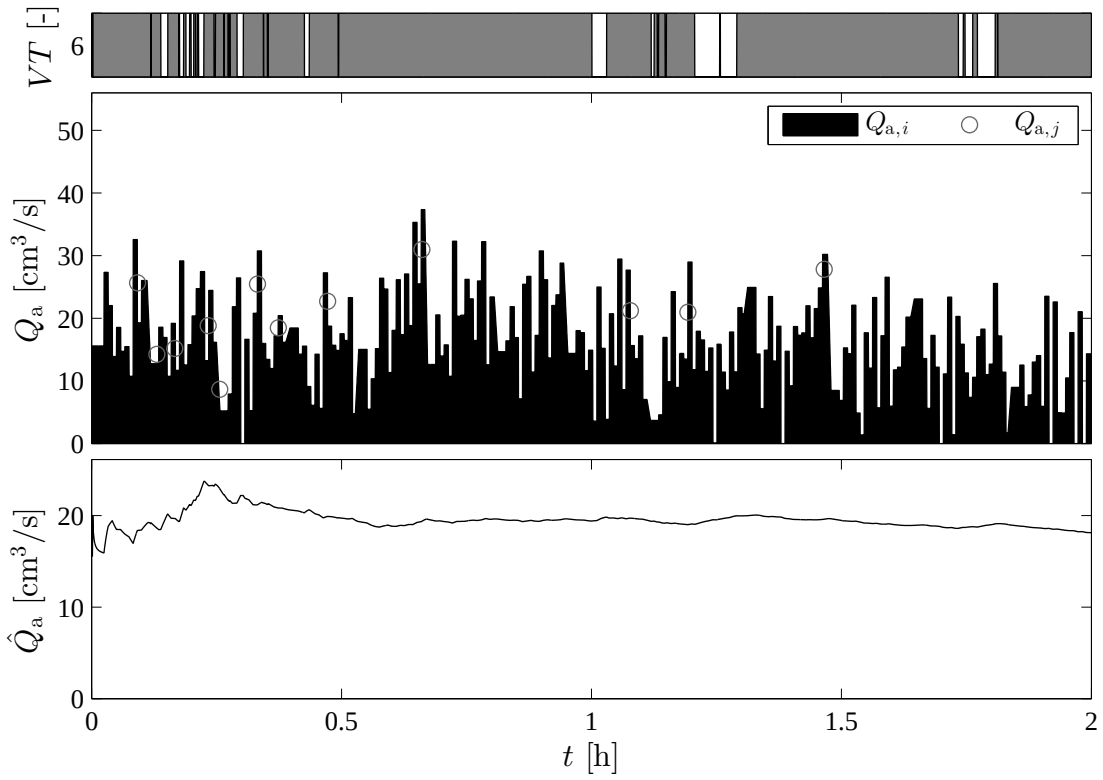

Figure A.1: Time series of vortex types VT, actual air discharge $Q_{\mathrm{a},i}$ and $VT6$ phase average $Q_{\mathrm{a},j}$, and running average $\hat{Q}_{\mathrm{a},i}$ for run #1 ($h/D = 1.25$, $\mathsf{F}_D = 0.6$, see Table 4.2).

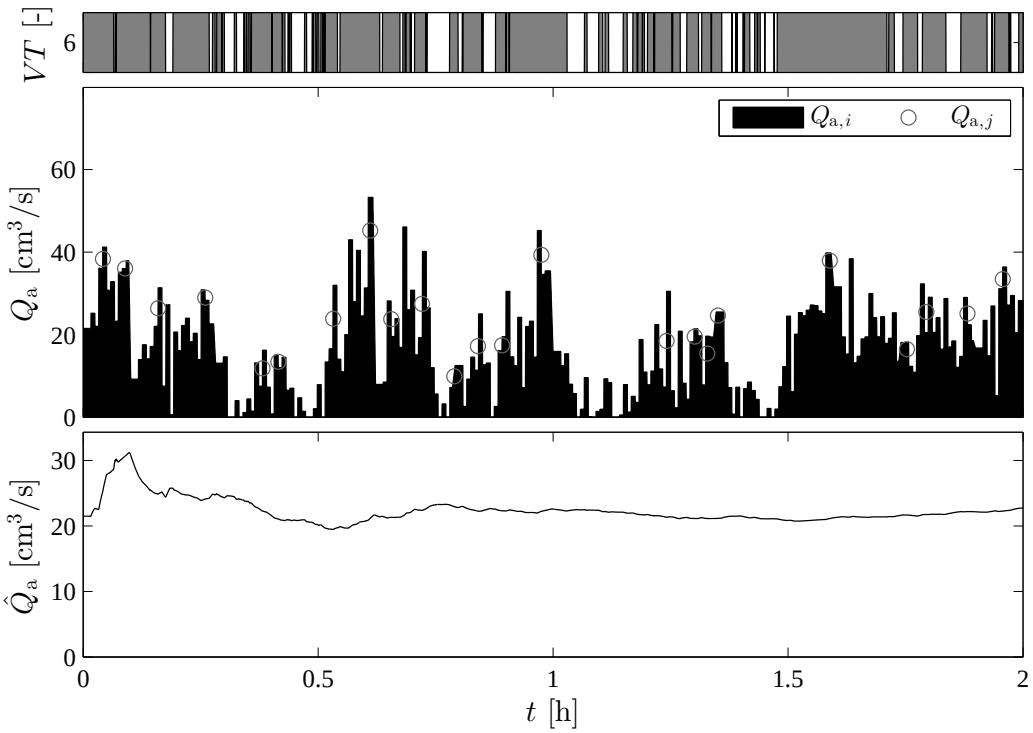

Figure A.2: Time series of vortex types VT, actual air discharge $Q_{\mathrm{a},i}$ and $VT6$ phase average $Q_{\mathrm{a},j}$, and running average $\hat{Q}_{\mathrm{a},i}$ for run #8 ($h/D = 1.5$, $\mathsf{F}_D = 0.7$, see Table 4.2).

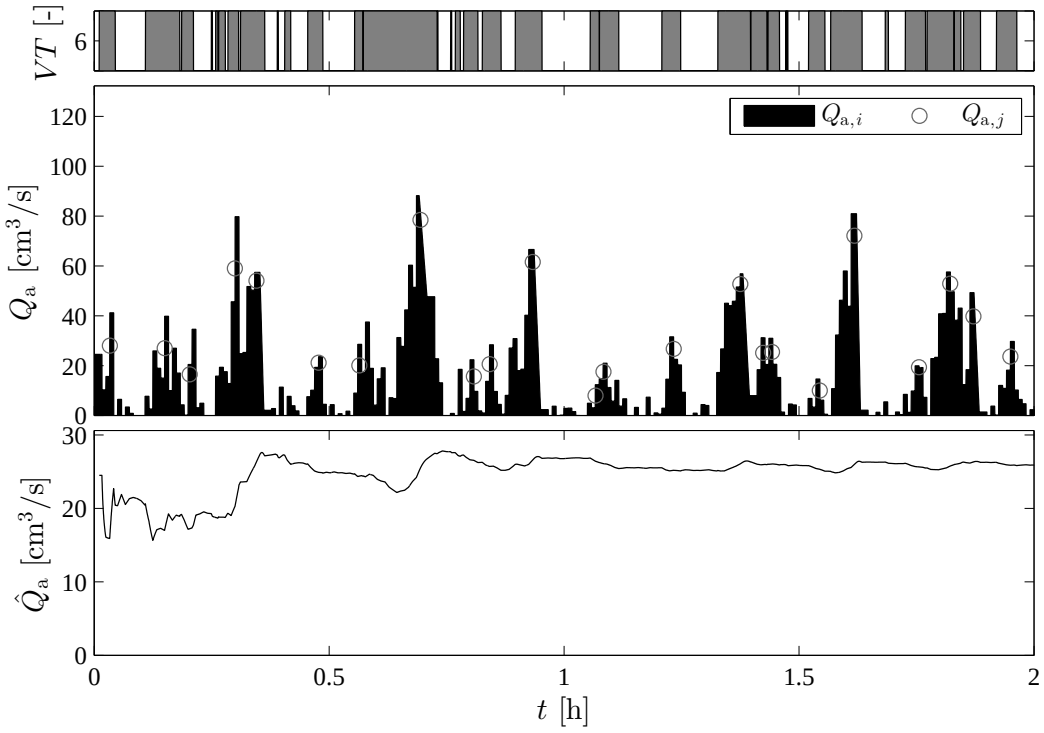

Figure A.3: Time series of vortex types VT, actual air discharge $Q_{\mathrm{a},i}$ and $VT6$ phase average $Q_{\mathrm{a},j}$, and running average $\hat{Q}_{\mathrm{a},i}$ for run #16 ($h/D = 1.75$, $\mathsf{F}_D = 0.8$, see Table 4.2).

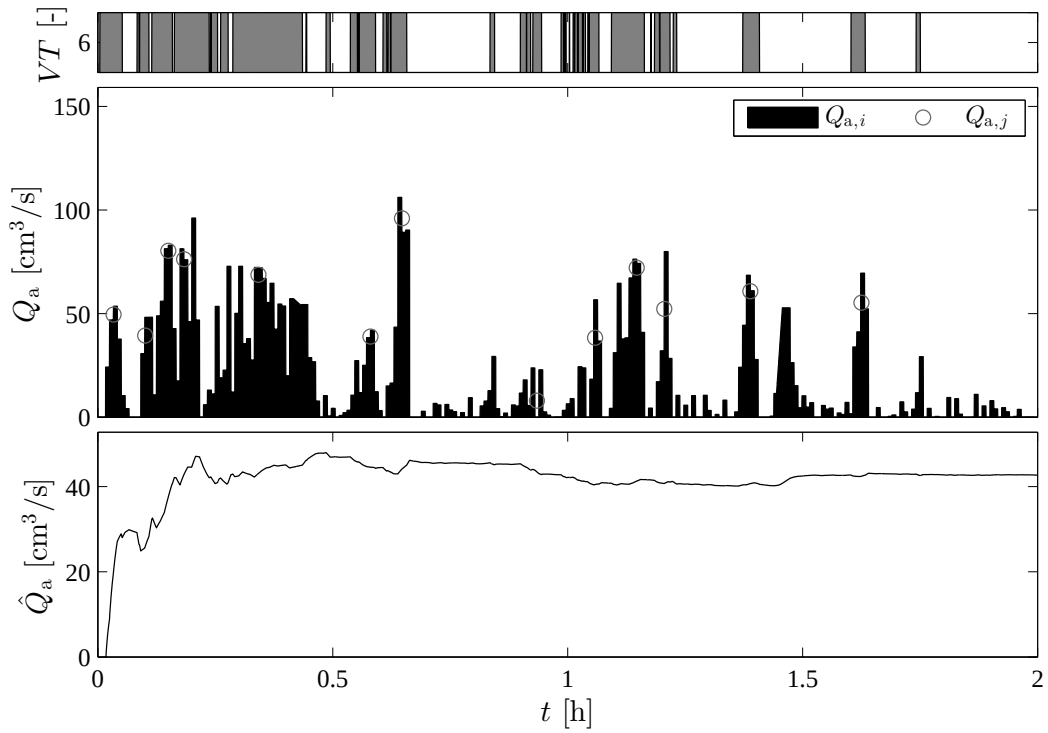

Figure A.4: Time series of vortex types VT, actual air discharge $Q_{\mathrm{a},i}$ and $VT6$ phase average $Q_{\mathrm{a},j}$, and running average $\hat{Q}_{\mathrm{a},i}$ for run #22 ($h/D = 2$, $\mathsf{F}_D = 0.9$, see Table 4.2).

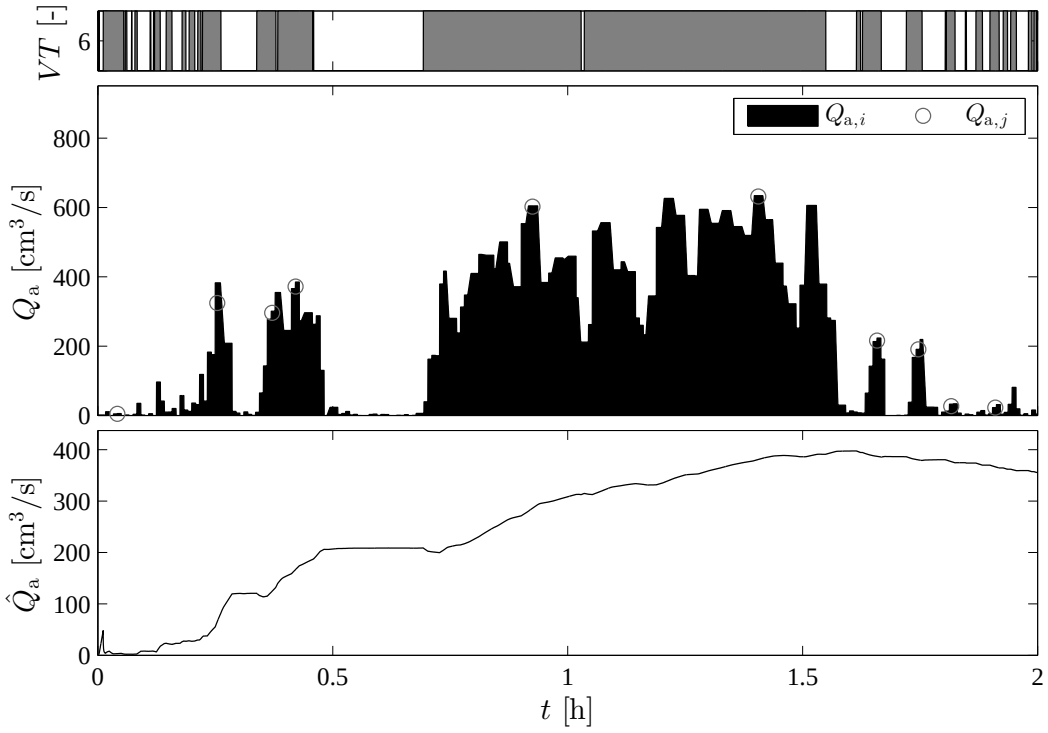

Figure A.5: Time series of vortex types VT, actual air discharge $Q_{\mathrm{a},i}$ and $VT6$ phase average $Q_{\mathrm{a},j}$, and running average $\hat{Q}_{\mathrm{a},i}$ for run #28 ($h/D = 2.25$, $\mathsf{F}_D = 1$, see Table 4.2).

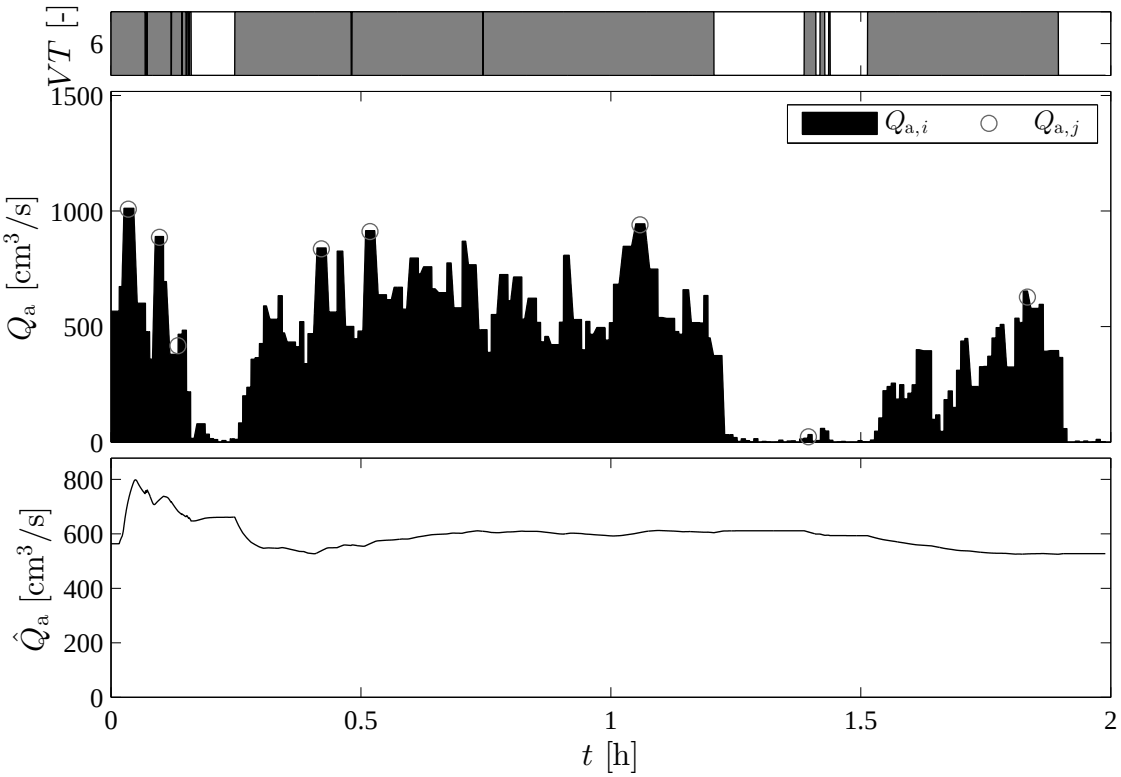

Figure A.6: Time series of vortex types VT, actual air discharge $Q_{\mathrm{a},i}$ and $VT6$ phase average $Q_{\mathrm{a},j}$, and running average $\hat{Q}_{\mathrm{a},i}$ for run #33 ($h/D = 2.5$, $\mathsf{F}_D = 1.1$, see Table 4.2).

Appendix B

Velocity Fields of the Vortex

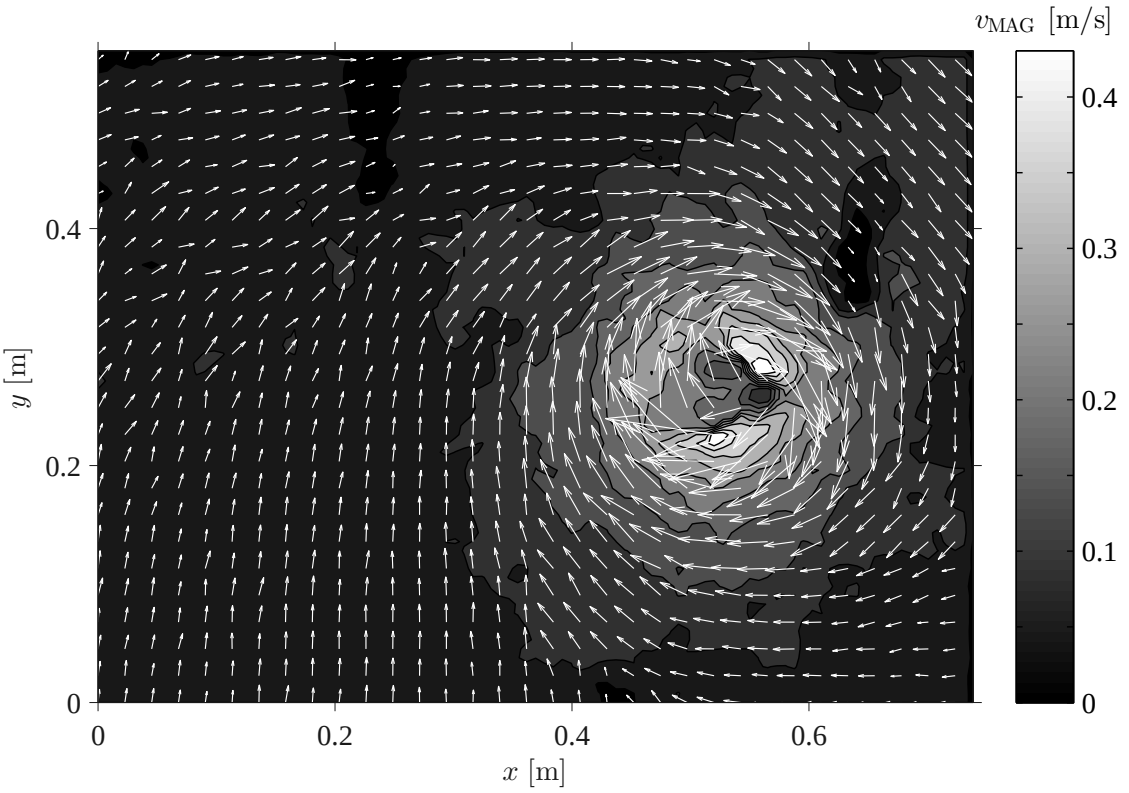

Figure B.1: Bottom upwards view to the velocity field of an intake vortex (run #8.13.2).

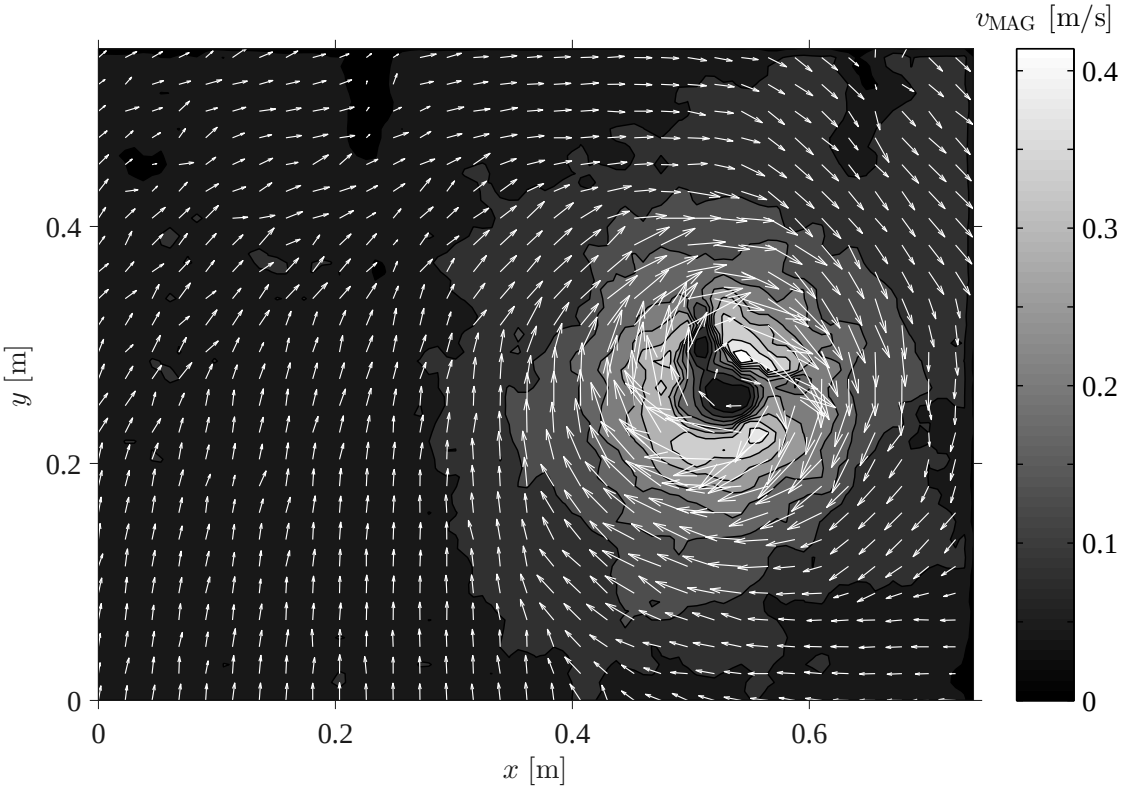

(a) #8.13.3

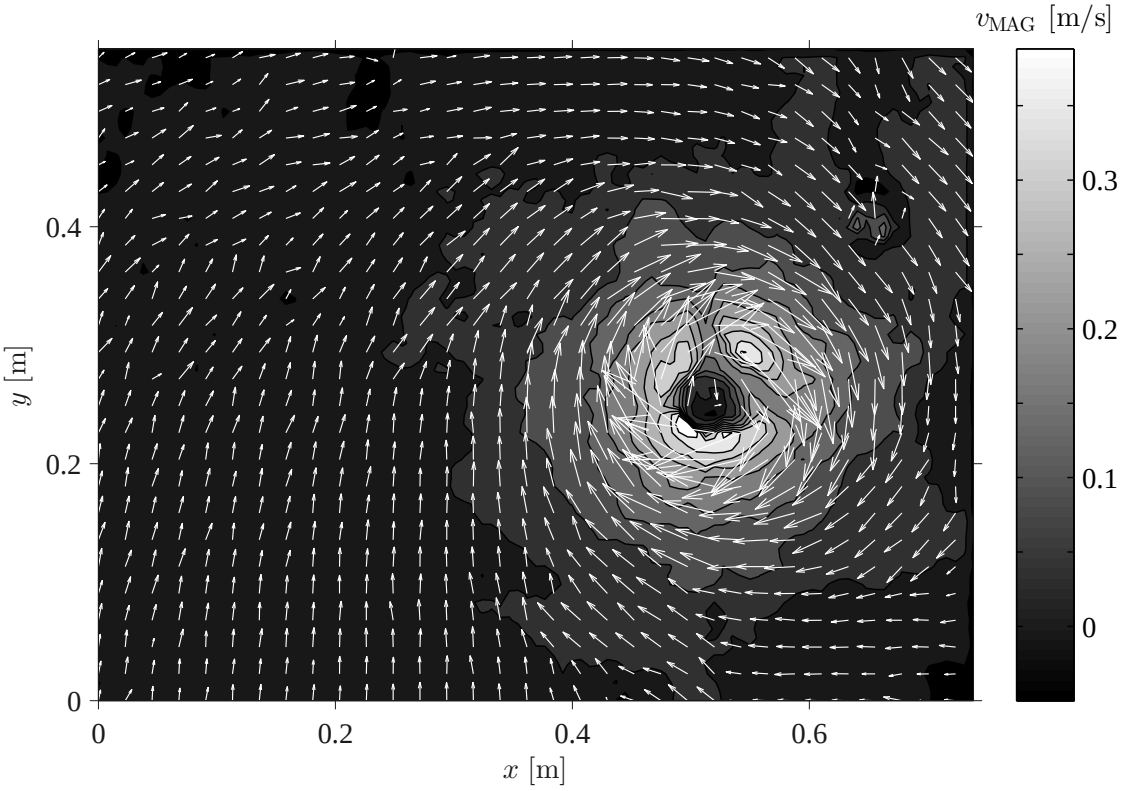

(b) #8.13.4

Figure B.2: Bottom upwards view to the velocity field of an intake vortex (run #8.13.3–4).

Appendix C

Vortex Wandering

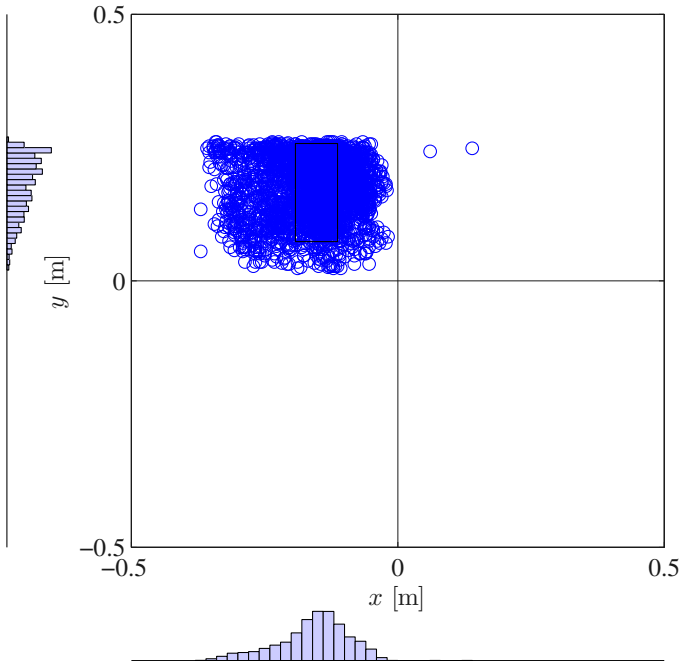

Figure C.1: Center coordinates determined within the circulation procedure which enables to track the vortex path. The black rectangle indicates the 2D IQR that can be derived by the distributions shown next to the x-axis and the y-axis (Run #20, $h/D = 2.00$, $\mathsf{F}_D = 0.8$).

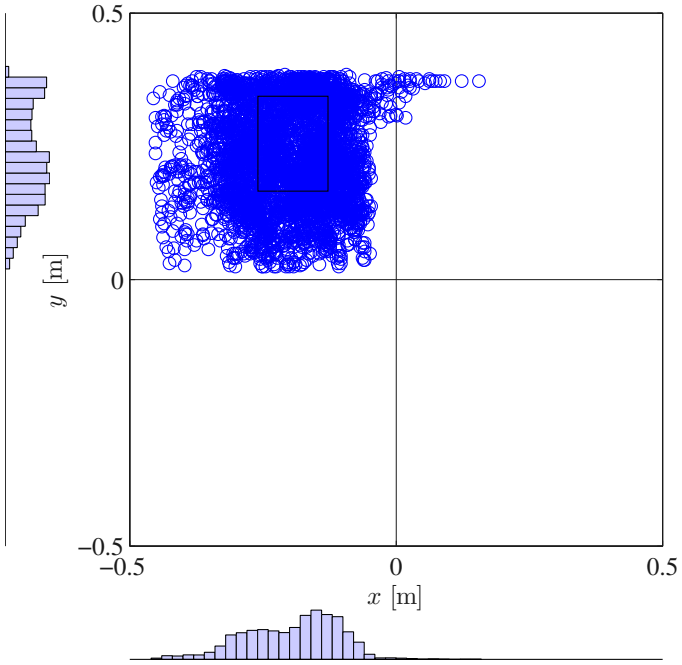

Figure C.2: Center coordinates determined within the circulation procedure which enables to track the vortex path. The black rectangle indicates the 2D IQR that can be derived by the distributions shown next to the x-axis and the y-axis (Run #27, $h/D = 2.25$, $\mathsf{F}_D = 0.9$).

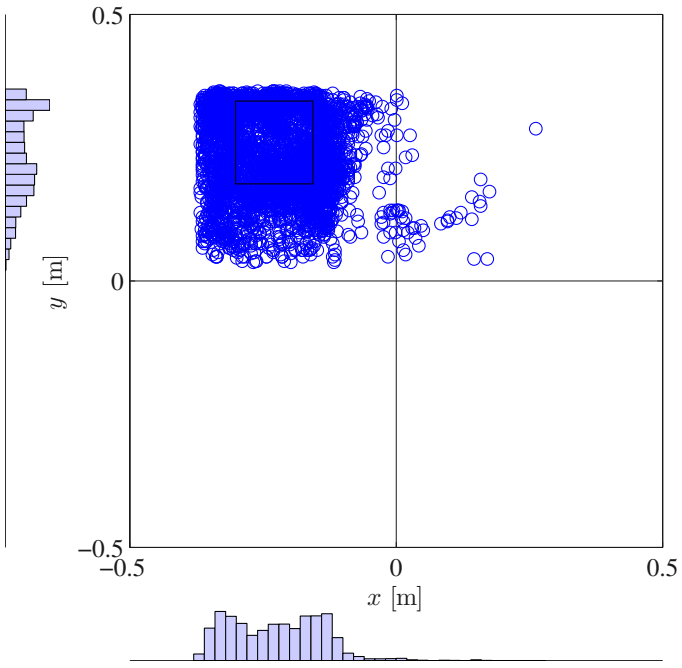

Figure C.3: Center coordinates determined within the circulation procedure which enables to track the vortex path. The black rectangle indicates the 2D IQR that can be derived by the distributions shown next to the x-axis and the y-axis (Run #32, $h/D = 2.50$, $\mathsf{F}_D = 1.0$).

Appendix D

Appearance of Intake Vortices

The appearance of intake-vortices is fascinating. Some visual examples are given below.

Figs. D.1a–d visualize the birth of a second vortex. If this phenomenon occurs the two vortices affect each other as described in chapter 2.2.6. Thus, this stadium is very unstable and remains only a short duration.

Figs. D.2a–d show an example of a straight air core tube. This stadium is almost stable. The air core wall is superimposed by capillary waves. These waves have a spiral downwards shape, and the vertical velocity component is small. It can be assumed that the vertical velocity component introduced in chapter 2.3.1 causes this spiral behavior.

Figs. D.3a–h form a series of photographs wherein the birth and decay of a second vortex is shown. The two vortices exist close to each other and wrap around each other from time to time. This stadium is short as well.

The appearance of vortices is largely manifold. The appearance can be determined systematically by the PIV measurements and the developed procedure described in chapter 4.4 and chapter 4.5.

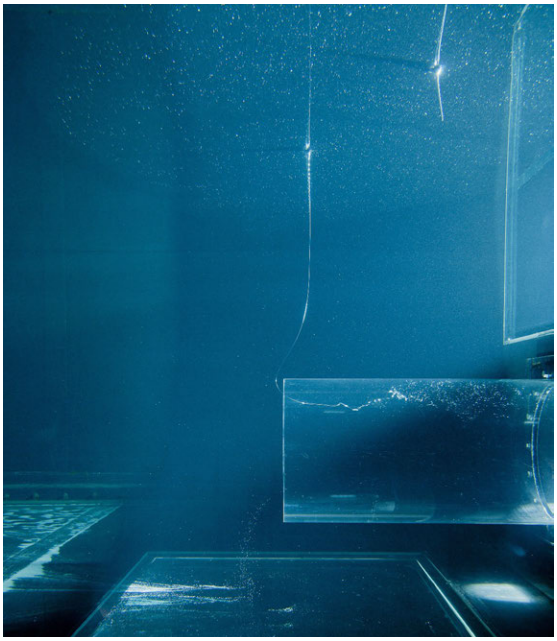

(a) Time: 8:46:40

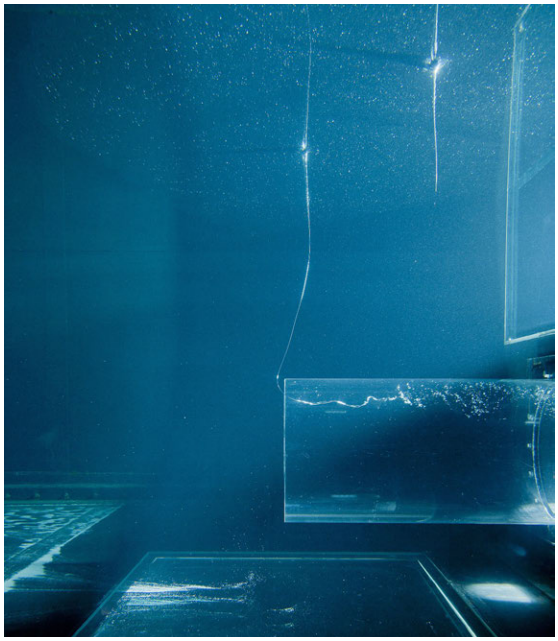

(b) Time: 8:46:45

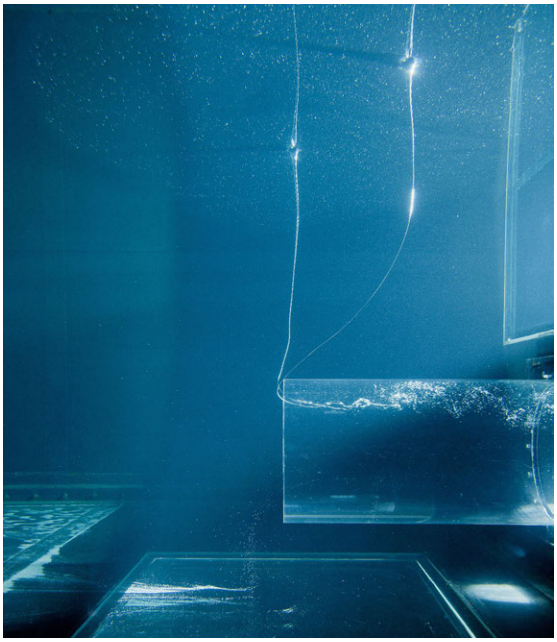

(c) Time: 8:46:48

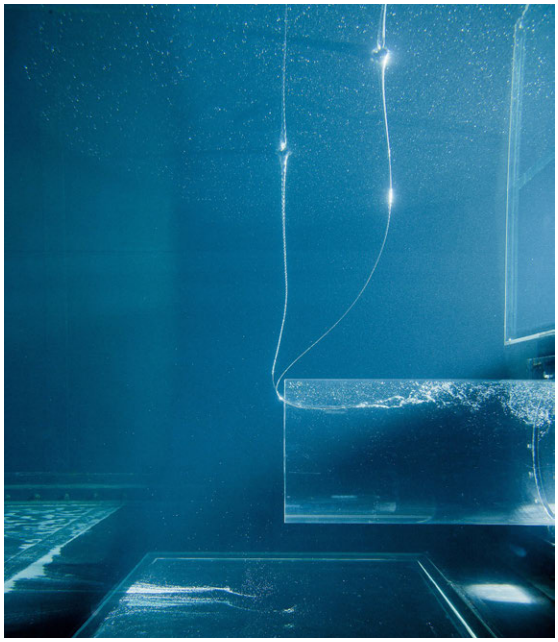

(d) Time: 8:46:51

Figure D.1: Birth of a second intake vortex.

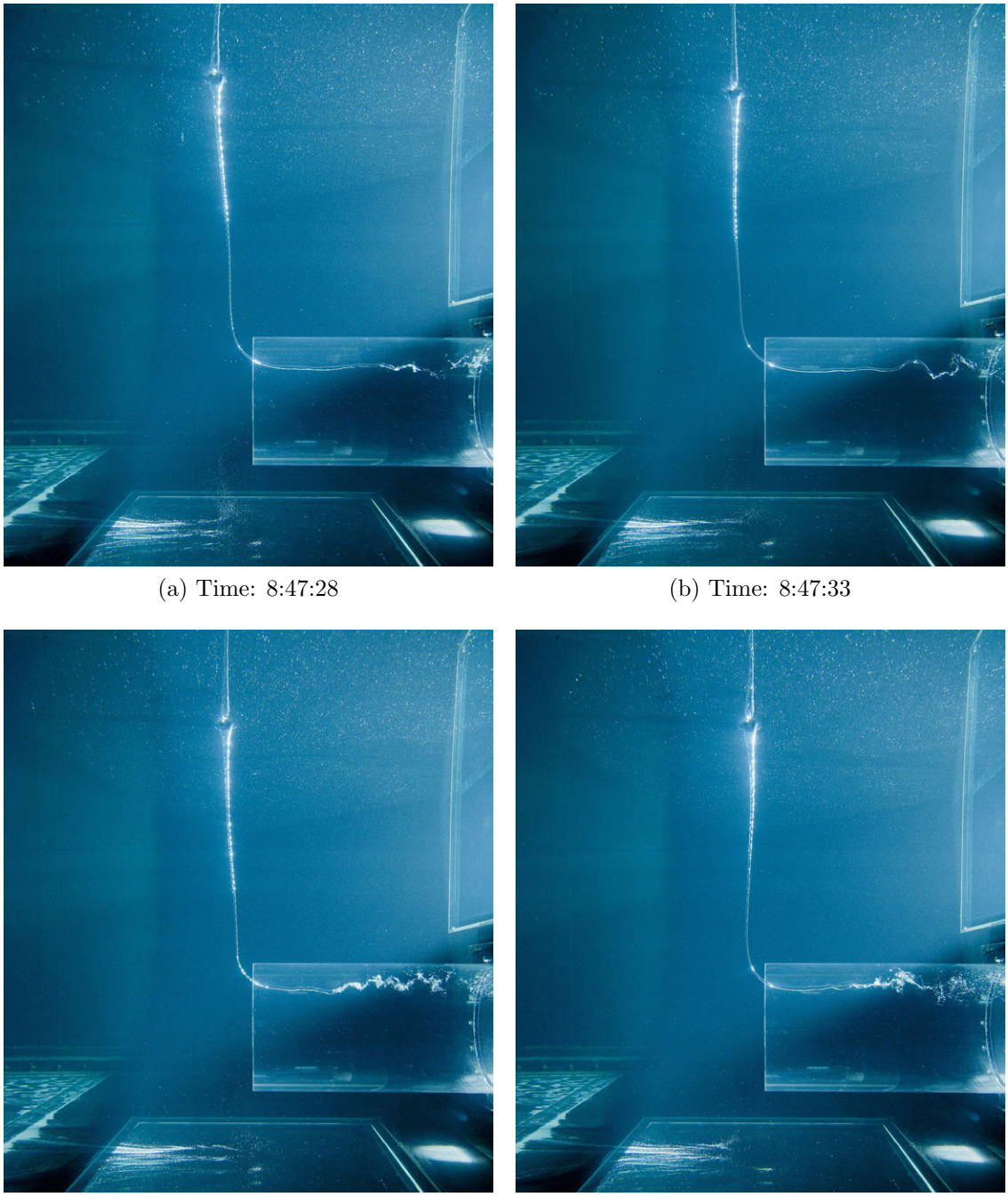

(a) Time: 8:47:28

(b) Time: 8:47:33

(c) Time: 8:47:36

(d) Time: 8:47:42

Figure D.2: Straight and stable vortex air core intruding deeply into the intake pipe. The tube wall is superimposed by capillary waves.

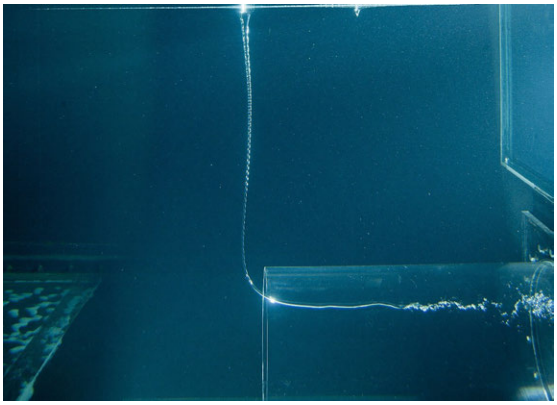

(a) Time: 9:06:40

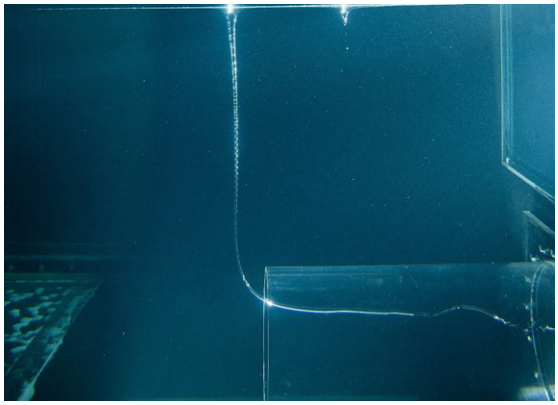

(b) Time: 9:06:43

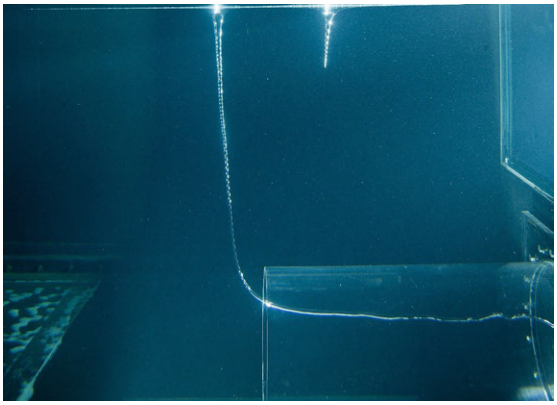

(c) Time: 9:06:46

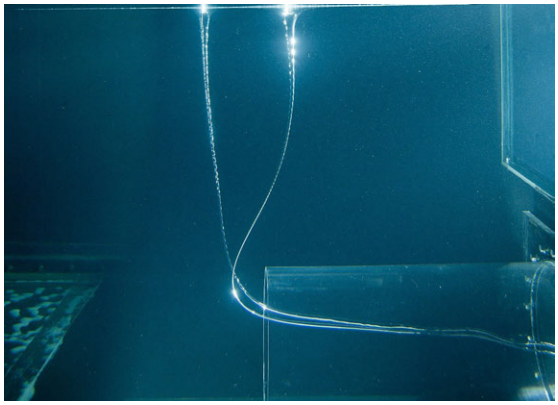

(d) Time: 9:06:50

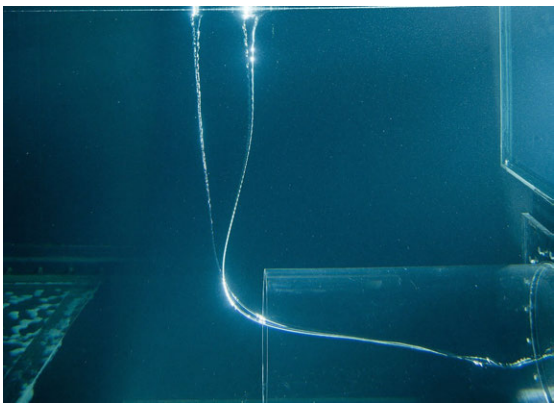

(e) Time: 9:06:53

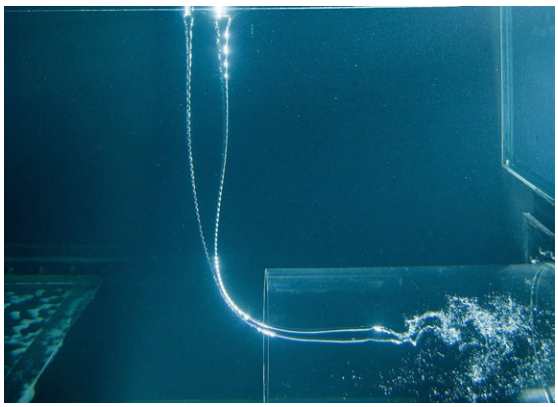

(f) Time: 9:06:55

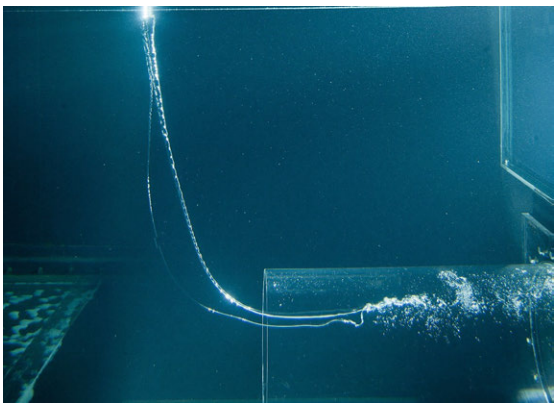

(g) Time: 9:07:03

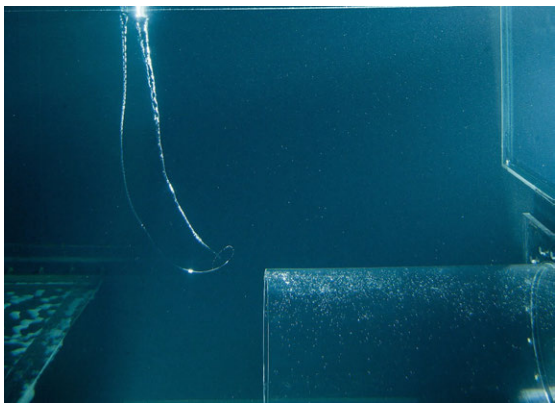

(h) Time: 9:07:05

Figure D.3: Birth and decay of a second intake vortex. Image series within 25 s.

Appendix E

Data-CD

A data-CD is offered containing the relevant data that led to this Thesis. It is available on request at

email: info@vaw.baug.ethz.ch
URL: www.vaw.ethz.ch/